Probing Protein Interfaces in Health and Disease by Single-Molecule Magnetic Tweezers Force Spectroscopy

Sophia Gruber

Munich, November 2021

Probing Protein Interfaces in Health and Disease by Single-Molecule Magnetic Tweezers Force Spectroscopy

Dissertation

an der
Fakultät für Physik
Ludwig–Maximilians–Universität München

vorgelegt von
Sophia Gruber
aus Erlangen

München, den 30.11.2021

Erstgutachter:	Prof. Dr. Jan Lipfert
Zweitgutachter:	Dr. Katarzyna Tych
Tag der mündlichen Prüfung:	13.01.2022

Kräfte sind in der Natur allgegenwärtig. Sie beeinflussen und kontrollieren viele lebensnotwenige Prozesse wie Zellmotilität und -adhäsion, Blutgerinnung, oder Pathogen:Wirt Interaktionen. Auf molekularer Ebene werden Kraft-aktivierte Prozesse von Kraft-sensitiven Proteinen eingeleitet, die durch externe mechanische Stimuli getriggert werden und komplexe Ereignisketten in Gang setzen. Abgesehen von Regulation und Aktivierung einzelner Proteine können Kräfte auch Interaktionen zwischen mehreren Proteinen entgegenwirken. Dies erschwert beispielsweise Protein-basiertes Binden von Pathogenen an Wirtszellen. Um zahlreiche biologische Prozesse, die unter Krafteinfluss stattfinden zu verstehen, ist es notwendig, den Einfluss mechanischer Stimuli auf einzelne Proteine und Protein:Protein Interaktionen zu untersuchen. Auf dem Level einzelner Proteine werden Kräfte beispielsweise durch hydrodynamischen Widerstand, Membrandeformationen, oder Spannungen an Zell-Zell und Zell-Extrazellulären Kontakten ausgeübt [1]. Die Größenordnung der Kräfte, die dabei auf einzelne Proteine wirken, reicht von wenigen Pikonewton für einzelne Muskelproteine während Muskelkontraktionen [2] bis hin zu einigen Nanonewton für Proteine, die Pathogen Adhäsion vermitteln [3].
Magnetische Pinzetten (engl. Magnetic tweezers, “MT”) sind ein Instrument für Einzelmolekül Kraftspektroskopie (engl. single-molecule force spectroscopy, “SMFS”), mit dem die Reaktion einzelner Proteine auf konstante Kräfte untersucht werden kann. Das Spektrum der Kräfte, die mit MT angelegt werden können, reicht von 0.01 pN bis hin zu 100 pN und deckt damit einen großen Bereich physiologisch relevanter Kräfte für Proteinaktivierung und Protein:Protein Interaktionen ab. Das Verhalten einzelner Proteine ist aufgrund verschiedener Entfaltungspfade und thermodynamischer Stochastik inhärent heterogen. MT können diese Heterogenität auflösen, da sie das Verhalten einzelner Moleküle untersuchen. Zugleich können MT viele Proteine gleichzeitig über lange Zeiträume hinweg beobachten, was es ermöglicht, seltene Zustände wahrzunehmen und zu charakterisieren. Daher sind MT ideal geeignet, um die Stabilität von Protein:Protein Interaktionen zu charakterisieren, Kraft-aktivierte Proteine zu untersuchen, oder die freie Energielandschaft von Proteinfaltungen abzubilden. Im Rahmen der Arbeit, die ich hier präsentiere, habe ich die Möglichkeiten von MT voll ausgeschöpft und sowohl Protein:Protein Interaktionen, als auch einzelne Proteine untersucht.
Die meisten Strategien, um Proteine für MT SMFS an magnetischen Kugeln zu befestigen, basieren auf der nicht-kovalenten, aber sehr stabilen Bindung zwischen dem Protein Streptavidin (SA) und dem kleinen Molekül Biotin. Wir haben ein Protokoll entwickelt, um die Anbindungsgeometrie von SA an magnetische Kugeln präzise zu kontrollieren. Dies erhöht die Lebensdauer der SA:Biotin Interaktion drastisch [4] (Kapitel 3). In Zukunft wird dieses Protokoll dadurch lange Messungen bei hohen Kräften erleichtern. Darauf basierend, habe ich die (Ent-)Faltungskinetik und mechanische Stabilität einiger medizinisch relevanter Proteine und Protein:Protein Wechselwirkungen untersucht.
Von Willebrand Faktor (VWF) ist ein multimeres, vaskuläres Glykoprotein, das wesentlich in die Blutgerinnung involviert ist. Für diese Funktion wird VWF durch erhöhte hydrodynamische Kräfte bei vaskulären Verletzungen aktiviert. Zentral für diese Kraftaktivierung ist die Länge der VWF Multimere, da die Spitzenkräfte, die auf sie wirken abhängig vom Quadrat ihrer Länge sind [5;6]. Im Rahmen meiner Dissertation habe ich MT verwendet, um eine Konformationsänderung in der D’D3 Domäne von VWF zu untersuchen (Kapitel 4). Unsere Ergebnisse zeigen eine starke pH-Abhängigkeit der Konformationsänderung, die zwei ungebundene Cysteine – Cys1099 und Cys 1142 – freilegt und damit die Multimerisierung von VWF ermöglicht. Darüber hinaus stellten wir fest, dass Koagulationsfaktor VIII einen Einfluss auf die Kinetik der Konformationsänderung hat, was eine unbekannte Bindungsstelle in der D Domäne nahelegt.
Während meiner Dissertation kam es zum Ausbruch eines neuartigen Coronaviruses (SARS-CoV-2), der zu einer globalen Pandemie führte [7–9]. SARS-CoV-2 Infektionen werden durch das Binden der Rezeptor-bindenden Domäne (“RBD”, lokalisiert an der Spitze jedes Spike Proteins) an den menschlichen Rezeptor ACE2 eingeleitet. Die virale Anbindung passiert in der dynamischen Umgebung der Atemwege, wo mechanische Kräfte der Bindung ununterbrochen entgegenwirken. Wir haben eine neue Methode entwickelt, um die Wechselwirkung zwischen Rezeptoren und Liganden unter Kraft zu untersuchen [10] (Kapitel 5). Im Kontext von SARS-CoV-2 haben wir mit dieser Methode die RBD:ACE2 Wechselwirkung bezüglich ihrer Stabilität und Affinität charakterisiert. Wir haben drei Techniken — MT-basierte SMFS, AFM-basierte SMFS und computer-basierte nicht-Gleichgewicht Molekulardynamik Simulationen — verwendet, um die Interaktion im gesamten physiologisch relevanten Kraftbereich zu untersuchen. So konnten wir eine deutlich erhöhte Kraftstabilität und Affinität der SARS-CoV-2 RBD:ACE2 Interaktion gegenüber der SARS-CoV-1 RBD:ACE2 Interaktion (Auslöser der Epidemie von 2002–2004) mit allen drei Techniken nachweisen. Konzeptuell konnten wir darüber hinaus zeigen, dass unsere Methode in MT nachweisen kann, wenn Moleküle die Interaktion zwischen RBD und ACE2 blockieren. Damit bietet sich unsere Methode an, um potentielle therapeutische Antikörper im Hinblick auf ihre blockierenden Eigenschaften zu untersuchen. Basierend auf diesen Ergebnissen haben wir unsere Experimente mit aktuellen Varianten des SARS-CoV-2 wiederholt, um diese mit dem Wildtyp (WT) bezüglich ihrer Kraftstabilität und Affinität zu vergleichen (Kapitel 6). Indem wir die Kraft-abhängigen Lebenszeiten der In-

teraktion nach null Kraft extrapoliert haben, konnten wir vorher veröffentlichte Affinitätsdaten akkurat reproduzieren [11–17]. Dabei wiesen wir höhere Affinitäten für alle Varianten verglichen mit dem WT nach. Trotz der Unterschiede in der *Affinität* konnten wir zeigen, dass nur die α Variante signifikant Kraft-stabiler ist als der WT. Unsere Ergebnisse deuten darauf hin, dass Kraft-Stabilität die virale Übertragbarkeit komplementär zu einer erhöhten Affinität vergrößern kann.

Zusammenfassend habe ich mit meinen Resultaten bestätigt, dass MT ein wertvolles Instrument sind, um vielfältige Aspekte einzelner Proteinfaltungen und Protein:Protein Wechselwirkungen zu untersuchen. Ich erwarte, dass die von uns entwickelte, verbesserte Anbindungsstrategie von großem Nutzen für viele zukünftige Protein SMFS Experimente sein wird. Außerdem hoffe ich, dass unsere Methode zur Untersuchung der Stabilität von Rezeptor:Ligand Interaktionen zukünftig verwendet werden kann, um Antikörper Bindungen nachzuweisen sowie die Bindung anderer Viren an ihre Wirtszellen, die unter dynamischen Bedingungen zustande kommen, zu charakterisieren.

Forces are omni-present in nature, governing many vital processes including cell motility and adhesion, blood coagulation, or host:pathogen interactions. At the molecular level, they can induce processes by triggering force-sensing proteins, which react to external mechanical stimuli and initiate complex signaling cascades. Besides regulating and triggering individual proteins, mechanical forces also counteract protein:protein interactions (PPI), impeding for example protein-mediated pathogen attachment to host cells. Studying how force influences force-sensing proteins and how it affects PPI is thus fundamental to understanding many biological processes. On the protein-level, mechanical force can be generated by hydrodynamic drag, membrane deformation, or stresses at cell-cell and cell-extracellular matrix junctions [1]. The magnitude of forces acting on individual proteins can be diverse, ranging from a few piconewton for individual muscle proteins during muscle contraction [2] to several nanonewton for proteins mediating pathogen adhesion [3].

Magnetic tweezers (MT) are a single-molecule force spectroscopy (SMFS) technique enabling investigation of the force-response of individual proteins. They can access a force range from 0.01 to 100 pN, which is physiologically relevant for many conformational changes in force-activated proteins and PPI. By investigating the force-response of individual molecules, MT can capture population heterogeneity caused for example by different (un-)folding pathways and thermodynamic stochasticity. At the same time, they allow multiplexing and long-term measurements, enabling observation of rare events. Thus, MT are ideally suited to characterize the stability of PPI, investigate force-activated proteins and map the free energy landscape of protein unfolding. With the work presented in this thesis I take full advantage of the diverse capabilities of MT for studying individual proteins as well as PPI.

Most tethering strategies used for protein SMFS experiments with MT rely on coupling proteins to magnetic beads using the non-covalent, but highly stable bond formed by the protein streptavidin (SA) and the small molecule biotin. Developing a protocol for precisely controlling the anchoring geometry of SA, we were able to increase the lifetime of the SA:biotin interaction drastically [4] (Chapter 3). Our coupling strategy facilitates future long-term and high-force measurements. Building upon this method development, I investigated the (un)-folding kinetics and stability of a range of medically relevant proteins and PPI.

Von Willebrand Factor (VWF) is a multimeric, vascular glycoprotein crucially involved in hemostasis. Its hemostatic function is activated by increased hydrodynamic forces acting at sites of vascular injury. Crucial for its function is the enormous length of VWF multimers, as the peak hydrodynamic forces acting on VWF scale with the square of the multimers' length [5;6]. Using MT, I revealed a conformational transition, opening an interface in the D'D3 domain. Our results show pH-dependent destabilization of the D'D3 interface, priming VWF for multimerization by exposing Cys1099 and Cys1142 (Chapter 4). The stability of the D'D3 interface is increased by coagulation Factor VIII – suggesting a binding site within the D3 submodules.

During my dissertation a novel Coronavirus (SARS-CoV-2) emerged, causing a global pandemic [7–9]. SARS-CoV-2 infections are initiated by binding of the receptor binding domain (RBD), located at the tip of each spike protein to the human angiotensin converting enzyme 2 (ACE2) receptor. Viral attachment takes place in the dynamic environment of the respiratory tract where mechanical forces constantly counteract the attachment. Pioneering a novel tethered-ligand assay, we were able to characterize the RBD:ACE2 interactions under force [10] (Chapter 5). We combined three techniques – MT SMFS, atomic force microscopy-based SMFS, and *in-silico* steered molecular dynamics simulations – to investigate the bond under the whole physiologically relevant force range. We could show that the SARS-CoV-2 RBD:ACE2 interaction has a higher force-stability compared to SARS-CoV-1 (the causative agent of the 2002–2004 epidemic) across all three techniques. In a proof-of-concept measurement with free ACE2 we could furthermore show that our MT assay is sensitive to agents blocking the RBD:ACE2 interaction, suggesting it as a potential screening tool for e.g. therapeutic antibodies or small-molecule drugs. Building upon this initial work, we implemented variant-of-concern (VOC) mutations located in the RBD into our tethered ligand assay, comparing their force-stability in MT with the force-stability of the wild type (wt) (Chapter 6). Extrapolating our force-dependent lifetimes to zero force, we could accurately reproduce affinity data reported in the literature [11–17], finding an increased affinity for all VOC compared to wt. Despite these differences in *affinity*, only the α VOC showed a statistically significant increase in force-stability compared to the wt. Our results suggest that – at least in some cases – force-stability is a better predictor of viral transmissibility than affinity.

Taken together, my results highlight that MT are a versatile tool to study proteins and PPI. I anticipate the value of the improved tethering strategy for future measurements and the use of the novel tethered ligand assay for studying antibody blocking or force stability of other viruses binding their hosts in dynamic, force-exposed environments.

Contents

Zusammenfassung **v**

Abstract **vii**

Table of Contents **xi**

List of Figures **xiv**

List of Tables **xv**

1 Context **1**
1.1 Proteins . . . 1
1.2 Single-Molecule Force Spectroscopy . . . 2
1.3 Magnetic Tweezers . . . 4
1.3.1 Background . . . 4
1.3.2 Force calibration . . . 4
1.3.3 Advantages and applications . . . 5
1.4 Proteins in Magnetic Tweezers . . . 6
1.4.1 Theory . . . 6
1.4.2 Short tether force calibration . . . 7
1.4.3 Attachment strategies . . . 7
1.4.3.1 Surface attachment . . . 7
1.4.3.2 Bead attachment . . . 8
1.4.3.3 Protein attachment via linkers and handles . . . 8
1.4.4 Applications . . . 8
1.4.4.1 Protein unfolding dynamics . . . 9
1.4.4.2 Binding studies . . . 10
1.5 Outline . . . 10

2 Multiplexed Protein Force Spectroscopy With Magnetic Tweezers - Protocols **13**
2.1 Introduction . . . 13
2.2 Materials . . . 14
2.2.1 ELP preparation . . . 14
2.2.1.1 Buffers and media . . . 14
2.2.1.2 Instrumentation . . . 16
2.2.1.3 Further reagents . . . 16
2.2.2 Flowcell preparation . . . 16
2.2.2.1 Buffers . . . 16
2.2.2.2 Instrumentation . . . 16
2.2.2.3 Further reagents . . . 17
2.2.3 Measurements . . . 17
2.2.3.1 Proteins . . . 17
2.2.3.2 Measurement buffer . . . 17
2.2.3.3 Instrumentation . . . 17
2.2.3.4 Further reagents . . . 17
2.3 Methods . . . 18
2.3.1 ELP preparation . . . 18
2.3.1.1 Protein expression . . . 18

2.3.1.2 Protein purification . . . 19
2.3.2 Flowcell preparation . . . 23
2.3.2.1 Amino-silanization . . . 23
2.3.2.2 Flowcell functionalization . . . 24
2.3.2.3 Flowcell assembly . . . 25
2.3.3 Protein measurements . . . 26
2.3.3.1 Measurement preparation . . . 26
2.3.3.2 Measurement optimization . . . 28
2.3.3.3 A multi-channel flowcell holder . . . 29

3 Designed Anchoring Geometries Determine Lifetimes of Biotin-Streptavidin Bonds Under Constant Load and Enable Ultra-Stable Coupling 31
3.1 Introduction . . . 31
3.2 Results and Discussion . . . 33
3.2.1 AFM imaging reveals binding stoichiometry . . . 33
3.2.2 Thermodynamic parameters determined by isothermal titration calorimetry . . . 33
3.2.3 Single-molecule MT measurements determine lifetimes under force . . . 34
3.2.4 MT measurements at 65 pN reveal different lifetime populations . . . 34
3.2.5 Lifetimes depend exponentially on applied load . . . 36
3.3 Conclusions . . . 37
3.4 Materials and Methods . . . 38
3.4.1 Expression of SA constructs . . . 38
3.4.2 Purification of SA constructs . . . 38
3.4.3 Expression and purification of ddFLN4 . . . 38
3.4.4 Preparation of biotinylated DNA . . . 39
3.4.5 AFM imaging . . . 39
3.4.6 Isothermal titration calorimetry . . . 39
3.4.7 Fitting of the ITC data . . . 39
3.4.8 Functionalization of magnetic beads with SA constructs . . . 40
3.4.9 Magnetic tweezers setup . . . 41
3.4.10 Magnetic tweezers experiments . . . 41
3.4.11 Analysis of magnetic tweezers measurements . . . 42
3.5 Supplementary Material . . . 43
3.5.1 Tables . . . 43
3.5.2 Sequences of protein constructs . . . 43
3.5.3 Figures . . . 44

4 A Conformational Transition of Von Willebrand Factor's D'D3 Domain Primes It For Multimerization 49
4.1 Introduction . . . 49
4.2 Results . . . 51
4.2.1 Conformational transition in the D'D3 domain is revealed by MT . . . 52
4.2.2 Transitions are inhibited in a fraction of D3 domains . . . 53
4.2.3 Force-dependent stability of the D3 interface . . . 53
4.2.4 Kinetics of the conformational changes in the D3 interface . . . 54
4.2.5 Lowering pH destabilizes the D3 interface . . . 54
4.2.6 FVIII binding stabilizes the D3 interface . . . 55
4.3 Discussion . . . 55
4.4 Materials and Methods . . . 56
4.4.1 VWF constructs . . . 56
4.4.2 Steered molecular dynamics simulations . . . 58
4.4.3 MT instrument . . . 58
4.4.4 Single-molecule MT measurements . . . 58
4.4.5 Data analysis . . . 59
4.5 Supplementary Material . . . 59
4.5.1 Tables . . . 59
4.5.2 Figures . . . 59

5 A Tethered Ligand Assay to Probe SARS-CoV-2:ACE2 Interactions 65
5.1 Introduction . . . 65
5.2 Results . . . 67
5.2.1 A tethered ligand assay to probe viral attachment under physiological forces using MT and AFM . . . 67
5.2.2 Dynamic AFM force spectroscopy reveals a characteristic unfolding pattern . . . 67
5.2.3 All-atom steered molecular dynamic (SMD) simulations provide insights into the unfolding patterns in molecular detail . . . 69
5.2.4 Unfolding patterns across different force-loading rate regimes are highly reproducible . 70
5.2.5 MT measurements probe the RBD:ACE2 interaction under load in equilibrium . . . 70
5.2.6 SARS-CoV-2 attachment is more stable and longer-lived than SARS-CoV-1 under constant load . . . 73
5.2.7 Magnetic tweezers provide a sensitive assay to study molecules that block the RBD:ACE2 interaction . . . 74
5.2.8 Molecular modeling provides insights into the molecular origin of higher mechanostability of SARS-CoV-2 . . . 75
5.3 Discussion . . . 75
5.4 Materials and Methods . . . 77
5.4.1 Cloning and protein construct design . . . 77
5.4.2 In vitro protein expression . . . 78
5.4.3 Protein purification . . . 78
5.4.4 Atomic force microscopy setup . . . 78
5.4.5 AFM surface and cantilever preparation . . . 79
5.4.6 AFM data analysis . . . 80
5.4.7 Molecular dynamics simulation . . . 80
5.4.8 Chimera protein construction . . . 81
5.4.9 Magnetic tweezers instrument . . . 81
5.4.10 Flowcell preparation and magnetic tweezers measurements . . . 82
5.4.11 Data analysis of MT traces . . . 83
5.4.12 Estimate of forces on viral particles at the cell surface . . . 83
5.5 Supplementary Material . . . 83
5.5.1 Tables . . . 83
5.5.2 Figures . . . 83

6 Stability of SARS-CoV-2 Variants of Concern Under Constant Force 91
6.1 Main Text . . . 91

7 Conclusions and Outlook 95

A List of Publications 97

B Technical Drawings 99

C Custom MT Setup 103

Bibliography 105

Acknowledgements 127

List of Figures

1.1 Schematic of a peptide bond . . . 1
1.2 Local and global protein structure . . . 2
1.3 Single-molecule force spectroscopy techniques . . . 3
1.4 Magnetic tweezer setup . . . 4
1.5 144 h-long measurement at constant force in MT . . . 6
1.6 Proteins in magnetic tweezers . . . 7
1.7 Attachment strategy used for protein measurements in this thesis . . . 8
1.8 Tethered ligand assay to study receptor:ligand interactions . . . 10

2.1 Attachment strategy . . . 13
2.2 Overnight cultures for ELP expression . . . 18
2.3 ZY media for ELP expression . . . 19
2.4 Expression culture for ELP expression . . . 19
2.5 Harvest of ELP expression culture . . . 20
2.6 Preparation for lysis . . . 20
2.7 Lysis . . . 21
2.8 First purification cycle . . . 21
2.9 Second purification cycle . . . 22
2.10 Third purification cycle . . . 22
2.11 Native protein gel to check ELP coupling . . . 23
2.12 Preparation for flowcell functionalization . . . 24
2.13 Application of reagents onto flowcells . . . 24
2.14 Washing flowcells . . . 25
2.15 Flowcell assembly . . . 26
2.16 Measurement preparation . . . 28
2.17 An alternative multi-channel flowcell holder . . . 29

3.1 SA's tetravalency results in different force-loading geometries . . . 32
3.2 Probing SA variants with different valencies by AFM and ITC . . . 33
3.3 Lifetimes of SA-biotin interactions under constant force . . . 35
3.4 AFM imaging of 4SA with biotinylated DNA . . . 44
3.5 AFM imaging of 3SA with biotinylated DNA . . . 45
3.6 AFM imaging of 1SA with biotinylated DNA . . . 45
3.7 AFM imaging of 0SA with biotinylated DNA . . . 46
3.8 Number of biotinylated DNA strands bound to SA of different valencies . . . 46
3.9 Binding enthalpies per binding site for biotin binding to different SA variants . . . 46
3.10 Discretization effects in ITC binding curves . . . 47
3.11 Survival fractions of 1SA and 3SA at 45 pN and 55 pN . . . 47

4.1 Von Willebrand Factor (VWF) domain structure and magnetic tweezers assay . . . 50
4.2 MT force spectroscopy reveals conformational change in the D'D3 domain . . . 51
4.3 The conformational change in the D'D3 domain is unaffected by other domains . . . 52
4.4 Stability and dynamics of the D3 interface probed by MT force spectroscopy . . . 54
4.5 The stability of the D3 interface is modulated by pH and FVIII binding. . . . 55
4.6 Domain deletions to proof origin of transitions in the D'D3 domain . . . 60
4.7 Analysis procedure of force ramps with three-state transitions . . . 61
4.8 Exemplary dwell time evaluation for one plateau of constant force . . . 62

4.9 Two-state transitions . . . 63
4.10 Physiological force-loading of an inverted dimer . . . 63

5.1 Single-molecule assays to probe the SARS-CoV-2 RBD:ACE2 interface under force . . . 66
5.2 AFM force spectroscopy reveals multiple defined transitions in the tethered ligand construct . . 68
5.3 Steered molecular dynamics (SMD) simulations . . . 69
5.4 SARS-CoV-2 RBD:ACE2 interface opening and unfolding in MT . . . 71
5.5 Comparison of mechanical stability and kinetics of ACE2 binding to SARS-CoV-1 and SARS-CoV-2 RBD . . . 72
5.6 Blocking of ACE2:SARS-CoV-RBD bond with soluble ACE2 . . . 74
5.7 Full force-extension curve of the tethered ligand protein construct including the RBD of SARS-CoV-2 and ACE2 . . . 85
5.8 Disulfide bridges shield large parts of the SARS-CoV-1 and SARS-CoV-2 RBD structure . . . 85
5.9 Unfolding of individual ACE2 by AFM SMFS . . . 86
5.10 Dwell time analysis of the tethered ligand extension-time traces in MT . . . 87
5.11 ACE2 unfolding events observed in different constructs in MT . . . 88
5.12 Dynamic force spectrum of the SARS-CoV-2 RBD:ACE2 dissociation recorded by AFM SMFS 88
5.13 Depiction of the interface between SARS-CoV-1 RBD-based Chimera and ACE2 . . . 89

6.1 A single -molecule tethered ligand assay to study RBD binding to ACE2 for current variants of concern of SARS-CoV-2 . . . 92
6.2 Effects of current VOCs on interface stability and affinity . . . 93

B.1 Technical drawing FC holder bottom . . . 99
B.2 Technical drawing multichannel FC holder top . . . 100
B.3 Technical drawing FC holder bottom . . . 100
B.4 Technical drawing holder reverse tweezers . . . 101

C.1 Custom MT Setup . . . 104
C.2 Calibration of custom MT setup . . . 104

List of Tables

3.1 Models for biotin-streptavidin lifetimes 43

4.1 Equations and fit functions used to describe transitions in the D3 domain. 57
4.2 Buffers used for VWF D'D3 transition measurements 59

5.1 Increments of high-force transitions in MT and unfolding peaks in the AFM of the SARS-CoV-2 RBD:ACE2 tethered ligand construct 71
5.2 Interaction parameters for ACE2 and SARS-CoV-2 or SARS-CoV-1 RBD determined using the tethered ligand assay 74
5.3 Mutations on the interface of SARS-CoV-1 and SARS-CoV-2 RBD:ACE2 84
5.4 Equilibrium binding data for ACE2 binding to SARS-CoV-1 or SARS-CoV-2 RBD or S1 proteins 84

6.1 Overview over SARS-CoV-2 variants of concern 94

C.1 Parts implemented into custom MT setup used for most experiments 103

1 Context

This chapter introduces relevant biological background on proteins and the fundamentals of single-molecule force spectroscopy. It gives a detailed description of the basic principles of magnetic tweezers (MT) and presents an overview of state-of-the-art research in protein force spectroscopy using MT. This provides the necessary background for putting my research on protein interfaces examined with MT into context. An outline of the work presented in this thesis is included at the end of this chapter.

1.1 Proteins

Proteins play a crucial role in most biological processes from deoxyribonucleic acid (DNA) replication on a microscopic scale to wound healing or muscle contraction on a macroscopic scale. The human proteome alone contains more than 17800 different proteins fulfilling diverse tasks [18].
At the same time all proteins consist of the same building blocks: 20 different amino acids [19]. The amino-acid sequence of each protein is encoded by DNA with three nucleic acid bases encoding for one amino acid. Amino acids are interconnected by peptide bonds (Figure 1.1, bottom, orange), creating the so-called *polypeptide backbone* of long polypeptide chains. The ends of these chains are referred to as "N-terminus" (where the NH_2 group is located) and "C-terminus" (where the COOH group is located) [19]. The sequence of amino acids is called "*primary structure*" (Figure 1.2A).
The order of amino acids in the primary structure can be diverse; accordingly, the final fold of proteins can vary drastically from protein to protein. On a more local folding level, however, re-occurring patterns emerge that are found in almost any larger protein. These folding segments are referred to as "*secondary structure*". Even though there are multiple secondary structure elements, the two most common ones are α helices and β sheets, joined together by short, flexible loops [19;20] (Figure 1.2B). α helices consist of a chain of amino acids twisting around itself, while β sheets are formed by several chains of amino acids arranging next to each other in parallel or anti-parallel conformation. These structural elements are stabilized purely by hydrogen bonds between the N–H and C=O atoms in the polypeptide backbone [19]. The "backbone structure" is the same for every amino acid, but the side chains have different properties including hydrophobicity/-philicity, charge, and size. Although not directly involved in secondary structure bonding, these side chains influence secondary structure formation due to their properties: Not every primary sequence is equally likely to form α helices or β sheets. Proline and glycine for example very rarely form α helices due to their rigidity and conformational freedom, respectively.
The next level in structure formation is the "*tertiary structure*" (Figure 1.2C), describing the three dimensional fold of the protein. This level is heavily influenced by the side chain properties of the amino acids. Generally, it is energetically favored that hydrophobic, non-polar secondary structural elements and side chains are packed together and shielded by

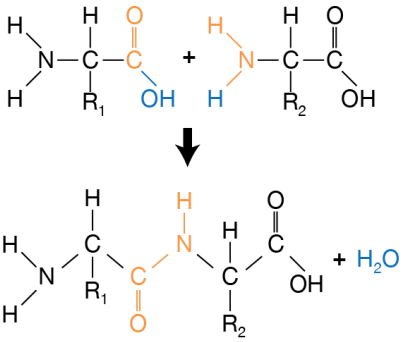

Figure 1.1: **Schematic of a peptide bond.** The peptide bond (bottom, orange) is formed between the C-terminus (carboxyl, COOH) of one amino acid and the N-terminus (amino group, NH_2) of a second amino acid under release of an H_2O molecule. R_1 and R_2 represent different side chains.

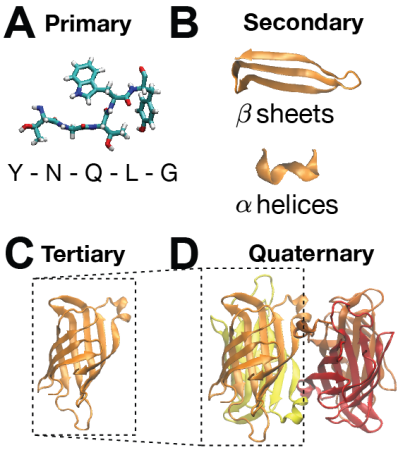

Figure 1.2: **Local and global protein structure.** **A** The peptide chain synthesized from individual amino acids without any geometrical information is called "*primary structure*". Each letter corresponds to one amino acid. **B** The "*secondary structure*" describes local structures. **C** The protein fold is described as "*tertiary structure*" **D** The "*quaternary structure*" describes combinations of several tertiary structures. All structures show (parts) of the tetrameric protein streptavidin (PDB-ID: 6M9B[21]) and were rendered using VMD[22].

hydrophilic structures against solvent exposure in the mostly aqueous surrounding of proteins[19]. This process is referred to as the hydrophobic collapse.
Multiple tertiary structured proteins arranging into a larger complex is called the "*quaternary structure*". Not all proteins exhibit this level of structure. Examples for proteins that do are hemoglobin, where two pairs of different subunits arrange into a quaternary structure able to bind four oxygen atoms, or the tetramer streptavidin, consisting of four equal subunits with one binding site for the small molecule biotin each (Figure 1.2D, Chapter 3).
The function of most proteins is closely related to and dependent on their fold. Misfolded proteins in turn often lose their functionality and can cause severe disease or malfunctions in organisms, such as human Alzheimer's disease (related to the Amyloid precursor protein), Parkinson's disease (related to α-synuclein), Huntington's disease (related to Huntingtin) disease, or type II diabetes (related to islet amyloid polypeptide) to name but a few[23;24].
The basis for understanding these diseases is solving the protein structure and understanding what leads to misfolding. The most established techniques to solve protein structures are cryo-electron microscopy (cryo-EM)[25;26], X-ray crystallography[27], and nuclear magnetic resonance (NMR) spectroscopy[28]. Depending on the proteins' complexity the procedure of solving its structure can be very difficult. Thus, many protein structures are still unknown, even though the primary structure is well-established and proteins can often be readily synthesized. *In-silico* structural predictions on the basis of the amino-acid sequence would thus be favorable. However, even though secondary structure prediction on the basis of the primary structure is relatively simple[29;30], prediction of the tertiary structure is much more complex[31]. Recently, however, novel approaches utilizing machine learning lead to extreme advances on this field[32–34].
Protein function critically depends on the protein structure. Solving the structure thus helps to understand protein functionality in many cases. There are, however proteins which change their conformation triggered by external stimuli, thus obtaining the ability to perform new functions. These stimuli include chemical stimuli such as ligand binding, photophysical stimuli such as illumination, or mechanical force[1]. For these proteins dysfunctionality cannot only be caused by misfolding in the native state, but also by reduced/no response to the external stimulus. Studying these proteins under trigger-conditions is thus interesting and at the heart of understanding their functionality.

1.2 Single-Molecule Force Spectroscopy

Forces are omni-present in nature. On the molecular level, they govern many important processes including DNA compaction, cell motility, cell adhesion, or blood coagulation. These processes in turn are governed by conformational changes of individual, force-sensitive macromolecules, including nucleic acids and proteins. Understanding their force-response is the basis of understanding the processes themselves. The force-response of biological macromolecules, however, is inherently heterogeneous, reflecting different (un-)folding pathways and thermodynamic stochasticity. Measuring force-response in bulk assays does not reflect this heterogeneity, and less populated states and pathways cannot be resolved. Single-molecule force spectroscopy (SMFS) experiments overcome this limitation by investigating the influence of force on individual macromolecules. Over recent years, multiple SMFS techniques have been developed, allowing the effect of force on individual molecules to be precisely studied.
For SMFS experiments, molecules of interest (MOI) are tethered between a surface and a force probe, enabling the stretching of the tethered molecule and the application of precisely controlled force and force loading rates[2;35]. The type of force probe and mode of force application is different for each SMFS technique.
Atomic force microscopy (AFM)-based SMFS (Figure 1.3A) is one of the most established SMFS techniques[35;39;40]. For AFM-SMFS, the MOI is tethered between a glass surface and a silicon nitride microcantilever acting as force probe[2]. Increasing the distance between surface and cantilever by either retracting the cantilever or the surface stretches the MOI and thus applies a force. The applied force is, according to Hooke's Law, directly proportional to the deflection of the cantilever: $F = k \cdot x$, with k being the spring constant of the cantilever. The deflection is measured by means of the position of a laser that is reflected off the backside of the cantilever onto a position-sensitive detector. In this manner, force-distance curves can be recorded. The MOI is stretched until the tether ruptures. Subsequently, a

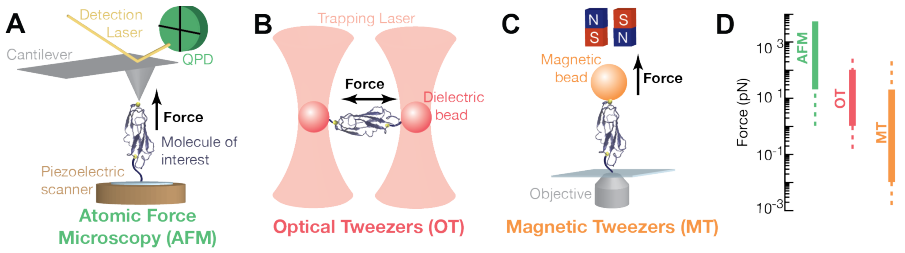

Figure 1.3: Overview of the most common SMFS techniques. A AFM-based force spectroscopy. In AFM-based single-molecule force spectroscopy, the MOI is tethered between a surface and a cantilever. Force is applied by increasing the distance between surface and cantilever. The position of a laser beam reflected off the cantilever is detected on a quadrant photo diode (QPD) and relates to the cantilever position and thus the applied force. **B** OT-based SMFS (Dumbbell assay). In OT, a dielectric bead is trapped by a strongly focused laser beam. The MOI is tethered between this bead and either a surface (”*tethered assay*”), a surface-bound receptor (”*interaction assay*”), or a second trapped dielectric bead (”*Dumbbell assay*”). Force is applied by moving the laser focus. **C** MT-based SMFS. In MT, the MOI is tethered between a magnetic bead and a surface. Force is a applied by a magnetic field gradient, pulling the magnetic bead upwards. The molecule of interest that is depicted in the three SMFS modalities is the small protein domain ddFLN4 [36] (PDB-ID: 1KSR, rendered using VMD [22]), whose unfolding kinetics were carefully analyzed using SMFS and that is now often employed as a fingerprint [3;37;38]. **D** Typical force ranges of the three SMFS techniques.

piezo-electric scanner can move the sample stage, the cantilever can approach the surface, tethering a new molecule and the process can be repeated.

AFM-SMFS has proven to be a powerful tool to study unfolding of numerous proteins, nucleic acids, and even covalent bonds [41–47]. However, the high cantilever stiffness as well as rapid drift impose a lower bound of $\sim$ 10 pN onto the forces accessible in classic AFM-SMFS experiments (Figure 1.3D) [48;49]. Application of lower forces, mimicking many physiologically relevant conditions, is thus difficult with this SMFS technique.

Optical tweezers (OT) are a versatile tool for SMFS experiments, based upon trapping particles optically in the focus of a laser beam. For this purpose, a laser is focused to a diffraction-limited spot with a high numerical aperture microscope objective. Dielectric particles close to the laser focus experience a restoring force towards the focus. Attaching one end of the MOI to a trapped dielectric bead allows force-application either by tethering the other end of the MOI to a surface (”tethered assay”), through interaction with a surface-bound interaction partner (”interaction assay”), or by tethering the other side of the MOI to a second trapped dielectric bead, altering the relative position of either of the beads (”Dumbbell assay”, Figure 1.3B). The force acting on the molecule of interest is directly proportional to the displacement of the bead from the focus x: $F = k \cdot x$ with k being the spring constant or stiffness of the trap, which depends on the steepness of the optical gradient, the laser power and the polarizability of the trapped object. The displacement is most commonly measured by detection of the scattering profile in the back focal plane.

OT offer excellent spatio-temporal resolution and can arbitrarily manipulate the bead in three dimensions. Amongst others, they have been used to characterize processive nucleic acid enzymes [50], forces exhibited by individual proteins [51], the mechanical unfolding of proteins [52], and nucleic acid structures [53]. However, limitations of OT include local heating and photo-damage of the sample due to the high laser intensity required for optical trapping. Furthermore, they are incapable of multiplexing, limiting the throughput of this technique considerably [35].

Other, more recently developed **force spectroscopy techniques** include centrifugal single-molecule force spectroscopy (CSMFS) [54–56]. Here, the MOI is tethered between a vertical glass surface and a bead inside a flowcell. The flowcell is illuminated from above and the transmitted light is bundled by an objective and imaged using a camera. The whole setup is arranged horizontally inside a centrifuge rotor. By spinning the centrifuge, centrifugal forces in a range of $(10^{-4} - 10^{4})$ pN act upon the beads and thus the tethered molecules. Adjusting the acceleration and the size of the utilized beads, the force-loading ratio can be

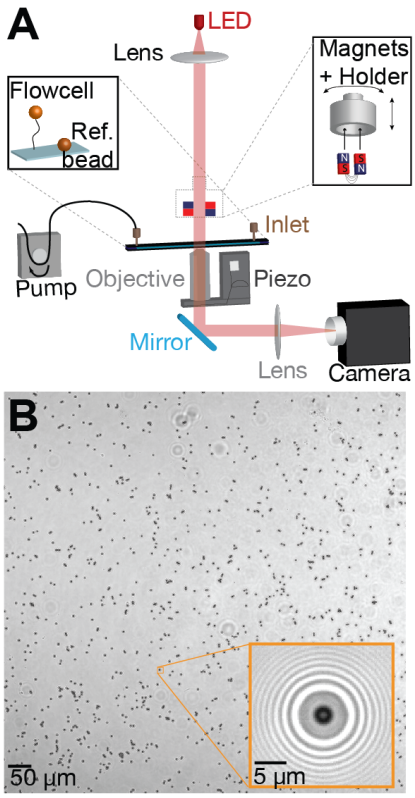

Figure 1.4: **MT setup. A** Schematic of a conventional MT setup. A flowcell with tethered MOIs and reference beads ("Ref. bead") stuck to the flowcell bottom is illuminated from above with a collimated LED light. Transmitted light is imaged with an objective and a lens onto a camera. The objective can be moved in z direction with a piezo. Fluid inside the flowcell can be exchanged with the help of a peristaltic pump. Magnets are installed in a vertical configuration above the flowcell. By reducing their distance to the flowcell the force can be increased. **B** Field of view in our current setup (appendix Section C). More than 150 beads can be tracked simultaneously. Inset: Individual bead with diffraction pattern. Diffraction pattern changes depending on the relative distance between bead and objective and is used to measure the tether extension.

controlled[55]. CSMFS furthermore allows multiplexing.
Another less frequently employed SMFS technique is acoustic force spectroscopy (AFS)[57]. Similar to CSMFS, the MOI is tethered between a glass surface and a bead inside a flowcell. Here, force is applied by an acoustic signal, generated by a piezo plate that is attached to the upper glass slide. Bead positions are recorded with an inverted microscope.

1.3 Magnetic Tweezers

1.3.1 Background

MT are a versatile tool to apply external forces and torques to biological (macro-)molecules. For this purpose, the MOI is tethered between a glass surface and a $\sim$ µm-sized superparamagnetic bead inside a flowcell (Figure 1.3C). In a magnetic field, superparamagnetic beads are magnetized and precise forces can be applied by a magnetic field gradient:

$$\vec{F} = \frac{1}{2}\vec{\nabla}(\vec{m} \cdot \vec{B}) \tag{1.1}$$

with F being the applied force, m the magnetization, and B the magnetic field. Magnetic field gradients can either be generated using permanent or electromagnets located above the flowcell. The simplest and most common method employs two permanent magnets arranged in vertical, anti-parallel configuration (i.e. south pole of one and north pole of the other magnet facing the flowcell) with a small, 0.5 to 1 mm gap in between them (Figure 1.4A, referred to as "Conventional MT")[35;58]. However, there have also been approaches using permanent magnets in a horizontal configuration, making use of the altered distance-force relation[59]. Unlike AFM or OT, MT naturally operate in constant force mode. In the simplest setup where forces are exerted by means of two permanent magnets, the magnitude of the force can be altered by changing the height of the magnets with respect to the flowcell. Reducing their distance will increase the magnetic field acting on the superparamagnetic bead, pull it upwards and thus generate a higher force on the tethered MOI. With commonly used 5 mm N52 magnetized neodymium magnet cubes, spaced 1 mm from each other and commercially available Dynabeads™ MyOne™ (#65001, Invitrogen™, diameter 1 µm) or Dynabeads™ M-270 (#65305, Invitrogen™, diameter 2.8 µm), this allows force application in a range of 0.01 to 70 pN. Decreasing the gap distance between the two magnets or utilizing larger superparamagnetic beads increases the applicable forces considerably[59;60]. Alternative configurations of permanent magnets have been used for different applications[58]. A second possibility for force-application involves utilization of electromagnets[61]. This offers the advantage of more flexible and faster, non-mechanical adjustment of forces. However, they suffer from a range of limitations. To increase the accessible force range with electromagnets, the coils are typically wrapped around soft iron or mu-metal pole pieces, introducing considerable hysteresis in the magnetic field depending on the function of the applied current[35]. Furthermore, high currents creating high magnetic forces generate significant heat necessitating cooling[35].
Regardless of the magnet modality or geometry, MT cannot only apply vertical forces, but also induce torque to rotationally constrained molecules. This feature of MT has been used to extensively characterize mechanical properties of nucleic acids[58].
The extension of the tethered MOI is indirectly determined by camera-based tracking of the (x, y, z)-position of the superparamagnetic bead. For this purpose, the bead is imaged using an inverted microscope (1.4A). Beads are tracked slightly out of focus, inducing a diffraction ring pattern depending on the relative distance between objective and bead (Figure 1.4B, inset)[62;63]. The center of the diffraction pattern determines the (x, y) coordinates with sub-nanometer resolution[64], while the z position is determined with $\approx$ nm resolution by comparing the diffraction pattern with a look-up table. The look-up table is created for each bead at the beginning of the experiment by applying a low, constant force and scanning the objective over a range of $\approx$ 10 µm, while recording the pattern at each relative objective-bead distance.

1.3.2 Force calibration

In order to apply precisely controlled forces with conventional MT, the relationship between magnet-flowcell distance and applied force needs to be accurately determined. The

force acting on each bead can be calculated based on its Brownian motion in the plane perpendicular to force application[35;63]. For this purpose, the time-span in which the fluctuations are recorded needs to be larger than the characteristic time τ_C of the tether:

$$\tau_{C,\leq 1pN} = \frac{8 \cdot \pi^2 \cdot \eta \cdot R \cdot L_P \cdot L_C}{F \cdot \epsilon^2} \tag{1.2}$$

for F ≤ 1 pN and

$$\tau_{C,>1pN} = \frac{12 \cdot \pi^2 \cdot \eta \cdot R \cdot L_C}{F \cdot \epsilon^2} \tag{1.3}$$

for F > 1 pN, where η is the viscosity, R the bead radius, L_P the persistence length of the tether, L_C the contour length of the tether, F the force, and ϵ the statistical accuracy[65;66]. This ensures that the tether has sufficient time to explore his whole spacial freedom at a given force. Furthermore, the frequency at which the fluctuations are recorded needs exceed the corner frequency f_c:

$$f_c = \frac{F}{2\pi \cdot z \cdot (6\pi \cdot \eta \cdot R)} \tag{1.4}$$

where F is the applied force, z is the tether extension, η is the viscosity and R is the bead radius. Principally, the force can be calibrated based on either x- or y-fluctuations. The fluctuation amplitude in both directions are, however, different: In the direction where the beads' magnetization is aligned with the magnetic field, the fluctuation amplitude only arises from tether motion. Calibration based on this direction is referred to as "short-pendulum calibration"[67]. In the perpendicular direction, the bead rotation is not constrained by the magnetic field and thus adds upon tether fluctuations, leading to a larger fluctuation amplitude. Thus, the bead radius adds to the tether length[67–69]. This complicates the calculation of the force, as different angular displacement of bead and tether need to be considered in the calculation[67]. Calibration along this axis is referred to as "long-pendulum calibration"[67]. The force can be calculated based on the equipartition theorem as :

$$F = k_B T \cdot z/\delta_x^2 \tag{1.5}$$

where k_B is the Boltzmann constant, T the temperature, z the tether extension and δ_x^2 the variance of the lateral bead position[63;70]. Hereby the tether length should be known, for example by using a specific DNA construct with a known length. The relation between distance and force is double exponential[63;65].

The accuracy of this simple calibration is impaired by instrument limitations: Due to finite shutter time, bead positions are averaged and high frequency fluctuations average out. Furthermore, frequencies larger than half of the shutter frequency are affected by aliasing and thus shifted to lower frequencies. Both effects lead to a reduction of variance and an overestimation of force[65]. Several methods have been introduced to overcome this limitation including an increase of the camera frequency[65], calculating the power spectral density (PSD) and combining this with a correction of acquisition artifacts and low-frequency drift[66;68;71], as well as using the Allan variance[72;73].

Calibration is facilitated by using long tethers as it reduces the corner frequency. In theory, calibration can be performed with long (DNA) tethers and the found force-distance relationship can be utilized for any measurement, also with shorter tethers. However, this approach suffers from bead-to-bead magnetization variability, causing a slightly different force-distance relationship for each magnetic bead[69]. In the case of commercially available streptavidin-coated Dynabeads™ M-270 (#65305, Invitrogen™), this variability is roughly 10 %[74–77]. This problem can be circumvented by a bead-specific force calibration. It is not necessary to fully calibrate each tether, but it suffices to measure bead fluctuations only at a small number of distances. This allows a correlation parameter, c, to be found relating each beads' force-distance relationship to the master calibration curve obtained by long-tether calibration via $F(d) = c \cdot F_{master}(d)$[63;69] with d being the magnet-flowcell distance.

1.3.3 Advantages and applications

MT offer a range of advantages, making them a valuable tool for SMFS experiments. With an applicable force range from 0.01 to ∼ 100 pN, conventional MT provide access to a physiologically relevant force regime inaccessible in AFM experiments, but comparable to OT.

Compared to OT however, MT do not suffer from optical heating or photodamage. They are simple to implement and offer the possibility of measuring many molecules at the same time, increasing throughput and thus enabling observation of rare events [78]. While OT and AFM both cannot apply constant forces without implementing extensive feedback controls, MT inherently apply constant forces, allowing long-term measurements of the kinetics of the same molecules at low forces (Figure 1.5). Such long-term measurements are facilitated by utilizing a reference bead stuck to the bottom side of the flowcell which can be used to correct for large drift by subtracting it from the trajectories of tethered beads. In addition to stable long-term measurements, MT allow buffer exchange in between measurements of the same molecule making them a valuable tool to study the dynamics of macromolecules under different conditions.

Originally pioneered by Croquette and coworkers [70], MT were initially mainly used to study nucleic acids [58;59;70;79], where it is particularly interesting to apply torque (in combination with linear force). In this context, MT were used to study mechanical properties of DNA, such as its buckling transition, plectoneme formation, or force-induced melting [58;80–82]. Apart from studying mere mechanical properties, MT were used to study DNA-protein interactions and how they affect structural properties of the DNA [58;83–86].

To improve certain aspects of MT, researchers came up with modifications, such as combining MT with flow stretching for improved detection of slow or intermittent enzymatic activities [87], or increased throughput [88]. Furthermore, different magnet geometries have been used to improve torque measurements, yielding freely orbiting MT (FOMT), or magnetic torque tweezers [58]. In the past, several groups started to also employ MT for investigation of proteins [78;89].

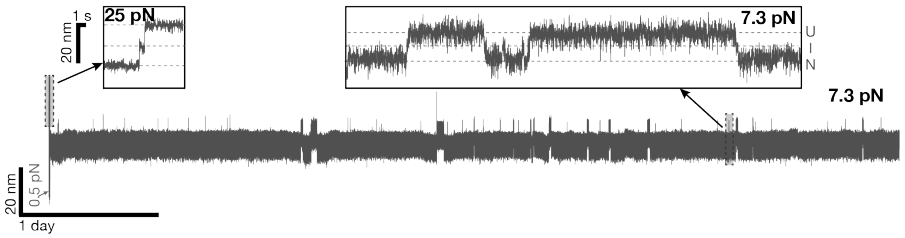

Figure 1.5: 144 h-long measurement at constant force in MT. Measurement of the small protein domain ddFLN4 in magnetic tweezers at 7.3 pN over the course of 144 hours. ddFLN4 transitions throughout the whole measurement from the native state (N) via an intermediate state (I) into the unfolded state (U) and back. Data were recorded at 58 Hz and a reference bead was subtracted.

1.4 Proteins in Magnetic Tweezers

The structure of proteins is critical for their function, as discussed in Section 1.1 ("Proteins"). There are proteins that can undergo externally triggered conformational changes, changing their functionality. Triggers include light, hormones, neurotransmitters, or force, to name but a few [1]. Proteins changing their structural conformation leading to changes in functionality upon force-application are referred to as "force-activated". MT-based SMFS experiments can shed light upon the processes underlying force activation.

Beyond studying force-activated proteins, MT SMFS can also be used to investigate the free energy landscape of protein folding in general, giving access to biologically relevant, but rarely populated folding states. Furthermore, protein:protein interactions can be studies with MT.

1.4.1 Theory

When applying a constant force to a protein tether in MT, initially unfolded protein and linker parts (if present) are stretched (Figure 1.6B, ΔL). At protein-specific sufficiently high forces, proteins unfold. In MT, this relates to sudden increases in tether extension without corresponding changes in the x- or y-coordinate (Figure 1.6A, B, Δz). Here, the extension increment Δz is directly proportional to the number of amino acids in the unfolded protein structure [90]. From the measured increment at a given force F, the contour length of the unfolded protein structure can be calculated using polymer-elasticity models. A commonly employed model is the worm-like chain (WLC) model, which assumes a continuous, flexible, and isotropic rod that is subjected to Brownian motion. A simple approximation of the force-extension relation of a WLC with $\approx 1\,\%$ relative error [91] is:

$$\frac{FL_P}{k_BT} = \frac{1}{4}(1 - \frac{x}{L_C})^{-2} - \frac{1}{4} + \frac{x}{L_C} - 0.8(\frac{x}{L_C})^{2.15} \tag{1.6}$$

with F being the applied force, L_P being the persistence length (a measure for the polymer stiffness; typical values for unfolded protein chains reported in literature are in the range of 0.4 to 0.58 nm [38;90]), k_B the Boltzmann constant, T the temperature, L_C the contour length, and x the measured extension. Another polymer elasticity model typically used for relating measured extension to contour length in SMFS experiments is the freely jointed chain (FJC) model which describes the polymer as a chain of rigid segments of fixed length with equiprobable bond and torsion angles [92]. Both are reported to produce equivalent results [78].

In addition to giving information about the contour length of the unfolded protein segment, MT measurements can also give access to the protein folding and unfolding kinetics. At constant forces, where there is a non-zero probability for the protein to be folded or unfolded, the lifetime τ in the folded or unfolded state can be directly inferred from the distribution of observed dwell times $\tau_{folded/unfolded}$ in the respective state (Figure 1.6A, $\tau_{folded/unfolded}$). The lifetimes are inversely proportional to the folding and unfolding rates $k_{folded/unfolded}$.

In many cases protein unfolding and refolding can be described as a two-state system, where the Gibbs free energy G has two minima (Figure 1.6C, state I [folded] and state II [unfolded]) along the reaction coordinate x, separated by a single energy barrier ΔG_0. In thermal equilibrium, both states are populated with a ratio of $e^{\Delta G_0/k_BT}$ and the rates depend exponentially on the distance between energy minimum and energy barrier along the reaction coordinate. Application of a force F adds an additional energy term $-Fx$ to the free energy. This results in a decreased energy barrier ΔG_F, leading to a shift of the equilibrium state population to $e^{(\Delta G_0 - Fx)/k_BT}$. The effect of force on the rates is described by the Bell model [93]. Assuming no change in Δx, the force-dependent rates are given by:

$$k_{folded/unfolded} = k_{0,folded/unfolded} \cdot e^{\mp \frac{F \cdot \Delta x_{folded/unfolded}}{k_B T}} \tag{1.7}$$

with $k_{0,folded/unfolded}$ being the rates at zero force and $x_{folded/unfolded}$ being the distance between the two minima and the energy barrier. Measuring the rates at different forces thus allows extrapolation of rates in the absence of force as well as distances to the transition state.

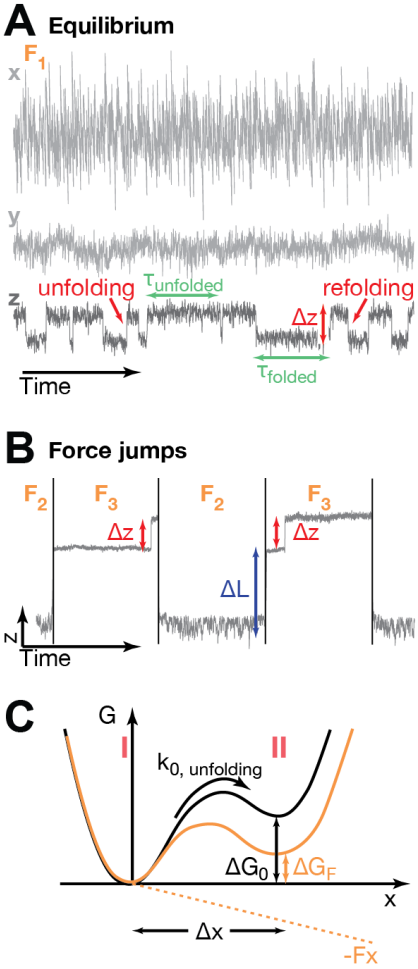

Figure 1.6: **Proteins in magnetic tweezers. A** x (top), y (middle), and z (bottom) trajectory during equilibrium measurement of protein un- and refolding at constant force in MT. Protein unfolding events ("unfolding") are marked by sudden extension increase Δz in the z trajectory without corresponding steps in the x or y trajectory of the bead. Refolding events ("refolding") are marked by extension decrease. Within a certain force range, unfolding and refolding of the protein are possible. Keeping the force constant in this force range results in multiple un- and refolding events allowing force-dependent dwell times τ_{folded} and $\tau_{unfolded}$ in the folded and unfolded states of one individual protein to be measured. **B** When starting at a low force $F_2 < F_1$ in A, the protein is predominantly folded. Increasing the force to a higher force $F_3 > F_1$ results in stretching of unstructured protein parts according to the WLC model (ΔL). If the force is sufficiently high, protein domains unfold leading to an increase in extension Δz. Some unfoldings are reversible (as in this figure) and protein domains can refold when decreasing the force, allowing subsequent repeated unfolding. **C** Schematic of a one dimensional Gibbs free energy landscape describing a two-state single-barrier model sufficient to describe many protein unfolding kinetics. Two states (I, II) are separated along the reaction coordinate x by an energy barrier. Application of force (orange) adds a negative term - *Fx* to the Gibbs free energy and tilts the energy landscape, thus shifting the thermodynamic equilibrium towards the second state by decreasing the energy difference ΔG_0 to ΔG_F.

1.4.2 Short tether force calibration

Bead-to-bead variability in magnetization can lead to inter-bead force differences at a given flowcell-magnet distance of up to ≈ 10 % when using commercially available streptavidin-coated Dynabeads™ M-270 (#65305, Invitrogen™), as discussed already in Section 1.3.2 ("Force calibration"). Circumventing this problem by a bead-specific calibration as discussed in Section 1.3.2 is challenging when working with proteins. Protein tethers without handles usually have a length between 20 and 300 nm [78]. Apart from increased relative length error impeding force-calculation according to equation 1.5, this presents the challenge of an extremely high corner frequency (see equation 1.4), complicating calibration based on brownian fluctuations [67]. In this case, it is of great advantage to calibrate the forces along the direction perpendicular to the magnetic field [67–69]. As described in Section 1.3.2, the beads' radius then adds to the tether length, leading to an effective tether length of $l_{effective} = l_{tether} + r_{bead}$, significantly decreasing the corner frequency and facilitating calibration.

An alternative approach for force calibration uses the force-dependent protein unfolding step sizes of a polyprotein. Measuring the step sizes at multiple magnet distances, a WLC model can be fitted to obtain the corresponding forces [78].

1.4.3 Attachment strategies

In order to take full advantage of the opportunities of MT to apply forces up to 100 pN, or measure protein dynamcis at lower forces over the course of hours and days [38;78], stable protein tethering is crucial. In the past, several approaches have been described in literature.

1.4.3.1 Surface attachment

In the past, various approaches have been proposed for (non-)covalent (site-specific) attachment of proteins to a glass surface for SMFS experiments in MT. In the beginning of protein

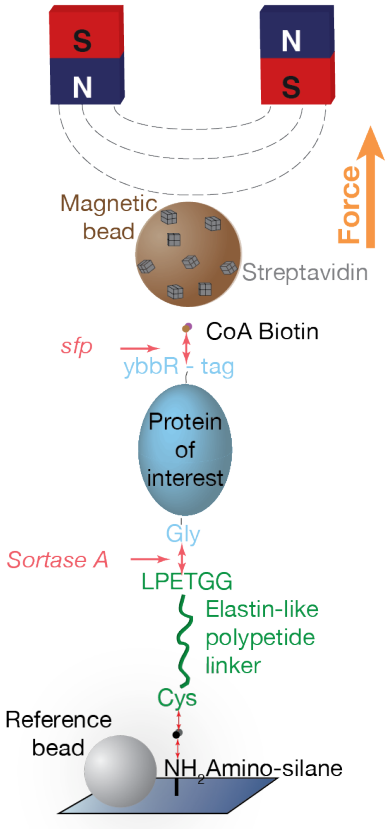

Figure 1.7: **Attachment strategy used for protein measurements in this thesis.** The attachment strategy is based upon a protocol described earlier[38]. Proteins used for measurements in this thesis are expressed with three N-terminal glycines and a C-terminal ybbR tag[119]. This allows eSortase A-mediated covalent coupling (drawn in red) to an elastin-like polypeptide (ELP) linker[120] (drawn in green). The 120 nm long linker increases the distance of the protein and the magnetic bead from the surface, minimizing unspecific interactions and shows no unfolding transitions upon force application. The C-terminus of the protein is biotinylated in an sfp-mediated coupling of coenzyme A (CoA)-biotin to the ybbR tag on the protein. Streptavidin-coated magnetic beads can then bind to the biotin and thus tether the protein of interest allowing site-specific force application. Controlling the anchoring geometry of streptavidin on the magnetic beads increases the lifetime of the non-covalent biotin-streptavidin interaction and allows week-long measurements on the same tether under force[4;38] (Chapter 3).

pulling experiments in MT, proteins were often non-covalently attached to surfaces by unspecific physical adsorption[94], or site-specific attachment using antibodies[95;96], or Ni-/Cu-NTA chemistry. The latter attachment requires a His-tag on the protein of interest[97–101]. When applying higher forces, or monitoring proteins over a long time, these tethering strategies based on non-covalent surface tethering suffer from reduced force-stability. The most common covalent surface-coupling strategy employed in MT was originally described for AFM SMFS experiments[102;103]. It involves Halo-tagged proteins binding to chloroalkane ligands on a glass surface[89;90;104–111]. This tethering strategy offers extreme force-stability exceeding 2 nN[103]. It suffers, however, from the disadvantage that the Halo-tag itself can unfold under force, possibly interfering with the protein unfolding signal. A covalent alternative to the Halo-tag is the SpyCatcher:SpyTag system. Inspired by the FbaB protein domain, forming an exceptionally stable isopeptide bond between Lys and Asp, Zakeri et al. engineered a peptide tag ("SpyTag", 13 amino acids) and a protein binding partner ("SpyCatcher", 138 amino acids)[112]. They form a covalent bond under diverse conditions including pH, temperature, and buffer. SpyTag and SpyCatcher react within minutes and their bond exceeds forces up to 1 nN[112]. By integrating a SpyTag into either protein terminus and functionalizing the surface with SpyCatchers, this system was used for multiple protein SMFS experiments in MT[113–118].

1.4.3.2 Bead attachment

One of the most common approaches to attach proteins of interest to magnetic beads is based upon the non-covalent, but extremely stable bond formed by the tetrameric protein streptavidin (SA), or its close relative avidin and the small molecule biotin[89;90;94–101;104–106–111;115;117;118]. While SA-coated magnetic beads are widely commercially available[63], proteins of interest can be biotinylated with an Avi-tag[63] or an enzyme-mediated fusion of a CoA-Biotin to a protein-bound ybbR-tag[38]. Stability of the biotin-SA bond can be further increased when controlling the anchoring geometry of SA on the beads[4] (Chapter 3). Covalent alternatives for protein-bead attachment include the utilization of Halo- and/or SpyCatcher/-Tags[113;114]. Other alternatives involve EDAC-mediated direct coupling of the proteins' carboxyl group to an amine-coated bead[121], or direct protein binding to an antibody-coated bead[105].

1.4.3.3 Protein attachment via linkers and handles

Tethering proteins directly between surface and magnetic beads results in extremely short tether lengths, as mentioned in Section 1.4.2 ("Short tether force calibration"). This drastically increases the chance of unspecific bead-surface interactions. Using passivating agents such as bovine serum albumin or casein certainly reduces this. Increasing the tether length by use of handles, or polyproteins, however, is even more effective. Handles inserted between protein and surface in the past include small protein domains, such as the well-characterized titin I91 (formally I27) domain[106;107;116–118], or IgFLNa 1-3 domains[98]. Their well-characterized unfolding was then also used as a fingerprint to identify specific tethers[117]. Other approaches were based upon measuring long polyproteins with multiple repeats[90;104;113;114]. Recently, elastin-like polypeptide (ELP) linkers were described for protein SMFS experiments in MT[38] (Figure 1.7). Being unstructured, they do not unfold under mechanical forces and thus do not interfere with investigation of unfolding of the protein of interest. Expressing them with a cysteine at one terminus and a sortase/ybbR tag at their other terminus allows covalent surface- and protein attachment[38].

1.4.4 Applications

All advantages listed in Section 1.3.3 ("Advantages and applications") also apply to *protein* SMFS experiments with MT. Particularly the possibility to multiplex and apply physiologically relevant forces < 10 pN to proteins makes MT complementary to other SMFS techniques. Protein unfolding can be studied by force jump protocols, where high forces causing protein unfolding are applied in turn with low forces, allowing reversible protein structures to refold (Figure 1.6B). In this way, sequential unfolding of multiple protein domains can be observed and this can be used to identify specific tethers if the force-response of a protein is known. Apart from jump protocols, MT can mimic AFM or OT measurements by

increasing the force with a specific constant or changing force-loading rate. Due to the exponential force-distance relationship, the magnet needs to be lowered in a logarithmic fashion when using conventional MT. Unlike the AFM that has a lower bound in force-loading rate due to drift and fluctuations, MT can in principle go arbitrarily low in force-loading rate. Protein subdomains folding reversibly have an equilibrium force, where they unfold and refold with the same probability as shown in Figure 1.6A. Ramping the force around this equilibrium allows to obtain force-dependent dwell times in the folded and unfolded state and according to Equation 1.7, the lifetimes and rates at zero force can be extrapolated. This in turn gives access to the free energy landscape (Figure 1.6C). This can also be done in the presence of interaction partners, studying their effect on force-stability and binding kinetics. Furthermore, MT can be used for binding studies of force-activated proteins: In some force-activated proteins force-induced conformational changes reveal cryptic binding sites for potential binding partners, whose binding can then be quantified in MT. Recently, MT were also used to directly probe the stability of the bond formed by receptor ligand pairs by directly applying force to them and investigating bond dissociation. The following sections give an overview over proteins studies in MT.

1.4.4.1 Protein unfolding dynamics

The muscle protein **titin** is with 3.7 MDa the largest known human protein, containing a variable number of immunoglobulin (Ig) domains[2]. Spanning an entire half sarcomere, titin filaments experience forces between 4 and 15 pN in vivo, making MT the ideal tool to study them under physiologically relevant force[2]. There have been several MT studies investigating the behavior of Ig10 and Ig91 domains under force[89;109;111]. They found that Ig domains have an equilibrium force of around 5.4 pN, extending or shortening by $\sim$ 13 nm[89]. At 5.7 pN, individual titin Ig domains generate peak work of 46 zJ, which is comparable to the mechanical energy delivered by a myosin power stroke[2]. On the basis of their characterization in MT it was concluded, that Ig domains play a crucial role in muscle contraction. Saving elastic energy by unfolding at forces > 6 pN, they can subsequently release it during muscle contraction upon re-folding[2;89;90;109;111].

Talin is a protein critically involved in cell-cell contacts and cell adhesion by linking the integrin-mediated cell–matrix contacts to the actin cytoskeleton via its binding partner vinculin[110]. Its C-terminal rod-domain consist of 13 helical bundles[110] with 11 (partially cryptic) vinculin binding sites. These binding sites are exposed upon force-activation of talin[97] (see in Section 1.4.4.2). Unfolding of talin is thus crucial for successful cell adhesion and has been studied in multiple MT-based SMFS experiments: The folding kinetics of a full FL-talin rod were determined and traced back to individual subdomains[110]. Tapia-Rojo et al. focused on studying force-dependent unfolding kinetics of the weakest of all talin domains, the R3 domain, which harbors two vinculin binding sites and is thought to be the precursor of talin-mediated adhesion[107]. Application of "mechanical noise" (fluctuating forces, applied with electromagnetic tweezers) shows that talin can filter out mechanical noise, but detect periodic force signals[107]. Tapia-Rojo et al. interpret this as talin acting as a "mechanical bandpass filter", reading and interpreting frequency-dependent mechanical information through its folding dynamics[107]. For their study they used "magnetic tape-head tweezers", tape-head-based electromagnetic tweezers allowing rigorously fast adjustment of the magnetic field at a bandwidth of $\sim$10 kHz[108].

Another naturally force-activated protein that was studied in MT is **von Willebrand Factor** (VWF)[38]. VWF is a multimeric, vascular glycoprotein travelling through blood in a globular conformation. Upon sensing increased hydrodynamic forces - as present at sites of vascular injury - VWF unfolds. This exposes binding sites for platelets that form a hemostatic plug attaching to collagen-bound VWF at the injured vessel wall. MT were used to characterize A2 domain unfolding in the presence and absence of calcium[38]. Furthermore, MT studies could reveal low-force dynamics of dimeric stem opening and closing happening at forces around 1 pN. This likely constitutes a critical first step in the force activation of VWF[38].

Other proteins whose un- and refolding dynamics were investigated with MT include bacterial adhesion **Protein L**[61], the **SH3 domain of SRC Kinase**[117], the intrinsically disordered **neurofilament low (NFL)** protein tail[122], and **Cpa** protein, mediating pathogen adhesion of Streptococcus pyogenes[113].

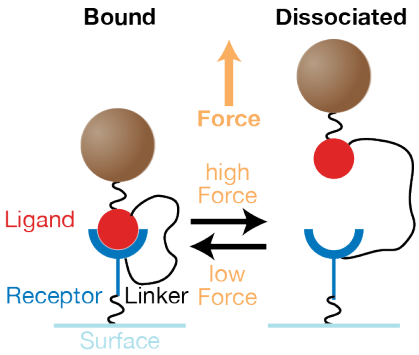

Figure 1.8: **Tethered ligand assay to study receptor:ligand interactions.** A tethered ligand assay can be used to characterize receptor:ligand interactions. Receptor (blue) and ligand (red) are connected by a flexible linker (black). Upon force application the bond eventually breaks, but both interaction partners are held in proximity by the linker. By decreasing the force, receptor and ligand can rebind and be probed again.

1.4.4.2 Binding studies

Vinculin-binding to α-**actinin 1** and **talin** is crucial for cell adhesion and cell-cell contacts and critically relies on force. Early experiments combined MT SMFS with *single-molecule fluorescence experiments* to show that vinculin binding to talin was increased after force application to talin [97]. For this purpose, a conventional MT setup was complemented with a total internal reflection (TIRF) objective to monitor Alexa488-labelled vinculin molecules after force application to tethered talin. Combining both single-molecule techniques, del Rio et al. could show that the number of vinculin molecules bound to talin increased with increased stretching force applied to talin. This offers evidence that talin needs to be force-activated by conformational changes exposing cryptic binding sites prior to vinculin binding [97]. Adapting this protocol, Yao et al. performed a similar experiment with vinculin binding to α-actinin 1, after force application of the latter. This revealed that similar to talin, α-actinin 1 needs to be force-activated prior to vinculin binding [100]. In following studies, the binding of vinculin to talin or α-actinin 1 was studied more closely using MT-SMFS experiments only. It was shown that vinculin inhibits refolding of talin and unbinding is induced by forces larger than 25 pN [101]. Le et al. used a *tethered ligand assay* (Figure 1.8) to access the binding kinetics of vinculin and talin / α-actinin 1 [116]. Therefore, vinculin and talin / α-actinin 1 were connected by a flexible peptide linker and the resulting fusion construct was tethered in MT. Upon applying high forces, the receptor:ligand bond breaks, but both interaction partners are held together by the flexible peptide linker. When lowering the force, the same receptor ligand pair can rebind and be probed again in MT. In this way, Le et al. obtained force-dependent lifetimes of vinculin binding. Later, real-time force-dependent vinculin head binding to talin R3 domain was measured and a conformational transition in talin upon vinculin binding was resolved. This conformational change was reported to induce an energy penalty positively depending on the applied force. The authors hypothesized this to be a negative feedback loop to stabilize force on focal adhesions [106].
Another assay combining single-molecule fluorescence with MT SMFS experiments was presented to show force-dependent enzyme:substrate interactions [123;124]. To this end, **6-hydroxymethyl-7,8-dihydropterin pyrophosphokinase** (HPPK) was labelled with Cy3 and Cy5 molecules and force-dependent conformational dynamics were probed using *Förster resonance energy transfer* (FRET) in the presence and absence of **enzymatic substrates**. Using this combined approach, Guo et al. were able to directly observe entropy trapping in the enzyme-substrate reactive transition state.
Other binding studies conducted with MT SMFS experiments include the folding dynamics of **protein L** in the presence and absence of the **chaperone trigger factor** [104], the energy landscape of **aptamer-protein** interactions (for Ara h 1 and hIgE protein) [94], and force-dependent **collagen** cleavage through **matrix metalloproteinase-1** (MMP-1) [95;96].

Taken together, MT have proven to be a valuable tool for studying (un-)folding kinetics and obtaining the free energy landscape for individual proteins, as well as investigating protein:protein interactions. Thus, MT have the potential to be used for studying many more proteins and their interactions.

1.5 Outline

The work included in this thesis contributes to the growing field of protein single-molecule force spectroscopy with MT by providing methods as well as describing findings of studies on medically relevant proteins. Chapter 3 to Chapter 6 are either already published or are intended to be published in a similar way as presented in the respective chapter. The presented work was thus a team effort. A statement on my contribution to the presented work is given at the beginning of each chapter. The content of the thesis is as follows:

Chapter 2 provides a collection of protocols and methods used for multiplexed protein force spectroscopy with MT. It includes a detailed description of the expression and purification of elastin-like polypeptide (ELP) linkers, flowcell functionalization, and measurement preparation, as well as measurement optimization.

Chapter 3 presents a method for extremely stable, non-covalent anchoring based upon the streptavidin (SA):biotin linkage. We engineer SA to precisely control its anchoring geom-

etry and thus significantly increase its bond lifetime with biotin. With our results, we furthermore conceptually highlight that affinity is unequal to force-stability. The work presented in this chapter is of great value for protein-coupling to SA-coated magnetic beads for MT experiments and enables week-long measurements on the same protein. Besides for MT experiments, the stable SA:biotin linkage can also be advantageous for any (force-spectroscopy) technique relying on stable, non-covalent, specific anchoring.

Chapter 4 shows results obtained when studying the force-activated blood protein von Willebrand Factor (VWF). Here, we use MT force spectroscopy to reveal and characterize a previously unknown conformational transition in the N-terminal D'D3 domain, involved in VWF multimerization. Our results furthermore contribute to the understanding of factor-VIII binding to VWF.

Chapter 5 introduces a novel tethered ligand assay allowing to characterize receptor:ligand interactions under force. With this assay, we study the interaction of the severe acute respiratory syndrome coronavirus (SARS-CoV) with its human receptor angiotensin converting enzyme 2 (ACE2) using the two single-molecule force spectroscopy techniques MT and AFM. We complement our results with steered molecular dynamics (SMD) simulations and are able to match results from all three techniques. Comparing SARS-CoV-1 and SARS-CoV-2 RBD:ACE2 interactions, we find significant differences in force-stability throughout all techniques.

Chapter 6 presents results on the force-stability of current SARS-CoV-2 variants of concern (VOC) α, β, γ, and δ based on the assay presented in the previous chapter. By extrapolating the force-dependent lifetimes to zero force, we can accurately reproduce reported affinities measured with bulk-assays. We find that all VOCs have a higher affinity for ACE2 than the wildtype. Opposed to this, we find α to be the only VOC with a significantly stronger bond to ACE2 under force than the wildtype, suggesting that force-stability might contribute to increased transmissibility complementary to zero-force affinity.

Chapter 7 summarizes the findings presented in the previous chapters and discusses their value for the current state-of-the-art in protein MT single-molecule force spectroscopy. Furthermore, ideas are given how to continue and advance the research presented in this thesis.

Appendix C presents a newly assembled custom MT setup that was used for most measurements described in this thesis.

2

Multiplexed Protein Force Spectroscopy With Magnetic Tweezers - Protocols

Abstract

Single-molecule force spectroscopy (SMFS) with magnetic tweezers (MT) is a valuable tool for studying the force-response of individual proteins, or characterizing the stability of protein:protein interactions. Here, we describe a selection of protocols enabling multiplexed, specific SMFS using MT. Our coupling strategy relies on eSortase A-mediated protein coupling to elastin-like polypeptide (ELP) linkers attached to an amino-silanized glass surface. This ensures stable covalent bonding, and increased distance between bead and surface, which minimizes unspecific bead:surface interactions. Protein-tethering is achieved by biotinylation of the protein and coupling to streptavidin-coated magnetic beads. Our coupling strategy results in stable protein tethering, enabling long-term MT measurements.

2.1 Introduction

For protein SMFS in MT, protein constructs are tethered between a surface and a magnetic bead. Precisely controlled forces are applied by a magnetic field gradient either generated with electro- or permanent magnets, pulling the magnetic bead upwards and thus stretching the protein tether[61;63]. Conformational changes are tracked by indirectly monitoring tether extension through the position of the magnetic bead[63].

Stable tethering is crucial not only for studying high-force behaviour, but also for enabling long-term measurements. In the past, many different covalent and non-covalent tethering strategies have been presented. Most protein:bead attachment strategies rely on the non-covalent, but highly stable interaction between the tetrameric protein streptavidin, or its close relative avidin and the small molecule biotin[89;90;94–101;104;106–111;115;117;118]. Methods to covalently attach proteins to a surface include utilization of Halotags[89;90;104–111], or the SpyTag:SpyCatcher interaction[112–118]. However, all these surface-attachment strategies suffer from the small length of protein tethers typically on the order of 20 to 100 nm, resulting in a small distance between the magnetic bead and the surface. This fosters unwanted unspecific bead:surface interactions. Addition of a linker either between the surface and the protein or between the protein and the bead reduces this effect.

Here, we present a selection of protocols allowing multiplexed protein force-spectroscopy with magnetic tweezers over long measurement periods and with minimal unspecific surface interaction due to a flexible elastin-like polypeptide (ELP) linker between the surface and the protein (see Figure 2.1). The protocols described here are for N-terminal protein

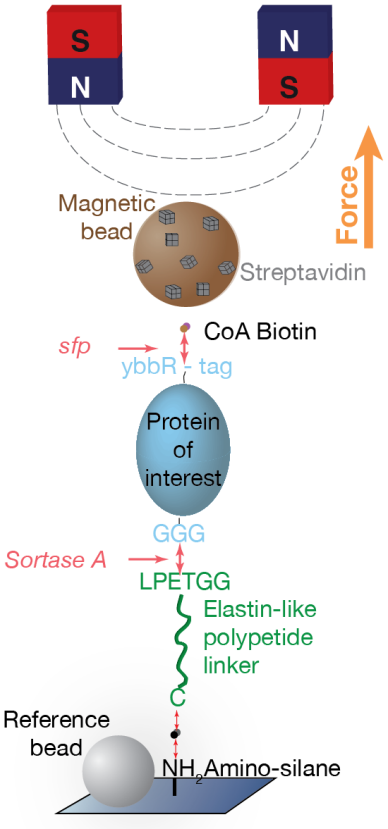

Figure 2.1: **Attachment strategy.** The attachment strategy is based upon a protocol by Löf et al.[38]. Proteins are expressed with three N-terminal glycines and a ybbR tag at their other terminus[119]. This allows eSortase A-mediated covalent coupling to an elastin-like polypeptide (ELP) linker[120]. The C-terminus of the protein is biotinylated in an sfp-mediated coupling of coenzyme A (CoA)-biotin to the ybbR tag on the protein. Streptavidin-coated magnetic beads can then bind to the biotin and thus tether the protein of interest allowing site-specific force application. Controlling the anchoring geometry of streptavidin on the magnetic beads increases the lifetime of the non-covalent biotin-streptavidin interaction and allows week-long measurements on the same tether under force[4;38].

This Chapter is an invited chapter in the lab protocol series *Methods in Molecular Biology*.

attachment to ELP linkers. For C-terminal attachment, proteins need to carry a C-terminal LPXTGG motiv and ELPs an N-terminal GGG motif. All other steps are identical.

2.2 Materials

All chemicals used, if not further specified, were supplied by Carl Roth (Karlsruhe, Germany) or Sigma-Aldrich (St. Louis, MO, USA). All buffers and media were sterilized by autoclaving or sterile filtration.

2.2.1 ELP preparation

2.2.1.1 Buffers and media

LB-Kana media

- 25 g LB media (Carl Roth, #6673.2)
- 1 l MilliQ

Dissolve LB media in MilliQ using a magnetic stirrer. Autoclave before adding 50 µg/ml Kanamycin in a sterile environment.

ZY media

- 10 mg/ml trypton (Carl Roth, #8952.3)
- 5 mg/ml yeast extract (Carl Roth, #2363.2)

Refer to section 2.3.1 for making this media.

1000x trace metal solution (100 ml)

- 36 ml MilliQ
- 50 ml 0.1 M $FeCl_3$ in 0.12 M HCl
- 2 ml 1 M $CaCl_2$
- 1 ml 1 M $MnCl_2$-$4H_2O$
- 1 ml 1 M $ZnCl_2$
- 1 ml 0.2 M $CoCl_2$-$6H_2O$
- 2 ml 0.1 M $CuCl_2$-$2H_2O$
- 1 ml 0.2 M $NiCl_2$-$6H_2O$
- 2 ml 0.1 M Na_2MoO_4-$2H_2O$
- 2 ml 0.1 M Na_2SeO_3-$5H_2O$
- 2 ml 0.1 M H_3BO_3

Except for $FeCl_3$, stock solutions of individual metals are autoclaved and solutions stored at room temperature. $FeCl_3$ is filtered through a 0.42 µm sterile, hydrophilic filter.

50x 5052 solution (500 ml)

- 500 ml MilliQ
- 25 % (w/v) Glycerol (Sigma-Aldrich, #G5516)
- 12.5 % (w/v) Glucose (Sigma-Aldrich, #49163)
- 10 % (w/v) Alpha-lactose monohydrate (Sigma-Aldrich, #L8783)

All substances are dissolved during autoclaving.

50x M solution

- 1.25 M Na_2HPO_4
- 1.25 M KH_2PO_4
- 2.5 M NH_4Cl
- 0.25 M Na_2SO_4

The solution is autoclaved after dissolving all substances.

ZYM media (for 1 l)

- 958 ml ZY media
- 0.2 ml 1000x trace metal solution
- 2 ml $MgSO_4$ solution (1 M)
- 20 ml 5052 solution (50x)
- 20 ml M solution (50x)

Refer to section 2.3.1 for making this media.

Autoinduction media

- ZYM media
- 1 µg/ml Kanamycin

Refer to section 2.3.1 for making this media.

Lysis buffer, pH 8.0 at RT

- 50 mM TRIS
- 50 mM NaCl
- 10 % (w/v) Glycerol (Sigma-Aldrich, #G5516)
- 0.1 % (v/v) Triton X-100
- 5 mM $MgCl_2$

This buffer is filtered through a 0.22 µm hydrophilic filter after adjusting the pH with NaOH/HCl.

Coupling buffer, pH 7.2

- 50 mM Disodium phosphate
- 50 mM NaCl
- 10 mM EDTA

This buffer is filtered through a 0.22 µm hydrophilic filter after adjusting the pH with NaOH/HCl.

CD buffer, pH 7.2 at RT

- 25 mM TRIS
- 72 mM NaCl
- 1 mM $CaCl_2$

This buffer is filtered through a 0.22 µm hydrophilic filter after adjusting the pH with NaOH/HCl.

2.2.1.2 Instrumentation

- Autoclave
- Incubator/shaker for overnight bacterial cultures (5 – 7 ml, shaking at 220 rpm at 37 °C)
- Large shaker for expression culture (2 l glass falcons, shaking at 105 rpm at 37 °C)
- Centrifuge for high speed spinning (6 000 g) of large (∼400 ml) volumes at 4 °C
- Centrifuge for high speed spinning (15 000 g) of medium (∼15 ml) volumes at 4 °C
- Centrifuge for lower speed spinning (3 200 g) of medium (∼15 ml) volumes at 40 °C
- Table top centrifuge for spinning 1 ml at 20 000 g at 4 °C
- Heatbath
- Gel electrophoresis equipment to run and visualize a protein gel

2.2.1.3 Further reagents

- Glycerol stock / clones of ELPs. Plasmids are provided on Addgene by Ott et al.[120] (Addgene accession number 90472)

  Competent cells: NiCo21 (DE3)

  Vector: pET28a (Resistance: Kanamycin)
- Amino acids: Glycine, valine, proline
- Salt: NaCl
- For lysis: DNAse I (Roche, #10104159001), Lysozyme (Carl Roth, #8259.1), Protease Inhibitor (cOmplete, Roche, #45582400)
- TCEP Bond breaker solution (Thermo Scientific, #77720)
- Precast, stain-free protein gel, any kD (BioRad, #456-8126); protein ladders, GGG-dye (e.g. GGG-SGSGSG-Cy3, available at peptide elephants), and Maleimide dye (e.g. Atto 647N maleimide, Sigma-Aldrich, #05316-1MG-F)

2.2.2 Flowcell preparation

2.2.2.1 Buffers

Hepes Buffer
Dissolve 50 mM Hepes in MilliQ, adjust the pH to 7.4 using NaOH and HCl, and sterile filtrate through 0.22 µm filter.

Coupling Buffer
See Section 2.2.1.1.

2.2.2.2 Instrumentation

- Reverse tweezers (see Figure 2.12, "Tweezers")
- Humidity chamber (see Figure 2.12)
- Hot plate
- *Optional:* Holder for reverse tweezers (see Figure B.4)

2.2.2.3 Further reagents

- (3-Aminopropyl)dimethylethoxysilane (Amino-Silane, abcr, #146193)
- H_2SO_4
- H_2O_2
- Glass slides (see Figure 2.12, Carl Roth, #LH26.1)
- Perforated top-glass slides (Carl Roth, #LH26.1) with two holes (r = 0.5 mm, spaced 5 mm from the edge, and cut into the glass with a laser cutter) as in- and outlet
- sulfosuccinimidyl 4-(N-maleimidomethyl)cyclohexane-1-carboxylate (sulfo-SMCC; Thermo Fisher, #22322)
- Cys-6xELPs-LPETGG (see Section 2.3.1)
- Cysteine
- Polystyrene spheres (Polysciences, Inc., #07310)

2.2.3 Measurements

2.2.3.1 Proteins

- Protein of interest: The protein of interest should feature an N-terminal triple glycine motif for eSortase A-mediated ligation to the LPETGG tag of the ELP linker. Our attachment protocol further relies on a ybbR-tag (with the amino acid sequence DSLEFIASKLA) on the other side of the protein, which is then biotinylated via sfp-mediated CoA-Biotin coupling.
- 4'-phosphopantetheinyl transferase (Sfp) enzyme [119]
- Enhanced, pentamutant sortase A (with mutations P94R, D160N, D165A, K190E, and K196T, "eSortase A") [125;126]

2.2.3.2 Measurement buffer

Generally, the measurement buffer depends on the protein of interest and the scientific question that should be answered. Using our coupling strategy it should be noted, that sfp and eSortase A activity rely on the presence of magnesium and calcium, respectively. In order to enable sfp-mediated biotinylation via CoA-Biotin attachment to the ybbR tag, as well as eSortase A-mediated protein coupling to ELP linkers, it is thus crucial to ensure presence of magnesium and calcium. We typically operate with 10 – 100 mM $MgCl_2$ during sfp-mediated biotinylation and 1 mM $CaCl_2$ for eSortase A-mediated protein:ELP attachment.
During the measurement, we use the same buffer with 0.1 % Tween-20 added to it in order to minimize unspecific bead:surface interactions.
The measurement buffer is filtered through a 0.22 µm hydrophilic filter.

2.2.3.3 Instrumentation

- FC holder (see Appendix B)
- MT Setup

2.2.3.4 Further reagents

- Casein (Merck, #C4765)
- Coenzyme A (CoA) - Biotin (Sichem, #SC-8618)
- Streptavidin-coated Dynabeads™ M-270 (Invitrogen™, #65305)

2.3 Methods

2.3.1 ELP preparation

This is a protocol for recombinantly expressing and purifying ELP linkers, whose plasmid is provided on Addgene by Ott et al.[120] (Addgene accession number 90472). The ≈ 300 amino acid ELP linkers with a contour length of ≈ 120 nm and a molecular weight of ≈ 24.9 kDa have the repetitive amino acid sequence $[(VPGEG)\text{-}(VPGVG)_4\text{-}(VPGAG)_2\text{-}(VPGGG)_2\text{-}(VPGEG)]_6$ and additionally possess a single N-terminal cysteine and the C-terminal sortase recognition motif LPETGG. They do not feature a His-tag as constructs with His-tag seemed to be less stable in MT measurements with decreased pH (for example used in this thesis in Chapter 4 when studying VWF dimers).
Expression in *E. coli* and purification are based upon a protocol established by Dr. Wolfgang Ott[120]. As the construct does not have a tag for purification via an affinity column, purification relies on an iterative change between high temperature/salt condition (where ELPs precipitate) and low temperature condition (where ELPs go into solution).

2.3.1.1 Protein expression

This protocol starts from either a glycerol stock of NiCo21 (DE3) cells or a clone.

Day 1: Overnight culture

Under sterile hood (see Figure 2.2):

- Add 7 ml LB Kana into 15 ml falcon
- Dip pipette tip into glycerol stock / clone (very light dipping already enough!) and drop it into falcon
- Shake: 220 rpm, 37 °C for 15-18 h (overnight)

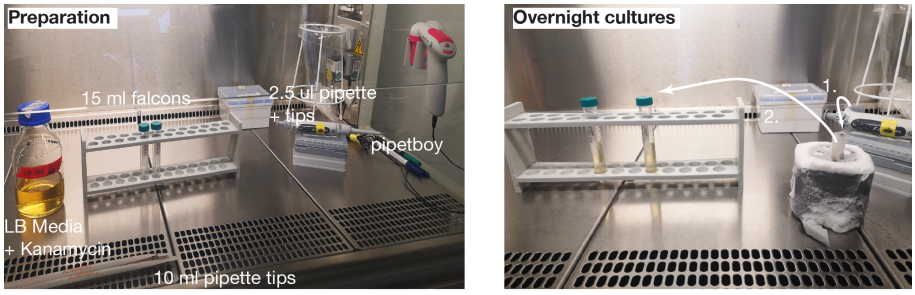

Figure 2.2: Overnight cultures for ELP expression. Necessary for overnight cultures are: LB media with 50 µg/ml Kanamycin (see Appendix 2.2), 15 ml falcons, 10 ml pipette tips + a pipetboy, and 2.5 µl pipette tips + a pipette. After filling 7 ml LB media + Kanamycin into the falcons with the pipetboy, a 2.5 µl tip is carefully dipped into the glycerol stock (very light dipping already enough!) and the tip is dropped into the falcon. The glycerol stock is kept in an isolation rack to ensure continuous freezing.

Preparation for the next day (see Figure 2.3):

- Prepare ZY media and add 10 gr glycine, 5 g proline and 5 g valine; Mix with magnetic stirrer
- Autoclave ZY media
- Autoclave 2l Erlenmeyer flask

Day 2: Expression

Under sterile hood (see Figure 2.4):

- Prepare ZYM and then autoinduction media by adding the antibiotic; Mix by gently shaking the bottle
- Add 400 ml autoinduction media into autoclaved 2 l Erlenmeyer flask

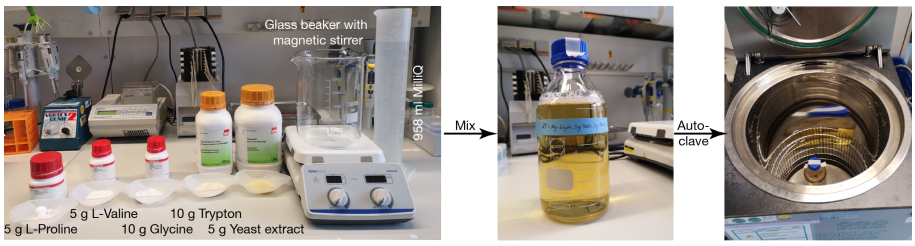

Figure 2.3: ZY media for ELP expression. All ingredients (left) are mixed with a magnetic stirrer until they are completely dissolved. Media is filled into a glass bottle (middle) and autoclaved (right).

- Add the 7 ml overnight culture to the autoinduction media
- Shake: 105 rpm, 37 °C for 24 h

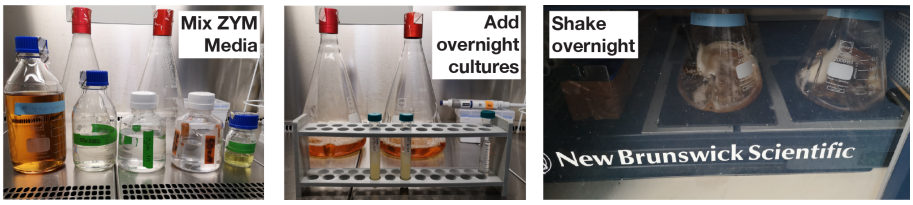

Figure 2.4: Expression culture for ELP expression. ZYM media is made from previously prepared ZY media with amino acids by adding trace metals, $MgSO_4$, M, and 5052. 0.1 mg/ml Kanamycin is added to avoid bacterial contamination. Overnight cultures are added into ≈ 400 ml autoinduction media. Expression culture is transferred into a shaker, where it shakes overnight. Shaking frequency is adjusted such that there is foam at the surface of the fluid in the Erlenmeyer flask. In the photos shown here, two expression cultures are prepared from two overnight cultures.

See Figure 2.5

Day 3: Harvest

- Centrifuge cells: 6 000 g, 4 °C, 15 min
- Discard supernatant (SN)
- Collect pellet into 50 ml falcon and spin down: 1 000 g, room temperature, 1 min
- Weigh pellet and store at -80 °C (facilitates lysis, can be stored up to weeks)

2.3.1.2 Protein purification

Preparation (Figure 2.6):

Day 4: Purification

- Thaw cell pellet in a mixture of ice/water (Figure 2.6A)
- Heat water bath to 65 °C
- Prepare final lysis buffer (Figure 2.6B, C):

  100 ml lysis buffer

  10 µg/ml DNAse I, dissolved in lysis buffer

  100 µg/ml Lysozyme, dissolved in lysis buffer

  1 Protease inhibitor tablet/100 ml lysis buffer

  1 mM TCEP

General consideration: ELPs are dissolved at low temperatures and precipitate at high temperatures/high salt.

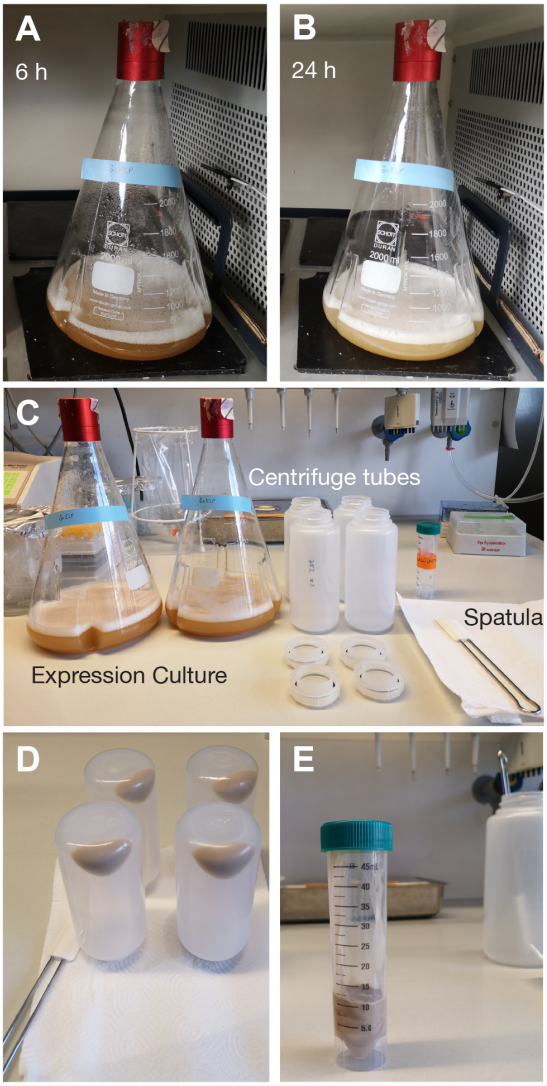

Figure 2.5: Harvest of ELP expression culture. **A** Expression culture after 6 h of shaking at 37 °C. **B** Expression culture after 24 h of shaking at 37 °C. **C** Preparation for harvesting cells: Expression culture, centrifugation tubes for 370 ml, and a plastic spatula are required. Expression culture is distributed between centrifugation tubes and centrifuged. **D** Supernatant is discarded and pellets are collected into 50 ml falcon with the spatula. **E** Pellet is spun down and frozen at -80 °C.

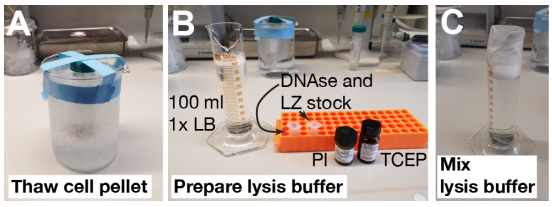

Figure 2.6: Preparation for lysis. Cell pellet stored at -80 °C after the harvest is thawed in an ice/water bath. Final lysis buffer is prepared by adding DNAse, lysozyme, protease inhibitor, and TCEP. For mixing, measurement cylinder is closed with a parafilm and mixed by repeatedly inverting until protease inhibitor tablet is completely dissolved.

i. Resuspend cell pellet in final lysis buffer (~ 1.43 ml/g) (Figure 2.7A)
Note: It is important to solve the pellet in as little volume as possible to allow crowding of the ELPs!

ii. Sonicate 2 x 7 min on ice with 5 min on roller bank at 4 °C in between (Figure 2.7B, C) to cool down fluid

iii. Centrifuge lysate: 15 000 g, 4 °C, 1 h (Figure 2.7D)

iv. Transfer SN into new tube (Figure 2.7F)

v. Heat SN to 65 °C in heatbath for 20 min (Figure 2.8A)

vi. Cool on ice for 20 min (Figure 2.8B)

vii. Put on roller bank at 4 °C for 30-60 min

viii. Centrifuge: 15 000 g, 4 °C, 15 min (Figure 2.8C)

ix. Transfer SN into new tube (Figure 2.8D)

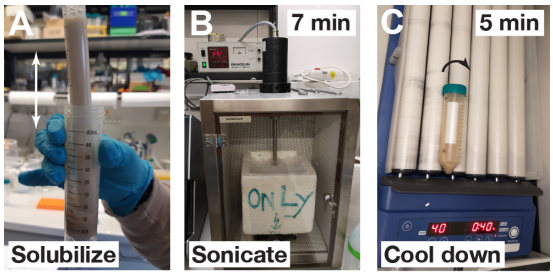

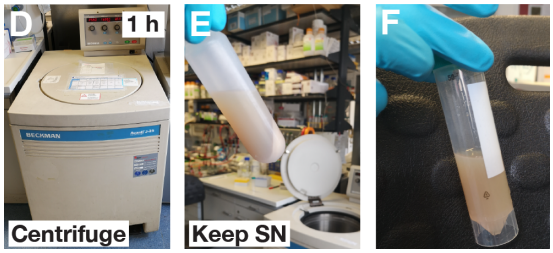

Figure 2.7: Lysis (steps i. - iv.). Pellet is solubilized in lysis buffer (**A**) and sonicated twice for 7 min on ice (**B**) with 5 min in between on roller bank at 4 °C to cool down (**C**). Lysate is centrifuged (**D**) and supernatant (cloudy, **E**) is transferred into new tube (**F**).

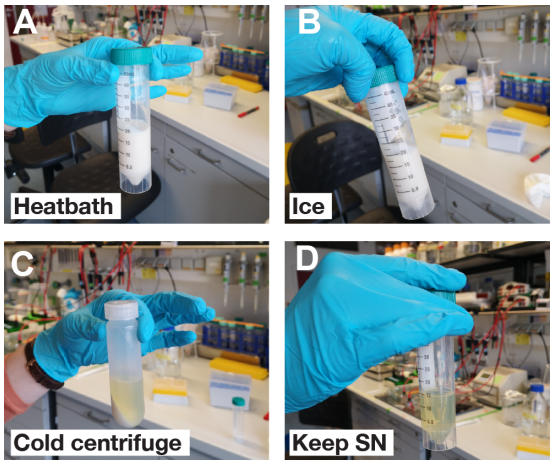

Figure 2.8: First purification cycle (steps v. - ix.). All proteins in supernatant are denatured in a heatbath at 65 °C. Solution is white and cloudy afterwards (**A**, "Heatbath"). ELPs fold back during 4 °C step. Solution looks similar to before (**B**, "Ice"). After centrifuging, supernatant is yellow and clear (**C**) and is collected in new tube (**D**, "Keep SN").

x. Add 3 M NaCl (solution should turn cloudy) (Figure 2.9A, B)

xi. Heat SN to 65 °C in heatbath for 20 min (Figure 2.9C)

xii. Centrifuge: 3 220 g, 40 °C, 20 min (Figure 2.9D)

xiii. Discard SN and invert falcon to allow pellet to dry completely

xiv. Resuspend pellet in 2 ml MilliQ + 1.5 mM TCEP (Figure 2.10A)

xv. Transfer into 2 ml eppi

xvi. Cool on ice for 10 min

xvii. Centrifuge: 20 000 g, 4 °C, 5 min

xviii. Save SN in new eppi (Figure 2.10B)

xix. Take away ∼ 2 – 5 µl for protein gel

xx. Add 3 M NaCl *

xxi. Heat SN to 65 °C in heatbath for 30 min (Figure 2.10C)

xxii. Centrifuge: 20 000 g, 24 °C, 5 min (Figure 2.10D)

xxiii. Discard SN (pellet should be yellowish clear now) **

xxiv. Resuspend pellet in 1 ml coupling buffer (Figure 2.10E)

xxv. Cool on ice for 5 min

xxvi. Centrifuge: 20 000 g, 4 °C, 5 min

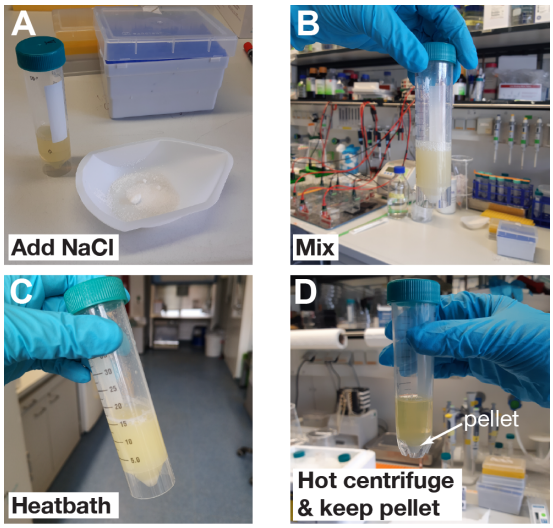

Figure 2.9: Second purification cycle (steps x. - xiii.). Proteins are denatured under high salt (**A, B**) and heat conditions and solution turns cloudy (**C**, "Heatbath"). Solution is centrifuged at 40 °C (**D**) and supernatant is discarded, while pellet with denatured ELPs is kept.

xxvii. Save SN into new eppi

xxviii. Freeze using liquid nitrogen (Figure 2.10F)

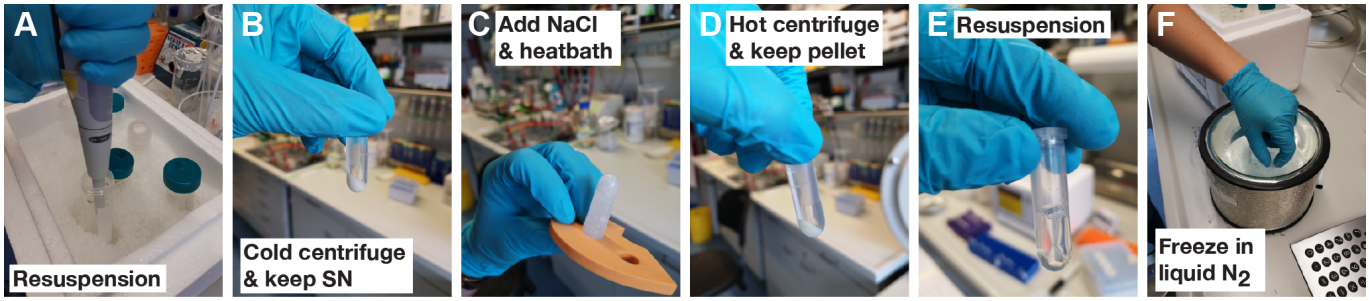

Figure 2.10: **Third purification cycle (steps xiv - xxviii).** Pellet is resuspended on ice (**A**). ELPs go into solution and are in the supernatant after cold centrifugation step (**B**). ELPs are again denatured and flakes appear in the previously clear solution (**C**, "Add NaCl and heatbath"). After hot centrifugation step, pellet is clear with a slightly yellowish tint (**D** "Hot centrifuge and keep pellet") and is resuspended in buffer (**E**). ELPs are shock-frozen in liquid nitrogen (**F**).

xxix. Long-term storage at -80 °C

Note: If the pellet in step ** is not yellow, the protocol can be repeated from * until the end.

- Run protein gel to test

  Cys-6xELP-LPETGG: By coupling to a maleimide-dye.

  Cys-6xELP-**LPETGG**: By coupling to a GGG-dye (e.g.: GGG-tagged GFP) in a eSortase A reaction.

Note: As the ELPs don't have a tryptophan, they are invisible under UV light and can only be indirectly visualized via gel electrophoresis by checking the coupling to fluorophores via their tags.
Note: Sortase-mediated coupling relies on $MgCl_2$. Coupling buffer contains EDTA, making the coupling highly inefficient. Therefore, a small protein sample ($\sim$ 2 – 5 µl) should be taken away one step before * and saved for the gel.

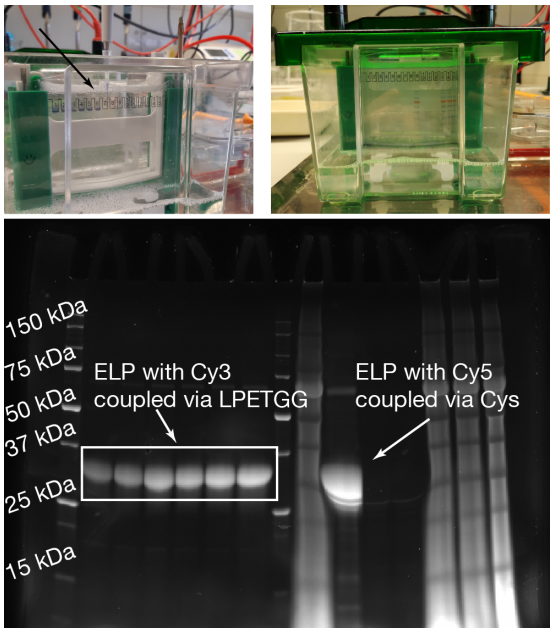

Figure 2.11: Native protein gel to check ELP coupling. A native protein gel is used to check ELP-coupling. Gel is loaded with prestained (lanes 9, 13 - 15) and unstained ladders (lanes 1, 8) and with 7 µl sample to check for coupling (top, left). Gel runs at 150 V for ∼ 50 min (top, right) and was visualized under UV light (bottom). ELPs were labelled with GG-Cy3 binding to the LPETGG motif in a eSortase A-mediated reaction. Lanes 2 - 7 show different eSortase A incubation times, from 15 min to 40 min in steps of 5 min. Efficiency of eSortase A ligation seems to increase with time. In line 10, attachment of an Atto-647N dye with a maleimide to the N-terminal cysteine of ELP is successfully tested. Line 11 and 12 are tests with ELP + Cy3 dye without eSortase A and only ELP, respectively.

2.3.2 Flowcell preparation

This is a protocol for flowcell (FC) preparation that is based upon protocols of Ott et al. [120] and Löf et al. [38].

2.3.2.1 Amino-silanization

Prior to functionalization, glass slides are amino-silanized:

- Sonicate glass slides in 50% 2-propanol and 50% MilliQ solution (this works best in a teflon slide holder)
- Rinse glass slides with MilliQ
- Freshly prepare a 1:1 mixture of H_2SO_4 and H_2O_2 in a glass beaker
- Incubate glass slides in this mixture for 20 min
- Rinse glass slides with MilliQ
  Note: The glass slides should now be hydrophilic.
- Store glass slides in MilliQ until silane solution is prepared
- Silane solution:
  - 88 % Ethanol
  - 10 % MilliQ
  - 2 % silane
- Rinse slides in 99.8 % Ethanol and directly transfer them into silane solution
- Incubate them in the silane solution for 60 min
- Rise slides in two beakers of ethanol and two beakers of MilliQ
- Blow-dry slides under N_2 and dry them at 80 °C

Glass slides are stored under argon atmosphere and stay reactive for several months.

2.3.2.2 Flowcell functionalization

Glass slides are handled with reverse tweezers. The minimal number of FCs functionalized at a time is two, as they need to be sandwiched on top of each other for incubation of reagents (see Figure 2.13). During incubation steps, sandwiched FCs are stored in a humidity chamber unless stated otherwise.

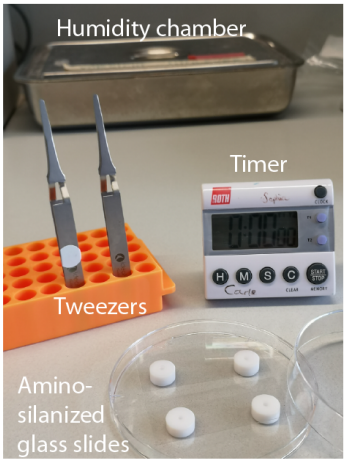

Figure 2.12: Preparation for flowcell functionalization. Two amino-silanized glass slides are functionalized at a time. They are handled with reverse tweezers ("Tweezers") and incubated in a humidity chamber. Incubation time is controlled with a timer.

- Dissolve 10 mM sulfo-SMCC in 50 mM Hepes buffer (pH 7.4) by vortexing
- Apply 180 µl sulfo-smcc solution onto the middle of an amino-silanized glass slide (Figure 2.13A, B) and sandwich two glass slides (Figure 2.13C) before incubating them in the humidity chamber for 45 min (Figure 2.13D)

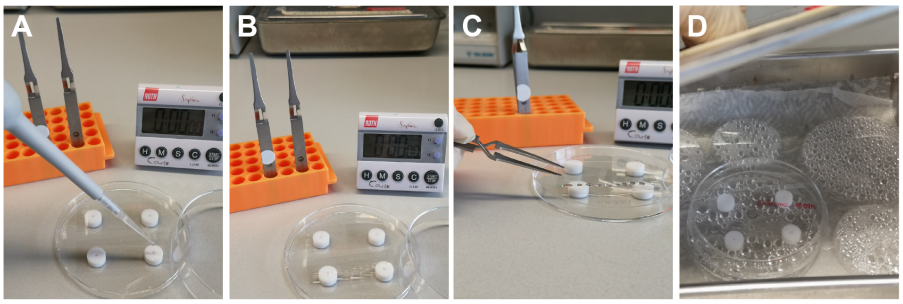

Figure 2.13: Application of reagents onto flowcells. A-B Dissolved reagent is applied to the middle of one slide. **C** The other slide is inverted with reverse tweezers and slowly lowered onto the fluid. Fluid is distributed between the slides by capillary forces. **D** Slides are stored in the humidity chamber during incubation.

- Preparations during incubation
  - Prepare six 800 ml glass beakers
    - Wash with 2-Propanol and MilliQ
    - Fill with MilliQ
  - Dissolve powdered cysteine in 1 ml Coupling Buffer by vortexing to obtain a final concentration of 10 mM and adjust the pH to 7.3 using NaOH
  - Thaw ELPs on ice
- Separate sandwiched slides (Figure 2.14A, B), drain remaining fluid (Figure 2.14C), and wash them individually successively in the six beakers of MilliQ water (Figure

2.14D-F). In the beginning, there will be a complete layer of water on the sulfo-SMCC-covered side of the slide. Over the course of the six beakers, this water layer decreases more and more. The aim is that after six beakers the slide can be pulled out of the water with no fluid film remaining.

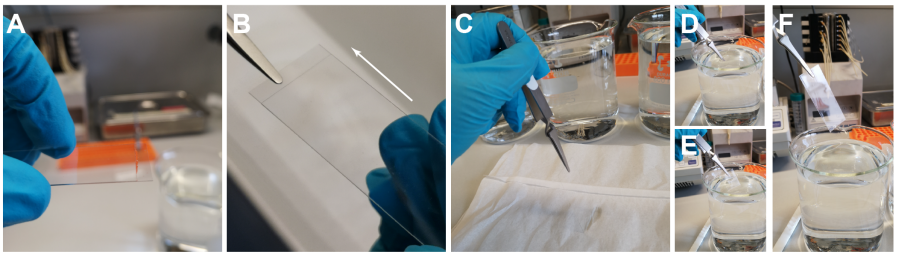

Figure 2.14: Washing flowcells. **A** The upper glass slide is carefully shifted against the lower one to create an overhang, which can be clamped with tweezers. **B** Tweezers are used to pull the upper glass slide off the lower one. **C** Remaining fluid is drained onto wipe. **D - F** Slides are rinsed in 800 ml glass beakers filled with MilliQ water. They are moved into the water and slowly pulled out, such that the water film has time to retract.

Note: Carefully mark which side of the glass slide is the one coated with sulfo-SMCC!

- Apply 100 µl Cys-6xELPs-LPETGG in coupling buffer (pH 7.2) onto the sulfo-SMCC-coated side of one slide and sandwich two glass slides before storing them in the humidity chamber for $>$ 60 min (identical to procedure in Figure 2.13).
  - During incubation: Prepare 4 fresh beakers with MilliQ according to the upper description
- Separate sandwiched slides and wash them individually successively in the four beakers of MilliQ water (identical to procedure in Figure 2.14).
- Apply 180 µl 10 mM cysteine (pH 7.3) onto the ELP-coated side of one slide and sandwich two glass slides before storing them in the humidity chamber for $>$ 60 min
- Preparations during incubation:
  - Re-fill 4 beakers with new MilliQ
  - Shortly before washing:
    * Sonicate polystyrene beads (diluted 0.6:2000 in EtOH)
    * Sonicate 2 non-functionalized, perforated top slides 10 min in 50:50 MilliQ and 2-propanol. Rinse them afterwards with 2-propanol and MilliQ before blow-drying them with N_2
- Separate sandwiched slides and wash them individually successively in the four beakers of MilliQ water.
- Add 130 µl of polystyrene bead solution on the two slides and wait for the ethanol to slowly evaporate (best in a closed petri dish)
- Heat for 5 min at $>$ 70 °C
- Wash slides in two beakers of MilliQ water

2.3.2.3 Flowcell assembly

After FC functionalization, FCs are assembled from one functionalized bottom slide and one perforated, unfunctionalized top slide.

- Cut separation layer out of parafilm according to a template (Figure 2.15A)

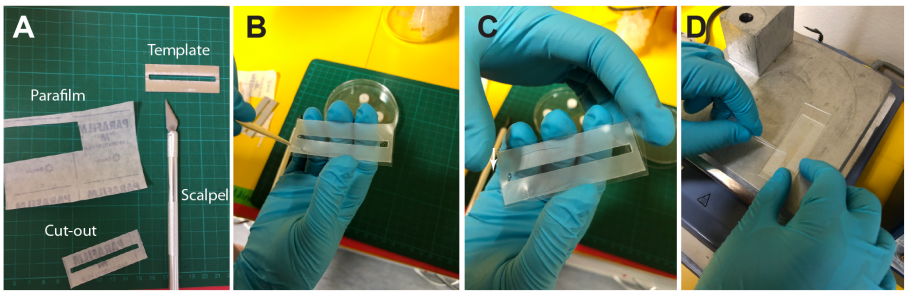

Figure 2.15: Flowcell assembly. A Separation layer is cut out of parafilm with a scalpel according to a template (outer rectangle dimensions: 59 mm x 21.5 mm, inner rectangle dimensions: 54 mm x 4 mm) **B** Parafilm is aligned on the unfunctionalized top-slides, such that the perforations are not covered. It is brought down onto the glass with a pipette tip. **C** Functionalized bottom slide is sandwiched onto the other side of the parafilm, such that the functionalized side faces the parafilm. **D** Slides are heated on a hot plate at $> 70\,^{\circ}C$ while removing air bubbles in the parafilm around the cut-out with a pipette tip.

- Align parafilm cut-out on unfunctionalized top slide such that perforations are not covered (Figure 2.15B). Carefully bring it down with a pipette tip. Sandwich functionalized bottom slide onto parafilm such that functionalized side is on the inside (Figure 2.15C)
- Heat assembled FCs at $> 70\,^{\circ}C$ while pressing them together with a pipette tip, until parafilm is molten (Figure 2.15D).
- Allow assembled FCs to cool down before using them for experiments

FCs can be stored in a dark, dry place at room temperature for up to 2 months.

2.3.3 Protein measurements

Prior to protein measurements, the magnet needs to be calibrated to obtain the relationship between the distance of the magnet to the flowcell and the applied force. As calibration of short tethers is cumbersome due to their high corner frequency, we typically record a master calibration curve using 21 kbp DNA tethers. The force is then calibrated based on tether fluctuations by calculating the Allan deviation and averaging over multiple tethers. This has been described previously [73;74].
Note: Using commercially available streptavidin-coated Dynabeads™ M-270 (#65305, Invitrogen™), there is a bead-to-bead variability in force of roughly 10 % [74–77] due to differences in magnetization. This problem can be circumvented by a bead-specific force calibration. It is not necessary to fully calibrate each tether, but it suffices to measure bead fluctuations only at a small number of distances. This allows to find a correlation parameter c, relating each beads' force-distance relationship to the master calibration curve obtained by long-tether calibration via $F(d) = c \cdot F_{master}(d)$ [63;69] with d being the magnet-flowcell distance.
Note: For fields of view only one order of magnitude smaller than gap distance between the two magnets, it should be carefully assessed whether the force is constant throughout the whole field of view.

2.3.3.1 Measurement preparation

Flowcell passivation

- Implement FC into FC holder (Figure 2.16A, B; for a technical drawing of the FC holder, see Appendix B)
- Add 200 µl 1% casein solution (5% Casein solution diluted to 1% in MilliQ) into the inlet and incubate for >1 h
- Install FC holder with FC onto the sample stage of MT setup and introduce tubing into the outlet (Figure 2.16C)
- After casein incubation: Flush with 1 ml measurement buffer

Protein biotinylation

The protein of interest is biotinylated via sfp-mediated attachment of CoA-Biotin to its ybbR tag in a bulk reaction. The active site of sfp needs a magnesium ion for coordination and proper function. Accordingly, enough $MgCl_2$ should be provided in the measurement buffer. sfp-mediated ligation of CoA with a ybbR tag has no back-reaction. Thus, biotinylation can be performed overnight at 4°C, or for one hour at 37°C, depending on the stability of the protein of interest.
Typical concentrations during the biotinylation reaction are:

- 50 – 150 nM protein of interest
- 50 – 75 μM CoA Biotin
- 2 – 5 μM sfp
- 10 – 100 mM $MgCl_2$

Note: If the concentration of the protein of interest is high, it can be beneficial to perform the biotinylation with higher protein concentrations and afterwards dilute the biotinylated protein.

eSortase A addition

- Dilute eSortase A
- Add 1 μl diluted Sortase to protein mix
- Final protein-mix parameters are:
  - Final volume: 80 – 100 μl
  - Final biotinylated protein of interest concentration: ∼ 20 nM
  - Final eSortase A concentration: ∼ 1 – 2 μM

Surface coupling

- Add 80 to 100 μl protein mix into the FC and incubate for 20 – 30 min
- Flush with 1 ml measurement buffer with tween to remove unbound protein.
  Note: The eSortase A-mediated protein attachment to ELPs has a back-reaction. The incubation time of the protein in the FC is thus critical (see Section 2.3.3.2)

Magnetic bead preparation

Wash 30 μl magnetic beads three times in 200 μl measurement buffer with tween:

- Fill 30 μl bead solution into eppi
- Bring permanent magnet close to the eppi to collect beads on one side. This can be achieved with a neodymium magnet or with a magrack (e.g. Merck, #GE28-9489-64)
- Remove fluid on the other side of the beads
- Add new fluid and mix by vortexing or shaking
- After three washing steps, dissolve dry beads in 120 μl measurement buffer + tween.

Protein tethering

- Add 8 – 30 μl bead solution into the FC
- Wait for beads to sink to the bottom of the FC
- Remove unbound beads by flushing with 1 ml measurement buffer + tween.

Bead selection and look-up table

Select beads and define regions of interest (ROIs) around them for diffraction pattern-based extension tracking. For beads with a 2.8 μm diameter we used ∼ 10 to 15 μm^2 squared ROIs. Beads should be selected in a way that no diffraction patterns of other beads are visible inside the ROI. Before starting measurements, a look-up table is generated for each bead:

- Move magnets to a distance corresponding to ∼ 2 pN (for two 5 mm neodymium cubes (W-05-N50-G, Supermagnete, Switzerland) with a gap distance of 1 mm, this is ∼ 5 mm from the FC)
- Iteratively move the objective upwards in steps of 100 nm while recording the diffraction pattern at each relative objective-bead distance

- For the measurement, move the objective to the position in the middle of the look-up table (i.e. for a 10 μm large look-up table, it would be moved to 5 μm above its starting position)

During the measurement, the current diffraction pattern of the bead is compared to the look-up table and thus the tether extension is tracked.

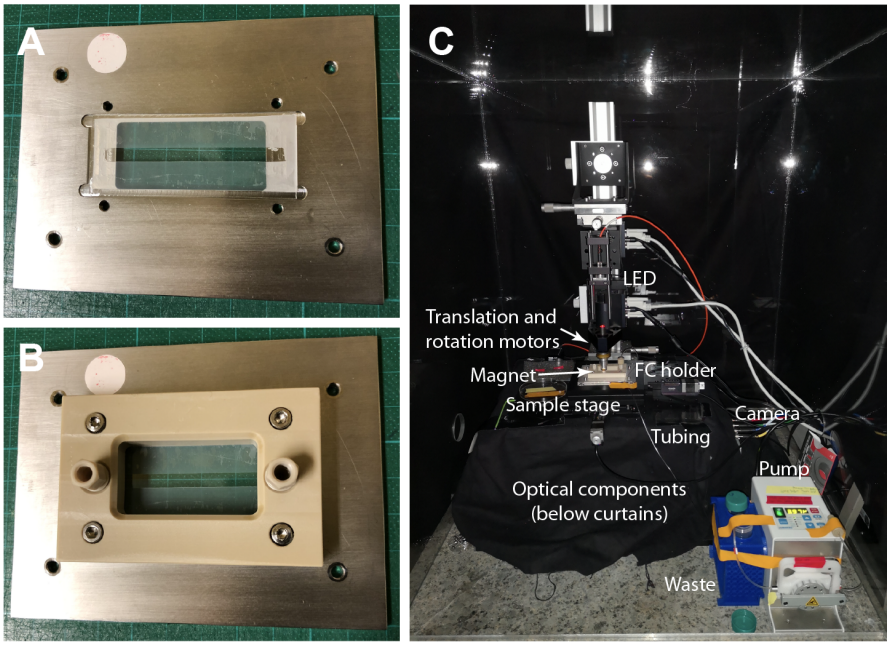

Figure 2.16: Measurement preparation. A Flowcell is placed with perforations facing upwards in metal frame with cutout for observation from the bottom with an inverse microscope. **B** Custom PTFE FC holder with inlet and outlet cylinders is installed on top. **C** FC holder is mounted onto the setup. Components of the setup include (top to bottom): LED for illumination, translation and rotation motors for magnet movement, magnet, FC holder ("FC holder") with tubing connected to the outlet, motorized sample stage with micrometer screws for positional adjustment, optical components (objective, mirror, and lens, covered with a black cloth to minimize background light), camera, and pump with liquid waste.

2.3.3.2 Measurement optimization

Our attachment protocol is based upon eSortase A-mediated covalent protein coupling to ELP linkers[38;127]. To optimize the yield of the measurements, we found five parameters to be critical:

- ELP concentration
- Protein of interest concentration
- eSortase A concentration
- Incubation time
- Concentration of magnetic beads

The first four points are highly inter-dependent, as the intermediate LPET· state in the eSortase A-mediated coupling is prone to hydrolysis and a back-reaction of the ligation can take place[127]. Thus, the efficiency of protein attachment can decay for prolonged reaction times, high eSortase A concentrations, or low protein/ELP concentrations. If the concentration of the protein of interest is high, optimization of the other parameters is not highly critical. However, if the concentration of the protein of interest is low, optimization can be crucial to obtain higher yields during measurements. Due to potential differences in tag-accessibility, the optimization process should be repeated for every new protein construct.
After protein ligation, magnetic beads are flushed into the FC, allowed to sink down, and after $\sim$ 30 s settlement time, all unbound beads are flushed out again. Even if the protein concentration is not high, it is not necessarily better to increase the bead concentration for increased yield. As the ELP functionalization as well as the protein distribution on the surface is not homogeneous, too many beads can increase the amount of multiply tethered beads. Furthermore, too high crowding within the FC can lead to tracking artifacts due to overlapping regions of interest. Therefore, the initial bead concentration should be carefully chosen.

2.3.3.3 A multi-channel flowcell holder

FCs can only be used once, as proteins cannot be removed from ELP linkers without hydrolyzing them and making them useless for binding new proteins. The measurement optimization process described above can be very cumbersome, if each FC can only be used to test one condition. To avoid this problem, multi-FCs can be employed (Figure 2.17).
For this purpose, silanized glass slides are functionalized as described above, before sticking

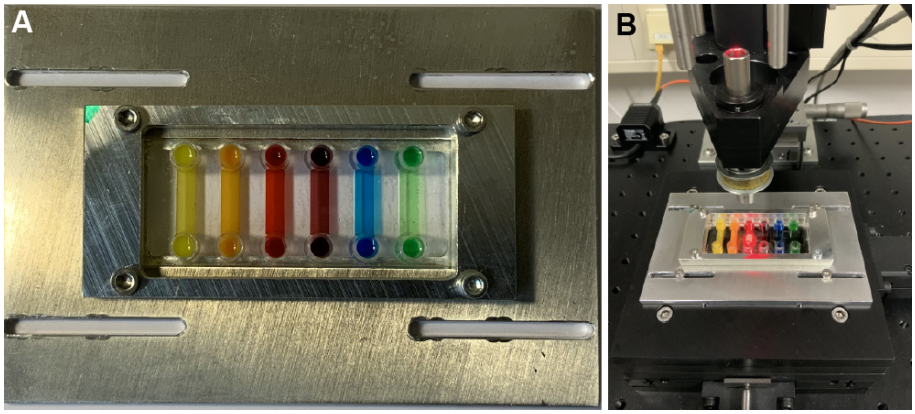

Figure 2.17: An alternative multi-channel flowcell holder. A A functionalized bottom slide is stuck onto the backside of a commercially available multi-channel slide and integrated into a modified FC holder. **B** FC holder is mounted onto the setup.

them on the backside of a commercially available µ-Slide VI 0.4 (# 80606, Ibidi). The six-channel FCs can be implemented into a modified FC holder (see Figure B.2 and Figure B.3) and installed onto the sample stage of an MT setup. Each channel can then be used separately, allowing to test six conditions on one slide. Even though these six-channel slides offer great advantages for optimization purposes, they also bear some disadvantages: Because of the size of inlet and outlet as well as the size of the magnet holder, only one FOV can be screened in vertical direction. Also, due to increased height of the channels, forces are limited, as the magnets cannot be brought as close to the bottom slide as for conventional FCs, where the minimal bead-magnet distance is given by the height of a single parafilm layer in addition to the 170 µm of the top glass slide. This needs to be considered as an offset for force-application as well, when wanting to use the identical force-calibration as for regular FCs.

3

Designed Anchoring Geometries Determine Lifetimes of Biotin-Streptavidin Bonds Under Constant Load and Enable Ultra-Stable Coupling

Summary

The small molecule biotin and the homotetrameric protein streptavidin (SA) form a stable and robust complex that plays a pivotal role in many biotechnological and medical applications. In particular, the SA-biotin linkage is frequently used in single-molecule force spectroscopy (SMFS) experiments. Recent data suggest that SA-biotin bonds show strong directional dependence and a broad range of multi-exponential lifetimes under load. Here, we investigate engineered SA variants with different valencies and a unique tethering point under constant forces using a magnetic tweezers assay. We observed orders-of-magnitude differences in the lifetimes under force, which we attribute to the distinct force-loading geometries in the different SA variants. Lifetimes showed exponential dependencies on force, with extrapolated lifetimes at zero force that are similar for the different SA variants and agree with parameters determined from constant-speed dynamic SMFS experiments. We identified an especially long-lived tethering geometry that will facilitate ultra-stable SMFS experiments.

3.1 Introduction

The non-covalent, high-affinity binding of the small molecule biotin to streptavidin (SA) is ubiquitously used in a variety of biological, chemical, biophysical and pharmaceutical applications [128–130]. Biotin can readily be covalently attached to nucleic acids [79;131;132], proteins [133;134], or linker molecules [135]. SA is stable over a wide range of conditions and easy to handle [128]. Owing to the specificity of the binding, as well as the robustness of the complex, the interaction has in particular become a popular tool in the context of single-molecule force spectroscopy (SMFS) assays [136–139]. It serves as a molecular handle to anchor molecules of interest and apply forces and torques to them [80;86;111;132;140–144]. The long lifetime of the

This Chapter was published by Gruber, Löf, and Sedlak *et al.* with Gruber, Löf, and Sedlak as equally contributing first authors at *Nanoscale* [4]. It was reproduced with permission from the Royal Society of Chemistry. My contribution: For this paper, I was involved in designing the research, streptavidin-functionalization of magnetic beads, performing and analyzing magnetic tweezer data, analyzing AFM imaging data, and writing the manuscript.

SA-biotin complex under external forces has enabled constant-force SMFS experiments lasting for hours and even up to weeks in magnetic tweezers (MT)[38;89]. Despite its widespread use, SA's tetravalency poses a problem, in particular in SMFS applications, since it is a priori ambiguous which of the four subunits biotin binds to. This ambiguity results in four different force-loading geometries for a given attachment of the SA tetramer (Fig.3.1)[145]. Furthermore, if SA is non-specifically attached – as is the case in many commercially available SA-coated magnetic beads – a variety of attachment points combined with tetravalency results in an even larger range of possible force-loading geometries[38;146].

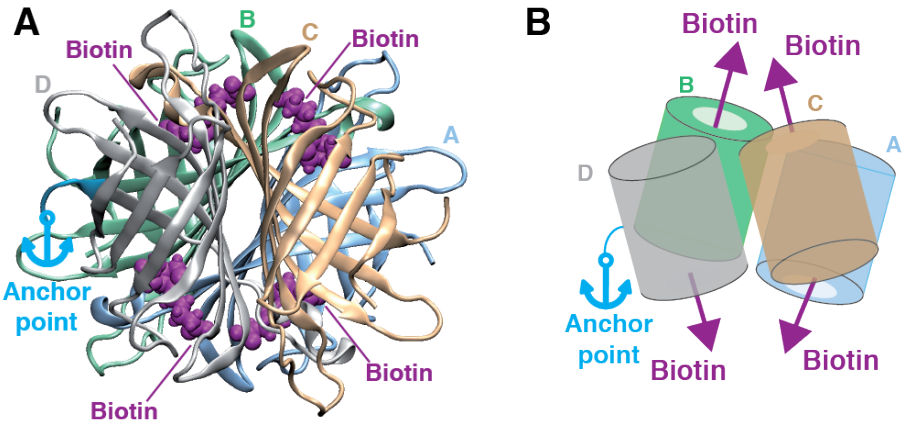

Figure 3.1: SA's tetravalency results in different force-loading geometries. A Crystal structure of the SA tetramer (PDB-ID: 6M9B[21], rendered using VMD[22] with the four subunits shown in different colors. Four bound biotin molecules are shown in purple. The light blue anchor marks the attachment point (C-terminus of subunit D). **B** Schematic representation of the tetramer structure. The colored barrels represent the four subunits. Arrows indicate the initial force-loading directions in the SMFS experiments: The light blue anchor marks the C-terminus of subunit D used for site-specific immobilization. Purple arrows indicate the four possible directions of pulling biotin out of the different binding pockets. Under constant load, the complex will rotate and rearrange in such a way that the sum of forces acting on it equals zero. Depending on which subunit biotin is bound to, the orientation of the complex will be different resulting in different force propagation pathways.

Atomic force microscopy (AFM)-based constant speed SMFS experiments have recently shown that the force needed to unbind biotin from the SA binding pocket is strongly dependent on the force-loading direction[147;148]: Tethering SA by a single defined residue and pulling biotin out of one of the binding pockets results in different force-loading geometries, depending on which SA subunit the biotin has bound to. For some of the pulling directions, the SA subunit is deformed such that the energy barrier of the binding is decreased, causing lower biotin unbinding forces[148]. However, the influence of the tethering geometry of SA on the lifetime of the SA-biotin interaction under constant forces is currently unknown.

Here, we employ engineered variants of SA with different defined valencies and a unique tethering point to restrict and control the number of possible force-loading geometries for SMFS measurements. We use AFM imaging to verify the valencies by showing that only the competent subunits can bind biotin. Furthermore, we employ isothermal titration calorimetry (ITC) to directly measure the binding enthalpies of the different SA variants. With an MT assay we assess the stability of the SA-biotin interaction under different levels of constant load and demonstrate large differences in the lifetime depending on the attachment geometry. The different stabilities give rise to multi-exponential lifetime distributions for multivalent constructs. We observe an exponential decrease of lifetimes with increasing force, with parameters for the force dependencies fully consistent with findings from constant speed SMFS experiments. By using one well-defined attachment and a monovalent SA construct, a single extremely stable population is achieved. We expect our results to be highly relevant for force spectroscopy, and, in general, to improve assays where the SA-biotin bond is under load, e.g. through fluid flow or rinsing steps.

3.2 Results and Discussion

To systematically investigate the stability of the SA-biotin complex under constant mechanical load, we prepared tetra-, tri-, and monovalent variants of SA. These comprise four, three, and one functional subunit(s), while the remaining subunits are incapable of biotin binding (4SA, 3SA, and 1SA; Fig. 3.2A) due to three mutations located around the binding pocket (N23A, S27D, S45A)[149]. In addition, a variant consisting of four non-functional subunits (0SA) was prepared. All variants possess a single cysteine residue at the C-terminus of their subunit D, allowing for site-specific immobilization[140;145;148]. For 3SA and 0SA, subunit D is non-functional, whereas for 1SA and 4SA, it is functional (Fig.3.2A; for details on protein engineering see Materials and Methods).

3.2.1 AFM imaging reveals binding stoichiometry

To verify the valency of the different variants, we incubated them with biotinylated 250 bp double-stranded DNA constructs and directly visualized the resulting SA-biotinylated DNA complexes by AFM imaging (Fig. 3.2B and Fig. 3.4-3.7). An excess of biotinylated DNA over SA (approximately twenty-fold for 4SA and 3SA, and four-fold for 1SA and 0SA) was used to ensure that SA molecules with DNA strands bound to all functional subunits could be observed. Indeed, a maximum of four, three, and one bound biotinylated DNA strand(s) was observed for 4SA, 3SA and 1SA, respectively, confirming the expected valencies (Fig. 3.8). In the case of 0SA, no SA-biotinylated DNA complexes were observed.

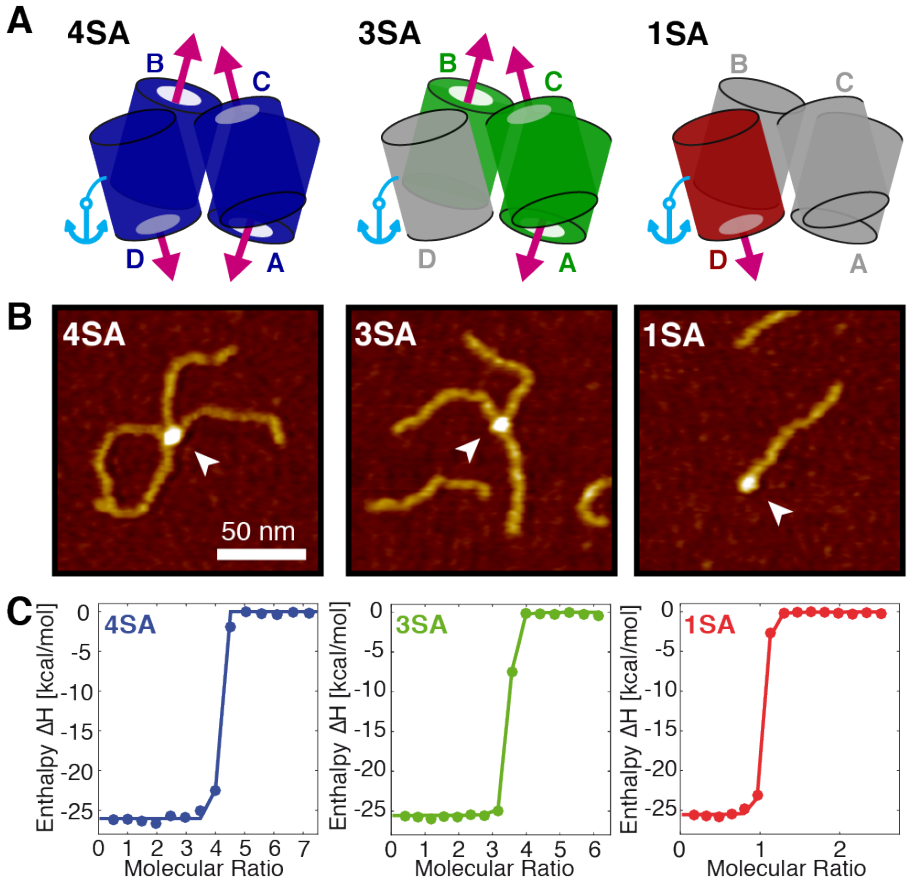

Figure 3.2: Probing SA variants with different valencies by AFM and ITC. A Schematic structure of SA constructs with different valencies. 4SA (left), 3SA (middle), and 1SA (right) have four, three and one functional subunit(s) (colored), respectively. The remaining subunits (gray) are incapable of binding biotin. All constructs have a single C-terminal cysteine at their subunit D –nonfunctional for 3SA, functional for 1SA and 4SA– for site-specific immobilization (light blue line). The light blue anchors mark the anchoring site of SA for the SMFS experiments, while the purple arrows indicate the possible directions in which biotin can be pulled out of the binding pockets. **B** AFM images of 4SA (left), 3SA (middle), and 1SA (right) with the maximal number (four, three, and one, respectively) of biotinylated DNA strands bound. Arrows mark the SA molecules. Height range of color scale is 2 nm. **C** Isothermal titration calorimetry data of free biotin binding to SA of different valencies. Colored dots are the measured heat release per mole upon adding biotin to SA plotted against the molecular ratio (biotin per SA) in the measurement cell. Lines are fits to the data (taking the discreteness of the measurement into account). For details of the fits see supplementary material.

3.2.2 Thermodynamic parameters determined by isothermal titration calorimetry

Next, we performed isothermal titration calorimetry (ITC) measurements to determine the thermodynamic parameters of biotin-binding to the different SA constructs in the absence of force (Fig. 3.2C). In principle, ITC allows determination of the stoichiometry, the affinity, and the binding enthalpy. To ensure good comparability across measurements, we used the same biotin stock solution with an estimated 5% uncertainty in absolute concentration

for all measurements. The uncertainty in the concentrations of the SA stocks was estimated to be 10% (see Materials and Methods). Fits to the ITC data give values for the binding stoichiometries of 1.0 ± 0.2 for 1SA, 3.3 ± 0.5 for 3SA, and 3.9 ± 0.6 for 4SA (Fig. 3.2C), in excellent agreement with the results from AFM imaging (Fig. 3.2B and Fig. 3.8). The largest contributions to the measurement errors result from the uncertainties in concentration. The uncertainties of the values increase with the number of available binding sites, because a given uncertainty in protein concentration has a larger impact on the uncertainty with increasing stoichiometry. Due to limitations of our instrument and the very high affinity of biotin to SA, the binding constant could not be obtained directly and we can only determine that the affinity is higher than 1 nM. We obtained binding enthalpies per binding site of $-(25.0 \pm 1.3)\ \frac{kcal}{mol}$ for 1SA, $-(25.6 \pm 1.4)\ \frac{kcal}{mol}$ for 3SA and $-(26.1 \pm 1.3)\ \frac{kcal}{mol}$ for 4SA (Fig. 3.9). These results agree well with enthalpies measured in previous studies[145;150;151]. Within experimental errors, the binding enthalpies per binding site for all SA variants are the same, suggesting that in the absence of force all subunits are equivalent with regard to biotin binding and that no effects of binding geometries or binding cooperativity come into play.

3.2.3 Single-molecule MT measurements determine lifetimes under force

To directly measure the lifetimes of the SA-biotin interactions under constant force and to investigate the influence of different force-loading geometries, we performed MT measurements using the different SA variants (Fig. 3.3). In MT, the molecular construct of interest is tethered between the bottom surface of a flow cell and a superparamagnetic bead (Fig. 3.3A). By applying a magnetic field, generated by permanent magnets, a constant force is exerted on the bead and thereby on the tether[59;70]. We track the 3D position of the bead and the extension of the tether can be determined with nanometer resolution. Importantly, with our MT setup we can track approximately 100 beads in parallel, enabling us to obtain good statistics in a short amount of time[38]. In addition, MT provide excellent force and drift stability, facilitating long measurements[38], which are critical due to the high stability of the SA-biotin bonds.

For the MT measurements, the small protein domain ddFLN4 (fourth F-actin cross-linker filamin rod domain of Dictyostelium Discoideum[37]) was biotinylated and covalently coupled to the bottom surface of a flow cell by an elastin-like polypeptide (ELP) linker[120]. The different SA variants (4SA, 3SA, or 1SA) were site-specifically and covalently immobilized on magnetic beads via polyethylene glycol (PEG) linkers, by reacting the C-terminal cysteine of subunit D with a thiol-reactive maleimide group on the PEG linker (Fig. 3.3A). The SA-functionalized beads were introduced into the flow cell and one of the functional subunits of the respective SA construct bound to the biotinylated ddFLN4, thereby tethering the magnetic bead to the surface. Upon force application, the molecular linkers are stretched and ddFLN4 unfolds in a characteristic two-step manner[38;152] (Fig. 3.3B). We use the distinct two-step unfolding pattern as fingerprint to identify specific, single-tethered beads, i.e. beads that are bound to the surface via a single SA-biotin interaction.

3.2.4 MT measurements at 65 pN reveal different lifetime populations

In a first set of measurements, beads were subjected to a constant force of 65 pN and the time until bead rupture was recorded. The rupture events are attributed to the unbinding of biotin from SA, as this is the only non-covalent bond within the tether connecting the beads with the surface and as the ddFLN4 protein fingerprint allows us to limit the analysis to correctly tethered beads.

Measurements of 1SA, the monovalent variant, exhibited a survival time distribution that is well described by a single-exponential fit (Fig. 3.2C, red) with a lifetime of $\tau_1 = 7.2\ h \pm 0.2\ h$ ($2.61 \cdot 10^4\ s \pm 680\ s$; see Materials and Methods for details of the fits). The fitted lifetime is in good agreement with the $6.7\ h$ reported recently for a smaller data set[38]. The single-exponential lifetime suggests the presence of a single population, consistent with the expectation that for 1SA only subunit D (attached to the bead via its C-terminus) is capable of binding biotin. All 1SA-functionalized beads are thus tethered in the same geometry, resulting in one well-defined force-loading direction.

3SA is complementary to the 1SA variant, in the sense that all but the attached subunit are functional, so that three different pulling geometries are possible for 3SA. The lifetime

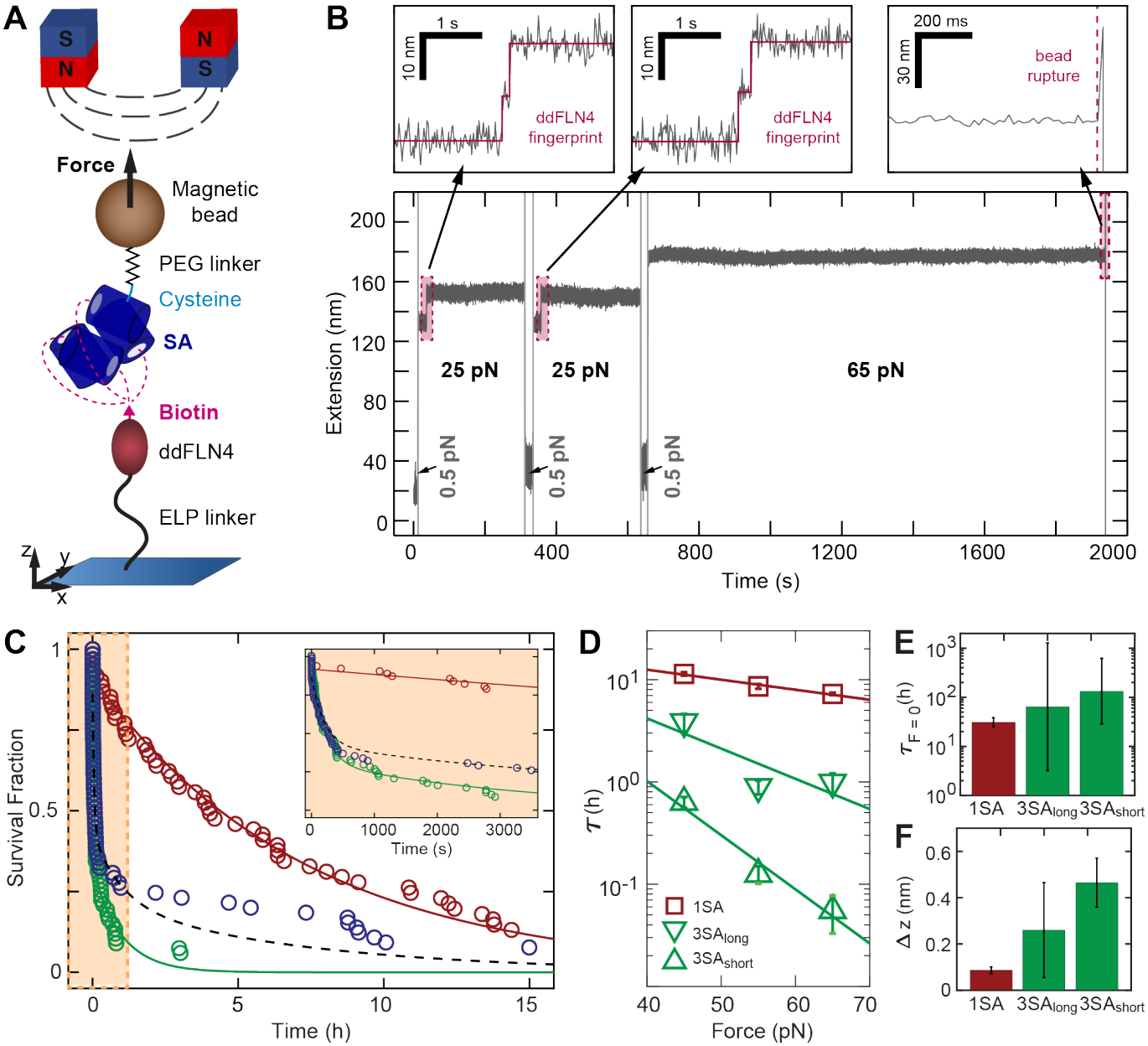

Figure 3.3: **Lifetimes of SA-biotin interactions under constant force. A** Schematic of MT experiments (not to scale). SA (4SA, 3SA, or 1SA) is site-specifically and covalently immobilized on magnetic beads via the single C-terminal cysteine at its subunit D using a PEG linker with a thiol-reactive maleimide group. Biotinylated ddFLN4 is covalently immobilized on the bottom slide of the MT flowcell via an ELP linker. Binding of the biotin to one of the functional subunits of the respective SA construct tethers the beads by a single SA-biotin bond. Force is exerted on the magnetic beads by permanent magnets positioned above the flowcell. **B** Time trace of the tether extension during an MT measurement. At the beginning of the measurement, beads are subjected to two 5-min intervals at 25 pN, to observe unfolding of ddFLN4 in a characteristic two-step pattern (left and middle zoom-in), which serves as fingerprint to identify specific, single-tethered beads. Short low force intervals (0.5 pN) allow for ddFLN4 refolding. Tethers are then subjected to a constant force of 65 pN and the time until bead rupture due to unbinding of biotin from SA is monitored (right zoom-in). **C** Survival fractions at 65 pN as a function of time for 1SA (red), 3SA (green), and 4SA (blue). 1SA data were fit with a single exponential (red line) with a mean lifetime of $2.6 \cdot 10^4$ s. 3SA data were fit with a two-component model (Materials and Methods) with a short lifetime of 199 s and a long lifetime of $3.6 \cdot 10^3$ s (green line). 4SA data are well described by the predicted response from the combination of 1SA and 3SA lifetimes that takes into account the binding site stoichiometry (black dashed line, not a fit). The inset shows a zoom on the first hour of the data. **D** Lifetimes for 1SA (τ_1) and for the long- and short-lived 3SA interactions (τ_2 and $\tau 3$) as a function of applied force. Data points are from fits of the survival fractions in panel C and in Fig. 3.11. Error bars are from the bootstrap analysis. Solid lines are fits of the Bell model. **E** Lifetimes at zero force τ_0 from fits of the Bell model in panel D. **F** Distances to the transition state Δz from fits to the Bell model. Error bars in E and F correspond to 95% confidence intervals from the fits.

measurements reveal much shorter overall lifetimes for 3SA compared to 1SA (Fig. 3.3C, compare red and green data points). In addition, the data are not well described by a single exponential, suggesting that the different possible pulling geometries for 3SA give rise to different lifetimes. The 3SA data are well described by a fit with the sum of three exponentials and we find two relatively short and one longer lifetime (fitted lifetimes are 98 s $\pm$ 12 s, 365 s $\pm$ 30 s, and 3100 s $\pm$ 230 s). A simpler model that combines the two shorter

lifetimes into one exponential,

$$f(t) = \frac{f_2}{3} \cdot [1 \cdot exp(-t/\tau_2) + 2 \cdot exp(-t/\tau_3)]$$

, fits the 3SA data almost equally well (Fig. 3.3C, green). From this fit we obtain the two distinct lifetimes as $\tau_2 = 3600\ s \pm 350\ s$ and $\tau_3 = 199\ s \pm 10\ s$, where the weighting factors of the fit formula are chosen such that two thirds of the interaction of biotin and 3SA exhibit the short lifetime and one third exhibits the long one. We hypothesize that the longer-lived population corresponds to binding to one subunit, while the other two subunits exhibit lifetimes under mechanical tension that are similar.
Using steered molecular dynamics simulations, Sedlak et al.[148] have shown that for pulling biotin out of subunit A or C of SA tethered by the C-terminus of subunit D, the molecular linker adjacent to biotin gets pushed against a flexible peptide loop, significantly lowering the mechanical stability of the binding pocket. For pulling biotin out of subunit B, the same effect occurs, yet markedly less pronounced. Therefore, we assign the longer lifetime for the 3SA construct to biotin unbinding from subunit B. The shorter-lived population that comprises approximately two thirds of all unbinding events is consequently assigned to the sum of unbinding events from subunits A and C. Remarkably, the lifetime of this shortest-lived population at 65 pN is 130-fold lower than the one observed for the 1SA construct and even the long lifetime observed for 3SA is still approximately one order of magnitude shorter than the lifetime observed for 1SA.
For 4SA, we observe a rapid initial decay of bonds, but also very long-lived tethers (Fig. 3.3C, blue). Since for 4SA all force-loading geometries realized in 3SA and 1SA are possible, we expect a combination of the short-lived populations observed for 3SA and the long-lived population observed for 1SA constructs. Based on this assumption, we co-plotted a prediction for the 4SA survival fraction over time as given by

$$f(t) = \frac{f_3}{4} \cdot [exp(-t/\tau_1) + exp(-t/\tau_2) + 2 \cdot exp(-t/\tau_3)]$$

using the lifetimes obtained from fitting the 1SA and 3SA data (Fig. 3.3C, black dashed line). The prediction using the fitted lifetimes from the 1SA and 3SA data closely matches the experimentally determined lifetimes for the 4SA variant, confirming the validity of our lifetime model and suggesting essentially random binding to the different subunits.

3.2.5 Lifetimes depend exponentially on applied load

To determine the force dependencies of the lifetimes, we performed a set of experiments at lower forces on the 1SA and 3SA constructs. The lifetime data at 45 and 55 pN are well described by the single and double exponential models used at 65 pN for 1SA and 3SA, respectively (Fig. 3.11). We found that all observed lifetimes ($\tau_1 - \tau_3$) systematically increase with decreasing force (Fig. 3.3D). For example, τ_1 for 1SA increases to $11.5\ h \pm 0.4\ h$ at 45 pN. The force dependencies of the lifetimes are well described by the Bell model[93] with an exponential dependence on the force:

$$\tau(F) = \tau_0 \cdot exp(\frac{-F\Delta z}{k_B T})$$

where Δz is the distance to the transition state, τ_0 the lifetime in the absence of force, and $k_B T$ the Boltzmann constant times the absolute temperature (Fig. 3.3D). From fits of the Bell model, we find similar lifetimes in the absence of force for τ_1, τ_2, and τ_3 in the range of $\tau_0 \sim 50\ h$ (Fig. 3.3E). In contrast, the fitted distances to the transition state Δz are significantly different for the three lifetimes. Δz is smallest for 1SA and increases for the long-lived and again for the short-lived 3SA population (Fig. 3.3F). The observed convergence of lifetimes, within error, at zero force would be expected, since in the absence of force the force-loading direction should be irrelevant. The orders-of-magnitude differences between lifetimes under force for the different force-loading directions is accounted for in the Bell model by the different distances to the transition state, which correspond to the slopes of log(lifetime) vs. applied force (Fig. 3.3D). With the caveat that extrapolation over orders-of-magnitude to zero force is necessarily somewhat imprecise, we find off-rates at zero

force $k_{0,off} = \tau_0^{-1}$ of 2 to $8 \cdot 10^{-6} s^{-1}$ from our constant force measurements in the MT, well within the range of results from dynamic AFM force spectroscopy measurements that reported values of $10^{-5} s^{-1}$ to $10^{-7} s^{-1}$ for the 1SA construct from fits of the Bell-Evans model to data at defined loading rates[147;148;153]. The observed off-rates at zero force from force spectroscopy are also in reasonable agreement with the value of $6.1 \cdot 10^{-5} s^{-1}$ determined in bulk from a radiolabeled biotin assay[149]. Further, we find reasonable agreement between $\Delta z_{1SA} = 0.09\,nm \pm 0.03\,nm$ from fits of the Bell model to constant force MT data and the values in the range of 0.13 to 0.23 nm from fits of the Bell-Evans model to constant retraction velocity AFM data[147;148]. The small value of Δz_{1SA} corresponds to a highly cooperative unbinding transition and ensures high stability even under load. In contrast, Δz for the force-loading directions probed with the 3SA construct are larger, which can likely be attributed to the molecular mechanism observed in constant-speed force spectroscopy experiments combined with all-atom steered-molecular dynamics simulations: For certain pulling directions, the SA binding pocket is deformed before biotin leaves the pocket and, consequently, the unbinding pathway is altered, resulting in lower unbinding forces for measurements at constant retraction velocities[148], and in shorter lifetimes for constant force experiments.

More importantly, from an application perspective, the force-loading geometry that yields the longest lifetime corresponds to pulling biotin out of the binding pocket of the subunit that is C-terminally tethered. The lifetime for this geometry is, at the forces probed here, almost two orders-of-magnitude larger than for the other possible geometries. Thus, it is highly beneficial to utilize this geometry in applications for which high yield of tethers with high force stability is desirable.

Importantly, this can straightforwardly be realized employing the 1SA variant used in our experiments.

Finally, we note that the lifetimes obtained for the site-specifically attached 4SA used here were, both for the longest- and for the shortest-lived population, appreciably higher than the respective lifetimes measured for commercially available SA-coated beads (Dynabeads M-270 Streptavidin, Invitrogen/Thermo Fisher)[38] or beads randomly coupled via lysine residues[138]. This difference may be explained considering that the SA-biotin complex can withstand higher forces when loaded with force from the C-terminus as compared to pulling from the N-terminus, as it has recently been demonstrated for 1SA in AFM SMFS[147;154]. The attachment of commercially available beads is likely not site-specific, resulting in a variety of pulling geometries, whereas in the custom SA constructs, force was specifically applied from the C-terminus, ensuring highest stability.

3.3 Conclusions

To conclude, we show that the lifetimes of the SA-biotin interaction subjected to constant mechanical load strongly depend on the force-loading geometry and exponentially decrease with increasing force. Different geometries arise from binding of biotin to one of the four binding pockets of SA and result in lifetimes under force that differ by orders-of-magnitude, despite identical thermodynamic stabilities for binding to the different subunits and similar extrapolated off-rates at zero force. Our results illustrate that it is, in general, not possible to infer the mechanical stability of a receptor-ligand complex from its affinity and binding enthalpy.

Such differences between thermal and forced dissociation of molecular complexes are plausible considering the high-dimensional binding energy landscape. Unbinding pathways under mechanical load can be very different from each other and also very different from the thermally preferred ones, as it is also observed e.g. for the force-induced melting of double-stranded DNA in shear- or zipper-geometry[155]. For proteins, similar behavior of monovalent SA has recently been employed by Erlich et al. to create a force hierarchy of receptor-ligand complexes[156]. Also, the mechanically most stable receptor-ligand complex measured to date[3] has just ordinary thermodynamic binding characteristics.

Our work provides a clear route to improving the yield of force spectroscopy experiments and in general of assays where SA-biotin is used for attachment and experiences mechanical loads, e.g. due to fluid flow or magnetic actuation. For measurements utilizing the SA-biotin interaction as a handle, and in particular for constant force SMFS measurements, it is highly beneficial to implement a specific SA tethering geometry that yields a single pop-

ulation with high lifetime to enable long measurement durations even at high forces. The tethering geometry that we identified as the one yielding the longest lifetimes can be easily realized in experiments by employing the 1SA variant presented in this study. Thus, our results give a straightforward approach for highly specific and stable experiments that employ the SA-biotin linkage.

3.4 Materials and Methods

3.4.1 Expression of SA constructs

Non-functional SA subunits are created by mutating three amino acids (N234A, S27D, S45A) as described by Howarth et al.1. Amino acid sequences of all subunits are provided in the section "Sequences of the protein constructs" below. Functional and non-functional SA subunits were expressed separately and then mixed to obtain SA of different valencies: Tetravalent SA (4SA), trivalent SA (3SA), monovalent SA (1SA), and non-functional SA (0SA). 4SA and 1SA contained a unique cysteine for surface immobilization at the C-terminus of one functional subunit. 3SA and 0SA contained a unique cysteine for surface immobilization at the C-terminus of one non-functional subunit. To select for the correct SA stoichiometry, the cysteine-labeled subunit further contained a polyhistidine tag for purification by nickel-immobilized metal ion affinity chromatography. The unique subunits used for purification and immobilization were incubated either with a 10-fold excess of untagged functional (4SA or 3SA) or untagged non-functional (1SA and 0SA) subunits to assemble the SA tetramers with defined valencies.
All SA subunits were cloned into pET vectors (Merck Millipore, Burlington, USA). SA plasmids were transferred to E. coli BL21(DE3)-CodonPlus cells (Agilent Technologies Inc., Santa Clara, USA) and expressed in SB medium. 15 ml of preculture, which was grown overnight at 37 °C, was used to inoculate 500 ml of SB medium containing the appropriate antibiotic. Cells were grown at 37 °C. At an OD_{600} of 0.8, expression was induced with 0.2 mM IPTG and the temperature was reduced to 18 °C for 16 h. The cultures were spun down so that bacterial pellets formed, which were then stored at - 80 °C.

3.4.2 Purification of SA constructs

All steps were performed on ice or at 4 °C, respectively. SA cell pellets were thawed, suspended in 5 ml/g Bacterial Protein Extraction Reagent (B-PER, Thermo Fisher Scientific, Waltham, MA) and incubated with 1 µg lysozyme and 0.05 µg DNAse I per gram bacterial pellet on a rolling shaker for 20 minutes. To ensure full break-up, cells were subsequently sonicated. The lysed cells were then centrifuged. The supernatants were discarded. The pellets were resuspended in lysis buffer (PBS, 1 mM DTT, 0.1% Triton X-100). Sonification, centrifugation and resuspension were repeated four to five times until the supernatant was a clear liquid. The pellets were then resuspended in denaturing buffer (PBS, 6 M guanidine hydrochloride), sonicated and centrifuged. This time, supernatants contained the protein. Supernatants were filtered through a sterile 0.22 µm filter. Then, the absorption at 280 nm was determined. Denatured subunits were mixed in a 1:10 ratio (subunits with and without polyhistidine tag). The mixture was then slowly diluted into 500 ml PBS and stirred overnight using a magnetic stirrer. This solution containing the refolded and reassembled SA was loaded onto a Ni-NTA column (HisTrap FF, GE Healthcare, Chicago, USA). We employed a gradient elution (increasing the imidazole concentration from 20 to 250 mM) to elute SA from the column and selected for those SA containing a single polyhistidine tag (elution fractions were checked by SDS-PAGE). Elution fractions containing the protein were dialyzed against PBS and then stored in PBS at 4 °C. We found SA to be functional (such that successful MT experiments were possible) even after two years of continuous storage in PBS at 4 °C after purification.

3.4.3 Expression and purification of ddFLN4

The recombinant ddFLN4 construct[157] expressed in E.coli (with the internal cysteine at position 18 mutated to serine) was a kind gift from Lukas F. Milles. At its C-terminus, the ddFLN4 construct possesses a polyhistidine-tag for purification and a ybbR-tag. At its N-terminus, the construct possesses a short linker sequence (*MGTGSGSGSGSAGTGSG*)

with the N-terminal methionine being followed by a single glycine. Due to efficient cleavage of the methionine by E.coli methionine aminopeptidases, the glycine is available for Sortase-catalyzed ligation.
The ddFLN4 gene was synthesized codon-optimized for expression in E.coli as a linear DNA fragment (GeneArt – Thermo Fisher Scientific, Regensburg, Germany), and inserted into pET28a vectors via Gibson assembly (New England Biolabs, Frankfurt, Germany). Protein expression in E.coli NiCo21 (DE3) (New England Biolabs) and purification via the polyhistidine-tag were carried out as previously described [157].

3.4.4 Preparation of biotinylated DNA

To prepare biotinylated DNA, we performed a polymerase chain reaction using a biotinylated primer and a regular DNA reverse primer. As the template DNA, we used the pET28a vector encoding for the functional SA subunit. Primers (BIO-TEG (Biotin-Triethylenglycol)-5'-atggaagcggggattaccggc-3' and 5'-ctgaccgctccaagtcgtagcg-3') were purchased from Eurofins Genomics, Ebersberg, Germany. For purification of the PCR product, we performed size-exclusion chromatography (with a Superdex 75 Increase 10/300 GL column) on an Äkta Explorer FPLC system (GE Healthcare, Chicago, USA) using PBS as running buffer.

3.4.5 AFM imaging

SA constructs were reduced using 50 mM dithiothreitol and mixed with biotinylated 250 bp double-stranded DNA in PBS buffer, with DNA being in excess to ensure that SA molecules with the maximum possible number of bound DNA strands can be observed. A 1:20 SA:DNA stoichiometry was chosen for 4SA and 3SA, and a 1:4 stoichiometry for 1SA and 0SA, with a final DNA concentration of approximately 4 nM.
Preparation of poly-l-lysine (PLL) coated mica substrates for AFM imaging was performed analogously to a recently described protocol [158;159]. After at least 1 h of incubation, 20 µl of the SA–DNA mix were incubated on a PLL-coated substrate for 30 s, which was subsequently rinsed with water and finally dried in a gentle stream of nitrogen. The positively charged PLL allows for stable attachment of negatively charged DNA and of DNA-streptavidin complexes. Free streptavidin without bound DNA strands, however, does not stably attach to the substrate.
AFM images of 1 µm x 1 µm or 2 µm x 2 µm and 1024 x 1024 pixels were recorded in tapping mode in air, using an MFP-3D AFM (Asylum Research, Santa Barbara, CA) and cantilevers with silicon tips (AC160TS, Olympus, Japan), with a nominal spring constant of 26 N/m and a resonance frequency of approximately 300 kHz. Raw image data were processed using SPIP software (v6.5.1; Image Metrology, Denmark). Image processing involved plane correction (third order polynomial plane-fitting), line-wise flattening (according to the histogram alignment routine), and Gaussian smoothing (for zoom-ins only).

3.4.6 Isothermal titration calorimetry

ITC was performed at 25 °C on a MicroCal iTC200 (Malvern, Worcestershire, UK). 8.0 mg Biotin were weighed out and dissolved in 40 ml PBS to obtain a stock solution of about 820 µM. SA was dissolved in PBS, using Zeba Spin Desalting Columns, 40K MWCO (Thermo Fisher Scientific, Waltham, USA) for buffer exchange. The concentration of SA was determined from the absorption at 280 nm using a spectrophotometer (NanoDrop 1000, Thermo Fisher Scientific, Waltham, USA) and a molar attenuation coefficient of ϵ_{280} = 167,760 M^{-1} cm^{-1}. SA was used as analyte, biotin as titrant. A 10-fold concentration of biotin was used for 1SA, a 30-fold excess for 3SA, and a 40-fold excess for 4SA, as the ratio of the measurement cell volume to the total titrant volume is five to one.

3.4.7 Fitting of the ITC data

ITC data are fitted as described in the Appendix of the "ITC Data Analysis in Origin® Tutorial Guide" by MicroCal, LLC. In brief, the fit is approached as follows: First, the concentration of receptor R_i and ligand L_i molecules in the sample cell after each injection i of volume ΔV_i has to be calculated. With V_0 as the volume of the measurement cell and

X as the ligand concentration in the syringe, we can set up the following relations

$$R_{i+1} \cdot \Delta V_0 = R_i \cdot V_0 - 0.5 \cdot (R_{i+1} + R_i) \cdot \Delta V_i$$
$$L_{i+1} \cdot \Delta V_0 = L_i \cdot V_0 - 0.5 \cdot (L_{i+1} + L_i) \cdot \Delta V_i + X \cdot \Delta V_i$$

These formulas take into account that with each injection of volume ΔV_i, the same volume ΔV_i is displaced from the measurement cell containing both ligands and receptor at the current concentration – on average $0.5 \cdot (R_{i+1} + R_i)$.
We obtain the recursive relations

$$R_{i+1} = R_i \cdot \frac{V_0 - 0.5 \cdot \Delta V_i}{V_0 + 0.5 \cdot \Delta V_i}$$

$$L_{i+1} = \frac{X \cdot \Delta V_i + L_i \cdot (V_0 - 0.5 \cdot \Delta V_i)}{V_0 + 0.5 \cdot \Delta V_i}$$

For a set of identical binding sites, the fraction bound for each R_i and L_i, can be calculated according to

$$f = 0.5 \cdot (1 + \frac{L_i}{n \cdot R_i} + \frac{K_d}{n \cdot R_i} - \sqrt{(1 + \frac{L_i}{n \cdot R_i} + \frac{K_d}{n \cdot R_i})^2 - \frac{4 \cdot L_i}{n \cdot R_i}})$$

where n is the stoichiometry and K_D is the affinity constant. The total heat Q that would be released going from $(R_0, L = 0)$ to (R_i, L_i) is then calculated by

$$Q = n \cdot f \cdot H \cdot R_i \cdot V_0$$

where H is the binding enthalpy per mole. In the experiment not the total heat Q, but the difference in heat between two injections is measured

$$\Delta Q_i = Q_i - Q_{i-1} + 0.5 \cdot (Q_i + Q_{i-1}) \cdot \frac{\Delta V_i}{V_0}$$

where the last term takes into account that also the molecules contained in the replaced volume ΔV_i contribute to the heat while being pushed out of the measurement cell.
For fitting the data, initial values for n, K_D and H are guesses. Then all ΔQ_i for all injections are calculated and compared with the experimental values. The values for n, K_D and H are then improved and the procedure is repeated until no further improvement of the fit occurs.
We note that due to the discretization of the measurement, the fit does not represent an ideal sigmoidal binding curve (which would be obtained for an infinite number of infinitesimal injections). Instead, the data points represent discrete heat differences between distinct injections, i.e. they can be rather seen as an average over a certain part of the ideal binding curve (Fig. 3.10). Due to the high affinity of the SA-biotin interaction, the saturation of receptors is very abrupt and leads to a sudden change in the released heat. Averaging over this part of the ideal binding curve leads to data points that are no longer on the ideal binding curve. Since the heat released in a single injection is always plotted against the final molecular ratio (the ratio after the injection), this discretized curve is shifted to the right of the underlying ideal binding curve (Fig. 3.10). Nevertheless, n and H can be reliably obtained from the fit, which takes into account the discretization. The true value for K_D can however (for the SA-biotin system) not be measured.

3.4.8 Functionalization of magnetic beads with SA constructs

5 µM of 1SA, 3SA, or 4SA were supplemented with 5 mM Bond-Breaker TCEP Solution (Thermo Fisher Scientific). After 30 minutes, the mixture was purified using Zeba Spin Desalting Columns, 40K MWCO (Thermo Fisher Scientific) equilibrated with coupling buffer (50 mM NaCl, 50 mM $NaHPO_4$, 10 mM EDTA, pH 7.2) according to the manufacturer's instructions.
Bifunctional polyethylene glycol of 5,000 g/mol molecular weight with an N-hydroxysuccinimide group at one end and a maleimide group at the other (NHS-PEG5000-MAL, Rapp Polymere, Tübingen, Germany) was dissolved in 50 mM HEPES, pH 7.5, to a final concentration of 25 mM and immediately used to incubate superparamagnetic beads with amine

groups (Dynabeads M-270 Amine, Invitrogen/Thermo Fisher). After 45 min, beads were washed extensively first with DMSO and then with ultrapure water. Beads were then incubated with the respective SA construct in coupling buffer for 90 min and extensively washed with measurement buffer (20 mM HEPES, 150 mM NaCl, 1 mM $MgCl_2$, 1 mM $CaCl_2$, 0.1% (v/v) Tween-20, pH 7.4).

3.4.9 Magnetic tweezers setup

MT experiments were performed on a previously described custom setup [38;160]. The setup employs a pair of permanent magnets (5×5×5 mm^3 each; W-05-N50-G, Supermagnete, Switzerland) in vertical configuration [59]. The distance between magnets and flow cell (and, thus, the force) is controlled by a DC-motor (M-126.PD2; PI Physikinstrumente, Germany). An LED (69647, Lumitronix LED Technik GmbH, Germany) is used for illumination. A 40x oil immersion objective (UPLFLN 40x, Olympus, Japan) and a CMOS sensor camera with 4096×3072 pixels (12M Falcon2, Teledyne Dalsa, Canada) allow to image a large field of view of approximately 440 × 330 μm^2 at a frame rate of 58 Hz. Images are transferred to a frame grabber (PCIe 1433; National Instruments, Austin, TX) and analyzed with a LabView-based open-source tracking software [64]. The bead tracking accuracy of the setup is $\sim$ 0.6 nm in (x, y) and $\sim$ 1.5 nm in z direction. For creating the look-up table required for tracking the bead positions in z, the objective is mounted on a piezo stage (Pifoc P-726.1CD, PI Physikinstrumente). Force calibration was conducted as described by te Velthuis et al. [68] based on the transverse fluctuations of long DNA tethers. Importantly, for the small extension changes on the length scales of our protein tethers, the force stays essentially constant [38], with the relative change in force due to tether stretching or protein unfolding being $< 10^{-4}$. Force deviations due to magnetic field inhomogeneities across the full range of the field of view are $< 3\%$. The largest source of force uncertainty is the bead-to-bead variation, which is on the order of $\leq 10\%$ for the beads used in this study [38;59;62;77].

3.4.10 Magnetic tweezers experiments

Preparation of flow cells was performed as described [38]. In brief, aminosilanized glass slides were functionalized with elastin-like polypeptide (ELP) linkers [120], possessing a single cysteine at their N terminus as well as a C-terminal Sortase motif, via a small-molecule crosslinker with a thiol-reactive maleimide group [sulfosuccinimidyl 4-(N-maleimidomethyl)cyclohexane-1-carboxylate; Sulfo-SMCC, Thermo Fisher Scientific]. Flow cells were then assembled from an ELP-functionalized slide as bottom and a non-functionalized glass slide with two small holes for inlet and outlet as top, with a layer of cut-out parafilm (Pechiney Plastic Packaging Inc., Chicago, IL) in between to form a channel. Flow cells were incubated with 1% casein solution (Sigma-Aldrich) for 1 h and flushed with 1 ml (approximately 20 flowcell volumes) of buffer (20 mM HEPES, 150 mM NaCl, 1 mM $MgCl_2$, 1 mM $CaCl_2$, pH 7.4). CoA-biotin (New England Biolabs) was coupled to the ybbR-tag of the ddFLN4 construct in a bulk reaction in the presence of 5 µM sfp phosphopantetheinyl transferase [119] and 10 mM $MgCl_2$ at 37 °C for 60 min. Afterwards, ddFLN4 was diluted to a final concentration of approximately 20 nM in 20 mM HEPES, 150 mM NaCl, 1 mM $MgCl_2$, 1 mM $CaCl_2$, pH 7.4, and incubated in the flow cell in the presence of 2 µM evolved pentamutant Sortase A [125;126] for 30 min. Subsequently, the flow cell was flushed with 1 ml of measurement buffer (20 mM HEPES, 150 mM NaCl, 1 mM $MgCl_2$, 1 mM $CaCl_2$, 0.1% (v/v) Tweene-20, pH 7.4). Finally, beads functionalized with the respective SA construct were incubated in the flow cell for 60 s, and unbound beads were flushed out with 2 ml of measurement buffer.

At the beginning of each measurement, the tethered beads were subjected to two 5-min intervals of a constant force of 25 pN to allow for identification of specific, single-tethered beads by the characteristic two-step unfolding pattern of ddFLN4 [37;38] (Fig. 3.3). Only beads that showed the ddFLN4 pattern were analyzed further. Importantly, essentially no specifically attached beads ruptured during this phase of the measurement. After 30 s at a low resting force of 0.5 pN, beads were subjected to a constant force of 65 pN for either 15 h (4SA and 1SA) or 5 h (3SA), or 55 and 45 pN for 25 h (1SA) and 10 h (3SA), respectively and the time until bead rupture was monitored. All measurements were performed at room temperature ($\sim$ 22 °C).

3.4.11 Analysis of magnetic tweezers measurements

Lifetimes were determined from the survival fraction vs. time data. Datasets at 65 pN (Fig. 3.3C) have > 50 tether rupture events for each SA construct. Number of events at lower forces are indicated in Fig. 3.11. To estimate the robustness of fits and determine errors for the fitted parameters, we used a bootstrapping procedure. From each experimental data set, 1000 synthetic data sets of the same number of observations were generated by random drawing of data points from the experimental data set with repeats. Synthetic data sets were fit individually and the uncertainties on the final parameters reported are standard deviations over the bootstrap ensemble. We tested different models for each data set at 65 pN to investigate the robustness of the analyses with respect to different modeling choices. The models, fitted parameters, and quality of fits are summarized in the table below. The quality of the fits was evaluated by considering the residuals defined as

$$Res = \frac{(\sum_{i=1}^{N} \cdot (f_{exp,i}(t_i) - f_i(t_i))^2)^{0.5}}{N}$$

where $f_{exp,i}$ are the measured survival fractions and f_i are the modeled survival fractions at times t_i. N is the number of data points in each data set. The models used in Fig. 3.3 and Fig. 3.11 are the first for each construct. We note that while the fitted values change depending on modeling choices (number of exponentials, inclusion of a scale factor in the fit), our key findings are independent of the modeling choices made.

Acknowledgements

The authors thank Thomas Nicolaus and Angelika Kardinal for laboratory assistance, Leonard Schendel and Philipp U. Walker for helpful discussions, and Wolfgang Ott, Magnus S. Bauer, and Lukas F. Milles for providing ELP linkers and the ddFLN4 construct, respectively. This project was funded by the Deutsche Forschungsgemeinschaft (DFG, German Research Foundation) Project-ID 201269156, SFB 1032 and Project-ID 386143268, "Unraveling the Mechano-Regulation of Von Willebrand Factor".

3.5 Supplementary Material

3.5.1 Tables

Data Set	Model	Fitting Parameter (65 pN Data)	Residuals
1SA	$f(t) = f_1 \cdot \exp(-t/\tau_1)$	$f_1 = 0.92 \pm 0.01$ $\tau_1 = 2.61 \cdot 10^4$ s ± 680 s	0.0041
	$f(t) = \exp(-t/\tau_1)$	$\tau_1 = 2.61 \cdot 10^4$ s ± 680 s	0.0073
3SA	$f(t) = \frac{f_2}{3} \cdot [\exp(-t/\tau_2) + 2 \cdot \exp(-t/\tau_2)]$	$f_2 = 0.95 \pm 0.01$ $\tau_2 = 3.61 \cdot 10^3$ s ± 350 s $\tau_3 = 199$ s ± 10 s	0.0034
	$f(t) = \frac{1}{3} \cdot [\exp(-t/\tau_2) + 2 \cdot \exp(-t/\tau_2)]$	$\tau_2 = 3.36 \cdot 10^3$ s $\tau_3 = 167$ s	0.0042
	$f(t) = \frac{f_2}{3} \cdot [\exp(-t/\tau_A) + \exp(-t/\tau_B) + \exp(-t/\tau_C)]$	$f_2 = 0.97 \pm 0.01$ $\tau_A = 98$ s ± 12 s $\tau_B = 365$ s ± 30 s $\tau_C = 3.1 \cdot 10^3$ s ± 230 s	0.007
	$f(t) = f_2 \cdot \exp(-t/\tau_2)$	$f_2 = 0.87$ $\tau_2 = 560$ s	0.010
4SA	$f(t) = \frac{f_3}{4} \cdot [\exp(-t/\tau_1) + \exp(-t/\tau_2) + 2 \cdot \exp(-t/\tau_3)]$	$f_3 = 0.86 \pm 0.01$	0.0073
	$f(t) = \frac{1}{4} \cdot [\exp(-t/\tau_1) + \exp(-t/\tau_2) + 2 \cdot \exp(-t/\tau_3)]$	None	0.0142

Table 3.1: Models for biotin-streptavidin lifetimes. Errors were determined from bootstrapping.

3.5.2 Sequences of protein constructs

Functional SA subunit:
MEAGITGTWYNQLGSTFIVTAGADGALTGTYESAVGNAESRYVLTGRY
DSAPATDGSGTALGWTVAWKNNYRNAHSATTWSGQYVGGAEARINTQWL
LTSGTTEANAWKSTLVGHDTFTKVKPSAAS
Functional SA subunit with C-terminal cysteine and His-tag:
MEAGITGTWYNQLGSTFIVTAGADGALTGTYESAVGNAESRYVLTGRY
DSAPATDGSGTALGWTVAWKNNYRNAHSATTWSGQYVGGAEARINTQWL
LTSGTTEANAWKSTLVGHDTFTKVKPSAASCLEHHHHHH
Non-functional SA subunit:
MEAGITGTWYAQLGDTFIVTAGADGALTGTYEAAVGNAESRYVLTGRY
DSAPATDGSGTALGWTVAWKNNYRNAHSATTWSGQYVGGAEARINTQWL
LTSGTTEANAWKSTLVGHDTFTKVKPSAAS
Non-functional SA subunit with C-terminal cysteine and His-tag:
MEAGITGTWYAQLGDTFIVTAGADGALTGTYEAAVGNAESRYVLTGRY
DSAPATDGSGTALGWTVAWKNNYRNAHSATTWSGQYVGGAEARINTQWL
LTSGTTEANAWKSTLVGHDTFTKVKPSAASCLEHHHHHH
ddFLN4 (C18S) construct with N-terminal glycine and short linker sequence, and C-terminal His-tag and ybbR-tag:
MGTGSGSGSGSAGTGSGADPEKSYAEGPGLDGGESFQPSKFKIHAVDPD
GVHRTDGGDGFVV TIEGPAPVDPVMVDNGDGTYDVEFEPKEAGDYVIN
LTLDGDNVNGFPKTVTVKPAPSG HHHHHHGSDSLEFIASKLA

3.5.3 Figures

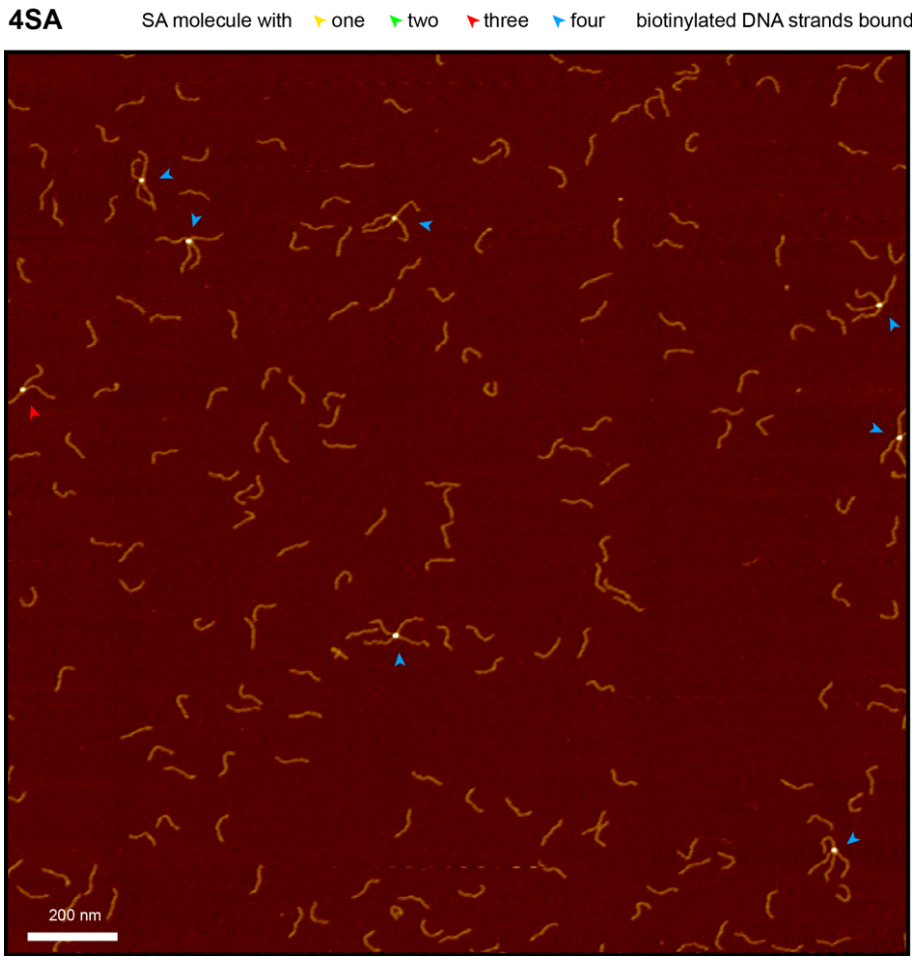

Figure 3.4: AFM imaging of 4SA with biotinylated DNA. Representative AFM image of 4SA and biotinylated 250 bp dsDNA after incubation in a 1:20 ratio. Arrowheads mark streptavidin molecules, with the color of arrowheads indicating the number of bound DNA strands (yellow – one, green – two, red – three, blue – four). For 4SA, up to four bound strands were observed. A full quantification from multiple images is shown in Fig. 3.8. Height range of color scale is 2.5 nm.

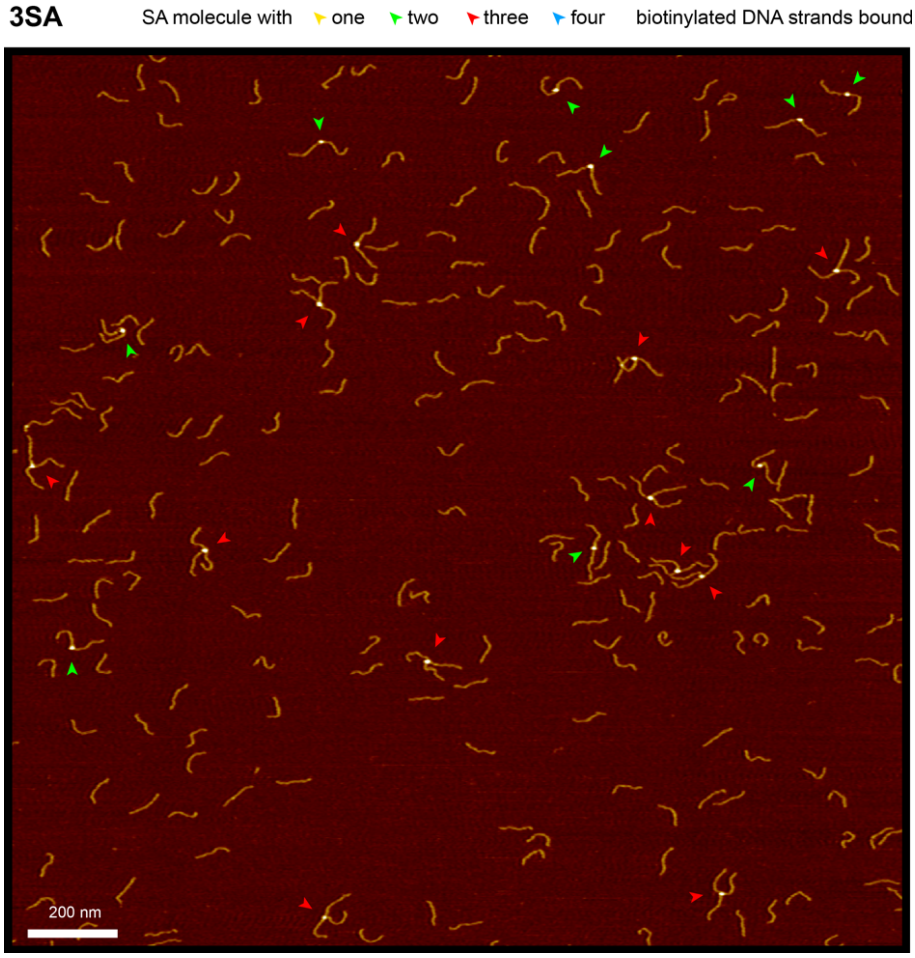

Figure 3.5: AFM imaging of 3SA with biotinylated DNA. Representative AFM image of 3SA and biotinylated 250 bp dsDNA after incubation in a 1:20 ratio. Arrowheads mark streptavidin molecules, with the color of arrowheads indicating the number of bound DNA strands (yellow – one, green – two, red – three, blue – four). For 3SA, up to three bound strands were observed. No 3SA molecules with four strands were observed. A full quantification from multiple images is shown in Fig. 3.8. Height range of color scale is 2 nm

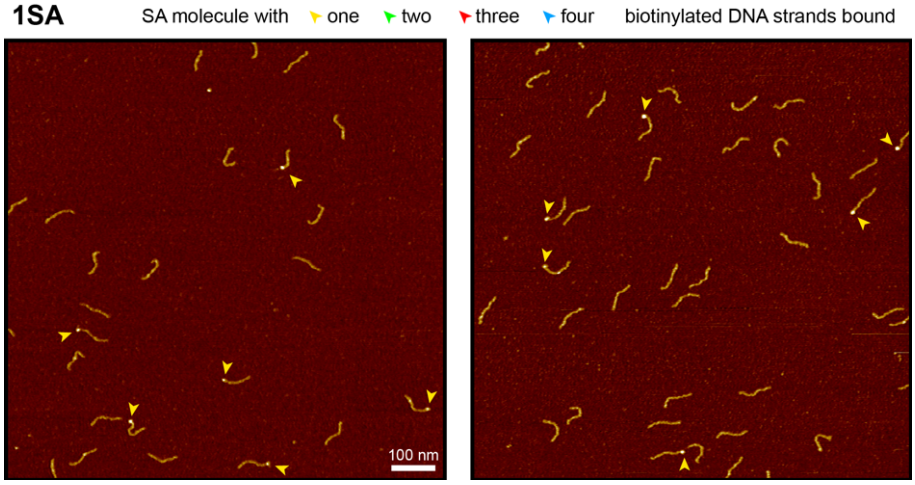

Figure 3.6: AFM imaging of 1SA with biotinylated DNA. Representative AFM images of 1SA and biotinylated 250 bp dsDNA after incubation in a 1:4 ratio. Arrowheads mark streptavidin molecules, with the color of arrowheads indicating the number of bound DNA strands (yellow – one, green – two, red – three, blue – four). Only 1SA molecules with a single bound DNA strand were observed. A full quantification from multiple images is shown in Fig. 3.8. Height range of color scale is 2 nm.

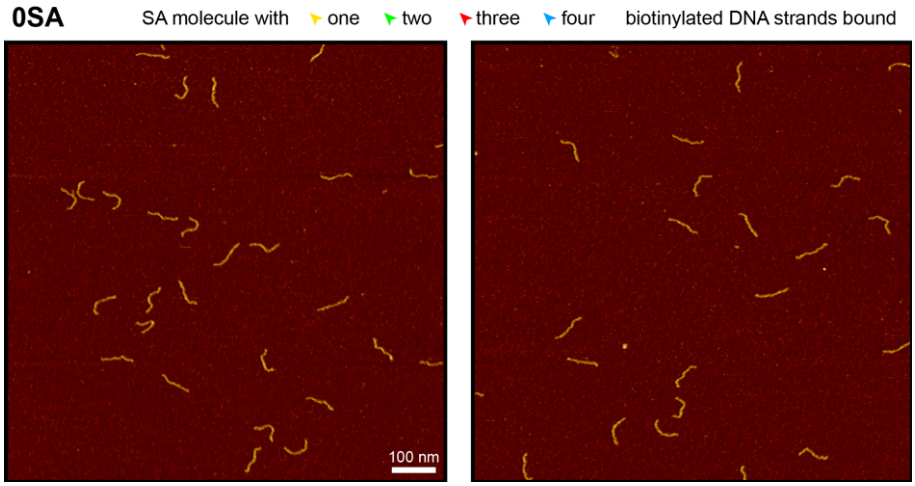

Figure 3.7: AFM imaging of 0SA with biotinylated DNA. Representative AFM images of 0SA and biotinylated 250 bp dsDNA after incubation in a 1:4 ratio. Only free DNA strands not bound to 0SA were observed. Free 0SA molecules could not be observed since they do not stably attach to the positively charged poly-L-lysine coated mica substrate. Height range of color scale is 2 nm.

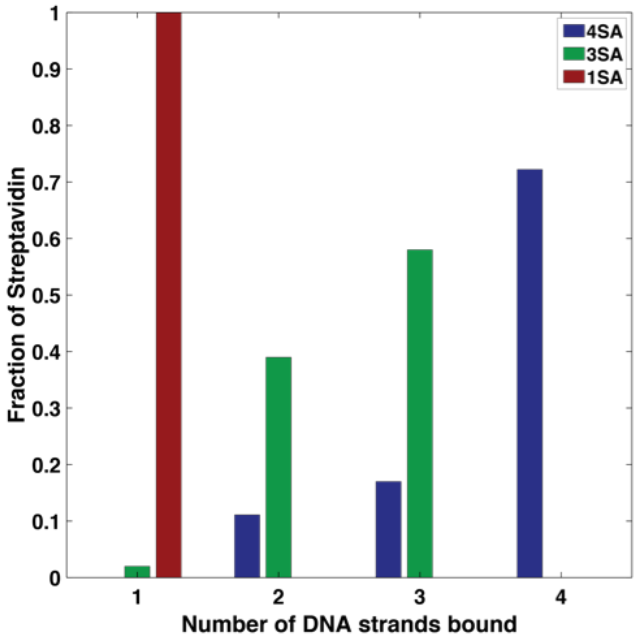

Figure 3.8: Number of biotinylated DNA strands bound to SA of different valencies. The numbers were obtained from multiple AFM images as described in the Materials and Methods. Representative AFM images are shown in Fig. 3.4-3.7. All images included in the analysis had comparable height and lateral resolution. The total number of SA molecules observed was 1SA: 33, 3SA: 43, 4SA: 18. The AFM image analysis confirms the valency of the SA molecules: The number of biotinylated DNA strands bound to one SA molecule is strictly limited by the number of functional subunits.

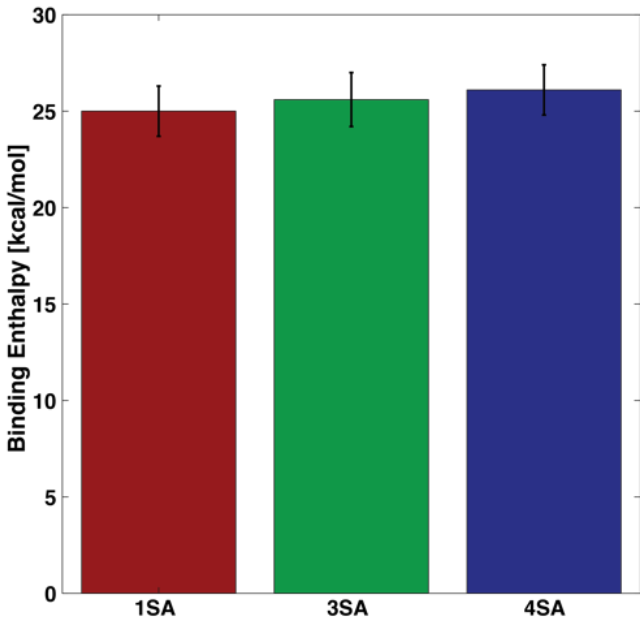

Figure 3.9: Binding enthalpies per binding site for biotin binding to different SA variants. Values are determined from fits to the ITC data sets shown in Fig. 3.2C (one ITC titration for each construct). Error bars are computed by taking into account the uncertainty in the stock concentrations, assuming an uncertainty of 10% in SA concentration and a 5% uncertainty in biotin concentration. Within experimental errors, the binding enthalpies for all SA variants are the same, suggesting that in the absence of force all subunits are equivalent with regard to biotin binding and that there are no effects of binding geometry or binding cooperativity.

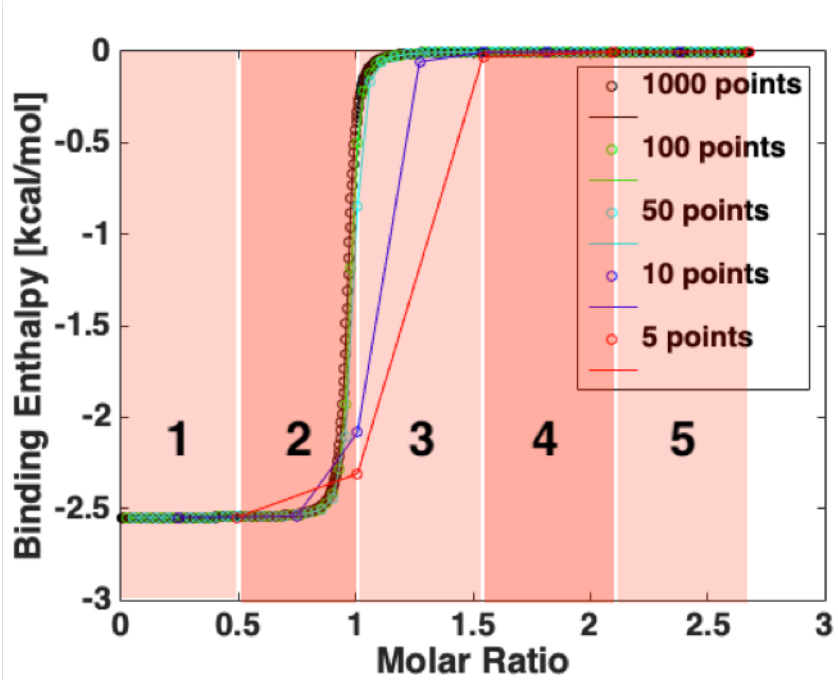

Figure 3.10: Discretization effects in ITC binding curves. Theoretical binding curve for n = 1.0, $K_D = 10^{-9}$ M and H = -2.5 kcal/mol. For a large number of very small injections, an ideal binding curve is obtained (black). With small numbers of injections (blue or red), the curve deviates from the ideal binding curve. For only five injections (red), different parts of the curve, which are averaged, are indicated by the numbered red areas in the background of the plot. For flat parts of the curve (area 1, 4 and 5) the discretization only has minor effects, while for the steep parts of the curve (area 2 and 3) the average points are no longer on the ideal curve. Fitting the discretized data, H and n can still be reliably determined. However, the value for the affinity K_D can not be reliably obtained. See the "Fitting of the ITC data" section in the Materials and Methods for details.

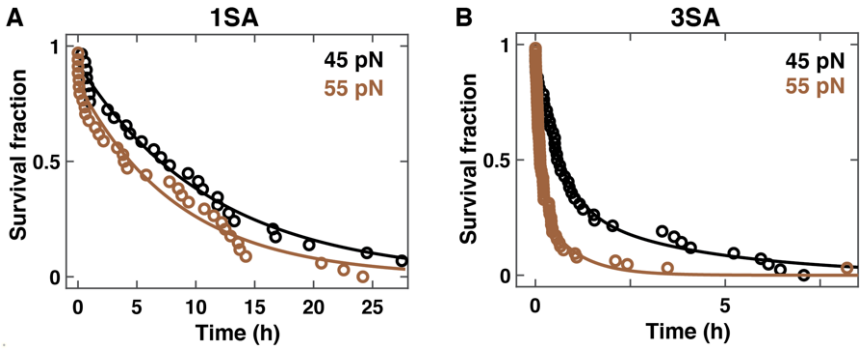

Figure 3.11: Survival fractions of 1SA and 3SA at 45 pN and 55 pN. A Survival fraction as a function of time for 1SA under constant forces of 45 pN and 55 pN. Data sets include 42 and 34 beads for 45 pN and 55 pN, respectively. Solid lines are fits of the single exponential model highlighted for 1SA in Table 1. From the fits, the lifetimes are $\tau_1 = 4.1 \cdot 10^4$ s ± $1.4 \cdot 10^3$ s at 45 pN and $\tau_1 = 3.1 \cdot 10^4$ s ± $1.6 \cdot 10^3$ s at 55 pN (errors are from a bootstrap analysis, see Materials and Methods). **B** Survival fraction as a function of time for 3SA under constant forces of 45 pN and 55 pN. Data sets include 42 and 73 beads for 45 pN and 55 pN, respectively. Solid lines are fits of a double exponential model highlighted for 3SA in Table 1. From the fits, the lifetimes are $\tau_2 = 1.4 \cdot 10^4$ s ± $1.3 \cdot 10^3$ s and $\tau_3 = 2.3 \cdot 10^3$ s ± $1.1 \cdot 10^2$ s at 45 pN and $\tau_2 = 3.2 \cdot 10^3$ s ± $2.2 \cdot 10^2$ s and $\tau_3 = 4.5 \cdot 10^2$ s ± $1.3 \cdot 10^1$ s at 55 pN (errors are from a bootstrap analysis, see Materials and Methods). All measurements used the same procedures –including the identification of the ddFLN4 unfolding fingerprint– as the experiments shown in Fig. 3.3A, B, except for the value of the force in the final plateau.

4

A Conformational Transition of Von Willebrand Factor's D'D3 Domain Primes It For Multimerization

Summary

Von Willebrand factor (VWF) is a multimeric plasma glycoprotein that is critically involved in hemostasis. Biosynthesis of long VWF concatemers in the endoplasmic reticulum and the (trans-)Golgi is still not fully understood. We use the single-molecule force spectroscopy technique magnetic tweezers to analyze a previously hypothesized conformational change in the D'D3 domain crucial for VWF multimerization. We find that the interface formed by submodules C8-3, TIL3, and E3 wrapping around VWD3 can open and expose two previously buried cysteines that are known to mediate multimerization. By characterizing the conformational change at varying levels of force, we are able to quantify the kinetics of the transition and the stability of the interface. We find a pronounced destabilization of the interface upon lowering the pH to 6.2 and 5.5. This is consistent with initiation of the conformational change that enables VWF multimerization at the D'D3 domain by a decrease in pH in the trans-Golgi network and Weibel Palade bodies. Furthermore, we find a stabilization of the interface in the presence of coagulation factor VIII (FVIII), providing evidence for a previously hypothesized binding site in submodule C8-3. Our findings highlight the critical role of the D'D3 domain in VWF biosynthesis and function and we anticipate our methodology to be applicable to study other, similar conformational changes in VWF and beyond.

4.1 Introduction

Von Willebrand Factor (VWF) is a large plasma glycoprotein, critically involved in primary hemostasis. Long VWF multimers travel in the blood stream in a globular conformation and undergo conformational changes upon sensing increased hydrodynamic forces, present e.g. at sites of vascular injury[75]. Through these changes, VWF exposes binding sites for blood platelets[161]. After binding to collagen in the injured vessel wall, force-activated VWF thus enables formation of a hemostatic plug, built by multiple platelets binding to it[162] (Figure 4.1A). The peak hydrodynamic forces acting on VWF scale with the square of its

This manuscript is based on a manuscript by Gruber, Löf *et al.* with Gruber and Löf equally contributing first authors (under review at *Blood Advances*). My contribution: For this paper, I was involved in designing the research and performing MT experiments. I analyzed the data and wrote the manuscript with input from Prof. Jan Lipfert, Dr. Achim Löf, Dr. Martin Benoit, and Prof. Maria Brehm.

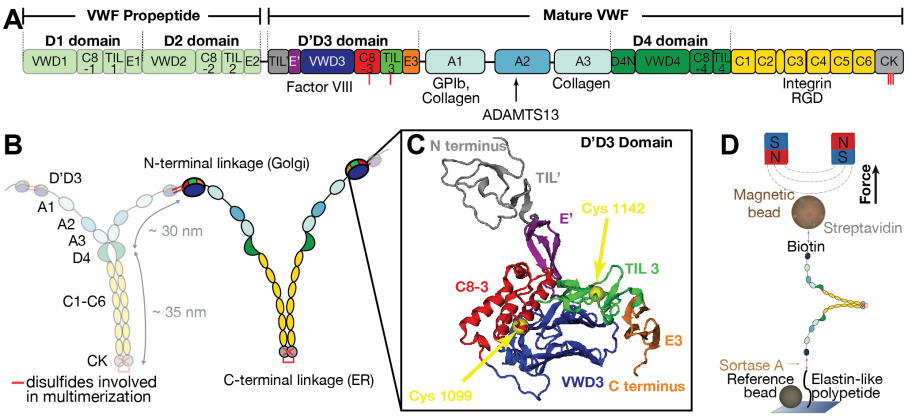

Figure 4.1: Von Willebrand Factor (VWF) domain structure and magnetic tweezers assay. **A** Domain sequence of a full VWF monomer [162]. Domains are scaled to length. The propeptide is cleaved by furin before mature VWF concatemers are secreted into the bloodstream. Binding sites of different interaction partners of VWF are indicated. **B** Mature monomers are dimerized via C-terminal linkage of the CK domains in the endoplasmic reticulum (ER) and subsequently multimerized via N-terminal linkage of two D'D3 domains in the trans-Golgi network. **C** Crystal structure of the D'D3 domain in its closed conformation (PDB accession code 6N29) [164]. The D'D3 domain comprises six submodules: TIL' and E' ("D' submodules") project out, while C8-3, TIL3, and E3 form a wedge with the larger VWD3 module ("D submodules"). Cysteines for multimerization are buried in the interface and indicated by yellow spheres. The crystal structure was rendered using VMD [22]. **D** Schematic of VWF dimer in magnetic tweezers. VWF is covalently attached to a flow cell surface via an elastin-like polypeptide (ELP) linker. Coupling to a paramagnetic bead is achieved via a stable biotin-streptavidin linkage. Reference beads are baked to the surface to account for drift. Force is applied through two permanent magnets above the flow cell.

length [5;6]. VWF's occurrence in form of ultra-large concatemers, reaching lengths up to 15 µm upon unfolding [6;163], is thus vital for effective force-activation through hydrodynamic forces at sites of vascular injury.

Biosynthesis of such long concatemers is a highly complex process [165–168]: VWF is expressed as a prepropeptide, comprising a short signal peptide and the prodomains D1 and D2 in addition to the domains featured in mature VWF [158] (Figure 4.1A). The signal peptide is cleaved during transport of proVWF to the endoplasmic reticulum (ER), where numerous cysteine bridges form, which shield most domains against unfolding under force [169]. In the ER, monomers dimerize via formation of three cysteine bridges between the C-terminal cystin knot (CK) domains [163;169] (Figure 4.1B) and glycosylation is initiated. After dimerization, proteins are transferred to the Golgi (pH 6.2), where the stem region of VWF dimers is compacted into a "dimeric bouquet" [170] and VWF is extensively posttranslationally modified by N- and O-glycosylation, sialylation and sulfation. In the trans-Golgi network, furin cleaves off the propeptide [162;166;169;171;172], dimers assemble into a helical shape and multimerize by interdimer cysteine bonding at positions Cys1099-Cys'1099 and Cys1142-Cys'1142 in the N-terminal D'D3 domains. The multimers are stored in Weibel-Palade bodies (WPB) (secretory granules) at an even lower pH of 5.4 and secreted into the bloodstream [163;168].

To ensure unrestricted functionality, it is of vital importance that all cysteine bridges form natively. Most disulfide bridges are formed in the ER – with the notable exception of the two cysteine bridges (Cys1099-Cys'1099 and Cys1142-Cys'1142) in the D'D3 domain mediating VWF multimerization [172]. A crystal structure of the monomeric D'D3 domain at neutral pH, characteristic of the ER, has revealed a wedge-like conformation of the D assembly [164]. In this conformation, the C8-3, TIL3, and E3 submodules make close contact with the VWD3 domain (Figure 4.1C), effectively burying the cysteines at positions 1099 and 1142. This conformation likely prevents premature multimerization in the ER [164]. It has been hypothesized that in the acidic pH of the (trans-)Golgi, a conformational change in the D'D3 domain exposes the cysteines to enable multimerization [164]. However, details of this necessary conformational change are currently unknown.

In addition to enabling multimerization, the D'D3 domains serve another function critical for hemostasis: By binding coagulation factor VIII (FVIII), they protect FVIII from rapid clearance [173] and transport it to sites of vascular injury. Mutations within the VWF D'D3 domain that abrogate or abolish this high-affinity binding lead to type 2N von Willebrand disease, a condition characterized by reduced plasma levels of FVIII [174;175]. Structural and biochemical data reveal binding of the FVIII C1 domain to the D' modules of VWF and, additionally, hint at interactions of FVIII with the VWF D3 core [164;173;176;177].

Here, we employ magnetic tweezers (MT) to study the conformational change in the D'D3 domain necessary for multimerization as well as the interaction of the D'D3 domain with FVIII. MT are a powerful tool for single-molecule force spectroscopy, enabling multiplexed application of a large range of constant forces [70;79;132]. Recently, assays have been introduced employing MT for studying force-induced conformational changes in proteins [38;78;178]. For this purpose, single proteins are tethered between a glass surface and a magnetic bead. A magnetic field, generated by electro- or permanent magnets, exerts precisely controlled forces on the bead and thus the tethered molecule. Conformational changes in the tethered protein lead to changes in the bead position, which is monitored by video microscopy.

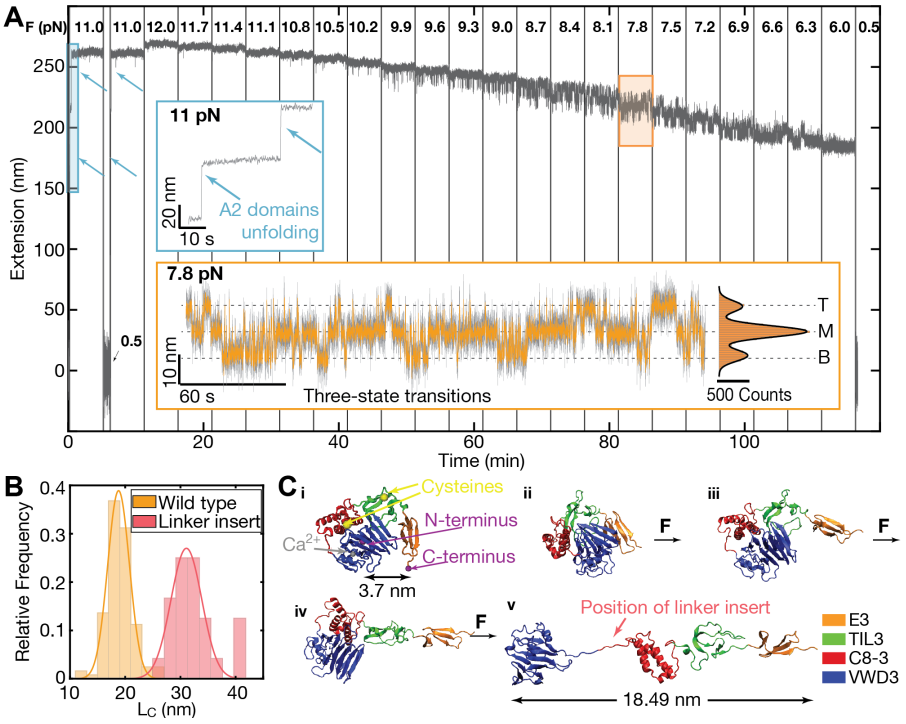

Figure 4.2: MT force spectroscopy reveals conformational change in the D'D3 domain. A Extension-time trace of a VWF dimer exhibiting fast, reversible transitions between three distinct states at forces around 8 pN. At the start of the measurement, two five min measurements at 11 pN serve to identify specific tethers by observing two ≈ 35 nm A2 unfolding events (blue inset, unfolding events indicated by arrows). Subsequently, the force is decreased from 12 pN to 6 pN in steps of 0.3 pN to systematically study the transitions between three states, separated by ≈ 7.5 nm. The population in the respective states shifts with decreasing force, with an increasing fraction of time spent in the lower extension levels at lower forces. At forces around 8 pN, transitions from the **M** state to the **T** or **B** state are equally likely (orange inset). In the inset, the three states (**T**op, **M**iddle, and **B**ottom) are indicated by dashed lines and are clearly visible in the extension histogram. The histogram is fit with a triple Gaussian function (black line, Table 4.1 Equation 10) to extract relative positions and populations of the three states. Traces recorded at 58 Hz are smoothed with an 11-frame moving average filter, and grey trace in the orange inset shows raw data. **B** Histogram of contour length transformed increment of the wild type dimer and a modified dimer with a 20 aa long linker insertion between VWD3 and C8-3 (position of the linker insert indicated in C v). Histograms were fitted with a single Gaussian (Table 4.1, Equation 8) using a maximum likelihood fit. Mean ± std are: $L_{C,wt}$ = 19.0 ± 2.4 nm, $L_{C,linker}$ = 32.4 ± 4.1 nm. **C** Steered molecular dynamics (SMD) simulations validate molecular mechanism in the D'D3 domain causing transitions. i Crystal structure of simulated part of the D'D3 domain with VWD3 (blue), C8-3 (red), TIL3 (green), and E3 (orange)[164]. Termini are marked with purple spheres. Two cysteines involved in multimerization are marked with yellow spheres. Ca^{2+} is shown as a silver sphere. ii Initial state of SMD simulation. The pulling direction is marked with an arrow. iii-iv Under the influence of force, E3, TIL3, and C8-3 are "peeled" off the large VWD3 submodule. v Final state. Subdomain structure is kept by long-range disulfide bridges[162;164]. Total length gain in the simulation is 14.8 nm. Arrow indicates position of linker insert in red histogram in panel B.

In this study, we investigate full-length VWF dimers under different levels of constant force (Figure 4.1D), to directly probe the stability of the D'D3 domain. We observe fast, reversible transitions at constant forces around 8 pN that we identify as a large-scale conformational change in the D'D3 domain (Figure 4.2A). Investigating the force-dependency of the transitions, we can infer the stability and dynamics of the interface. At the pH present in the Golgi and WPB, we find a significant destabilization of the interface burying the cysteines at positions 1099 and 1142 compared to neutral pH, validating the hypothesis that reduced pH plays a crucial role in VWF's biosynthesis. Furthermore, we find a stabilization of the interface in presence of FVIII, strongly supporting the hypothesis of a binding site of FVIII within the D submodules in addition to the D' submodules[164;177].

4.2 Results

To probe the stability of the wedge-like D3 interface formed by VWD3 with C8-3, TIL3, and E3, we use an assay that comprises VWF dimers, the smallest repeating subunits of long VWF concatemers (Figure 4.1D). We tether the dimers in MT between a flow cell surface and superparamagnetic beads using a previously described coupling strategy based upon covalent surface attachment via elastin-like polypeptide (ELP) linkers[38;120]. The other terminus is attached to a superparamagnetic bead via a non-covalent, highly stable biotin-streptavidin bond[4]. In our MT setups, we apply varying levels of constant force by precisely adjusting the height of two permanent magnets located above the flow cell (Figure 4.1D). Among the twelve domains of mature VWF monomers, only the A2 domain is not shielded against unfolding at comparably low forces by long-range disulfide bridges. The A2 unfolding is thus one of the first responses of VWF to mechanical force and has been extensively investigated using magnetic[38] and optical tweezers[6] as well as atomic force microscopy-based[179] single-molecule force spectroscopy. Here, we use the two A2 unfolding events (one from each monomer in the dimer) as a molecular fingerprint: in the beginning of each measurement, we apply a force of 11 pN and identify specifically coupled VWF dimers by observing two ≈ 35 nm steps that correspond to the A2 unfolding signature[38] (Figure 4.2A, blue inset).

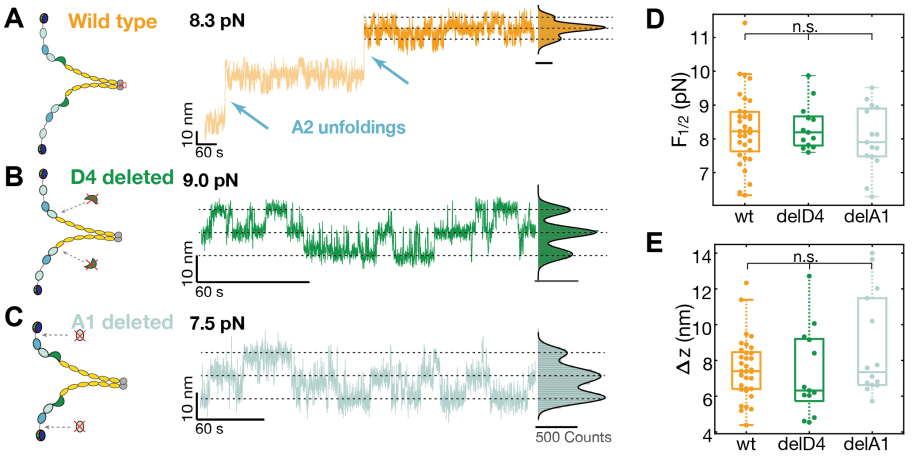

Figure 4.3: The conformational change in the D'D3 domain is unaffected by other domains. A Three-state transitions occur independent of the unfolding of the two A2 domains. Left: Schematic of wild type (wt) VWF dimer, right: Extension-time trace at 8.3 pN. Three-state transitions are observable before and after A2 unfolding. Extension histogram of the segment marked in dark orange reveals three distinct states that can be fitted with a three-term Gaussian (solid black line). **B** Three-state transitions occur independent of a deletion of the D4 domain. Left: Schematic of VWF dimer, where both D4 domains are deleted, right: Extension-time trace at 9.0 pN. Extension histogram reveals three distinct states that can be fitted with a three-term Gaussian (solid black line). **C** Three-state transitions occur independent of a deletion of the A1 domain. Left: Schematic of VWF dimer, where both A1 domains are deleted, right: Extension-time trace at 7.5 pN. Extension histogram reveals three distinct states that can be fitted with a three-term Gaussian (solid black line). **D, E** Neither midpoint forces (D) nor Δz (E) (see main text for a discussion of the model) of the deletion constructs are significantly different from the wt. In the boxplots in D and E each data point corresponds to an individual molecule. The line in the boxes indicates the median of all data points, the box the 25th and 75th percentile, and the whiskers the furthest data point outside the box, but within 1.5 times the box width. Number of molecules included in D and E: wt: 33, delD4: 13, delA1: 15.

4.2.1 Conformational transition in the D'D3 domain is revealed by MT

After selecting specific VWF tethers, we perform an inverted force ramp protocol, starting at 12 pN and decreasing the force iteratively in steps of 0.3 pN until 6 pN (Figure 4.2A). In the force-plateaus between 12 and 6 pN, we observe rapid, reversible transitions between a maximum of three states, named in the following **T**op, **M**iddle, and **B**ottom (Figure 4.2A, orange inset). The population of these states shifts with decreasing force towards the bottom state, and the midpoint force $F_{1/2}$, at which transitions from the M state to the T or B state are equally likely, is found to be at around 8 pN. The three states are separated by two equidistant steps of $\Delta z \approx 7.6$ nm at the applied forces, suggesting that the transitions stem from conformational changes that occur in each of the monomers independently. To uniquely assign the molecular origin of the observed transitions, we performed control measurements on different domain-deletion constructs, in which individual domains are deleted, but which are otherwise identical to the wild type dimer. We observe the three-state transitions independently of A2 unfolding (Figure 4.3A, Figure 4.6A) and independently of the deletion of the D4 domain (Figure 4.3B, Figure 4.6A) or deletion of the A1 domain (Figure 4.3C, Figure 4.6B). Furthermore, the characteristic parameters of the transition, namely the midpoint force and the distance between the states are not altered in the domain deletion constructs (Figure 4.3 D, E). Therefore, we can exclude an origin within or related to the A1, A2, or D4 domains. When deleting the D'D3 domain, however, the transitions vanish (Figure 4.6C), strongly suggesting that a conformational change in this domain causes the transitions.

Under neutral pH and in the absence of force, the C8-3, TIL3, and E3 submodules wrap around the large VWD3, forming a wedge-like assembly that buries the two unbound cysteines[164] Cys1099 and Cys1142 (Figure 4.1C). We hypothesized that by applying force, we unwrap this assembly and open the interface between VWD3, C8-3, TIL3, and E3. We verified this hypothesis by inserting 20 amino acids (aa) into the naturally occurring sequence between the VWD3 and C8-3 submodules (Figure 4.2B, C, "Linker insert") and evaluating the distance between the states. As unfolded protein chains exhibit entropic polymer elasticity and are not completely stretched at the forces we apply, the measured distance between the states depends on the force at which the transitions occur. For the construct with the linker insert, the transitions shift to lower forces compared to the wild type construct. To ensure that the difference in force does not systematically bias the measured distance, we take into account the stretching elasticity by calculating the contour lengths from the experimentally observed distances using the worm-like chain model[38], assuming bending persistence length L_P = 0.5 nm and contour length L_C = 0.4 nm per aa. The contour length is the length of an unfolded chain of amino acids that is completely stretched and is thus independent of force. We find that inserting the 20 aa leads to an increase in contour length by 13.4 nm $\pm$ 4.8 nm (Figure 4.2B), in agreement, within experimental error, with the predicted 8 nm.

As an additional validation, we perform steered molecular dynamics (SMD) simulations on the D submodules (Figure 4.2C) by fixing the N terminus of the VWD3 submodule and pulling on the C terminus of the E3 submodule, which mimics force propagation through

the D assembly in the MT assay. We find that in the simulations, the externally applied force opens the interface between VWD3 and C8-3, TIL3, and E3, while the individual subdomains initially remain folded (Figure 4.2C). Comparing the distance of the termini in the initial structure with their distance at the end of the simulation, we find an increase of 14.8 nm at the high forces of the SMD simulation, which is in good agreement with the experimentally determined length increase, again taking into account the protein elasticity. The results from pulling a construct with an elongated linker and the SMD simulations validate and visualize that we are opening the interface in the D3 domain in our MT assay.

4.2.2 Transitions are inhibited in a fraction of D3 domains

The above findings strongly suggest that the observed transitions between three states stem from independently opening the interfaces in the two D3 domains of the tethered dimers. Interestingly, three-state transitions are not observed in all specific tethers exhibiting two A2 unfolding steps. Transitions between three states are observed in roughly 15% of specific tethers, while in 36%, we observe transitions only between two states, however, with otherwise identical parameters (see next section), suggesting that these correspond to conformational changes in only one of two D3 domains. The rest of the specific tethers show no transitions at all, suggesting that no conformational changes in either of the two D3 domains occur. In some cases, we initially observed three-state transitions, but in a later experiment on the same tether under the same conditions only two-state transitions. Together, these findings indicate that the conformational change can be inhibited. Considering that interface opening exposes two unbound cysteines (Figure 4.1C, yellow spheres), a possible explanation could be formation of non-native cysteine bridges preventing interface formation.

4.2.3 Force-dependent stability of the D3 interface

To extract thermodynamic parameters of the underlying transitions, a triple Gaussian function (Table 4.1, Equation 10) is fit to the extension histogram in each plateau with three-state transitions (Figure 4.4A, right). Thresholds are defined at the two minima between the three states (states indicated by dashed lines in Figure 4.4A). Based on the thresholds, the relative populations of B, M, and T states are determined at each force as the number of data points below, between, and above the thresholds divided by the total number of data points. The relative population of the three states shifts systematically with force (Figure 4.4B, circles). To model the force-dependent fractions, we assume that the D3 interface can be either in a closed state or in a "peeled off" open state. The external force biases the free energy landscape towards the open state and we assume that the free energy difference between the open and closed interface depends linearly on force as $\Delta G(F) = \Delta G_0 - F_{1/2} \cdot \Delta z$. Here, ΔG_0 is the free energy difference in the absence of force and Δz is the distance between the free energy minima along the force direction. Assuming the two D3 domains in the dimer behave identically and independently, the probability of both domains being open (P_{top}), one domain being open and one closed (P_{middle}), and both domains being closed (P_{bottom}) can be described with Equations 1-3 (Table 4.1). Fitting these equations to the relative population of states (Figure 4.4B, solid lines) yields the fit parameters $F_{1/2}$, the midpoint force, at which it is equally likely for the domains to be open and closed, as well as Δz, the distance between the states. We find an excellent fit of the three-state model to the data (Figure 4.4B), which confirms the assumption of identical, independent transitions. The same analysis can be performed for molecules exhibiting two-state transitions, where only one D3 domain exhibits conformational changes (Figure 4.9A). Here, a two-state model is fit to the relative state populations (Equation 4-5, Table 4.1), providing an independent fit of the same parameters (Figure 4.9B). We find that the distributions of fit parameters obtained from analyzing molecules with two- and three-state transitions are nearly identical (Figure 4.9D, E), which further supports the hypothesis that the underlying processes are indeed identical and that the intra-D3 domain transition is prevented in a fraction of D3 domains. Taking all fit parameters from two- and three-state transition molecules together (> 30 molecules; Figure 4.4D, E, solid lines) we find $F_{1/2}$ = 8.3 ± 1.1 pN and Δz = 7.6 ± 1.7 nm (mean ± std), which corresponds to a mean free energy of $\Delta G = F_{1/2} \cdot \Delta z$ = 9.0 ± 2.3 kcal/mol and provides a measure of the interface stability.

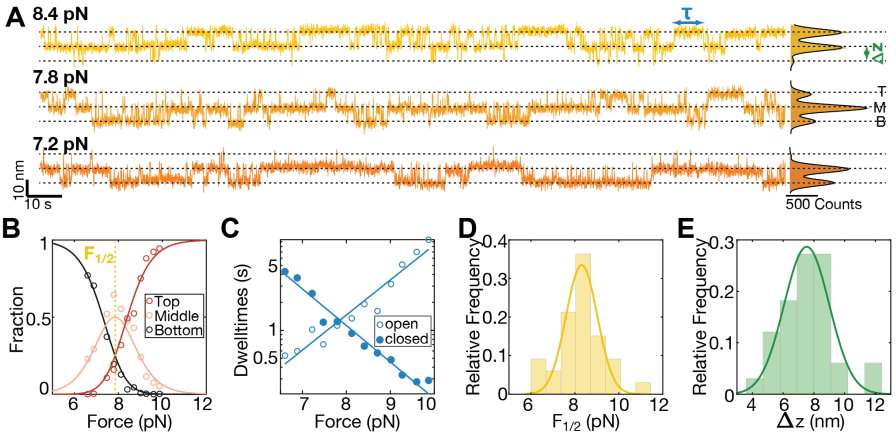

Figure 4.4: Stability and dynamics of the D3 interface probed by MT force spectroscopy. **A** Extension-time traces of VWF dimers in MT. Three-state transitions shift with decreasing force towards the bottom state. The three states (**T**op, **M**iddle, and **B**ottom) are indicated by dashed lines. Histograms of the extensions are shown on the right. Black lines show triple Gaussian fits. **B** Analysis of the relative population of the different states as a function of force. Circles represent experimental data with each circle corresponding to a 5 min force plateau. A three-state model assuming two independent transitions fits the experimental data well (solid lines, Table 4.1, Equations 1-3). Fit parameters are the mid-force $F_{1/2}$ (here $F_{1/2}$ = 7.85 pN), at which domains are equally likely open or closed, and the distance between the states Δz (here Δz = 6.5 nm). **C** Pseudo dwell time distributions. Pseudo dwell times for open and closed domains are calculated from dwell times in the top, middle, and bottom state. For each plateau, pseudo dwell times are determined and fit with an exponential to determine the mean dwell times for each force. Mean dwell times in the open (open circles) and the closed state (filled circles) depend exponentially on the applied force (solid lines are exponential fits, Table 4.1, Equations 6-7). **D** Histogram of mean midpoint forces determined from fitting the two or three-state model (panel B, Figure 4.9B). The solid line is a Gaussian fit with mean ± std: 8.3 ± 1.1 pN. **E** Histogram of Δz determined from fitting the two or three-state model (panel B, Figure 4.9B). The solid line is a Gaussian fit with mean ± std: 7.6 ± 1.7 nm. Histograms in D and E show distributions of 33 molecules.

4.2.4 Kinetics of the conformational changes in the D3 interface

In addition to providing insights into the force-dependent equilibrium, our MT extension time traces can reveal kinetic information from the transitions at different forces. Using the same thresholds as for state-population analysis, we identify dwell times (Figure 4.4A, τ; Figure 4.8A, B) as times that are spent in one state before crossing the threshold. The dwell times in the three-state transitions, however, reflect the kinetics of two equal processes happening independently at the same time. To access the dwell times of individual domains, τ_{open} and τ_{closed}, dwell times in the middle plateau are divided by two and associated with the dwell times in the bottom state and the top state, respectively. This procedure to obtain so-called *pseudo-dwell times* for individual domains takes into account the number of domains opened and closed in each state and weighs the measured dwell times accordingly[89;180]. We find the pseudo-dwell times for each plateau to be exponentially distributed (Figure 4.8C, D). The force-dependent mean pseudo dwell times are well-described by exponential, Arrhenius-like relationships[93] (Table 4.1, Equations 6 and 7; Figure 4.4C, Figure 4.9C, solid lines). Fitting parameters $\tau_{0,open}$ and $\tau_{0,closed}$ are the lifetimes of the open and closed conformation at zero force and Δz_{open} and Δz_{closed} are the distances to the transition state along the pulling direction. The sum of Δz_{open} and Δz_{closed} (3.1 nm + 4.7 nm = 7.8 nm) is found to be in excellent agreement with Δz obtained from fitting relative state populations, which provides a consistency check between equilibrium and kinetic analysis and suggests that there is a single dominant energy barrier along the reaction pathway. The extrapolated lifetimes at zero force of the closed conformation $\tau_{0,closed}$ are in the range of hours. In comparison, the lifetimes of the open states in the absence of load $\tau_{0,open}$ are much shorter, only on the order of milliseconds. The extrapolated lifetimes at zero force provide another route for calculating the mean free energy: $\Delta G_{0,\tau} = k_B T \cdot \log(\tau_{0,open}/\tau_{0,closed})$ = 9.3 ± 1.7 kcal/mol, in excellent agreement with the ΔG_0 value computed from the force-dependent populations in the previous section (Figure 4.5C). The good agreement between the free energy differences obtained from equilibrium and lifetime analysis provides another consistency check between the thermodynamic and kinetic analyses.

4.2.5 Lowering pH destabilizes the D3 interface

We analyzed the equilibrium and kinetics of the conformational change under different physiologically relevant conditions (Figure 4.5). Specifically, we compared pH 7.4, characteristic of blood, with the lower pH conditions of pH 6.2 and 5.5, representative of the conditions in the trans-Golgi network and WPB, respectively. We find that the extension change Δz is insensitive to pH (Figure 4.5B), suggesting that the overall fold of the D3 domain and geometry of the transition is not affected in this pH range. However, we find a significant destabilization of the interface ($p < 0.00412$; two-tailed t test for two independent means, performed on $F_{1/2}$), reflected both in a lower midpoint force (Figure 4.5 A, yellow [pH 7.4]: 8.3 ± 1.1 pN, orange [pH 6.2]: 7.2 ± 0.8 pN, and red [pH 5.5]: 6.6 ± 0.5 pN), and a corresponding decrease in ΔG_0 (Figure 4.5C, pH 7.4: 9.0 ± 2.3 kcal/mol, pH 6.2: 6.8 ± 2.3 kcal/mol, pH 5.5: 6.3 ± 1.5 kcal/mol). Furthermore, the D3 interface becomes more dynamic and in particular the extrapolated lifetime in the open conformation is increased

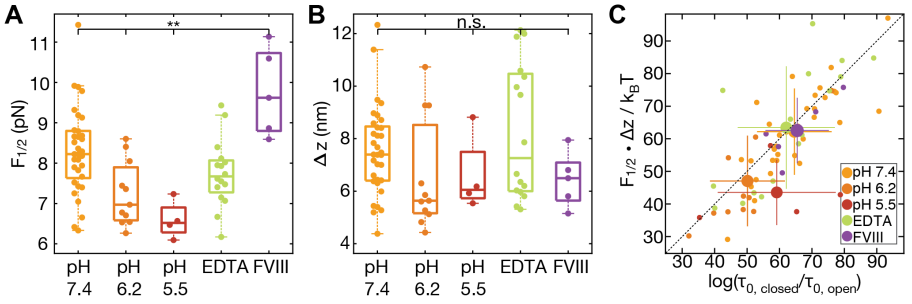

Figure 4.5: The stability of the D3 interface is modulated by pH and FVIII binding. **A** Midpoint force $F_{1/2}$ for different buffer conditions (pH 7.4 [yellow]; pH 6.2 [orange]; pH 5.5 [red]; pH 7.4 + EDTA [green]; pH 7.4 + FVIII [purple]). Buffer compositions are listed in Table 4.2. The D3 interface is destabilized by decreasing pH, not affected by addition of EDTA (removing the Ca^{2+} from the binding loop in VWD3), and stabilized by addition of FVIII. The difference between $F_{1/2}$ at pH 7.4 and pH 6.2 is highly significant at $p < 0.00412$ (two-tailed t test for two independent means). The difference between $F_{1/2}$ at pH 7.4 and pH 7.4 + FVIII is highly significant at $p < 0.00781$ (two-tailed t test for two independent means). **B** There are no significant differences in Δz values under all conditions. In the boxplots in A and B each data point corresponds to an individual molecule. The line in the boxes indicates the median of all data points, the box the 25th and 75th percentile, and the whiskers the furthest datapoint outside the box, but within 1.5 times the box width. **C** Free energy differences between the open and closed state of the D3 interface. The free energy differences were obtained from the equilibrium data as $F_{1/2} \cdot \Delta z$ and from the kinetics as $k_B T \cdot \log(\tau_{0,closed}/\tau_{0,open})$. The data fall along the 45° line (dashed), indicating that the two estimates give consistent values. Comparison of the different conditions reveals a lower free energy difference for decreased pH of 6.2 and 5.5, indicating a destabilization of the domain at low pH. Number of molecules for the five conditions: pH 7.4: 33; pH 6.2: 11; pH 5.5: 4; pH 7.4 + EDTA: 16; pH 7.4 + Factor 8: 5.

by decreased pH from 0.004 s at pH 7.4 to ~ 0.3 s at pH 6.2 and pH 5.5, suggesting an approximately 10-fold higher exposure of the cysteines buried by the D3 interface at acidic pH.

Previously, it was reported that for successful VWF multimerization low pH and Ca^{2+} are required [163]. To investigate the role of Ca^{2+}, we performed measurements in the presence of 10 mM EDTA, to chelate divalent ions. In contrast to decreased pH, we found that EDTA does not significantly affect the stability of the interface (Figure 4.5A-C). The fact that the addition of EDTA does not alter the stability of the interface could either indicate that Ca^{2+} ions have only limited influence on the interface or that structural ions, e.g. the ion positioned in a Ca^{2+} binding loop in VWD3 (Figure 4.2C, i), are so stably bound that they are not efficiently removed by EDTA.

4.2.6 FVIII binding stabilizes the D3 interface

We next used our MT assay to probe the transitions in the D3 domain in the presence of FVIII. We find a highly significant stabilization ($p < 0.00781$; two-tailed t test for two independent means, performed on $F_{1/2}$) of the D3 interface in the presence of ≈ 640 nM FVIII. FVIII has been reported to predominantly bind to the D' submodules [176;177]. Based on point mutations in the C8-3 domain, which lead to 2N von Willebrand disease phenotypes with decreased ability to bind FVIII, it was however hypothesized, that FVIII could also have a less prominent interaction site in the C8-3 module [164]. Our results strongly support a binding site in the D3 domain, as FVIII directly impacts the conformational change of the D3 interface.

There is currently no crystal structure available for a dimerized D'D3 domain. Therefore, the native force propagation through the D'D3 domain in multimerized VWF is not known. To assess whether the conformational change in the D3 domain would only play a role in biosynthesis or might also occur in VWF multimers and potentially be relevant for VWF force-activation, we investigated an "inverted" VWF dimer that is dimerized via its D'D3 domains (Figure 4.10). Here, we again observed A2 unfolding events, but no additional transitions, suggesting that the transition in the D3 interface only occurs prior to multimerization at the interface.

4.3 Discussion

VWF multimerization is a crucial process for successful hemostasis. It is known that the free cysteines Cys1099 and Cys1142, located in the N-terminal D'D3 domains, are crucially involved in multimerization in the trans-Golgi. However, the crystal structure of a monomeric D'D3 domain at neutral pH shows these two cysteines buried in a wedge-like structure formed by the VWD3 – C8-3, TIL3, and E3 interface. The details of how the cysteines are exposed to enable multimerization were previously unknown. Recently, Springer and coworkers hypothesized that Cys1099 attacks the cysteine bond between Cys1097 and Cys1091, forming a new bond with Cys1091 and releasing Cys1097 for disulfide bond formation with Cys1097' in a second dimer [181]. However, no matter if Cys1099 or Cys1097 forms an inter-dimer disulfide bond alongside Cys1142, there has to be a prior conformational change to expose both cysteines buried in the wedge. It has been hypothesized that this conformational change is induced by the acidic pH in the Golgi apparatus [164;181]. Here, we used MT to examine a conformational transition in the D3 domain, peeling submodules C8-3, TIL3, and E3 off the larger VWD3 submodule and thus exposing the unbound

cysteines. Studying the D3 interaction under various levels of constant force, we obtained force-dependent populations and rates that we extrapolated to zero load to characterize the stability of the interface. Both the extrapolated lifetimes and the estimated free energies suggest that the D3 interface is very stable at neutral pH, with a fraction of only about 1 in 10^7 molecules being in the open conformation at any given time in the absence of force, thus effectively shielding the free cysteines buried by the interface. At lower pH, characteristic of (trans-)Golgi and WPB, the D3 interface is significantly destabilized and becomes more dynamic. The pronounced pH dependency can be rationalized on the molecular level by the large number of histidine-residues in the interface that can be protonated at acidic pH and then likely destabilize the interaction between the four submodules [164]. Biologically, the regulation of the conformational change by pH is of great importance for VWF's biosynthesis to enable exposure of the buried cysteines involved in multimerization only under the acidic pH in the trans-Golgi network. The stability of the interface revealed by our assay suggests that VWF dimers are protected from forming premature cysteine bridges involving Cys1099 and Cys1142 in the ER, which would have the potential to disturb organized compaction and multimerization in the trans-Golgi network. Finally, we characterized the D3 interface opening in the presence of FVIII. We found a statistically significant stabilization of the interface, indicating that FVIII not only binds to the D' modules, but also to the D modules of the D'D3 domain, as had been suggested by structural and biochemical information. Our results highlight how complex interactions regulate the biosynthesis and function of VWF and demonstrate how MT force spectroscopy can probe biologically relevant conformational changes under a broad range of conditions.

Acknowledgements

We thank Thomas Nicolaus and Angelika Kardinal for laboratory assistance, Wolfgang Ott for providing ELP linkers, Magnus Bauer, Rafael C. Bernadi, Philipp U. Walker, Hermann E. Gaub, Frauke Gräter, Philip J. Hogg, Camilo Aponte-Santamaría, and Fabian Kutzki for helpful discussions. This project was funded by the Deutsche Forschungsgemeinschaft (DFG, German Research Foundation) Project-ID 201269156, SFB 1032 and Project-ID 386143268, "Unraveling the Mechano-Regulation of Von Willebrand Factor".

4.4 Materials and Methods

4.4.1 VWF constructs

Dimeric VWF constructs were designed as hetero-bifunctional dimers, consisting of two different types of monomers possessing different N-terminal peptide tags. One monomer possessed a ybbR-tag, allowing for covalent conjugation of CoA-biotin. The second monomer was equipped with a strep-tag II for high-affinity purification, followed by a tobacco etch virus (TEV) protease cleavage site [182] and the N-terminal sortase motif GG [183]. The TEV site served two purposes: First, to remove the strep-tag after purification, to avoid interaction with streptavidin on the magnetic beads, and second, to expose the sortase motif GG, which must be located terminally for the sortase-mediated ligation to the ELP linker. In addition to full-length dimers, comprising all domains present in mature VWF, also several constructs with deletions of certain domains were investigated as controls: delD4, with a deletion of the full D4 assembly (D4N-TIL4, aa 1873-2255), delD'D3, with a deletion of the full D'D3 assembly (TIL'-E3, aa 764-1273), and delA1, with a deletion of the A1 domain (aa 1272-1462).
Additionally, an "inverted" construct was expressed, which dimerized N-terminally. To produce such N-terminally, but not C-terminally linked dimers, monomers with mutation p.Cys2771Arg in the CK domain to impair C-terminal dimerization [184;185] and with C-terminal tags for site-specific protein attachment were expressed in the presence of the VWF propeptide (VWFpp) domains D1 and D2.
Hetero-bifunctional dimers were obtained by co-transfection of HEK-293 cells with two different plasmids so that the two different types of monomers were co-expressed. Multimerization was obstructed by deleting the VWF pro-peptide sequence (domains D1 and D2, aa 26-763). N-terminal tags were inserted after the required N-terminal signal peptide (aa 1-25). Plasmid construction, transfection of HEK-293 cells and protein expression were

Context	Formula	Variables and Fit parameters	#
Three-state transitions probability top state	$P_{top} = \frac{1}{(1+e^{-\frac{\Delta z \cdot (F-F_{1/2})}{k_B T}})^2}$	F Force k_B Boltzmann constant T Temperature Δ z & $F_{1/2}$ fit parameters	1
Three-state transitions probability middle state	$P_{middle} = \frac{1}{(1+\frac{1}{2}\cdot e^{\frac{\Delta z \cdot (F-F_{1/2})}{k_B T}} + \frac{1}{2}\cdot e^{-\frac{\Delta z \cdot (F-F_{1/2})}{k_B T}})}$	F Force k_B Boltzmann constant T Temperature Δ z & $F_{1/2}$ fit parameters	2
Three-state transitions probability bottom state	$P_{bottom} = \frac{1}{(1+e^{\frac{\Delta z \cdot (F-F_{1/2})}{k_B T}})^2}$	F Force k_B Boltzmann constant T Temperature Δ z & $F_{1/2}$ fit parameters	3
Two-state transitions probability top state	$P_{top} = \frac{1}{(1+e^{-\frac{\Delta z \cdot (F-F_{1/2})}{k_B T}})}$	F Force k_B Boltzmann constant T Temperature Δ z & $F_{1/2}$ fit parameters	4
Two-state transitions probability bottom state	$P_{bottom} = \frac{1}{(1+e^{\frac{\Delta z \cdot (F-F_{1/2})}{k_B T}})}$	F Force k_B Boltzmann constant T Temperature Δ z & $F_{1/2}$ fit parameters	5
Dwell times open state	$\tau_{open}(F) = \tau_{0,open} e^{(\frac{\Delta z_{open} \cdot F_{1/2}}{k_B T})}$	F Force k_B Boltzmann constant T Temperature Δz_{open} & $\tau_{0,open}$ fit parameters	6
Dwell times closed state	$\tau_{closed}(F) = \tau_{0,closed} e^{(-\frac{\Delta z_{closed} \cdot F_{1/2}}{k_B T})}$	F Force k_B Boltzmann constant T Temperature Δz_{closed} & $\tau_{0,closed}$ fit parameters	7
Gauss fit 1 term	$a \cdot e^{-(\frac{x-b}{c})^2}$	a, b, c fit parameters	8
Gauss fit 2 terms	$\sum_{i=1}^{2} a_i \cdot e^{-(\frac{x-b_i}{c_i})^2}$	a_i, b_i, c_i fit parameters	9
Gauss fit 3 terms	$\sum_{i=1}^{3} a_i \cdot e^{-(\frac{x-b_i}{c_i})^2}$	a_i, b_i, c_i fit parameters	10

Table 4.1: Equations and fit functions. Equations describing the equilibrium and the kinetics of the transitions in the D domains assuming independent processes.

performed as described in detail in [179]. In brief, 2 ·10^6 HEK-293 cells (DSMZ, Germany) were transfected in Dulbecco's modified Eagle's medium (Life Technologies) containing 10 % fetal bovine serum (Life Technologies),2 µg of each of the two plasmids, and 15 µl Lipofectamine 2000 (Life Technologies).
24 h after transfection, cells were transferred into selection medium containing 500 µg/ml G418 (Invivogen) and 250 µg/ml Hygromycin B (Invivogen). After 2–3 weeks, the polyclonal cell culture was seeded for expression. After 72 h of cell growth, the medium was exchanged against OPTIPRO serum-free medium (Life Technologies) for serum-free collection of secreted recombinant VWF. The culture supernatant was collected after 72 h and concentrated using Amicon Ultra-15 MWCO 100 kDa (Merck Millipore).
All dimeric constructs were purified via a HiTrap StrepTrap affinity chromatography column (GE Healthcare) using the AEKTA Explorer system (GE Healthcare). As running buffer, 20mM Hepes, 150mM NaCl, 1mM $MgCl_2$, 1mM $CaCl_2$, pH 7.4, was used. Elution buffer additionally contained 2:5mM d-desthiobiotin. Eluted VWF constructs were

buffer exchanged (to the running buffer) and concentrated by centrifuge filtration using Amicon UltraMWCO 100 kDa (Merck Millipore).

4.4.2 Steered molecular dynamics simulations

The steered molecular dynamics simulation has been performed using the crystal structure of the monomeric von Willebrand Factor D'D3 assembly from Dong et al. that has been resolved using X-ray crystallography (PDB-ID 6n29)[164]. Further structure preparation as well as the MD simulations have been done using VMD with the QwikMD plugin[22;186]. Standard parameters defined by QwikMD have been used for the simulations. The MD simulations were conducted using the NAMD molecular dynamics package6 together with the CHARMM36 force field[187;188].
The disulfide bonds that preserve the structure of the individual subdomains were treated using the classical MD forcefields parameters.
As a first pre-processing step, the original crystal structure was solvated in a box containing TIP3 water molecules and a NaCl concentration of 0.15 M. Before the pulling experiment, the protein was relaxed by molecular dynamics simulation for 100 ns. For the steered molecular dynamics experiment, the water box was enlarged in the pulling direction and the molecule was pulled at the C-terminal glycine while the N-terminal aspartate was anchored. The applied pulling speed of 1 A/ns was applied for 150 ns.

4.4.3 MT instrument

MT experiments were performed on a previously described custom setup[38;160]. The setup employs a pair of permanent magnets (5×5×5 mm^3 each; W-05-N50-G, Supermagnete, Switzerland) in vertical configuration[59]. The distance between magnets and flow cell (and, thus, the force) is controlled by a DC-motor (M-126.PD2; PI Physikinstrumente, Germany). An LED (69647, Lumitronix LED Technik GmbH, Germany) is used for illumination. A 40x oil immersion objective (UPLFLN 40x, Olympus, Japan) and a CMOS sensor camera with 4096×3072 pixels (12M Falcon2, Teledyne Dalsa, Canada) allow to image a large field of view of approximately 440 × 330 μm^2 at a frame rate of 58 Hz. Images are transferred to a frame grabber (PCIe 1433; National Instruments, Austin, TX) and analyzed with a LabView-based open-source tracking software[64]. The bead tracking accuracy of the setup is $\sim$ 0.6 nm in (x, y) and $\sim$ 1.5 nm in z direction. For creating the look-up table required for tracking the bead positions in z, the objective is mounted on a piezo stage (Pifoc P-726.1CD, PI Physikinstrumente). Force calibration was conducted as described by te Velthuis et al.[68] based on the transverse fluctuations of long DNA tethers. Importantly, for the small extension changes on the length scales of our protein tethers, the force stays essentially constant[38], with the relative change in force due to tether stretching or protein unfolding being $< 10^{-4}$. Force deviations due to magnetic field inhomogeneities across the full range of the field of view are $< 3\%$. The largest source of force uncertainty is the bead-to-bead variation, which is on the order of $\leq 10\%$ for the beads used in this study[38;59;62;77].

4.4.4 Single-molecule MT measurements

Preparation of flow cells was performed as described[38]. In brief, aminosilanized glass slides were functionalized with elastin-like polypeptide (ELP) linkers[120], possessing a single cysteine at their N terminus as well as a C-terminal Sortase motif, via a small-molecule crosslinker with a thiol-reactive maleimide group [sulfosuccinimidyl 4-(N-maleimidomethyl)cyclohexane-1-carboxylate; Sulfo-SMCC, Thermo Fisher Scientific]. Flow cells were then assembled from an ELP-functionalized slide as bottom and a non-functionalized glass slide with two small holes for inlet and outlet as top, with a layer of cut-out parafilm (Pechiney Plastic Packaging Inc., Chicago, IL) in between to form a channel. Flow cells were incubated with 1% casein solution (Sigma-Aldrich) for 1 h and flushed with 1 ml (approximately 20 flowcell volumes) of buffer (20 mM HEPES, 150 mM NaCl, 1 mM $MgCl_2$, 1 mM $CaCl_2$, pH 7.4). CoA-biotin (New England Biolabs) was coupled to the ybbR-tag of the VWF-dimer constructs in a bulk reaction in the presence of 5 μM sfp phosphopantetheinyl transferase[119] and 10 mM $MgCl_2$ at 37 °C for 60 min. Afterwards, VWF dimers were diluted to a final concentration of approximately 20 nM in 20 mM HEPES, 150 mM NaCl, 1 mM $MgCl_2$,

1 mM $CaCl_2$, pH 7.4, and incubated in the flow cell in the presence of 2 µM evolved pentamutant Sortase A [125;126] for 30 min. Subsequently, the flow cell was flushed with 1 ml of measurement buffer (20 mM HEPES, 150 mM NaCl, 1 mM $MgCl_2$, 1 mM $CaCl_2$, 0.1%(v/v) Tween-20, pH 7.4). Finally, beads functionalized with streptavidin were incubated in the flow cell for 60 s, and unbound beads were flushed out with 1 ml of measurement buffer.
At the beginning of each measurement, the tethered beads were subjected to two 5-min intervals of a constant force of 11 pN to allow for identification of specific, single-tethered beads by the characteristic unfolding of the two A2 domains [38] (Fig. 4.2A). Only beads that showed two A2 unfoldings were analyzed further. After 30 s at a low resting force of 0.5 pN, beads were subjected to a forceramp starting at 12 pN and going down to 6 pN in steps of 0.3 pN, with each plateau of constant force lasting for 5 minutes. All measurements were performed at room temperature ($\sim 22\,^{\circ}C$).

4.4.5 Data analysis

Data analysis was performed with custom MATLAB scripts. Specific VWF dimer tethers were selected on the basis of the two A2 fingerprint unfoldings, characterized previously [38;179]. Extension vs. time traces were subjected to a tether-specific smoothing with a moving average filter. The number of frames used for the smoothing was determined based on the distance of the states and the Allan deviation (AD) of the tether (see Figure 4.7): Distance between the states was determined from fitting a double or triple Gaussian function to the histogram of the extension in the lowest constant force plateau exhibiting a population in all two or three states, respectively and evaluating the distance between the peaks, as shown in Figure 4.7B to the left (1.)). The AD was calculated from a 30 second fragment of the trace at the lowest constant force plateau exhibiting no transitions and fit with a theoretical model of an overdamped bead (Figure 4.7B middle (2.))). The AD is defined as

$$\sigma_\theta(\tau) = \sqrt{\frac{1}{2} \cdot \langle(\overline{\theta}_{i+1} - \overline{\theta}_i)^2\rangle} \tag{4.1}$$

where $\overline{\theta}_i$ is the mean of the measurement interval of length τ. The angle bracket denotes the arithmetic mean over all measurement intervals. In other words, the AV is one-half of the averaged square distance between the means of neighboring intervals [72;189;190]. Intuitively, it gives a measure of the spatial resolution after averaging over a time interval τ. Under the assumption that the deviation should be at least four times smaller than the evaluated distance Δz, a smoothing factor for each trace can be determined by multiplication of the averaging interval τ, where AD equals $\Delta z/4$, with the measurement frequency. This smoothing factor is applied to the extension time trace before evaluation of the state-population and the dwell times in each force plateau.

4.5 Supplementary Material

4.5.1 Tables

Name	Ingredients
pH 7.4, near physiological	20 mM Hepes, 150 mM NaCl, 1 mM $CaCl_2$, 1 mM $MgCl_2$
pH 7.4, near physiological + EDTA	20 mM Hepes, 150 mM NaCl, 10 mM EDTA
pH 6.2	20 mM BisTris, 150 mM NaCl, 1 mM $CaCl_2$, 1 mM $MgCl_2$
pH 5.5	20 mM Na-Acetate, 150 mM NaCl, 1 mM $CaCl_2$, 1 mM $MgCl_2$

Table 4.2: Buffers used for MT measurements. The pH of buffers was adjusted with HCl and NaOH. For the measurement, buffers were supplemented with 0.1% Tween-20 to reduce unspecific interactions of specific beads.

4.5.2 Figures

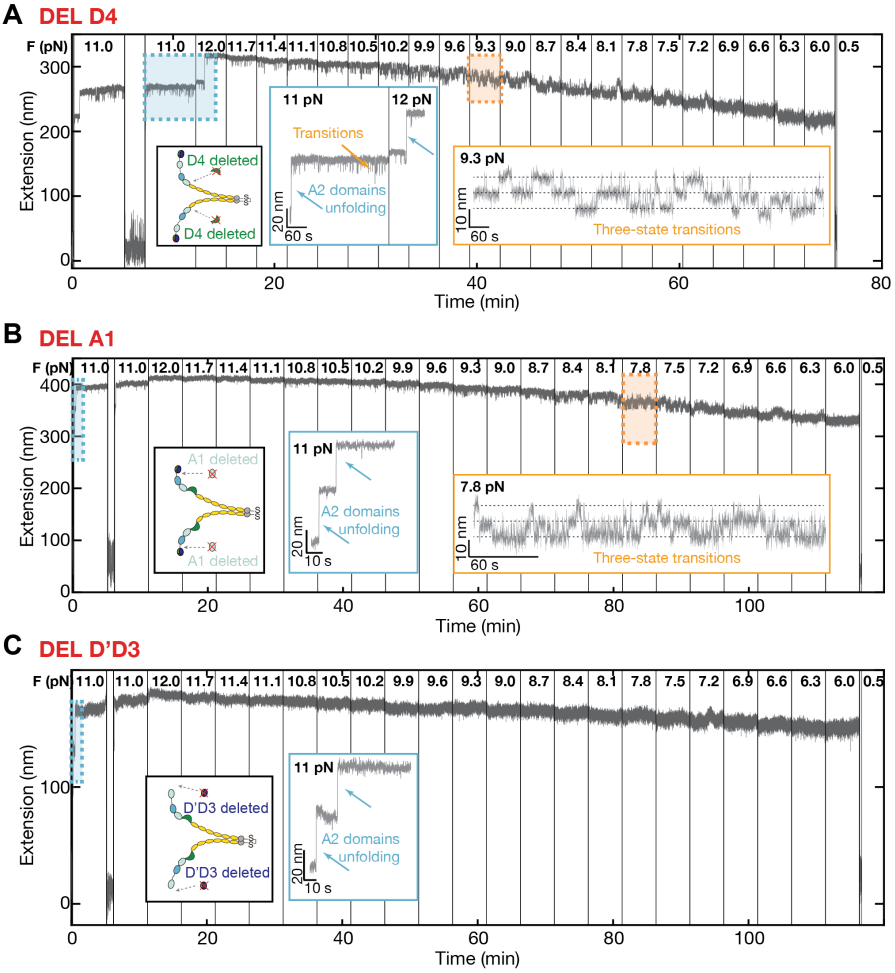

Figure 4.6: Domain deletions to proof origin of transitions in the D'D3 domain. Individual domains were deleted to verify the origin of the transitions in the D'D3 domain. Apart from deleted domains, constructs possessed the same tags and were objected to the same force protocol as the wild type. **A** Heterodimer with D4 domain deletions (schematic of construct shown as inset (black frame)). Molecules with D4 domain deletions show A2 domain unfoldings (inset with blue frame) and three-state transitions (inset with orange frame), proving transitions to be independent of the D4 domain. Notably, transitions also appear in between the two A2 unfoldings, suggesting that transitions are also independent of the A2 domain. **B** Heterodimer with A1 domain deletions (schematic of construct shown as inset (black frame)). Molecules with A1 domain deletions show A2 domain unfoldings (inset with blue frame) and three-state transitions (inset with orange frame), proving transitions to be independent of the A1 domain. **C** Heterodimer with D'D3 domain deletions (schematic of construct shown as inset (black frame)). Constructs with D'D3 domain deletions show A2 domain unfoldings, but no transitions. This was checked for > 40 molecules. This indicates that transitions originate in the D'D3 domain.

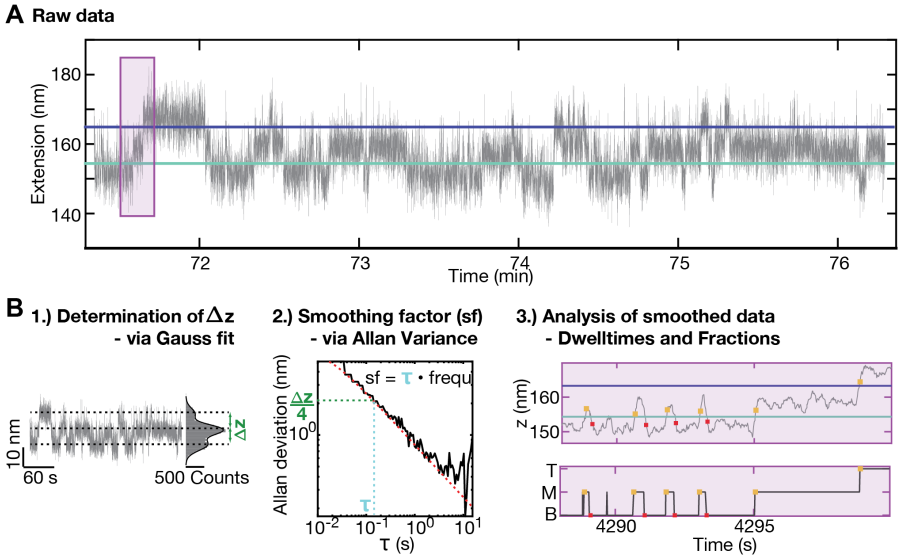

Figure 4.7: Analysis procedure of force ramps with three-state transitions. A Raw Data, recorded at 58 Hz in one constant force plateau. Thresholds separating bottom (B), middle (M), and top (T) states are shown as green and blue solid lines. Noise of the trace induces transitions over the thresholds in addition to transitions caused by domain opening and closing. Purple box indicates selection of trace analyzed in B3. **B** Procedure to determine smoothing factor for dwell time analysis. In a first step, a three-term Gaussian is fit to the extension histogram and the distance between the fitted peaks indicates the Δz that needs to be resolved for dwell time analysis. Dashed lines indicate the T, M, and B state. Secondly, the Allan deviation for a 30 second time interval at the lowest force plateau is calculated (solid black line, according to Equation 1) and fit with a theoretical model of the Allan deviation (red dashed line). The Allan deviation is defined as the square root of one-half of the averaged square distance between the means of neighbouring intervals of length τ[72]. Intuitively, it gives a measure of the spatial resolution after averaging over a time interval τ. Under the assumption that the deviation should be four times smaller than the distance Δz (green dashed line), a smoothing factor for each trace can be determined depending on its noise level (blue dashed line). This smoothing factor is applied to the trace before analyzing dwell times and fractions in a third step. Yellow squares indicate the first data point after crossing the threshold from below, i.e. transition from B to M or from M to T; red squares indicate the first data point after crossing the threshold from above, i.e. transition from T to M or M to B.

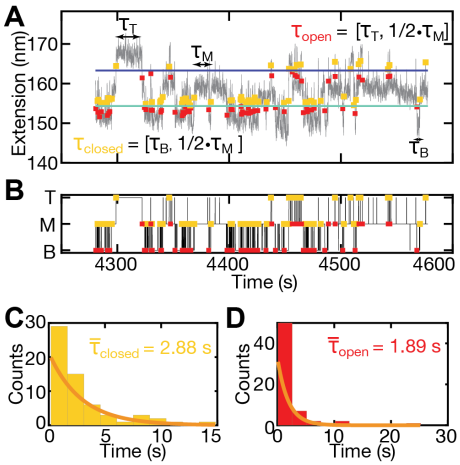

Figure 4.8: Exemplary dwell time evaluation for one plateau of constant force. A Short segment of a time-extension trace measured for a wild type D'D3 domain VWF dimer exhibiting three-state transitions at a force of 8.4 pN. Raw data is filtered with an 11-frame moving average (smoothing factor determined according to Figure 4.7). The green horizontal line is the threshold between the bottom state (B) and the middle state (M) and the blue horizontal line is the threshold between the middle state (M) and the top state (T); yellow squares indicate the first data point after crossing the threshold from below, i.e. transition from B to M or from M to T; red squares indicate the first data point after crossing the threshold from above, i.e. transition from T to M or M to B. **B** Time trace derived from the analysis shown in panel A, indicating the current state of D3 domains with "T" corresponding to both domains opened, "M" corresponding to one domain open and one domain closed and "B" corresponding to both domains closed. The time between the transitions between "B" and "M" and "M" and "T" corresponds to the dwell times. To obtain pseudo dwell time distributions of the individual domains, dwell times in the bottom state were collected together with half of the dwell times in the middle state for a distribution of τ_{closed} and dwell times in the top state were collected with half of the dwell times in the middle state for a distribution of τ_{open}. **C, D** Histograms of pseudo dwell time distribution in the closed state (C) and the open state (D) obtained from the analysis shown in panels A and B. The pseudo dwell times are well described by single exponential fits, shown as solid orange line. Insets show mean dwell time.

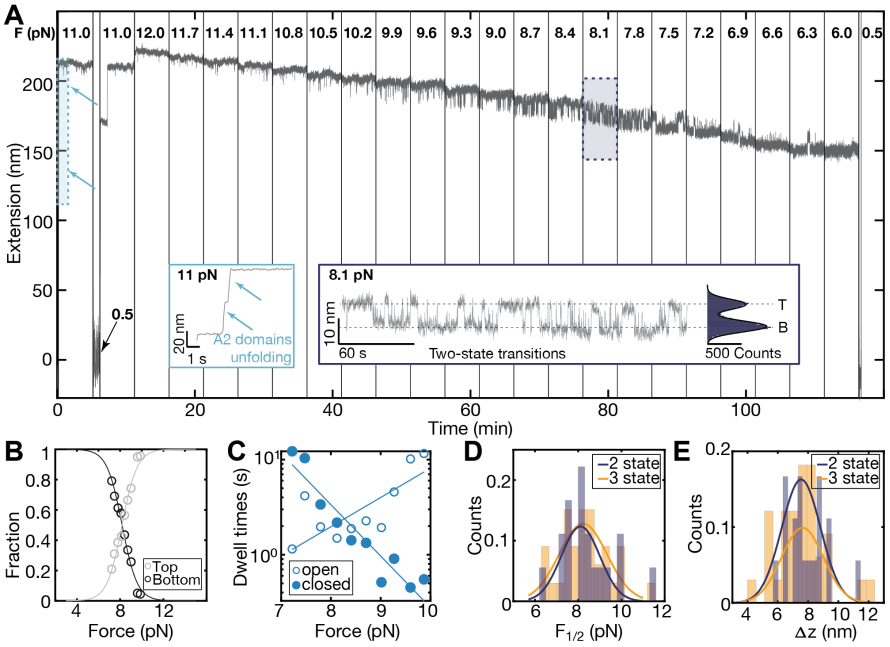

Figure 4.9: Two-state transitions. A Molecule showing only transitions between two states. Same experimental force ramp was conducted as for molecules exhibiting three-state transitions (see Figure 4.2). Insets show two A2 unfoldings, indicating specific dimer (blue inset), and two-state transitions close to the midpoint force at 8.1 pN together with a histogram of the extension (dark blue inset). Top and Bottom states are indicated with dashed lines. Extension was smoothed with a 9-frame moving average filter. **B** Two-state model fit to the fraction of time spent in the top and in the bottom state. Fit parameters are the midpoint force and the distance between the states. **C** Dwell time distributions in the top and in the bottom state. Unlike for the three-state transitions, dwell times for an individual domain can be determined directly for two-state transitions. **D** Distributions of midpoint forces evaluated from fitting two- and three-state transition molecules respectively. Solid lines are Gauss fits. Distributions are equal within experimental error. Mean ± std. are: $F_{1/2,3-state}$ = 8.2 ± 0.9 pN and $F_{1/2,2-state}$ = 8.4 ± 1.2 pN. **E** Distributions of Δz values evaluated from fitting two- and three-state transition molecules respectively. Solid lines are Gauss fits. Distributions are equal within experimental error. Mean ± std. are: $\Delta z_{3-state}$ = 7.1 ± 2.0 nm and $\Delta z_{2-state}$ = 8.0 ± 1.3 nm. Distributions in D and E are for 15 three-state transition molecules and 18 two-state transition molecules.

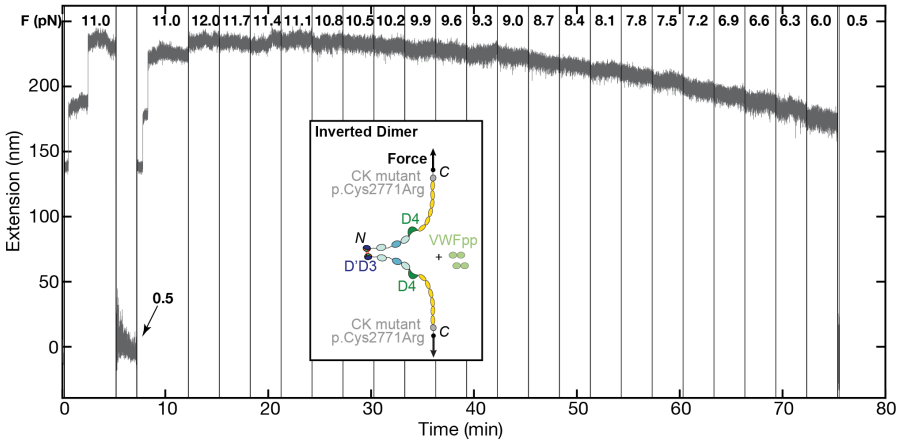

Figure 4.10: Physiological force-loading of an inverted dimer. Same force ramp as conducted to analyze the two- and three-state transitions with an inverted dimer (construct shown as inset). In this conformation, force propagates through the D'D3 domain as through VWF that is multimerized by cysteine linkage in the D'D3 domains (see Figure 4.1). Extension was smoothed with a 5-frame moving average filter. In total, >40 inverted molecules with two A2 unfoldings were screened for transitions, but none showed any.

5

A Tethered Ligand Assay to Probe SARS-CoV-2:ACE2 Interactions

Summary

SARS-CoV-2 infections are initiated by attachment of the receptor-binding domain (RBD) on the viral Spike protein to angiotensin-converting enzyme-2 (ACE2) on human host cells. This critical first step occurs in dynamic environments, where external forces act on the binding partners and avidity effects play an important role, creating an urgent need for assays that can quantitate SARS-CoV-2 interactions with ACE2 under mechanical load. Here, we introduce a tethered ligand assay that comprises the RBD and the ACE2 ectodomain joined by a flexible peptide linker. Using magnetic tweezers and atomic force spectroscopy as highly complementary single-molecule force spectroscopy techniques, we investigate the RBD:ACE2 interaction over the whole physiologically relevant force range. We combine the experimental results with steered molecular dynamics simulations and observe and assign fully consistent unbinding and unfolding events across the three techniques, enabling us to establish ACE2 unfolding as a molecular fingerprint. Measuring at forces of 2–5 pN, we quantify the force dependence and kinetics of the RBD:ACE2 bond in equilibrium. We show that the SARS-CoV-2 RBD:ACE2 interaction has higher mechanical stability, larger binding free energy, and a lower dissociation rate compared to SARS-CoV-1, which helps to rationalize the different infection patterns of the two viruses. By studying how free ACE2 outcompetes tethered ACE2, we show that our assay is sensitive to prevention of bond formation by external binders. We expect our results to provide a novel way to investigate the roles of viral mutations and blocking agents for targeted pharmaceutical intervention.

5.1 Introduction

A subset of coronaviruses (CoV) causes severe acute respiratory syndrome (SARS) in humans. We have seen three major recent outbreaks, including the first SARS pandemic from 2002–2004 (SARS-CoV-1), middle east respiratory syndrome (MERS-CoV) that emerged in 2012, and the ongoing COVID-19 pandemic (SARS-CoV-2). SARS-CoV-2 particles carry $\sim$ 100 copies of the trimeric viral glycoprotein Spike (S) on their surface[7], giving the appearance of an eponymous corona around the virus. Like SARS-CoV-1, SARS-CoV-2 attaches to human host cells by S binding to angiotensin-converting enzyme-2 (ACE2)[191–195]

This Chapter is based on a manuscript by Bauer, Gruber *et al.* with Gruber and Bauer as equally contributing first authors (in press at *Proceedings of the National Academy of Sciences of the United States of America*). My contribution: For this manuscript, I was involved in designing the research, developing an MT assay for measuring receptor:ligand interactions, performing MT experiments and analyzing MT data, and writing the manuscript.

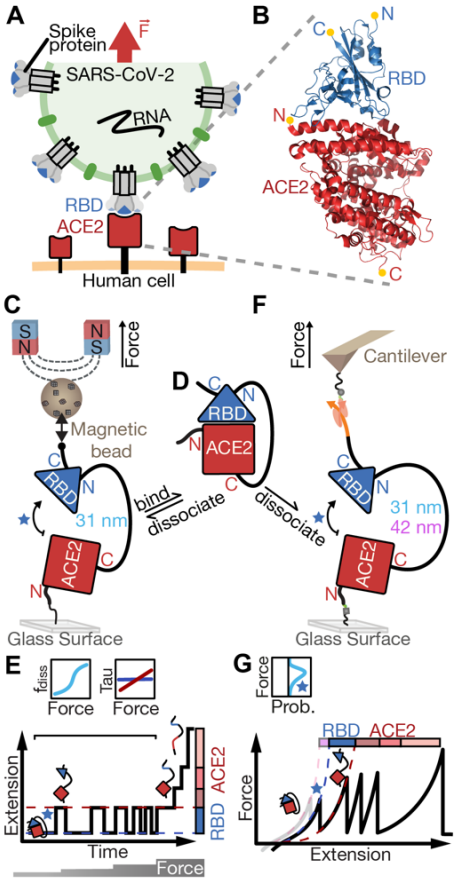

Figure 5.1: Single-molecule assays to probe the SARS-CoV-2 RBD:ACE2 interface under force. Motivation and overview of our tethered ligand assay for equilibrium and dynamic single-molecule force spectroscopy (SMFS) measurements in magnetic tweezers (MT) and atomic force microscopy (AFM). **A** Schematic of a SARS-CoV-2 virus particle (green) presenting spike protein trimers (grey) that can bind to human ACE2 (red) on the cell surface via their RBDs (blue). The bond between RBD and ACE2 is formed in a dynamic environment, where it must withstand external mechanical forces (indicated by the red arrow), e.g. caused by coughing or sneezing, in order to allow efficient infection of the human host cell (orange). **B** Crystal structure of the SARS-CoV-2 RBD:ACE2 complex (PDB ID: 6m0j)[204]. The N- and C-termini of the RBD (blue) and ACE2 (red) are indicated with yellow spheres. **C** Schematic (not to scale) of the tethered ligand assay in MT. The tethered ligand construct consists of the ACE2 ectodomain (red square) and RBD (blue triangle) joined by a flexible polypeptide linker (black line) of 85 amino acids (31 nm contour length) or 115 amino acids (42 nm contour length). **D** Tethered ligand construct in the absence of force, where the RBD remains bound to ACE2. **E** Stylized measurement of the tethered ligand construct in MT. To probe RBD:ACE2 bond dynamics, time traces of the tether extension are recorded at different levels of applied force (indicated at the bottom). At low forces, reversible transitions between the bound configuration (interface formed), and a dissociated configuration (interface dissociated and peptide linker stretched) are observed as jumps between two extension levels (red and blue dashed lines). At higher forces, further upward steps in the extension trace correspond to unfolding events of protein (sub-)domains. From the MT time traces, both the fraction of time spent in the dissociated state and the dwell times in the bound and dissociated state can be determined as a function of applied force (top). **F** Schematic (not to scale) of the tethered ligand construct in the AFM. **G** Stylized AFM measurement. The cantilever is retracted with constant velocity and the force response to the applied extension is shown as a force-extension curve. With increasing extension the RBD:ACE2 interface ruptures (blue star), protein subdomains unfold, and finally the ClfA:Fgγ bond ruptures, giving rise to distinct peaks in the force-extension curve. Histograms of rupture forces (top) are compiled from multiple measurements.

(Figure 5.1A). Specifically, each of the three S1 subunits in an S trimer carries a receptor-binding domain (RBD) at its tip, which is presented in an up or down conformation and can bind ACE2 in the up conformation (Figure 5.1B)[196]. Binding of the virus to host cells occurs in dynamic environments[197;198] where external forces act on the virus particle. In particular, in the respiratory tract, coughing, sneezing, and mucus clearance exert mechanical forces[199;200] that the virus must withstand for productive infection. The magnitude and dynamics of these forces are not known precisely and likely variable. A rough estimate from fluid dynamics suggests an upper limit of forces in the range of $\sim$ 2 pN to 2 nN and conversely cellular dynamics generate loading rates of micrometers per minute (estimates are provided in the methods section).

The SARS-CoV-2 S protein and its interaction with ACE2 have been target of intense research activity, as they are critical in the first steps of SARS-CoV-2 infection and S constitutes a major drug and the key vaccine target in the current fight against COVID-19. Further, differences in binding between ACE2 and the SARS-CoV-1 and SARS-CoV-2 RBDs have been linked to the different observed patterns in lower and upper respiratory tract infections by the two viruses[193]. Despite its importance, many questions about RBD:ACE2 interactions, particularly about their stability under external forces, are unresolved. Consequently, there is an urgent need for assays that can probe the affinity and kinetics of the interaction under a wide range of external forces. In nature, receptor:ligand pairs are often held in spatial proximity by neighboring interactions, creating high effective concentrations. Engagement of multiple interactions have been suggested to be important in other viral infections, including influenza, rabies, and HIV[201–203]. Since conventional affinity measurements do not take into account these effects, there is a need for novel *in vitro* assays mimicking these effects when measuring bond characteristics.

Tethered ligand assays have provided insights into a range of critical molecular interactions under mechanical load[54;55;116;205–210]. Under constant force, they allow observation of repeated interactions of the same binding partners, which are held in spatial proximity under mechanical control. Therefore, they can provide information on affinity, avidity, on- and off-rates, and mechanical stability[205;209].

Here, we present a tethered ligand assay to determine RBD interactions with ACE2 at

the single-molecule level subject to defined levels of applied force. Our assay utilizes fusion protein constructs of the SARS-CoV-1 or SARS-CoV-2 RBD and the human ACE2 ectodomain joined by flexible peptide linkers. To probe the linkage under a large range of mechanical forces and loading rates, we used two highly complementary single-molecule force spectroscopy (SMFS) approaches: an atomic force microscope (AFM) and magnetic tweezers (MT) (Figure 5.1C - G). We complemented the experiments with steered molecular dynamics (SMD) simulations to provide microscopic insights that are inaccessible experimentally.

AFM force spectroscopy can probe molecular interactions and protein stability dynamically [35;41;42], typically measuring at constant loading rate, and can investigate even the most stable host-pathogen interactions (at forces F > 2 000 pN) [3]. In AFM experiments, the molecular construct of interest is stretched between a surface and the tip of an AFM cantilever. The cantilever is retracted at a constant velocity, and the force is monitored from the cantilever deflection. Molecular rupture or protein (sub-)domain unfolding events give rise to a sawtooth-like pattern in the force vs. extension traces (Figure 5.1G). In contrast, MT typically operate at constant force and can resolve very low forces [59;70], down to F < 0.01 pN. In MT, molecules are tethered between a flow cell surface and magnetic beads. External magnets apply defined and constant stretching forces, and the tether extension is monitored by video microscopy. In MT, unbinding or unfolding events give rise to steps in the extension vs. time trace (Figure 5.1E).

Probing our tethered ligand construct by AFM force spectroscopy, we reveal the dynamic force stability of the assembly. In combination with SMD simulations, we assign the increments revealed by force spectroscopy and establish the ACE2 unfolding pattern as a molecular fingerprint to select properly assembled tethers. Using MT, we measure the on- and off-rates at different levels of mechanical load and extrapolate to the thermodynamic stability at zero load. We compare the stability of the SARS-CoV-1 and SARS-CoV-2 RBD:ACE2 interactions in all three assays and consistently find a lower force stability for SARS-CoV-1 across the different techniques.

5.2 Results

5.2.1 A tethered ligand assay to probe viral attachment under physiological forces using MT and AFM

We designed tethered ligand fusion proteins that consist of the SARS-CoV-1 RBD or SARS-CoV-2 RBD and the ectodomain of human ACE2 joined by flexible polypeptide linkers (Figure 5.1D). Protein constructs were designed based on the available crystal structures [204;211] of the SARS-COV-1 or SARS-COV-2 RBDs in complex with human ACE2 and carry short peptide tags at their termini for attachment in MT and the AFM (Materials and Methods). For MT experiments, the protein constructs were coupled covalently to the flow cell surface via elastin-like polypeptide (ELP) linkers [120] and to magnetic beads via a biotin:streptavidin linkage [38]. Tethering multiple proteins in MT enables parallel measurements of multiple molecules over extended periods (hours to weeks) at precisely controlled forces [38]. In MT, bead positions and, therefore, tether extensions are tracked by video microscopy with $\sim$ 1 nm spatial resolution and up to kHz frame rates [160;212;213]. For AFM experiments, we employ the same tethered ligand construct as used in the MT assay and covalently anchor it to a glass surface using PEG spacers. The key difference to the MT measurement is the use of an Fgɣ tag on the protein together with ClfA as a reversible handle system instead of the biotin:streptavidin linkage to attach it to the AFM cantilever. The ClfA:Fgɣ interaction is non-covalent, but can withstand extremely high forces of up to 2 nN, making it a reliable attachment modality with a built-in force fingerprint for AFM force spectroscopy [3]. Together with stable custom-built AFM setups [214], this enables highly automated and reliable recordings of specific force-extension traces.

5.2.2 Dynamic AFM force spectroscopy reveals a characteristic unfolding pattern

The AFM traces of the tethered ligand constructs feature a total of five sawtooth-like peaks, each corresponding to an unfolding or unbinding event (Figure 5.1G, Figure 5.2A, and

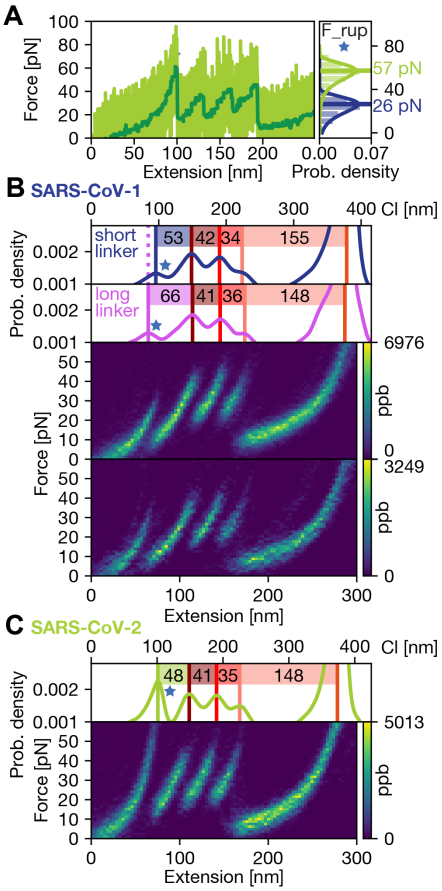

Figure 5.2: AFM force spectroscopy reveals multiple defined transitions in the tethered ligand construct. **A** AFM force-extension trace of the SARS-CoV-2 RBD:ACE2 tethered ligand construct (raw data in light green, total variation denoised dark green, recorded at 800 nm/s retraction velocity). Four defined peaks are clearly visible between 30 pN and 60 pN. The final ClfA:Fgγ rupture at 1500 pN is not shown for clarity. **B** Heatmaps of unfolding curves for the SARS-CoV-1 RBD:ACE2 fusion construct with short linker (31 nm, top) and long linker (42 nm, bottom) generated from 151/60 unfolding traces similar to the measurement shown in **A**. The colorbar indicates the mapping of points per bin (ppb) values to each pixel in the heatmap. **C** Heatmap of unfolding curves for the SARS-CoV-2 RBD:ACE2 fusion construct generated from 127 unfolding curves, including the curve shown in **A**. Overall, the unfolding patterns look very similar for SARS-CoV-1 and 2, the only clear difference is that the first peak (indicated by a blue star throughout) is at higher forces for SARS-CoV-2. The right inset in panel **A** directly compares the most probable rupture forces determined by the Bell-Evans model for the first peak for the two constructs. The insets in the top of panels **B** and **C** show transformations of the force-extension data to contour length space (Materials and Methods). For SARS-CoV-1 two different length linkers were measured (31 nm linker in blue and 42 nm in purple); the difference of 13 nm in contour length for the initial peak is very close to the expected value.

Figure 5.7). The last (right-most) peak exhibits forces well within the range previously established for the ultra-strong ClfA:Fgγ interaction [3], clearly indicating specific attachment of the protein construct. Consequently, the four peaks at lower forces must correspond to unfolding and unbinding events in a single tethered ligand construct. To visualize the most probable force-extension trace, we aligned and superimposed all individual curves [215;216] (Figure 5.2B and C). They all feature the final rupture peak assigned to the ClfA:Fgγ linkage and an initial (left-most) peak typically at lower forces around 26 pN for the SARS-CoV-1 fusion construct and about twice as high forces for the SARS-CoV-2 fusion construct (around 57 pN; Figure 5.2 A on the right). This initial peak is followed by a trident-shaped, three-peak pattern at around 40 pN. The released contour lengths corresponding to each of these unbinding/unfolding peaks were determined from contour length transformations [215;217] of each specific curve (see Materials and Methods). The four increments show the same order and very similar lengths for the SARS-CoV-1 and SARS-CoV-2 constructs (Figure 5.2B, C, top insets).

The fact that the first peak (Figure 5.2, blue star) has a notably different force signature for the SARS-CoV-1 and SARS-CoV-2 constructs, while all other peaks are very similar, suggests that the first peak involves the RBD domain, which is the only part that is different between the two constructs. To probe whether the first peak is due to the RBD:ACE2 interface opening or RBD unfolding, we performed control experiments with a longer linker (115 amino acids (aa) corresponding to $\sim$ 42 nm contour length, instead of 85 aa or $\sim$ 31 nm) between the two domains. The measurements with the longer linker reveal an increase in the contour length released in the first peak by 13 nm, very close to the expected 11 nm, which strongly suggests that the first peak represents dissociation of the RBD:ACE2 interface (Figure 5.2B). The contour length increments of the first peaks (53 nm and 66 nm for the short and long linker, respectively), are, however, larger than what is expected from interface opening only, which would release the linker lengths (31 nm or 42 nm) and involve reorientation of the domains. Conversely, full unfolding of the RBD domain would release 193 aa or 70 nm contour length, much longer than the increments that are experimentally observed. Therefore, the first peak must involve interface opening and partial unfolding of the RBD. Since all measurements were conducted under non-reducing con-

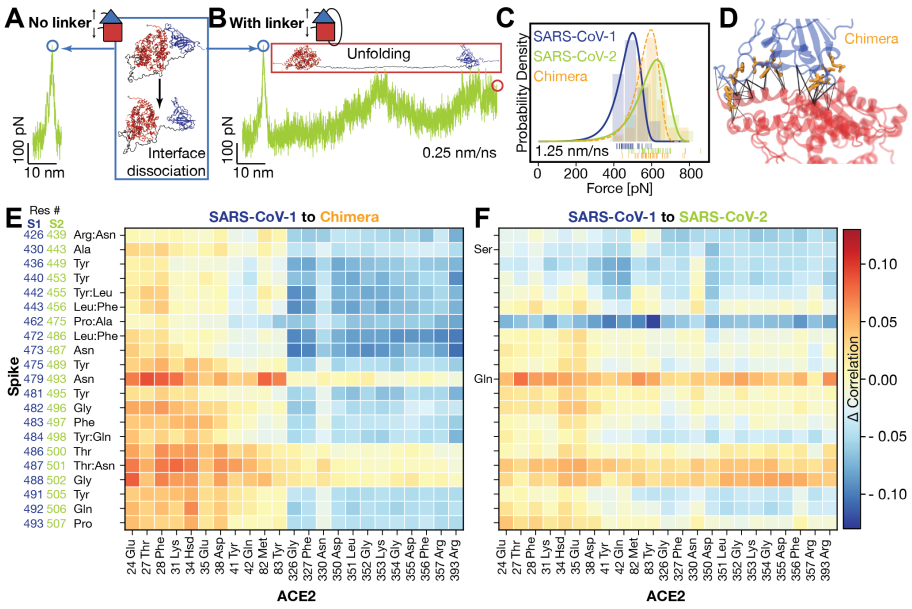

Figure 5.3: Steered molecular dynamics (SMD) simulations. **A** SMD force-extension curve for pulling on the SARS-CoV-2 RBD:ACE2 bond without additional linker. Inset (blue frame) shows rendering of the interface opening causing the peak in the trajectory. **B** SMD force-extension curve for pulling on tethered ligand SARS-CoV-2 RBD:ACE2 construct (same complex as investigated with the AFM and MT). Force and pathway of interface opening (indicated with blue circle) are equivalent to pulling on the interaction without linker as shown in **A**. Inset (red frame) shows rendering at the end of the simulation, when interface is dissociated and ACE2 and RBD are partially unfolded. **C** Force distribution of interface opening for SARS-CoV-1 (blue, most probable rupture force: 499 pN), SARS-CoV-2 (orange, most probable rupture force: 628 pN), and chimera (green, most probable rupture force: 597 pN) tethered ligand constructs. Chimera is a tethered ligand construct with the SARS-CoV-1 RBD with 12 amino acid replacements according to the SARS-CoV-2 RBD. These 12 amino acid replacements in the SARS-CoV-1 RBD nearly reproduce the force stability of SARS-CoV-2. Distributions are from 40 replicas for each construct. **D** Crystal structure of the SARS-CoV-1 RBD:ACE2 interaction (PDB-ID: 2ajf). Residues changed for chimera are indicated in orange. The thickness of the black lines quantifies the correlation between residues from the RBD and ACE2 shortly before interface rupture for the chimera system. The overall correlations between RBD and ACE2 residues determine the force propagation pathways through the interface and thus the stability of the interaction. **E** and **F** Heatmaps of the change in correlation of individual spike residues with ACE2 residues comparing SARS-CoV-1 with the chimera (**E**) and SARS-CoV-1 with SARS-CoV-2 (**F**). Residues were selected based on proximity to the interface. Modified residues in the chimera in close proximity with ACE2 are indicated in the y axis labels. Heatmaps indicate a change in mechanostability pattern throughout the interface. Difference in the interaction pattern under force load between SARS-CoV-1 and SARS-CoV-2 RBD:ACE2 interface help to rationalize their difference in force stability.

ditions (TBS buffer, see Materials and Methods), we expect disulfide bridges between cysteines to be formed, which shield large parts of the RBD structure from force [204;218] and allow only 51 aa to unfold, corresponding to 19 nm contour length, in excellent agreement with experimentally observed increments (Figure 5.8).

With the first peak assigned to the RBD:ACE2 interface opening and partial RBD unfolding, the subsequent trident-shaped, three-peak pattern is likely due to (step-wise) unfolding of the ACE2 domain. Control measurements with the ACE2 domain only and the same affinity tags resulted in traces showing the same trident-shaped pattern and no additional first peak (Figure 5.9), confirming the assignment of the trident-shaped pattern to the ACE2 domain. Comparing the same constructs with the SARS-CoV-1 and the SARS-CoV-2 RBD tethered to ACE2, reveals a lower force stability for the SARS-CoV-1 interface compared to SARS-CoV-2 (Figure 5.2A, histograms). In addition, the AFM data suggest that, after the opening of the interface, stepwise ACE2 unfolding gives rise to a defined pattern that can be used as a molecular fingerprint.

5.2.3 All-atom steered molecular dynamic (SMD) simulations provide insights into the unfolding patterns in molecular detail

In an *in-silico* SMFS approach, the tethered ligand protein probed in the AFM measurement was modeled using QwikMD [186]. Based on the available crystal structures, the RBD:ACE2 complex was modeled with and without the polypeptide linkers for both SARS-CoV-1 and SARS-CoV-2, in a total of 4 different systems (for details, see Materials and Methods). Over 300 SMD simulations were performed employing GPU-accelerated NAMD 3 [219]. The simulated behavior of the complexes agrees with the AFM experiments, starting with the dissociation of the RBD domain from ACE2 and consecutive partial unfolding of the RBD (Figure 5.3A, B). In the simulations, the unfolding of parts of the RBD is caused by the linker that gets stretched after the interface is released from ACE2. After the initial RBD dissociation, ACE2 unfolds in several substeps. The corresponding force-distance curve (Figure 5.3B) agrees with the observed unfolding pattern obtained by AFM measurements. The insets in Figure 5.3A and B show renderings at three different time points to visualize the forced RBD:ACE2 dissociation observed in SMD and AFM experiments.

Simulations of the RBD and ACE2 without and with the linker showed identical behavior until the point of the interface dissociation (Figure 3A, B) and the dissociation process was conserved for both protein models. For collecting statistics, the construct without linker was used to determine unbinding forces of the RBD:ACE2 interface. The simulations give 26% higher forces for SARS-CoV-2 compared to SARS-CoV-1 (Figure 5.3C). The observed higher forces for SARS-CoV-2 qualitatively agree with the differences in forces determined from the AFM measurements with an expected increase in absolute forces due to the much higher loading rates in the SMD simulation compared to AFM measurements.

5.2.4 Unfolding patterns across different force-loading rate regimes are highly reproducible

In contrast to AFM and SMD simulations, where tethered fusion constructs were subjected to forces with constant force-loading rate, MT were used to examine the fusion complex at constant forces, first studying equilibrium binding and dissociation between RBD and ACE2 at lower forces and then unfolding individual protein domains at high forces (Figure 5.4A). At forces between 2 to 5 pN, we observe systematic transitions in the extension traces, with jumps between a high extension "dissociated" and low extension "bound" state (Figure 5.4A, Equilibrium and Figure 5.5A,B). The transitions systematically shift towards the dissociated state with increasing force (Figure 5.5A). Alternating between levels of low force (0.5 pN) and higher forces (15, 20, 25, and 30 pN) (Figure 5.4A, "High Forces") reveals three distinct unfolding transitions. At forces of 15 and 20 pN, one unfolding transition repeatedly occurs after refolding during a low force interval. This reversible transition corresponds to the systematic transitions recorded at equilibrium between 2 and 5 pN (Figure 5.4A blue boxes and Figure 5.4B, blue histogram for high force transitions), while a subsequent two-step transition above 25 pN (Figure 5.4A, red box and Figure 5.4B, red histograms) is irreversible. Measuring just the ectodomain of ACE2 revealed the same characteristic irreversible two-step unfolding pattern above 25 pN without showing the systematic transitions at lower forces or the reversible unfolding at 15 and 20 pN (Figure 5.11). This allows a clear assignment of the two irreversible unfolding events to the unfolding of ACE2, while the equilibrium transitions, observed as reversible steps at 15 and 20 pN are attributed to the RBD:ACE2 interface opening and partial RBD unfolding, corresponding to the first peak in the AFM force-distance curves.

Unlike in the SMD simulations, where interface dissociation clearly precedes partial RBD unfolding, the processes can neither be discriminated within the resolution limits of the AFM, nor of MT. Thus, we are unable to clearly assign a temporal order or causality in the *in vitro* experiments. If the process in the AFM and MT was equal to what SMD simulations showed, the linker would be unstretched upon interface dissociation. It is highly likely that the subsequent partial RBD unfolding should be observable as a separate event at the loading rates in the *in vitro* experiments. The fact that both processes are not separable in both techniques suggests that the clear order found in SMD simulations is an artefact of the high force-loading rates and that in the experiments partial RBD unfolding might happen simultaneously or even precede interface dissociation.

Using the worm-like-chain model[220] with a persistence length of 0.5 nm[38] the contour length of the observed extension increments in MT are calculated (Figure 5.4B). The mean values of the increments in MT (Figure 5.4C, MT) are compared to the contour length transformed increments in the AFM (Figure 5.4C, AFM; all values given in Table 5.1). Strikingly, the increments observed with both single-molecule force spectroscopy techniques are in excellent agreement, within experimental errors, with each other and with theoretical expectations based on the crystal structure[204] and the fusion construct design. Comparing the total length gain from unfolding the tethered ligand ACE2 in the AFM (224 nm) and MT (233 ± 25.5 nm), reveals quantitative agreement within experimental errors. The first ACE2 unfolding event (Table 5.1, $ACE2_1$) in the AFM almost perfectly matches the first increment in MT. The second and third ACE2 unfolding (Table 5.1 $ACE2_2$ and $ACE2_3$) in the AFM cannot be separately resolved in MT for most molecules and typically occur as one single large step (Table 5.1 $ACE2_{combined}$). In a small subpopulation (8 of 42 total molecules), however, we observed a very short-lived intermediate level, splitting the large step into a smaller and yet another larger step, matching the increments observed in the AFM. In summary, ACE2 unfolding provides a highly specific and reproducible molecular fingerprint across AFM and MT measurements that we subsequently used to select for specific tethers to probe the RBD:ACE2 interface.

5.2.5 MT measurements probe the RBD:ACE2 interaction under load in equilibrium

After selecting specific tethers based on the ACE2 fingerprint, we analyze the equilibrium transitions measured in MT at forces between 2 and 5 pN. The transitions systematically change with applied force: At low forces, the interface is predominantly formed (bound state), while increasing the force increases the fraction of time with an open interface and

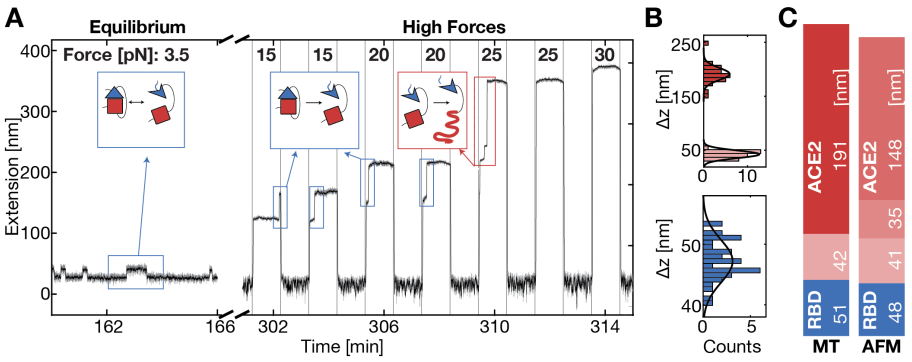

Figure 5.4: SARS-CoV-2 RBD:ACE2 interface opening and unfolding in MT. A Extension-time trace of an RBD:ACE2 tethered ligand construct in MT shows distinct transitions at different levels of constant force. At low forces (labelled "Equilibrium"), we observe stochastic transitions between two extension levels, separated by ΔRBD ≈ 13.5 nm at a force of 3.5 pN. In subsequent measurements at higher forces (labelled "High Forces"), the force is iteratively altered between 0.5 pN (low extension) and increasingly higher forces (indicated at the top). At 15 and 20 pN, the RBD:ACE2 interface ruptures together with a partial RBD unfolding (ΔRBD ≈ 32 nm) and refolds in the subsequent 0.5 pN interval. At 25 pN, ACE2 irreversibly unfolds in two steps, first a smaller one ($\Delta ACE2_{small} \approx$ 30 nm) and then a larger one ($\Delta ACE2_{large} \approx$ 135 nm). Grey trace: 5-frame moving average filtered; Black trace: 40-frame moving average filtered. **B** Histograms of unfolding increments at high forces of the RBD (blue) and the two parts of ACE2 (pink, red) in MT. The histograms are fitted with a Gaussian (solid black line). Some points are outside of the plotting range for clarity but included in the fit. **C** Mean unfolding increments observed for tethered ligand construct with constant forces in MT and with constant loading rate in AFM. The observed increments were transformed into contour lengths using a WLC model, assuming a persistence length of 0.5 nm in MT and 0.365 nm in the AFM. Values ± standard deviation for the increments in MT are: ΔRBD = (51 ± 10.8) nm, $\Delta ACE2_1$ = (42 ± 5.5) nm, Δ $ACE2_{combined}$ = (191 ± 18.7) nm. Values for the increments in the AFM are: ΔRBD = 48 nm, $\Delta ACE2_1$ = 41 nm, Δ $ACE2_2$ = 35 nm, and $\Delta ACE2_3$ = 148 nm. Values in B and C correspond to mean values from 42 molecules observed in MT and 127 molecules observed in AFM.

	MT increments (nm)	AFM increments (nm)
ΔRBD	50.7 ± 10.8	48
$\Delta ACE2_1$	42.1 ± 5.5	41
$\Delta ACE2_2$	45.7 ± 14.0	35
$\Delta ACE2_3$	147.6 ± 7.8	148
$\Delta ACE2_{combined}$	191.3 ± 18.7	–

Table 5.1: Increments of high-force transitions in MT and unfolding peaks in the AFM of the SARS-CoV-2 RBD:ACE2 tethered ligand construct. Data are mean and std for 42 molecules in MT and 127 molecules in the AFM. In MT, the $\Delta ACE2_2$ and $\Delta ACE2_3$ are observed separately only in a small sub-population (8 out of 42 molecules). Mostly they are combined into one step $\Delta ACE2_{combined}$. The large error for the smaller intermediate step is due to imprecisions in the increment measurement due to the short lifetime of this state.

a partially unfolded RBD (dissociated state) (Figure 5.5A). Histograms of the tether extension revealed two clearly separated peaks that are fit well by a double Gaussian (Figure 5.5B; black lines). By setting thresholds at the minimum between the extension peaks, we defined populations in the dissociated and bound states. The fraction in the dissociated state (Figure 5.5C; circles), follows a sigmoidal force dependence. The data are well-described by a two-state model (Figure 5.5C; solid line) where the free energy difference between the two states (bound vs. dissociated but still attached to each other with a linker) depends linearly on the applied force F, i.e. $\Delta G = \Delta G_0 - F_{1/2} \cdot \Delta z$, such that the fraction in the dissociated state is

$$f_{diss}(F) = \frac{1}{(1 + e^{\frac{-\Delta z \cdot (F - F_{1/2})}{k_B \cdot T}})} \tag{5.1}$$

where k_B is Boltzmann's constant and T the absolute temperature. $F_{1/2}$ and Δz are fitting parameters that represent the midpoint force, where the system spends half of the time in the dissociated and half of the time in the bound conformation, and the distance between the two states along the pulling direction, respectively. The free energy difference between the bound and dissociated state at zero force is given by $\Delta G_0 = F_{1/2} \cdot \Delta z$ and provides a direct measure of the stability of the binding interface.

From fits of Equation 5.1 to the data for the SARS-CoV-2 RBD:ACE2 construct, we found $F_{1/2}$ = 3.8 ± 0.4 pN and Δz = 10.2 ± 3.7 nm, and, therefore, $\Delta G_0 = F_{1/2} \cdot \Delta z$ = 5.5 ± 2.1 kcal/mol (data are the mean and standard deviation from fits to biological repeats; see Table 5.2 for a summary of all fitted parameters). The value of Δz determined from fitting Equation 5.1 is within experimental error in agreement with the distance between the dissociated and bound states Δz_G= 13.5 ± 1.8 nm determined from fitting two Gaussians to the extension histograms at the equilibrium force $F_{1/2}$ and evaluating the distance between the fitted center positions. The observed Δz is also in excellent agreement with the expected extension change of ≈ 13.4 nm, based on the crystal structure [204] (PDB ID: 6m0j) taking into account the stretching elasticity of the 85 aa protein linker and the unfolding of non-shielded parts of the RBD using the worm-like chain (WLC) model [38;221;222] with a bending persistence length of L_p = 0.5 nm and assuming 0.365 nm/aa.

In addition to providing information on the binding equilibrium, the MT assay gives ac-

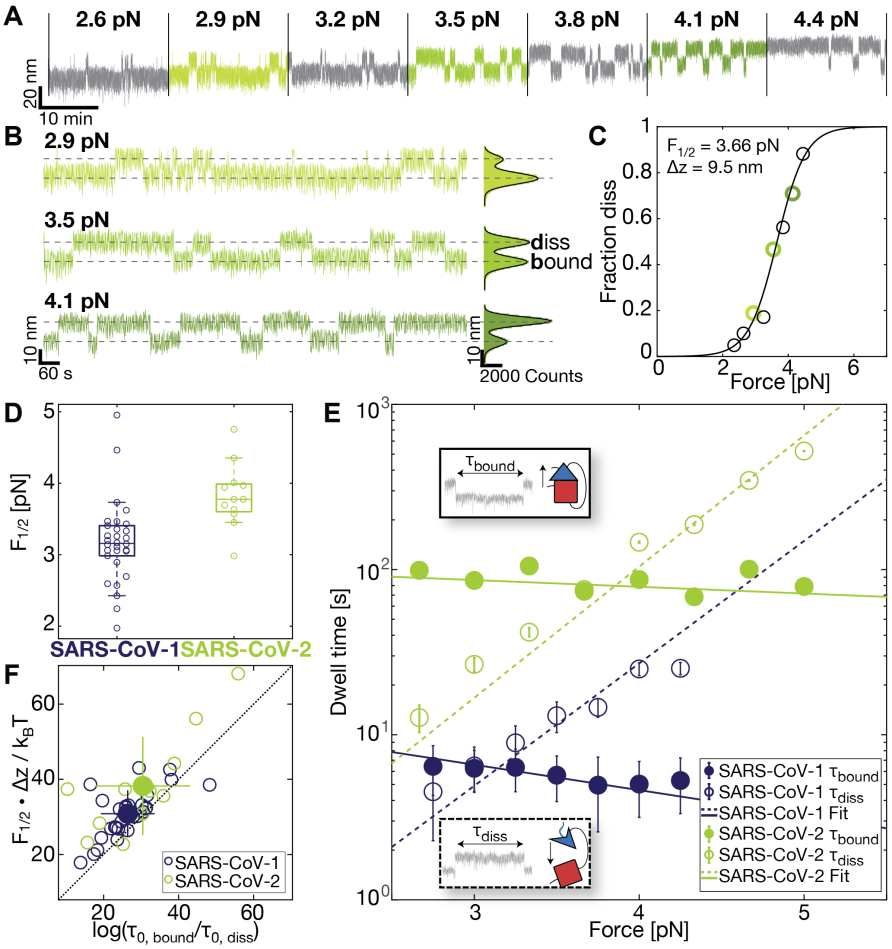

Figure 5.5: Comparison of mechanical stability and kinetics of ACE2 binding to SARS-CoV-1 and SARS-CoV-2 RBD. **A** Extension-time traces at different constant forces for the SARS-CoV-2 RBD:ACE2 fusion construct reveal stochastic transitions between two extension levels, corresponding to the bound and dissociated RBD:ACE2 interface, respectively. Increasing the force increases the fraction of time spent in the dissociated conformation. **B** Expanded views of extensions at three different forces below, at, and above the mid-force from the trace in A show shift towards the dissociated conformation with increasing force. Same color code as in panel A. The "dissociated" and "bound" states are indicated by dashed lines. The histograms of the extensions are fitted with a double Gaussian (solid black lines). **C** The fraction of time in the dissociated conformation determined from extension-time traces (circles; points determined from the traces in panel B are shown with matching color codes). The black line is a fit of Equation 5.1. Fitting parameters $F_{1/2}$ and Δx are shown as an inset. **D** Comparison of the $F_{1/2}$ distribution between SARS-CoV-1 and SARS-CoV-2 reveal a significantly higher force stability of the SARS-CoV-2 RBD:ACE2 bond (p = 0.00124; two-tailed p-test). Data points are the fitted $F_{1/2}$ from independent molecules. Boxes are the median and interquartile range. **E** Dwell times in the dissociated (open circles) and bound state (filled circles) determined from extension-time traces for SARS-CoV-1 (blue) and SARS-CoV-2 (green). Mean dwell times for individual molecules were determined from maximum likelihood fits of a single exponential to the dwell time distributions. The circles and error bars are the mean and standard deviation from log-averaging over 29 (SARS-CoV-1) and 12 (SARS-CoV-2) molecules. Dashed and solid lines correspond to the mean of the exponential fits to the individual dwell times in the bound state and dissociated state, respectively. The insets visualize dwell times in MT time-extension traces. **F** Free energy differences between the bound and dissociated state of the RBD:ACE2 tethered ligand constructs. The free energy differences were obtained from the equilibrium data as $F_{1/2} \cdot \Delta x$ and from the dynamics as $\log(\tau_{0,bound} / \tau_{0,diss})$. The data fall along the 45 degree line (dashed), indicating that the two estimates give consistent values. Comparison of the SARS-CoV-1 and SARS-CoV-2 data reveals a larger free energy difference for SARS-CoV-2, indicating a more stable interface. Distributions and mean values shown in panel D - F are for 29 (SARS-CoV-1) and 12 (SARS-CoV-2) molecules, respectively.

cess to the binding kinetics under force. Analyzing the extension-time traces using the same threshold that was used to determine the fraction dissociated vs. force, we identify dwell times in the dissociated and bound states (Figure 5.10A, B), which are exponentially distributed (Figure 5.10C, D). The mean dwell times in the dissociated state increase with increasing force, corresponding to the intuitive interpretation that the higher the force, the longer it takes for a dissociated receptor:ligand pair to rebind (Figure 5.5E, dashed green line). The mean dwell times in the bound state, on the other hand, decrease with increasing force, albeit only slightly, implying that the higher the force, the shorter the bond stays intact. The dependencies of the mean dwell times on the applied force F are well described by exponential, Arrhenius-like relationships[93]

$$\tau_{diss} = \tau_{0,diss} \cdot e^{\frac{\Delta z_{diss} \cdot F}{k_B \cdot T}} \text{ and } \tau_{bound} = \tau_{0,bound} \cdot e^{\frac{-\Delta z_{bound} \cdot F}{k_B \cdot T}} \tag{5.2}$$

where the fitting parameters $\tau_{0,diss}$ and $\tau_{0,bound}$ are the lifetimes of the dissociated and bound conformation in the absence of force and Δz_{diss} and Δz_{bound} are the distances to the transition state along the pulling direction.

The parameters Δz_{diss} and Δz_{bound} quantify the force-dependencies of the lifetimes of the respective states, and the slopes in the $\log(\tau_{diss/bound})$ vs. F plots (Figure 5.5E) are given by $\Delta z_{diss/bound} / k_B T$. Δz_{bound} is smaller than Δz_{diss} (by more than a factor of ~ 5), i.e. dissociation of the bound complex is less force-sensitive than rebinding from the dissociated conformation. The different force sensitivities can be rationalized from the underlying molecular processes: The bound complexes feature protein-protein interactions that will break over relatively short distances; in contrast, the dissociated conformations involve flexible peptide linkers that make rebinding from the dissociated states more force-dependent. The sum of Δz_{diss} and Δz_{bound} is 7.9 ± 5.1 nm and, within experimental error, equal to Δz obtained from fitting Equation 5.1, which indicates a single major energy barrier separating the bound and the dissociated states.

The extrapolated lifetimes at zero force of the bound conformations $\tau_{0,bound}$ are in the range of 115 s for SARS-CoV-2. In comparison, the lifetimes of the dissociated states in the

absence of load $\tau_{0,diss}$ are much shorter, similar to $\sim$ 0.07 s (Table 5.2). The extrapolated lifetimes at zero force provide an alternative route to computing the free energy difference between the previously described dissociated and bound states at F = 0, which is given by $\Delta G_{0,tau} = k_B T \cdot \log(\tau_{0,diss}/\tau_{0,bound})$. We find good agreement, within experimental error, between the free energy differences $\Delta G_{0,tau}$ determined from the extrapolated lifetimes and the values $\Delta G_0 = F_{1/2} \cdot \Delta z$ from Equation 5.1 (Table 5.2, Figure 5.5F), providing a consistency check between equilibrium and kinetic analysis. The results show that studying our tethered ligand assay in MT can yield consistent information on the binding equilibrium and on the interaction kinetics under external force.
Comparing the extrapolated lifetimes at zero force and the distances to the transition state obtained from MT measurements to values obtained from fitting a dynamic force spectrum recorded with the AFM, yields reasonable agreement (Figure 5.11). This suggests that both techniques probe similar pathways.

5.2.6 SARS-CoV-2 attachment is more stable and longer-lived than SARS-CoV-1 under constant load

A construct using the same 85 aa linker and attachment geometry, but the SARS-CoV-1 RBD instead of SARS-CoV-2 RBD, shows a qualitatively very similar force-response in MT, with stochastic transitions between a bound and a dissociated conformation at an equilibrium force below 5 pN and ACE2 unfolding at forces higher than 25 pN. The increments from unfolding the tethered ACE2 are in excellent agreement both with the increments from the ACE2 unfolding of the SARS-CoV-2 tethered ligand construct in MT and from the AFM ACE2 unfolding (Figure 5.9). Furthermore, they happened at comparable forces as in the SARS-CoV-2 tethered ligand construct and single ACE2 in MT. As for the SARS-CoV-2 tethered ligand construct, the molecules for equilibrium and kinetic analysis of the SARS-CoV-1 RBD:ACE2 bond could thus be selected based on the molecular fingerprint of ACE2 unfolding and directly compared to SARS-CoV-2 tethered ligand constructs.
From fits of Equation 5.1, we found $F_{1/2}$ = 3.2 ± 0.6 pN, Δz = 9.7 ± 1.7 nm and thus ΔG_0 = 4.4 ± 1.1 kcal/mol for the SARS-COV-1 RBD:ACE2 tethered ligand construct (Table 5.2). The length increment Δz is again, within experimental error, in good agreement with the value determined from fitting two Gaussians to the extension histogram near the midpoint of the transition (Δz_G = 11.3 ± 1.7 nm at $F_{1/2}$). The slightly shorter extension increment upon dissociation for the SARS-CoV-1 construct compared to SARS-CoV-2, despite using the same 85 aa linker and a very similar crystallographic geometry is mostly due to the smaller extension of the WLC at the lower midpoint force for SARS-CoV-1. Comparing the two lengths after contour length transformation yields $\Delta z_{SARS-CoV-1RBD,WLC}$ = 51.2 ± 7.9 nm and $\Delta z_{SARS-CoV-2RBD,WLC}$ = 50.3 ± 7.7 nm, in agreement, within error. In contrast, the SARS-CoV-1 RBD:ACE2 interface shows a significantly lower midpoint force $F_{1/2}$ than the SARS-CoV-2 RBD:ACE2 bond (Figure 5.5D; p = 0.0029 from a two-sample t-test), in line with the lower unbinding forces for SARS-CoV-1 observed in the AFM (Figure 5.2B, C) and SMD simulations. The difference also manifests in a reduced mean free energy of the SARS-CoV-1 RBD:ACE2 bond computed both from the midpoint forces and distances as well as from the rates (Figure 5.5F). Comparing the lifetimes of the bound and dissociated states (Figure 5.5E, blue and green lines) and extrapolating the mean lifetimes to zero force yields no significant difference between the lifetimes in the dissociated conformation (Figure 5.5E, dashed lines, $\tau_{0,diss,SARS-CoV-1}$ = 0.03 ± 0.05 s, $\tau_{0,diss,SARS-CoV-2}$ = 0.07 ± 0.19 s, p = 0.293). In contrast, the extrapolated lifetime in the bound state at zero force is significantly different at α = 0.1 ($\tau_{0,bound,SARS-CoV-1}$ = 19.0 ± 24.8 s, $\tau_{0,bound,SARS-CoV-2}$ = 114.5 ± 278.8 s, p = 0.072) and more than six times higher for the SARS-CoV-2 RBD, indicating a lower dissociation rate from ACE2. Furthermore, the lifetime of the SARS-CoV-2 RBD:ACE2 bond decreases less with force, i.e. has a shallower slope than the bond lifetime of SARS-CoV-1 RBD:ACE2. Therefore, the longer lifetime of the SARS-CoV-2 bond compared to SARS-CoV-1 becomes even more pronounced under mechanical load.

	SARS-CoV-2	SARS-CoV-1
$F_{1/2}$	3.8 ± 0.4 pN	3.2 ± 0.6 pN
Δz (from fit of Equation 5.1)	10.2 ± 3.7 nm	9.7 ± 1.7 nm
Δz_G (from fit of two Gaussians)	13.5 ± 1.8 nm	11.3 ± 1.7 nm
ΔG_0 (= $\Delta z \cdot F_{1/2}$)	5.5 ± 2.1 kcal/mol	4.4 ± 1.1 kcal/mol
$\tau_{0,diss}$	0.07 ± 0.19 s	0.03 ± 0.05 s
$\tau_{0,bound}$	114.5 ± 278.8 s	19.0 ± 24.8 s
$\Delta G_{0,tau}$ (= $k_B T \cdot \log(\tau_{0,diss}/\tau_{0,bound})$)	4.4 ± 1.7 kcal/mol	3.8 ± 2.0 kcal/mol
$\Delta z_{0,diss}$	7.5 ± 2.6 nm	7.0 ± 1.8 nm
$\Delta z_{0,bound}$	0.4 ± 2.5 nm	1.5 ± 1.6 nm

Table 5.2: Interaction parameters for ACE2 and SARS-CoV-2 or SARS-CoV-1 RBD determined using the MT tethered ligand assay. Data are the mean and std from N = 12 and 29 molecules, respectively.

5.2.7 Magnetic tweezers provide a sensitive assay to study molecules that block the RBD:ACE2 interaction

Apart from providing a tool to assess equilibrium binding and kinetics, investigation of the tethered ligand assay in MT also allows us to probe the influence of other binding partners on the bond dynamics. For this purpose, the equilibrium bond dynamics are first recorded under standard conditions before exchanging the buffer and conducting the same experiment in the presence of the compound of interest. As a proof-of-concept, we investigate the influence of soluble ACE2 on the bond dynamics (Figure 5.6). First, we recorded the equilibrium binding of the SARS-COV-2 RBD and the tethered ACE2 in a short measurement between 3.0 and 4.5 pN, observing the characteristic transitions between the dissociated and bound conformation (Figure 5.6A, "Without free ACE2"). We then added 3.8 μM free, soluble ACE2 and increased the force to 7 pN, to ensure the dissociation between the tethered receptor:ligand pair and enable binding of soluble ACE2, before conducting the same measurement in the presence of the soluble ACE2 (Figure 5.6A, "With free ACE2"). At the same forces, the system is now predominantly in the dissociated conformation, rebinding only occasionally. This matches the interpretation of soluble ACE2 binding to the RBD and thus preventing the tethered ACE2 from binding and transitioning into the bound conformation. Overall, we find that the number of dissociation and rebinding events is significantly reduced in the presence of soluble ACE2 (Figure 5.6B, p = 0.022 from a repeated measures t-test over 6 independent molecules).

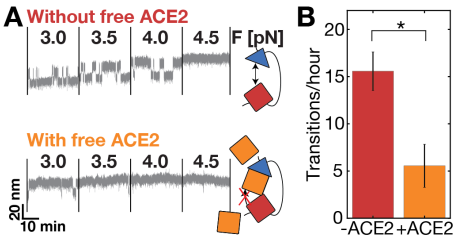

Figure 5.6: Blocking of ACE2:SARS-CoV-RBD bond with soluble ACE2. A Extension-time traces of a SARS-CoV-2 tethered ligand construct in MT around the equilibrium force, first without and then in the presence of soluble ACE2 (∼ 3.8 μM) in solution. Without soluble ACE2 (top), the RBD:ACE2 bond frequently dissociates and rebinds (corresponding to changes in the extension level). In the presence of soluble ACE2 (bottom), the bond is significantly longer dissociated already at low forces, rebinding only a few times (corresponding to a longer time spent at the level of high extension). **B** Quantification of mean number of transitions per hour during the forceramp shown in A with and without soluble ACE2 for 6 independent molecules. Error bars indicate standard error of the mean. The difference is statistically significant with p = 0.0218 (two-tailed t-test for two dependent means).

5.2.8 Molecular modeling provides insights into the molecular origin of higher mechanostability of SARS-CoV-2

In all simulations and experiments, the SARS-CoV-2 RBD:ACE2 complex was shown to be more resilient to mechanical load than the same complex from SARS-CoV-1. To investigate the origin of the higher mechanostability of the SARS-CoV-2 complex, we designed an *in-silico* protein chimera by combining the SARS-CoV-1 RBD core with SARS-CoV-2 RBD residues located on the RBD:ACE2 interface. Our protein chimera was built using a homology modeling approach, similar to the protocol previously developed to investigate mechanostable protein folds[223]. We compared the sequence and structural differences between SARS-CoV-1 and SARS-CoV-2 by investigating both RBD:ACE2 interfaces in PDBsum[224] and VMD[22]. While both RBDs have high structural similarity (with a root mean square deviation of 1.39 Ångstroms), they only share 72% sequence identity, revealing a total of 64 residue changes between SARS-CoV-1 and SARS-CoV-2 RBDs. After selecting the RBD amino acid residues that form the interface with ACE2 in both structures, we identified 12 residues that were different in the two SARS' RBDs. Using the structure of SARS-CoV-1 as template (PDB ID: 2ajf), Modeller[225] was employed to mutate the 12 selected residues (Table 5.3), to create a protein chimera that is identical to the SARS-CoV-1 sequence except for the 12 mutations that make the interface sequence similar to that of SARS-CoV-2 (Figure 5.3D).

The RBD chimera enables us to investigate the impact of the interface residues on the mechanism of force stability of the RBD-ACE2 complex (Figure 5.3C-F). Although interface residues are key players in the binding affinity of proteins[226], the same does not necessarily hold true for protein interface mechanostability, where unbinding pathways are frequently determined by complex force propagation profiles[227]. Strikingly, SMD simulations of the chimeric protein reveal rupture forces that are only 5% weaker than the SARS-CoV-2 complex (Figure 5.3C), suggesting that the 12 amino acid substitutions in the RBD of SARS-CoV-1 are enough to achieve similar force resilience as the SARS-CoV-2 complex. This observation is noteworthy because it shows that the modified surface residues alone were enough to significantly change the complex's resistance to mechanical stress.

To probe the contribution of the individual amino acid modifications, we employed a generalized correlation approach[228] to produce a detailed analysis of the contact network during the pulling simulations. In short, we calculate the correlation between the movement of residues to determine how cooperative their motion is. The higher the correlation, the more relevant their interaction is for the stability of the complex (Figure 5.3E,F). This analysis revealed that, at high forces, only 7 of these 12 amino acids remain in close proximity to ACE2, directly contributing to the stabilization of the complex. The 7 modifications are indicated in Figure 5.3E. Moreover, the analysis revealed that the 12 substitutions drastically increase the overall correlation between the spike residues and the two alpha helices of ACE2's contact surface (see Figure 5.12). Furthermore, the analysis also revealed that residue N479 in the chimera and its equivalent Q493 in the SARS-CoV-2 RBD plays a much bigger role in stabilizing the complex than in the SARS-CoV-1 RBD. This amino acid residue has been shown to be a key player in the binding of RBD to ACE2[229]. We could also observe that correlations between residues from the chimera and ACE2 consistently increased in the region around modified residue N487. The equivalent residue in SARS-CoV-2 RBD, N501, is mutated in several SARS-CoV-2 variants of concern. We note that for SARS-CoV-2 the interactions between RBD and the N-terminal helices of ACE2 (residues 24-83) are found to be significantly more stable than for SARS-CoV-1, as indicated by the stronger correlations in this region (Figure 5.3E, F).

5.3 Discussion

In order to infect human host cells, SARS coronaviruses engage with receptors in the turbulent and dynamic environment of the respiratory tract, where forces impact their anchoring. Force-stability of the RBD:ACE2 bond thus plays a crucial role for the virus to be able to infect host cells efficiently. Understanding the binding mechanism and being able to assess the stability of the RBD:ACE2 bond – also under the influence of external agents – opens opportunities to develop and test drugs and predict fitness advantages of mutated RBDs. Here, we have reported a tethered ligand assay to study and characterize the stability and binding mechanism of the SARS-CoV RBD:ACE2 bond with single-molecule precision.

Using the unfolding of ACE2 as a fingerprint pattern, we were able to bring together equilibrium studies using MT, high force rupture analysis carried out with an AFM, and molecular insights of the unfolding process obtained by SMD simulations. Combining these approaches, we were able to cover a large range of physiologically relevant forces. We compared the force-stability of the bond of the SARS-CoV-1 and SARS-CoV-2 RBD to human receptor ACE2 and found higher force stability for the novel coronavirus throughout all force regimes. This is in line with previously published *in-silico* and *in vitro* force spectroscopy studies that found a 20 to 40% difference in the force-stability of SARS-CoV-1 and SARS-CoV-2 RBD:ACE2 interactions [230;231]. The higher force stability of SARS-CoV-2 engaging ACE2 might contribute to the fact that SARS-CoV-2 more frequently infects the upper respiratory tract in addition to deep lung tissue compared to the 2002 SARS variant [198;199], which in turn appears to increase its population spread and to make the new virus harder to contain. Higher force stability might, therefore, increase transmissibility, which could also play a role in understanding fitness advantages of newly evolving SARS-CoV-2 variants.
In addition to force stability, we analyzed the binding kinetics of the complex under force obtained by MT measurements, finding an order of magnitude higher bond lifetime of the SARS-COV-2 RBD construct compared to the same construct with the SARS-COV-1 RBD at their respective equilibrium forces. Extrapolating these lifetimes to zero force yields a more than 5-fold higher bond lifetime ($\sim$ 115 s) for SARS-CoV-2 than for SARS-CoV-1 ($\sim$ 20 s). We can quantitatively relate our results to studies that have reported equilibrium dissociation constants and rates for the ACE2 interactions with SARS-CoV-1 and SARS-CoV-2 using traditional binding assays. While the values reported in the literature vary significantly, likely due to the different experimental methods and sample immobilization strategies used, clear and consistent trends can be identified. The zero-force lifetimes of the bound complex determined in our assay correspond to rates of $k_{off} \sim 5 \cdot 10^{-2}$ s^{-1} for SARS-CoV-1 and $\sim 8.7 \cdot 10^{-3}$ s^{-1} for SARS-CoV-2, well within the ranges of reported $k_{sol,off}$ values in literature [194;204;232–235] (for an overview see Table 5.4). Our value for the off-rate of SARS-CoV-2 RBD bound to ACE2 is also in excellent agreement with the value of $(8 \pm 5) \cdot 10^{-3}$ s^{-1} extrapolated from previous AFM force spectroscopy experiments [236].
In contrast to the difference in off-rates between SARS-CoV-1 and SARS-CoV-2, the (bimolecular) on-rates reported in literature are similar for both SARS variants, in the range of $\sim 10^5$ $M^{-1}s^{-1}$. Consistently, our tethered ligand assay finds similar (unimolecular) on-rates on the order of ~ 10 s^{-1}. Even though both bulk and single-molecule assays find similar on-rates for the two SARS viruses, the absolute values are not comparable, as solution-based assays determine bulk on-rates (with units of $M^{-1}s^{-1}$), whereas our tethered ligand assay measures molecular on-rates (in s^{-1}). To relate the two quantities, an effective concentration c_{eff} can be introduced, such that $k_{sol,on} = k_{on}/c_{eff}$ [205;237;238]. The data imply an effective concentration at zero force on the order of 35 μM for the construct with an 85 aa linker, in the range of concentrations found for other tethered ligand protein systems [237;239]. Under force, the complex will spend more time in the dissociated state (i.e. the force-dependent effective concentration decreases with applied force), which also explains why we observe blocking with soluble ACE2, even though the concentration of soluble ACE2 used is $\sim$ 10-fold lower (3.8 μM) than the effective tethered ACE2 concentration at zero force. Under force, the complex will still spend considerable time in the dissociated state, allowing soluble ACE2 from the solution to bind. Once soluble ACE2 is bound, it will be bound on average for $\tau_{0,bound} \sim 115$ s, since it experiences no force, and therefore bias the system towards the open conformation.
With our tethered ligand assay, we investigated the interaction of an individual RBD:ACE2 interaction. On the virus membrane of SARS-CoV particles, however, spike proteins are trimeric and multiple trimers are available for binding ACE2, which is known to cluster on the cell surface [192]. Previous studies suggest that at high loading rates the force stability increases linearly with the number of interaction partners, while at lower loading rates a square root or logarithmic scaling is observed [240;241]. Multiple parallel interactions between RBDs and ACE2 could thus significantly strengthen the overall force stability, in particular at high loading rates. Our data suggest that if held in close proximity, SARS-CoV-2 RBDs can engage ACE2 rapidly, within $\tau_{0,diss} \sim 70$ ms. While our assay is different from the situation *in vivo*, the tethered ligand mimics the effect of pre-formed interactions by other RBDs on the same SARS-CoV-2 particle, which suggests that multivalent interactions between the virus and its host cell could form rapidly after an initial binding event,

additionally providing increased stability of the interaction. We estimate the concentration of Spike *in vivo* as $\sim$ 1 pM, based on $7 \cdot 10^6$ viral copies in ml sputum [198] and 100 Spike proteins per virus [7]. This estimated bulk protein concentration *in vivo* is much lower than the dissociation constants reported, which are in the range $K_d \sim$ 1-100 nM for the SARS-CoV-2 RBD binding to ACE2 and 10-fold lower for SARS-CoV-1 (Table 5.4), suggesting that multivalency might be critical for efficient viral binding. The rapid binding of RBDs held in proximity to ACE2 revealed by our assay might, therefore, be an important component of SARS-CoV-2 infections. In addition, we can demonstrate and quantify blocking of the RBD:ACE2 bond. We anticipate that it will be a powerful tool to investigate the influence of mutations on interface stability and to assess the mode of action of potential therapeutic agents such as small molecules [242], neutralizing antibodies [232;243], nanobodies [235;244;245], or designer proteins [246;247] that interfere with S binding to ACE2. In particular, the tethered ligand assay could go beyond standard bulk assays and reveal heterogeneity, include avidity effects, the ability of direct displacement, and determine drug residence times, in addition to affinities. Investigating how mutations in the RBD affect force-stability might give valuable insights into reasons for fitness advantages of newly emerging variants and might even provide a tool to predict those advantages based on increased force-stability.

5.4 Materials and Methods

All chemicals used, if not further specified, were supplied by Carl Roth (Karlsruhe, Germany) or Sigma-Aldrich (St. Louis, MO, USA).

5.4.1 Cloning and protein construct design

Constructs for ACE2-linker-RBD of SARS-CoV-1 were designed in SnapGene Version 4.2.11 (GSL Biotech LLC, San Diego, CA, USA) based on a combination of the ACE2 sequence from Komatsu et al. [248] available from GenBank under accession number AB046569 and the SARS-CoV-1 sequence from Marra et al. [249] available from GenBank under accession number AY274119. The crystal structure by Li et al. [211] available from the Protein Data Bank (PDB ID: 2ajf) was used as a structural reference. The linker sequence and tag placement were adapted from Milles et al. [250]. The linker sequence is a combination of two sequences available at the iGEM parts databank (accession numbers BBa_K404300, BBa_K243029). We used a similar approach to design the fusion protein with the sequence of the RBD of SARS-CoV-2 from the sequence published by Wu et al. [251] available at GenBank under accession number MN908947. A 6x histidine (His) tag was added for purification. In addition, tags for specific pulling in magnetic tweezers and the atomic force microscope were introduced: a triple glycine for sortase-catalyzed attachment on the N-terminus and a ybbR-tag, AviTag, and Fgɣ tag on the C-terminus. In summary, the basic construct is built up as follows: MGGG-ACE2-linker-RBD-6xHIS-ybbR-AviTag-Fgɣ.
The constructs were cloned using Gibson assembly from linear DNA fragments (GeneArt, ThermoFisher Scientific, Regensburg, Germany) containing the sequence of choice codon-optimized for expression in *E. coli* into a Thermo Scientific pT7CFE1-NHis-GST-CHA Vector (Product No. 88871). The control constructs with a different sized linker and just ACE2 were obtained by blunt end cloning adding additional residues to the linker, or deleting parts of the construct. Replication of DNA plasmids was achieved by transforming in DH5-Alpha Cells and running overnight cultures with 7 ml lysogeny broth with 50 µg/ml carbenicillin. Plasmids were harvested using a QIAprep® Spin Miniprep Kit (QIAGEN, Germantown, MD, USA, # 27106). The used plasmids for force-spectroscopy measurements were deposited with and can be ordered from Addgene (www.addgene.org):

Plasmid	ID
pT7CFE1-MGGG-ACE2-link33nm-SARS-CoV-1-RBD-HIS-ybbr-AviTag-Fgɣ	174831
pT7CFE1-MGGG-ACE2-link33nm-SARS-CoV-2-RBD-HIS-ybbr-AviTag-Fgɣ	174832
pT7CFE1-MGGG-ACE2-link42nm-SARS-CoV-1-RBD-HIS-ybbr-AviTag-Fgɣ	174833
pT7CFE1-MGGG-ACE2-HIS-ybbr-AviTag-Fgɣ	174835

5.4.2 In vitro protein expression

Expression was conducted according to the manual of 1-Step Human High-Yield Mini *in vitro* translation (IVT) kit (# 88891X) distributed by ThermoFisher Scientific (Pierce Biotechnology, Rockford, IL, USA). All components, except 5X dialysis buffer, were thawed on ice. 5X dialysis buffer was thawed for 15 minutes and 280 µl were diluted with 1120 µl nuclease-free water to obtain a 1X dialysis buffer. The dialysis device provided was placed into the dialysis buffer and kept at room temperature until it was filled with the expression mix.
For preparing the IVT expression mix, 50 µl of the HeLa lysate was mixed with 10 µl of accessory proteins. After each pipetting step, the solution was gently mixed by stirring with the pipette. Then, the HeLa lysate and accessory proteins mix was incubated for 10 minutes. Afterwards, 20 µl of the reaction mix was added. Then, 8 µl of the specifically cloned DNA (0.5 µg/µl) was added. The reaction mix was then topped off with 12 µl of nuclease-free water to obtain a total of 100 µl. This mix was briefly centrifuged at 10 000 g for 2 minutes. A small white pellet appeared. The supernatant was filled into the dialysis device placed in the 1X dialysis buffer. The entire reaction was then incubated for 16 h at 30°C under constant shaking at 700 rpm. For incubation and shaking a ThermoMixer comfort 5355 (Eppendorf AG, Hamburg, Germany, # 5355) with a 2 ml insert was used. After 16 h the expression mix was removed and stored in a protein low binding reaction tube on ice until further use.

5.4.3 Protein purification

Purification was conducted using HIS Mag Sepharose® Excel beads (Cytiva Europe GmbH, Freiburg, Germany, # 17371222) together with a MagRack™ 6 (Cytiva Europe GmbH, Freiburg, Germany, # 28948964) closely following the provided protocol. Bead slurry was mixed thoroughly by vortexing. 200 µl of homogenous beads were dispersed in a 1.5 ml protein low binding reaction tube. Afterwards, the reaction tube was placed in the magnetic rack and the stock buffer was removed. Next, the beads were washed with 500 µl of HIS wash buffer (25 mM TRIS-HCl, 300 mM NaCl, 20 mM imidazole, 10% vol. glycerol, 0.25% vol. Tween 20, pH 7.8). Expressed protein from IVT was filled to 1 000 µl with TRIS buffered saline (25 mM TRIS, 72 mM NaCl, 1 mM $CaCl_2$, pH 7.2) and mixed with freshly washed beads. The mix was incubated in a shaker for 1 h at room temperature. Subsequently, the reaction tube was placed in the magnetic rack and the liquid was removed. The beads were washed three times with wash buffer, keeping the total incubation time to less than 1 min. Remaining wash buffer was removed and 100 µl elution buffer (25 mM TRIS-HCl, 300 mM NaCl, 300 mM imidazole, 10% vol. glycerol, 0.25% vol. Tween 20, pH 7.8) were added to wash protein off the beads. The bead elution buffer mix was then incubated for one minute with occasional gentle vortexing. Afterwards, the reaction tube was placed in the magnetic rack again to remove the eluted protein. This step was repeated for a second and third elution step. The buffer of the eluted protein was exchanged to TRIS buffered saline (TBS - 25mM TRIS, 72mM NaCl, 1mM $CaCl_2$ at pH 7.2) in 0.5 ml 40k Zeba spin columns distributed by ThermoFisher Scientific (Pierce Biotechnology, Rockford, IL, USA, # 87767) or 0.5 ml 50k Amicon Centrifugal Filters (Merck KGaA, Darmstadt, Germany, #UFC5050BK). Concentrations were determined photospectrometrically with a NanoDrop and aliquots were frozen in liquid nitrogen.

5.4.4 Atomic force microscopy setup

The AFM force spectroscopy datasets were collected on a custom-built AFM based on an MFP3D controller (Asylum Research, Santa Barbara, CA, USA). The AFM head was kept stationary, while the sample stage was moved by an xyz-movable piezo-driven sample stage (P-313.30D - P-313 PicoCube® XY(Z)-Piezoscanner - Physik Instrumente PI GmbH & Co KG, Karlsruhe, Germany) together with a high-precision xy-nanopositioner (P-621.2CD - Physik Instrumente PI GmbH & Co KG, Karlsruhe, Germany). Unfolding traces were recorded by (i) approaching the functionalized sample surface onto the functionalized cantilever until the cantilever was indented with 180 pN into the surface, allowing the linkage between ClfA:Fgγ to form; (ii) retraction of the cantilever with 0.8 µm/s (except for the dynamic force spectrum recorded at additional speeds of 0.4 µm/s, 1.6 µm/s and 3.2 µm/s)

while recording the deflection of the cantilever to obtain a force-distance curve of the mechanical response of the protein probed; (iii) after the surface moved 500 nm in z direction (assuming a complete unfolding) a new position was set by the xy-stage, moving the sample surface horizontally in steps of 100 nm in a spiral pattern and starting a new acquisition process in step (i). This process was operated by a software programmed in IgorPro6 (Wavemetrics, Portland, OR, USA) and the unfolding curves obtained were saved in hdf5 files.
For calibration, the Inverse Optical Cantilever Sensitivity (InvOLS) was obtained by 25 hard indentation curves allowing to correlate the movement of the cantilever with the voltage signal recorded on a quadrant photodetector. The spring constant of the cantilevers were calibrated based on thermal fluctuations using the equipartition theorem method[252;253] resulting in spring constants around 100 pN/nm. The spring constant per measurement are listed below. To be able to directly compare force values recorded with different cantilevers, the ACE2 fingerprint pattern was used to normalize the force histograms.
In the course of a measurement around 50 000 - 400 000 force-distance traces were recorded. Most force-distance traces didn't show any interactions and only a fraction showed specific single-molecule unfolding events.
List of spring constants (k) of cantilevers used for individual measurements used for comparing forces and contour length increments:
SARS-CoV-2 measurement - Figure 2A (exemplary curve), C and Figure 5.7: k = 101.4 pN/nm
SARS-CoV-1 short linker (33 nm) measurement - Figure 5.2B: k = 108.0 pN/nm
SARS-CoV-1 long linker (42 nm) measurement - Figure 5.2B (top only): k = 109.5 pN/nm
Ectodomain of ACE2 - Figure 5.9: k = 96.0 pN/nm
Dynamic force spectrum - Figure 5.11 k = 97.6 pN/nm

5.4.5 AFM surface and cantilever preparation

Cantilevers and sample surfaces were both silanized for further functionalization steps. Surface attachment and linkage was obtained by 5 000 Da heterobifunctional NHS-PEG-Maleimide spacers (Rapp Polymere, Tübingen, Germany, # 135000-65-35). Specific protein attachment was achieved using a sortase-mediated reaction on the sample surface and an 4'-phosphopantetheinyl transferase (sfp)-mediated reaction for the AFM cantilever ensuring a well-defined pulling geometry.
The cantilevers (BioLever mini, BL-AC40TS) were oxidized in an UV ozone cleaner (UVOH 150 LAB; FHR Anlagenbau GmbH, Ottendorf-Okrilla, Germany) and after that silanized for 2 min in 50% (vol/vol) ethanol and (3-aminopropyl)dimethylethoxysilane (abcr GmbH, Karlsruhe, Germany, AB146193, CAS 18306-79-1). To rinse off the residual silane cantilevers were stirred in 2-Propanol (IPA) and in MilliQ. After that, the cantilevers were dried at 80°C for 30 min. The heterobifunctional PEG spacers were solved in 100 mM HEPES (pH 7.4) to 50 mM. The cantilevers were incubated in droplets of PEG dissolved in 100 mM HEPES (pH 7.4) to 50 mM for 1 h. After a rinsing step the cantilevers were incubated in 20 mM Coenzyme A (CoA) (# 234101-100MG, Calbiochem distributed by Sigma-Aldrich) dissolved in coupling buffer (50 mM Disodium phosphate buffer, 50 mM NaCl, 10 mM EDTA, pH 7.2) for 1 h. Droplets with a mixture of 2 µM sfp, 100 mM $MgCl_2$ and 60 µM ClfA (in TBS buffer) were prepared to attach the ybbR tag of ClfA specifically to CoA. The cantilevers were incubated in these droplets for at least 1.5 h. To prepare the cantilevers for the measurement they were rinsed and stored in TBS.
Glass surfaces were cleaned by sonication in 50% (vol/vol) IPA in MilliQ for 15 min. To prime the surfaces for silanization they were incubated for 30 min in a solution of 50% (vol/vol) hydrogen peroxide (30%) and sulfuric acid. To wash off the residual solution the surfaces were washed in MilliQ and dried under a constant stream of N_2. For the actual silanization step the surfaces were incubated in 1.8% (vol/vol) ethanol and (3-aminopropyl)dimethylethoxysilane (abcr GmbH, Karlsruhe, Germany, AB146193, CAS 18306-79-1). Afterwards, the surfaces were washed with IPA and MilliQ and dried at 80°C for 45 min. To minimize sample volumes for the following incubations, silicone incubation wells (CultureWell reusable gaskets, Grace Bio-Labs, Bend, OR, USA, # 103250) were placed centered on the surfaces. Then heterobifunctional PEG spacers were dissolved in 100 mM HEPES (pH 7.4) to 50 mM and applied to the wells for 1 h. After that, the surfaces were rinsed with MilliQ and 5 mM Cys-LPETGG in coupling buffer (sodium phosphate, pH 7.2) was pipetted into the wells and incubated for 2 h. After washing the wells, the purified tethered

ligand protein was applied in solution together with 1 μM sortase and 10 mM $CaCl_2$ for 25 min. After incubation, the incubation wells were removed and the surface was rinsed with 10 ml TBS.
To validate the functionalization of the cantilever and the surfaces for each measurement (for each new surface and cantilever), a control surface of the same surface batch was prepared with a GGG-ddFLN4-Fgɣ construct using identical procedures as for the sample surface.

5.4.6 AFM data analysis

Data analysis was carried out in custom Python 2.7 (Python Software Foundation, Wilmington, DE, USA) scripts[254–256] and Python 2.7-based Jupyter notebooks[257].
The rupture forces were detected by a peak detection highlighting drops above the baseline noise level in total variation denoised (TVD) force-distance traces. A linear slope in force vs. time was used to determine the loading rate, taking into account 4 nm before the rupture event. Rupture forces of respective domains in the unfolding pattern were binned to histograms and fitted with the Bell-Evans model yielding the most probable rupture force[153].
All curves showing the characteristic unfolding pattern of the tethered ligand protein were aligned (accounting for the inhomogeneity in PEG lengths) and assembled to heatmaps to visualize the recurring, characteristic unfolding pattern. The heatmaps contain the raw unfolding curves in force-distance space binned in 90 bins in both x- and y-axis between -10 pN to 60 pN and -10 nm to 300 nm.
To transform force-extension data into contour length space[217], a three-regime model by Livadaru et. al[258] assuming a stiff element of b = 0.11 nm and bond angle ɣ = 41° was used. A Gaussian kernel density estimate, with a bandwidth of 4 nm, was applied to the gained contour length data to obtain density curves of each trace. These curves were aligned in contour length space using the following process previously described by Baumann et al.[215]: "the full set of transformed force-distance curves is aligned to a random curve from this data set according to least residual in cross-correlation. This process results in a first superposition which is used as a template in a second iteration of this process. Again, all contour-length transformed curves are aligned to a template curve but this time to the one formed by the first iteration. This two-step approach diminishes biasing effects given by the choice of the random curve used for initial alignment. Contour lengths of the individual domains are determined by a Gaussian fit of each determined peak and subtraction of the respective fitted means." The datasets can be found at figshare together with all analysis scripts at github executable with all datasets in google colab.

5.4.7 Molecular dynamics simulation

To examine the stability of the protein complex under mechanical load, we carried out steered molecular dynamics simulations employing NAMD 3[219]. Simulations were prepared using VMD[22] and its QwikMD[186] molecular dynamics interface. The structure of the complexes was prepared following established protocols[227]. For the SARS-CoV-1 RBD:ACE2 complex, the structure had been solved by X-ray crystallography at 2.90 Å resolution and is available at the protein data bank (PDB ID: 2ajf)[211]. The SARS-CoV-2 RBD:ACE2 complex had been similarly solved by X-ray crystallography, at 2.45 Å resolution, and is available at the protein data bank (PDB ID: 6m0j)[204]. SARS-CoV-1 RBD or SARS-CoV-2 RBD and the ectodomain of human ACE2 were joined by flexible polypeptide linkers. The structure of the complexes with the linkers was obtained using Modeller[225] and fitted with VMD[22]. Disulfide bonds were included following the literature information[218].
Employing advanced run options of QwikMD, structural models were solvated and the net charge of the proteins was neutralized using a 75 mM salt concentration of sodium chloride, which were randomly arranged in the solvent. The overall number of atoms included in MD simulations varied from approximately 200 000 in the RDB:ACE2 systems with no linker, to nearly 4 000 000 in the systems RDB:ACE2 connected by flexible polypeptide linkers. All simulations were performed employing the NAMD molecular dynamics package[219], and run on NVIDIA DGX-A100-based cluster nodes at Auburn University. The CHARMM force field[187;188] along with the TIP3 water model[259] was used to describe all systems. The simulations were performed assuming periodic boundary conditions in the

NpT ensemble with the temperature maintained at 300 K using Langevin dynamics for pressure, kept at 1 bar, and temperature coupling. A distance cut-off of 12.0 Å was applied to short-range, non-bonded interactions, whereas long-range electrostatic interactions were treated using the particle-mesh Ewald (PME)[260] method. The equations of motion were integrated using the r-RESPA multiple time step scheme[261] to update the van der Waals interactions every two steps and electrostatic interactions every four steps. The time step of integration was chosen to be 4 fs for all production simulations performed, and 2 fs for all equilibration runs. For the 4 fs simulations, hydrogen mass repartitioning was done using psfgen in VMD. Before the MD simulations, all the systems were submitted to an energy minimization protocol for 5 000 steps.
MD simulations with position restraints in the protein backbone atoms were performed for 1.0 ns and served to pre-equilibrate systems before the 10 ns equilibrium MD runs, which served to evaluate structural model stability. During the 1.0 ns pre-equilibration, the initial temperature was set to zero and was constantly increased by 1 K every 1 000 MD steps until the desired temperature (300 K) was reached.
In all simulations, totaling over 300 SMD simulations, SMD was employed by harmonically restraining the position of a terminal amino acid residue and moving a second restraint point at a terminal amino acid residue of the other domain, with constant velocity in the +z direction. The procedure is equivalent to attaching one end of a harmonic spring to the end of a domain and pulling on the other end of the spring. The force applied to the harmonic spring is then monitored during the time of the molecular dynamics simulation. The pulling point was moved with constant velocity along the z-axis and due to the single anchoring point and the single pulling point the system is quickly aligned along the z-axis. Owing to the flexibility of the linkers between the RDB:ACE2 and fingerprint domains, this approach mimics the experimental set-up. The SMD simulations[262] were performed using the constant velocity stretching (SMD-CV) protocol, with pulling velocity 12.5 and 2.5 Å/ns. With our *in-silico* SMFS approach, we performed many replicas of simulations (at least 24 per system). Values for the force on the pulling spring were saved every 50 steps. The spring constant of the pulling spring was set to 5.0 kcal/mol/Å, while the holding spring had a constant of 100 kcal/mol/Å. Analyses of MD trajectories were carried out employing VMD[22] and its plug-ins, as well as in-house python-based Jupyter notebooks[257]. Secondary structures were assigned using the Timeline plug-in, which employs STRIDE criteria. Force propagation profiles[263] were analyzed using generalized cross correlation-based network analysis[228]. A network was defined as a set of nodes, all α-carbons in our case, with connecting edges. Edges connect pairs of nodes if corresponding monomers are in contact, and 2 non-consecutive monomers are said to be in contact if they fulfil the proximity criterion that, namely any heavy atoms (non-hydrogen) from the 2 monomers are within 4.5 Å of each other for at least 75% of the frames analyzed.

5.4.8 Chimera protein construction

The structures of SARS-CoV-1 and SARS-CoV-2 RBDs complexed with human ACE2 were retrieved from the Protein Data Bank; PDB IDs: 2ajf and 6m0j, respectively. The RBD:ACE2 protein interfaces were investigated using PDBsum[224] and were visually inspected using VMD[22] to compare the amino acid differences between SARS-CoV-1 and SARS-CoV-2. Modeller[225] was employed to construct the model for the SARS-CoV-1 chimera based on the structure of SARS-CoV-1 (PDB ID: 2ajf) taking into account the residue substitutions on the SARS-CoV-2 RBD:ACE2 interface (Table 5.3). Crystallographic water molecules and Zn^{2+} ions were kept in place while other heteroatoms were removed. Residues 376–381 that are missing in the crystallographic structure were included into the model using Modeller.

5.4.9 Magnetic tweezers instrument

Measurements were performed on a custom MT setup described previously[38;160]. In the setup, molecules are tethered in a flow cell (FC; see next section); mounted above the FC is a pair of permanent magnets (5×5×5 mm3 each; W-05-N50-G, Supermagnete, Gottmadingen, Germany) in vertical configuration[59]. The distance between magnets and FC is controlled by a DC-motor (M-126.PD2, Physik Instrumente PI GmbH & Co KG, Karlsruhe, Germany) and the FC is illuminated by an LED (69647, Lumitronix LED Technik GmbH,

Germany). Using a 40x oil immersion objective (UPLFLN 40x, Olympus, Japan) and a CMOS sensor camera with 5120 x 5120 pixels (5120 x 5120 pixels, CP80-25-M-72, Optronis, Kehl, Germany) a field of view of approximately 680 × 680 μm^2 is imaged at a frame rate of 72 Hz. To control the focus and to create the look-up table required for tracking the bead positions in z, the objective is mounted on a piezo stage (Pifoc P-726.1CD, Physik Instrumente PI GmbH & Co KG, Karlsruhe, Germany). Images are transferred to a frame grabber (microEnable 5 ironman VQ8-CXP6D, Silicon Software, Mannheim, Germany) and analyzed with an open-source tracking software [64;264]. The tracking accuracy of our setup was determined to be ≈ 0.6 nm in (x, y) and ≈ 1.5 nm in z direction, as determined by tracking non-magnetic polystyrene beads, after baking them onto the flow cell surface. Force calibration was performed as described [68] by analysis of the fluctuations of long DNA tethers. Importantly, for the small extension changes on the length scales of our protein tethers, the force stays constant to very good approximation (to better than 10^{-4} relative change). The largest source of force uncertainty is due to bead-to-bead variation, which is on the order of ≤ 10% for the beads used in this study [59;62].

5.4.10 Flowcell preparation and magnetic tweezers measurements

FCs were prepared as described previously [38]. High precision microscope cover glasses (24 mm x 60 mm x 0.17 mm, Carl Roth) were amino-silanized for further functionalization (equal to AFM surface preparation). They were coated with sulfo-SMCC [265] (sulfosuccinimidyl 4-(N-maleimidomethyl)cyclohexane-1-carboxylate; sulfo-SMCC, ThermoFisher Scientific, Pierce Biotechnology, Rockford, IL, USA, # 22322). For this purpose, 180 µl sulfo-SMCC (10 mM in 50 mM Hepes buffer, pH 7.4) was applied to one amino-silanized slide that was sandwiched with another slide and incubated for 45 min. Unbound sulfo-SMCC was removed by rinsing with MilliQ. Next, elastin-like polypeptide (ELP) linkers [120] with a sortase motif at their C-terminus were coupled to the maleimide of the sulfo-SMCC via a single cysteine at their N-terminus, by sandwiching two slides with 100 µl ELP linkers (in 50 mM Disodium phosphate buffer with 50mM NaCl and 10mM EDTA, pH 7.2) and incubating them for 60 min. Subsequently, after further MilliQ rinsing to remove unbound ELP linkers, free sulfo-SMCC was neutralized with free cysteine (10 mM in 50 mM Disodium phosphate buffer with 50 mM NaCl and 10 mM EDTA, pH 7.3). 1 µm diameter polystyrene beads dissolved in ethanol were applied to the glass slides. After the ethanol evaporated, beads were baked onto the glass surface to serve as reference beads during the measurement. FCs were assembled from an ELP-functionalized bottom slide and an unfunctionalized high-precision microscope cover glass slide with two holes (inlet and outlet) on either side serving as top slide. Both slides were separated by a layer of parafilm (Pechiney Plastic Packaging Inc., Chicago, IL, USA), which was cut out to form a 50 µl channel. FCs were incubated with 1% (v/v) casein solution (# C4765-10ML, Sigma-Aldrich) for 2 h and flushed with 1 ml buffer (25 mM TRIS, 72 mM NaCl, 1 mM $CaCl_2$, pH 7.2 at room temperature).

CoA-biotin (# S9351 discontinued, New England Biolabs, Frankfurt am Main, Germany) was coupled to the ybbR-tag at the C-terminus of the fusion protein constructs in a 90 - 120 min bulk reaction in the presence of 4 µM sfp phosphopantetheinyl transferase [266] and 100 mM $MgCl_2$ at room temperature (≈ 22°C). Proteins were diluted to a final concentration of about 50 nM in 25 mM TRIS, 72 mM NaCl, 1 mM $CaCl_2$, pH 7.2 at room temperature. To couple the N-terminus of the fusion proteins carrying three glycines to the C-terminal LPETGG motif of the ELP-linkers, 100 µl of the protein mix was flushed into the FC and incubated for 24 min in the presence of 1.3 µM evolved pentamutant sortase A from Staphylococcus aureus [125;126]. Unbound proteins were flushed out with 1 ml measurement buffer (25 mM TRIS, 72 mM NaCl, 1 mM $CaCl_2$, 0.1% (v/v) Tween-20, pH 7.2 at room temperature). Finally, commercially available streptavidin-coated superparamagnetic beads (Dynabeads™ M-270 Streptavidin, Invitrogen, Life Technologies, Carlsbad, CA, USA) were added into the FC and incubated for 30 s before flushing out unbound beads with 1 ml measurement buffer. Receptor:ligand binding and unbinding under force was systematically investigated by subjecting the protein tethers to (2 - 30) min long plateaus of constant force, which was gradually increased in steps of 0.2 or 0.3 pN. All measurements were conducted at room temperature.

For blocking measurements, recombinant human ACE2 (Gln18-Ser740, C-terminal His-tag) from RayBiotech (Peachtree Corners, GA, USA, # 230-30165-100 distributed by anti-

bodies-online GmbH, Aachen, Germany, # ABIN6952473) was dissolved in measurement buffer for a final concentration of ∼ 3.8 µM. Dissolved ACE2 was spun down in a tabletop centrifuge at 4°C, 14 000 rcf for 5 min to avoid introduction of larger particles into the FC that could influence video tracking. 80 µl ACE2 were flushed into the FC and shortly incubated before applying 7 pN to force dissociation of the tethered ligand construct and allow the soluble ACE2 to bind. Afterwards, a measurement was conducted in the presence of soluble ACE2.

5.4.11 Data analysis of MT traces

MT traces for thermodynamic bond analysis were selected on the basis of the characteristic ACE2 two-step unfolding pattern above 25 pN, conducted at the end of each experiment. For each trace, (x, y)-fluctuations were also checked to avoid inclusion of tethers that exhibit inter-bead or bead-surface interactions, which would also cause changes in x or y. Non-magnetic reference beads were tracked simultaneously with magnetic beads and reference traces were subtracted for all measurements to correct for drift. Extension-time traces were smoothed to one second with a moving average filter to reduce noise. All analyses were performed with custom scripts in MATLAB.

5.4.12 Estimate of forces on viral particles at the cell surface

The human respiratory system is covered with a thin layer of mucus[267]. This layer exerts drag forces on virus particles bound to receptors. A simple upper estimate of the drag forces can be computed as follows: $F = \gamma \cdot v_{fluid}$ with $\gamma = 3\pi\eta r$ being the Einstein drag coefficient, η being the viscosity of the mucus layer, and r being the radius of the viral particle, in the case of SARS-CoV-2 r is in the range (60 nm – 140 nm)[268]. The rheology of human respiratory mucus has been characterized and values for the viscosity lie in the range of $\eta \sim$ (1 Pa·s – 100 Pa·s)[267]. Estimations for the velocity of particle clearance in the airways suggest velocities in the range of v ∼ (4 µm/s – 14 µm/s)[269]. Thus, an upper estimation of the relevant drag forces acting on a stationary virus particle in the human respiratory tract is F ∼ (2 pN – 2 nN).
The cellular cytoskeleton can generate forces greater than 40 pN on a single bond with extracellular ligands[270]. Forces in cellular adhesions can span 10 – 100 pN which can comparably be applied to an attached viral capsid[271–273]. Cellular movement occurs on the time scale of up to micrometers per minute[274] that can cause mechanical loading on a cell:virus bond. This sets the conditions viruses have to likely withstand to be able to stay attached to cells[275].

Acknowledgements

We thank Meike Bos, Joost de Graf, David Dulin, and Klaus Überla for helpful discussions and Nina Beier, Benedikt Böck, and Ellis Durner for help with initial experiments. This study was supported by German Research Foundation Projects 386143268 and 111166240, an EMBO long term fellowship to L.F.M. (ALTF 1047-2019), and the Physics Department of the LMU Munich. R.C.B. and P.S.F.C.G. are supported by start-up funds provided by Auburn University and D.L. acknowledges support from the Spanish Ministry of Science, Innovation and Universities for the Spanish State Research Agency Retos Grant RTI2018-099318-B-I00, cofunded by the European Regional Development Fund (FEDER).

5.5 Supplementary Material

5.5.1 Tables

5.5.2 Figures

SARS-CoV-1	SARS-CoV-2
V404	K417
R426	**N439**
T433	G446
Y442	**L455**
L443	**F456**
F460	Y473
P462	**A475**
P470	E484
L472	**F486**
Y484	**Q498**
T487	**N501**
I489	V503

Table 5.3: Mutations on the interface of SARS-CoV-1 and SARS-CoV-2 RBD:ACE2. Residues are labeled according to the corresponding crystal structure (PDB IDs: 2ajf and 6m0j for SARS-CoV-1 and 2, respectively). Residues highlighted in bold were identified as important contacts in the simulations (see "Molecular dynamics simulations" section).

Study	ACE2 binding to SARS-CoV-1 RBD	ACE2 binding to SARS-CoV-2 RBD	Methods and Comments
Lan et al.[204]	K_d = 31 $k_{sol,off}$ = 4.3·10^{-2} $k_{sol,on}$ = 1.4·10^6	K_d = 4.7 $k_{sol,off}$ = 6.5·10^{-3} $k_{sol,on}$ = 1.4·10^6	SPR
Shang et al.[194]	K_d = 185 $k_{sol,off}$ = 3.7·10^{-2} $k_{sol,on}$ = 2.0·10^5	K_d = 44.2 $k_{sol,off}$ = 7.8·10^{-3} $k_{sol,on}$ = 1.75·10^5	SPR
Starr et al.[232]	K_d = 0.12	K_d = 0.039	YDS
Walls et al.[233]	K_d = 5.0 ± 0.1 $k_{sol,off}$ = 8.7 ± 5.1·10^{-4} $k_{sol,on}$ = 1.7 ± 0.7·10^5	K_d = 1.2 ± 0.1 $k_{sol,off}$ = 1.7 ± 0.8·10^{-4} $k_{sol,on}$ = 2.3 ± 1.4·10^5	BLI; uses S protein for both variants
Wang et al.[234]	K_d = 408 ± 11 $k_{sol,off}$ = 1.9 ± 0.4·10^{-3} $k_{sol,on}$ = 2.9 ± 0.2·10^5	K_d = 95 ± 7 $k_{sol,off}$ = 3.8 ± 0.2·10^{-3} $k_{sol,on}$ = 4.0 ± 0.2·10^4	SPR; uses S1 domain for SARS-CoV-2
Wrapp et al.[235]	K_d = 325 $k_{sol,off}$ = 112 ·10^{-3} $k_{sol,on}$ = 3.62·10^5	K_d = 14.7 $k_{sol,off}$ = 2.76 ·10^{-3} $k_{sol,on}$ = 1.88 ·10^5	SPR; uses ectodomain for both variants

Table 5.4: Equilibrium binding data for ACE2 binding to SARS-CoV-1 or SARS-CoV-2 RBD or S1 proteins. Surface plasmon resonance (SPR), bio-layer interferometry (BLI), and yeast display screen (YDS) studies for both ACE2 binding to RBD constructs and to the S protein are included; Similarly, Yang et al. observe similar binding constants and mechanical stabilities for ACE2 binding to either the RBD or S using AFM force spectroscopy[236]. K_d is given in nM, $k_{sol,off}$ is given in s^{-1}, and $k_{sol,on}$ is given in $s^{-1}M^{-1}$.

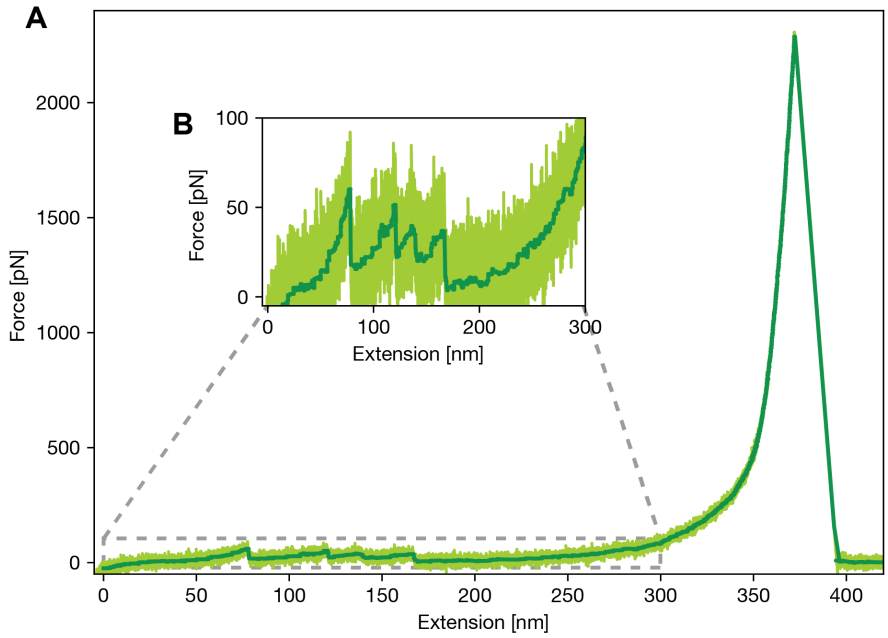

Figure 5.7: Full force-extension curve of the tethered ligand protein construct including the RBD of SARS-CoV-2 and ACE2. **A** Complete force-extension curve showing the entire unfolding and the final rupture of the ClfA:Fgγ linkage. The full curve shows 4 peaks at lower forces (< 100 pN) and one final rupture at high forces (> 1 000 pN). **B** Inset shows the extension range between 0 and 300 nm showing the low-force unfolding events attributed to the tethered ligand protein. The first low-force peak can be identified as the interface unbinding between SARS-CoV-2 RBD and ACE2 together with a partial unfolding of the RBD. This peak is followed by a trident shaped, three peak pattern that can be assigned to the unfolding of ACE2, see main text.

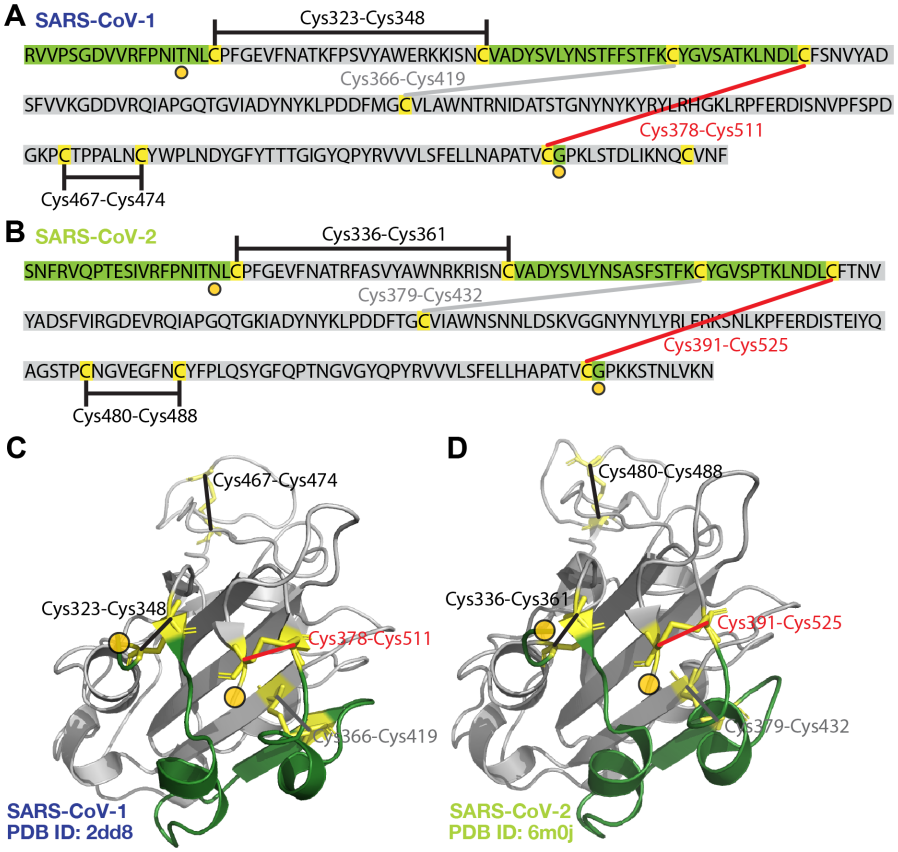

Figure 5.8: Disulfide bridges shield large parts of the SARS-CoV-1 and SARS-CoV-2 RBD structure. **A** and **B** show the sequence of the SARS-CoV-1 and SARS-CoV-2 RBD with all cysteines highlighted in yellow. The disulfide bridges are indicated as lines between the cysteines in the RBD sequences. These bridges shield parts of the folded protein structure from force and thereby restrict unfolding. The parts of the protein still under force are highlighted in green, shielded parts in grey. The sections under force add up to 51 amino acids (aa, 19 nm for 0.365 nm/aa) for the RBD of SARS-CoV-1 and 54 aa (20 nm for 0.365 nm/aa) for the RBD of SARS-CoV-2 (these include all folded residues as captured in the crystal structure). Some parts of the N-terminus of the RBD used in the tethered ligand protein are probably not folded but will also get released together with the linker increment. The unfolded parts on the C-terminus probably get stretched already in the initial stretching of the linkers for attachment and therefore will not contribute to the length released during the (partial) unfolding of the RBD. In **C** and **D** the corresponding RBDs of SARS-CoV-1 (PDB ID: 2dd8)[276] and SARS-CoV-2 (PDB ID: 6m0j)[204] are depicted, using the same color code as in A,B for parts of the protein under force (green), contributing to the increments observed, and parts shielded from unfolding (grey). The orange circles mark the N- and C-terminal end of the crystal structure whereas the sequence in (A, B) show the entire RBD sequence used in the tethered ligand protein.

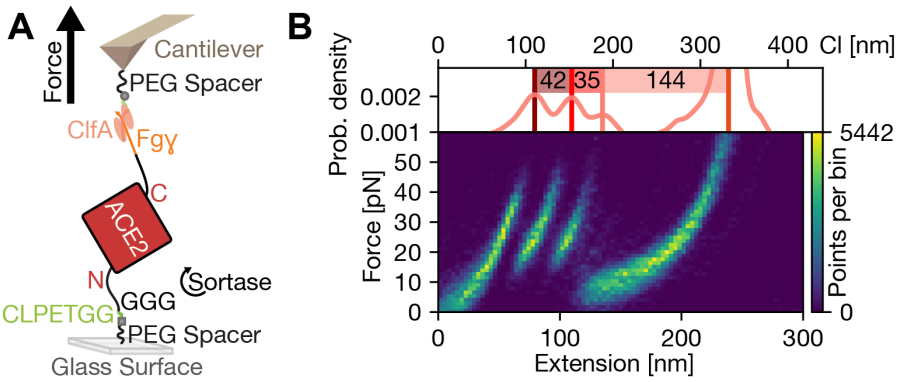

Figure 5.9: Unfolding of individual ACE2 by AFM SMFS. A Schematic of the experimental setup for pulling on individual ACE2 which (identical to tethered ligand proteins). ACE2 is coupled covalently on an aminosilanized glass surface using heterobifunctional polyethylene glycol (PEG) spacers. The construct is attached in a sortase-mediated reaction to a CLPETGG peptide attached to the maleimide of the PEG spacer. For reversible tethering the Fgγ tag on the tethered ligand protein can be pulled by a ClfA handle. ClfA is covalently attached to the cantilever in a sfp-mediated reaction, connecting the ybbR tag to a CoA coupled to a PEG spacer on the AFM cantilever. **B** Heatmap of AFM unfolding traces of ACE2. The heatmap of an overlay of 152 aligned curves shows the characteristic ACE2 trident shaped pattern also observed in the full unfolding of the tethered ligand protein. On top an alignment of all contour length transformed density curves is shown. The contour length increments of the ectodomain ACE2 match well with the last increments of the tethered ligand construct. This allows the assignment of the last three peaks before the final rupture in the RBD:ACE2 tethered ligand protein to the unfolding of the ACE2 ectodomain. The characteristic ACE2 unfolding pattern can be used as a fingerprint for identifying single-molecule traces and normalizing force distributions in measurements if they were recorded with different cantilevers.

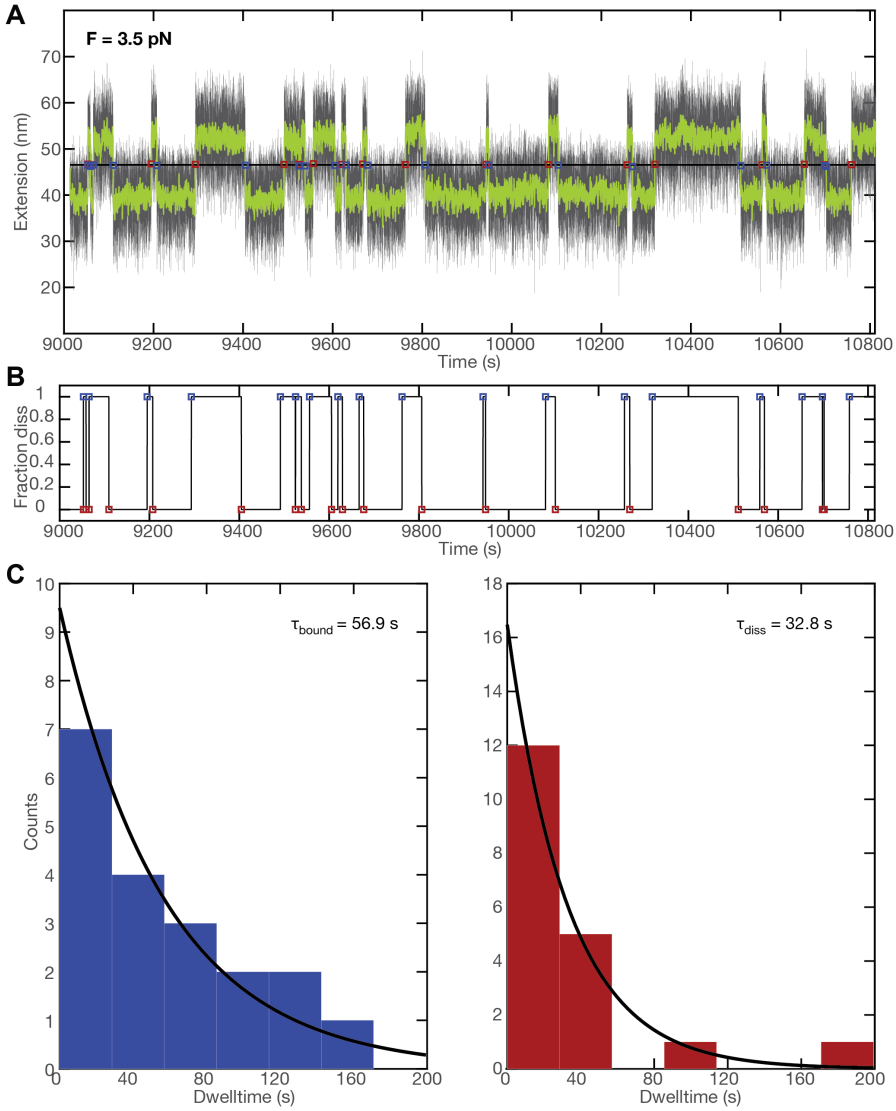

Figure 5.10: Dwell time analysis of the tethered ligand extension-time traces in MT. **A** Short segment of an extension-time trace measured for a SARS-CoV-2 RBD:ACE2 tethered ligand construct at a stretching force of 3.5 pN. Raw data at 72 Hz are shown in black and filtered data (50 frame moving average) are shown in green. Assignment of the dwell times is based on the filtered data. The black horizontal line is the threshold; blue squares indicate the first data point after crossing the threshold from below, i.e. transition from the bound to the dissociated state; red squares indicate the first data point after crossing the threshold from above, i.e. transition from the dissociated to the bound state. **B** Time trace derived from the analysis shown in panel A, indicating the current state of the tethered-ligand system with "1" corresponding to the dissociated state and "0" to the bound state. The time between the transitions between "0" and "1" correspond to the dwell times. **C**, **D** Histograms of dwell times in the bound state (C) and dissociated state (D) obtained from the analysis shown in panels A and B. The dwell times are well described by single exponential fits, shown as solid lines. Insets show the mean dwell times from maximum likelihood fits of the single exponentials.

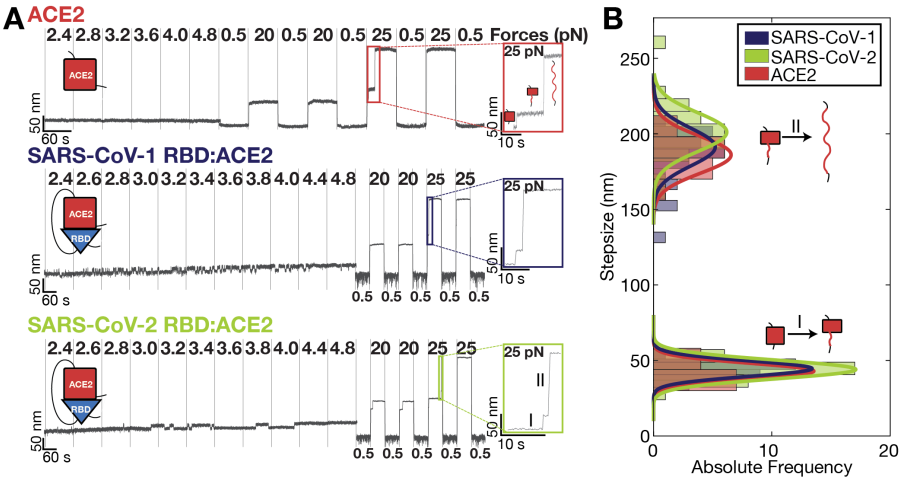

Figure 5.11: ACE2 unfolding events observed in different constructs in MT. A Short force ramps and unfolding jumps for single ACE2 (top), SARS-CoV-1 RBD:ACE2 (middle), and SARS-CoV-2 RBD:ACE2 (bottom), measured in MT. Both tethered ligand constructs show equilibrium hopping transitions in the range between 2.4 and 4.8 pN, corresponding to interface opening and partial RBD unfolding. It is apparent that the transitions are much more rapid, i.e. exhibit shorter dwell times, for SARS-CoV-1 compared to SAXS-CoV-2. During the force jumps, all constructs show characteristic two-step unfolding, marking unfolding of the ACE2 domains. **B** Histogram of jump-size distributions of the 2 step-unfolding events, after contour length transformation (with L_p = 0.5 nm) for all constructs shown in A. Solid lines represent Gaussian fits to the histograms. Distributions agree very well across the different constructs.

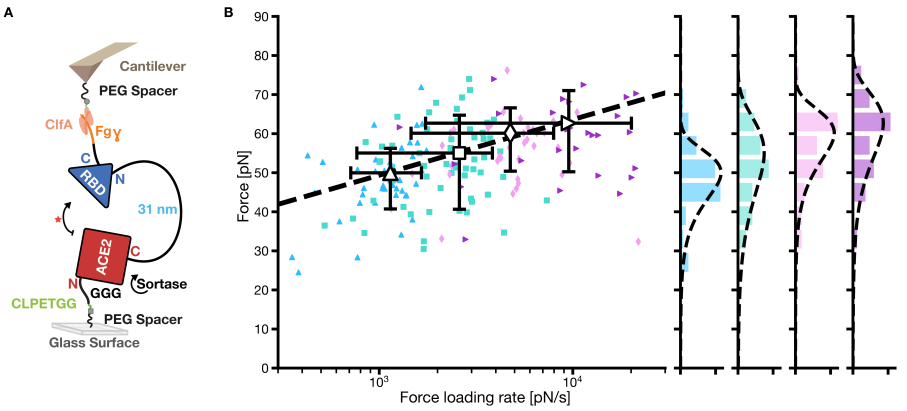

Figure 5.12: Dynamic force spectrum of the SARS-CoV-2 RBD:ACE2 dissociation (red star) recorded by AFM SMFS. A Schematic depiction of the dynamically probed tethered ligand protein consisting of a SARS-CoV-2 RBD and ACE2 joined by a 31 nm linker in the AFM. The attachment strategy is shown together with the probed protein. **B** AFM force spectroscopy measurements were performed with retraction velocities of the sample surface in relation to the cantilever of 0.4 μm/s (blue triangles), 0.8 μm/s (green squares), 1.6 μm/s (lavender diamonds), and 3.2 μm/s (purple forward triangles). The corresponding rupture force histograms are projected on the right and shown with a Bell-Evans fit (thin black dashed lines). A global Bell-Evans fit to the most-probable rupture force and force loading rate of each velocity (large open markers, with errors given as full-width at half maximum for each distribution) is shown as bold dashed line on the left. The fit yields a distance to the transition state of $\Delta x = 0.67 \pm 0.06$ nm and zero-force off rate $k_0 = 0.056 \pm 0.04$ 1/s.

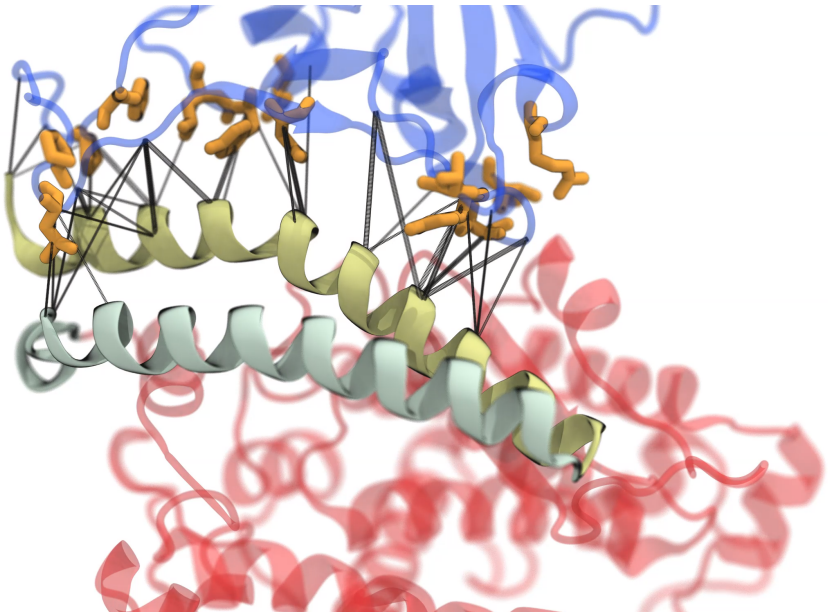

Figure 5.13: Depiction of the interface between SARS-CoV-1 RBD-based Chimera (blue) and ACE2 (red). The two N-terminal helices from ACE2 are highlighted in solid representations and cyan/green shades. Residues that were modified in the chimera are shown in orange licorice representations. Black lines indicate residues in close proximity, and the thickness of the black lines indicates the correlation between their movements. Under high-force load, most of the correlations between the chimeric RBD and ACE2 occur along the N-terminal helix of ACE2 (green, on top).

6

Stability of SARS-CoV-2 Variants of Concern Under Constant Force

Summary

Viruses mutate under a variety of selection pressures, allowing them to continuously adapt to their hosts. Past mutations of SARS-CoV-2 have shown effective evasion of population immunity and increased affinity to host factors, such as ACE2. In the dynamic environment of the respiratory tract, the question arises, if not only affinity, but also force-stability of the SARS-CoV-2:ACE2 bond, initiating infection of host cells, might be a selection factor for mutations. Here, we use magnetic tweezers (MT) to study the effect of variants of concern (VOCs) on RBD:ACE2 bond kinetics with and without external load using a previously established assay. Matching previous bulk-affinity measurements, we find higher affinity for all VOC compared to wt. In contrast to that, α is the only VOC markedly different from the wildtype under force. Studying the RBD:ACE2 interactions on a molecular level, we are able to rationalize this deviation. Our study emphasizes the diversity of contributions to the assertiveness of variants and establishes force-stability as one of several factors for fitness. Understanding fitness-advantages opens the possibility for prediction of likely mutations allowing rapid adjustment of therapeutics, vaccination, and intervention measures.

6.1 Main Text

Viruses quickly diverge into variants with small genomic changes. This can be facilitated, for instance, by random mutations due to errors in RNA replication. Most of these mutations are silent or inviable, but some result in increased fitness or effective evasion of population immunity. This causes an evolutionary advantage that allows the variant to supersede existing variants, as it was observed for example by the emergence and quick spread of variants of concern (VOC) of SARS-CoV-2 (Figure 6.1B,C). Interestingly, adaptations associated with increased fitness of SARS-CoV-2 often go along with higher affinity to host factors [12;277]. Attachment of SARS-CoV-2 to the human host factor ACE2 takes place in the dynamic environment of the respiratory tract, where external forces, caused for example by breathing or coughing, constantly counteract attachment (Figure 6.1A). For successful infection, it is thus crucial to establish a robust, force-enduring bond to the host. In this study, we investigate the SARS-CoV-2 attachment to ACE2 under external force using a previously established assay [10] and compare the wildtype (wt):ACE2 bond stability to the bond stability

This manuscript is in preparation. My contribution: For this paper, I was involved in designing the research, performing MT experiments, and MT data analysis, and writing the manuscript.

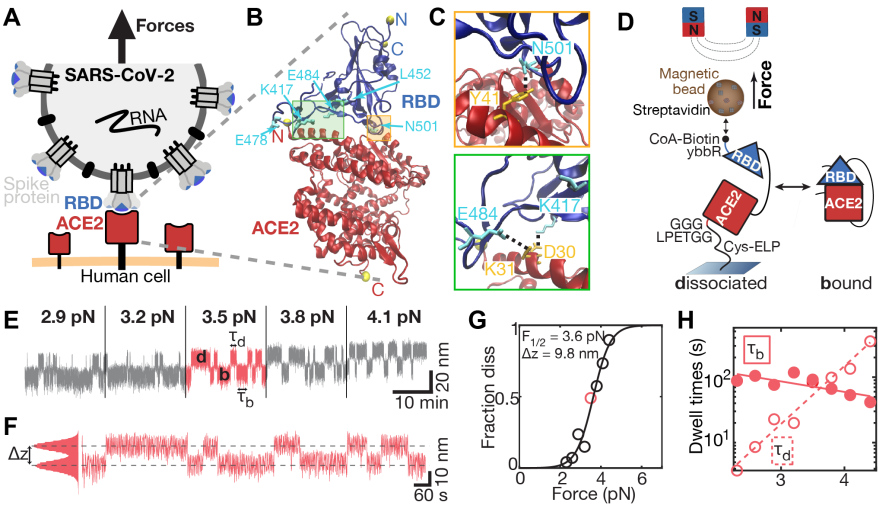

Figure 6.1: A single -molecule tethered ligand assay to study RBD binding to ACE2 for current variants of concern of SARS-CoV-2. **A** One SARS-CoV-2 virion in grey presents its spike protein trimers containing three RBDs (blue) ready for binding to human ACE2 (red). Attachment occurs in the dynamic environment of the respiratory tract, where the interaction must withstand external forces (black arrow). **B** Crystal structure of SARS-CoV-2 RBD (blue) bound to ACE2 (red) (PDB-ID 6M0J)[204]. Termini of protein chains are marked as yellow spheres. Point mutations featured in current variants of concern (VOCs) are indicated in cyan. Crystal structure was rendered using VMD[22]. **C** Zoom into interface in the regions indicated in B. Top: RBD residue 501 featured in VOCs α, beta, and gamma forms a hydrogen-bond with ACE2 residue 41[204]. Bottom: RBD residues 484 and 417 featured in VOCs beta and gamma form salt bridges and hydrogen bonds with ACE2 residues 31 and 30 respectively[11;204]. Bridges and bonds are indicated as black dashed lines. **D** Schematic representation of the tethered ligand construct in MT. SARS-CoV-2 RBD (blue) is tethered via a flexible peptide linker to ACE2 (red). The construct is covalently attached to the glass surface via an ELP linker (for details see Materials and Methods), and to a streptavidin-covered magnetic bead via biotin at the C-terminus of the protein construct. **E** Representative time vs extension trace recorded with MT shows binding and dissociation of the SARS-CoV-2 RBD:ACE2 interaction at plateaus of constant force. With increasing force, the interface is predominantly dissociated. Dwell times in the dissociated state (τ_d) and in the bound state (τ_b) are indicated. **F** Segment of the trace in E at 3.5 pN, where it is equally distributed between the bound (b) and dissociated (d) state. The fraction dissociated at this force is thus 0.5. **G** For all plateaus of constant force shown in E, the fraction dissociated are determined, and fitted with a two-state model. $F_{1/2}$ and Δz (shown as inset) are obtained from the fit. **H** Dwelltimes in the bound and dissociated state for the molecule shown in E-G are determined in each force plateau and fit with an exponential model.

of VOCs. Doing this, we can not only reproduce zero-force equilibrium affinities, but compare the zero-force behavior to bond lifetimes of the receptor binding domain (RBD):ACE2 complex under force. This allows us to draw conclusions on the influence of different mutations in the VOCs on the (force-) stability of their bond to ACE2. We design fusion protein constructs comprising the ectodomain of the human ACE2 receptor connected to the RBD of the SARS-CoV-2 virus and its VOCs by a flexible polypeptide linker (Figure 6.1D). Attaching these tethered ligand constructs to a glass surface on one end and to a magnetic bead on the other end allows to probe the stability of the RBD:ACE2 interaction at varying constant forces using MT. At low forces (< 10 pN), the linker ensures receptor and ligand proximity upon unbinding, allowing them to re-bind. We can thus study repetitive binding and dissociation of the same SARS-CoV-2 RBD and ACE2 interaction under different constant forces (Figure 6.1E). At low forces (< 2 pN), we find the bond to be predominantly formed, while increasing the force leads to elongated periods with a dissociated bond. Quantitating this behavior gives access to two key characteristics of the system: $F_{1/2}$ is the force at which it is equally likely to find the system in a bound or dissociated conformation (Figure 6.1F, b(bound), and d(issociated)). It is determined by fitting a two-state model to the fraction dissociated (f_{diss}) as a function of force (Figure 6.1G):

$$f_{diss}(F) = \frac{1}{(1 + e^{\frac{-\Delta z \cdot (F - F_{1/2})}{k_B \cdot T}})} \tag{6.1}$$

where k_B is Boltzmann's constant and T the absolute temperature. $F_{1/2}$ and Δz are fitting parameters that represent the midpoint force, where the system spends half of the time in the dissociated and half of the time in the bound conformation, and the distance between the two states along the pulling direction, respectively. The fraction dissociated is calculated for each plateau of constant force by dividing the time spent in the dissociated conformation by the total plateau time. Second, the mean dwell times of the dissociated and bound state, τ_{diss} and τ_{bound} (Figure 6.1F, τ_{diss}, τ_{bound}), are determined for each force (Figure 6.1H, circles). The force-dependent dwell times are fitted with an exponential model (Figure 6.1H, lines), and subsequently averaged over all measured molecules (Figure 6.2C). While the intersection of the fitted dwell times in the dissociated and bound state provides an alternative route to the midpoint force, extrapolation of the fits to zero force yields lifetimes of the bond under no force, relating to the affinity of the binding partners. We introduced the mutations featured in α (B.1.1.7), β (B.1.351), γ (P.1), and δ (B.1.617.2) (Figure 6.1B,C, Table 1) into our tethered RBD, and thus compared the characteristics of the RBD:ACE2 bond for the different VOCs. Comparing $F_{1/2}$ for different variants (Figure 6.2B), we find no statistically significant difference between SARS-CoV-2 wt and β (p-value > 0.80, two-tailed t-test, 13 vs. 10 molecules, respectively), wt and γ (p-value $>$ 0.26, two-tailed t-test, 13 vs. 14 molecules, respectively), nor between wt and δ (p-value $>$ 0.99, two-tailed t-test, 13 vs. 20 molecules, respectively). However, the difference in $F_{1/2}$ between wt and α is statistically very significant (p-value < 0.000515, two-tailed t-test, 13 vs. 11 molecules, respectively). This can be rationalized considering the interactions of the residues featured in the respective VOC with residues of ACE2. In wt SARS-CoV-2, N501

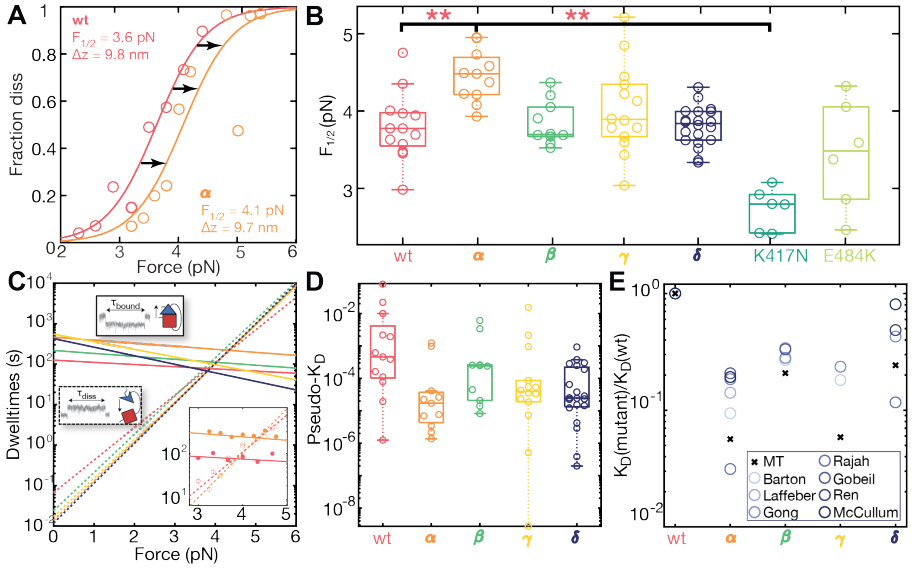

Figure 6.2: Effects of current VOCs on interface stability and affinity. **A** Representative force-dependent fraction dissociated for one wt (red), and one α (orange) tethered ligand molecule. Points represent experimental data and solid lines represent two-state fit. **B** Boxplot of midpoint forces determined for wt, α, β, γ, and δ VOCs and K417N, and E484K single mutations. $F_{1/2}$ of α (4.5 $\pm$ 0.33) pN and K417N (2.7 $\pm$ 0.27) pN deviate highly significantly from wt (3.8 $\pm$ 0.44) pN (p-values $p < 0.000515 and p < 0.000045$, respectively). β (3.8 $\pm$ 0.28) pN, γ (4.0 $\pm$ 0.57) pN, δ (3.8 $\pm$ 0.25) pN, and E484K (3.4 $\pm$ 0.70) show no statistically significant difference to the wt. **C** Exponential fit to the force-dependent dwell times in the bound (solid lines) and dissociated (dashed) state of wt and variant constructs. Color-coding matches D. Inset shows fit and experimental data around the respective midpoint forces for wt and α. **D** Boxplot of pseudo-K_D = τ_{up}/τ_{down} for the different mutants with τ_{up} and τ_{down} obtained from fits shown in C extrapolated to no force. **E** Dissociation constant normalized to the wt (K_d/K_d(wt)) determined from our measurements (**x**) and compared to traditional bulk affinity measurements (SPR or BLI) in literature [11–17]. Statistics in panels B - D reflect 13 molecules (wt), 11 molecules (α), 10 molecules (β), 14 molecules (γ), 20 molecules (δ), 6 molecules (E484K), and 6 molecules (K417N).

forms a hydrogen bond with Y41 of ACE2 [204]. Structural modeling predicts that mutation N501Y, though impeding the original hydrogen bond, allows formation of two new hydrogen bonds with ACE2 residues D38 and K353. Additionally, it causes a strong π stacking interaction between Y501 and Y41, potentially explaining the higher force stability of the α variant [278]. β and γ VOCs feature mutations at position E484K and K417N/T in addition to the mutation N501Y. In the wt, the residues at these positions form salt bridges with residues K31 and D30 of ACE2, respectively [11;204]. Due to a charge-reversal in the case of E484K and a charge removal in the case of K417N (β) and K417T (γ), these salt bridges are disrupted. A significant decrease in force-stability of a tethered ligand construct featuring only the K417N mutation compared to the wt construct supports the hypothesized influence of this salt bridge in destabilizing the force loaded complex (Figure 6.2B, turquoise, $p < 0.000045$, two-tailed t-test, 13 vs. 6 molecules, respectively). E484K, however, can form an alternative salt bridge with E35 [11], compensating the disrupted salt bridge. In agreement with this interpretation, $F_{1/2}$ of a tethered ligand construct featuring only the E484K mutation is within experimental error equal to the $F_{1/2}$ measured for the wt construct (Figure 6.2B, light green, p-value > 0.19, two-tailed t-test, 13 vs. 6 molecules, respectively). Taken together, the unreplaced salt bridge between K417 and D30 compensates for the effect of N501Y in the β and γ VOC, explaining the unaltered force-stability compared to the wt. The residues mutated in the δ VOC - L452 and T478 - are located further away from ACE2 residues and there have been no direct interactions described involving these residues. Therefore, there is no alteration in the force-stability of this VOC.

In addition to comparing bond stability under force, we studied the kinetics of the bond, analyzing the force-dependent lifetimes of the bound and the dissociated conformation. In Figure 6.1 G, the mean fitted dwell times of the bound (solid lines) and dissociated (dashed lines) states as a function of force are compared for wt and VOCs. The increase of the average time spent in the dissociated conformation with increasing force for all constructs is due to enhanced linker-stretching, impeding bond re-formation. The force-dependency of τ_{bound} for the different variants is based on the stability of the RBD:ACE2 bond under force. We find τ_{bound} to decrease with increasing force for all variants, however, they differ from the wt in slope and overall value for different variants. For α, we find higher τ_{bound} than for wt over the whole measured force range (Figure 6.1 G, inset), caused by the higher force-stability of α in this force range, also reflected by the higher $F_{1/2}$ parameter. The other VOCs are rather similar to the wt in terms of absolute dwell times close to $F_{1/2}$. The force-dependence of the bond lifetime (i.e. the slope), however, varies drastically, leading to highly different extrapolated lifetimes $\tau_{0,bound}$ and $\tau_{0,diss}$ in the absence of load, relating to the affinity of both binding partners. From the extrapolated lifetimes, a pseudo-dissociation constant ("Pseudo-K_D") can be calculated as the ratio of $\tau_{0,diss}/\tau_{0,bound}$ (Figure 6.2D). While $\tau_{0,bound}$ [s] directly relates to the off-rate (koff = $1/\tau_{0,bound}$), $\tau_{0,diss}$ [s] relates to the on-rate via $k_{on,sol} = 1/(c_{eff} \cdot \tau_{0,diss})$ due to increased effective concentration in the tethered ligand construct. Due to identical design of the VOC fusion constructs with ex-

ception of the point mutations, the effective concentration is the same for all constructs. Ratios of the Pseudo-K_Ds are thus comparable to traditional bulk affinity measurements conducted with SPR or BLI. Comparing the VOC affinities normalized to the wt affinities with literature values [11–17] reveals excellent agreement (Figure 6.2E, Table 1). In accordance with literature, all VOCs show a higher affinity for ACE2 than the wt, with the affinity of δ similar to the one of α. This is in contrast to the RBD:ACE2 bond-stability under force, where α is the only VOC markedly different from the wildtype. In the dynamic environment of the respiratory tract, the distinctly higher force-stability of α could provide an advantage acting as an evolutionary selection factor.

In conclusion, our assay offers a single-molecule approach for comparing affinities between wt and VOCs of SARS-CoV-2. As opposed to traditional bulk affinity measurements, we also provide insights into bond-stability and kinetics under low constant forces, mimicking the natural binding circumstances in the dynamic environment of the respiratory tract. Aside from many other evolutionary advantages caused for example by effective evasion of population immunity, force-enduring attachment provides a larger time window for conformational rearrangements necessary for fusion of the virus with the host-membrane. Studying force-stability thus provides valuable information helping to understand the spread of current VOCs, and a selection criterion for future variants.

WHO name	**Pango lineage**	**Country of first observation**	**Amino acid exchanges in RBD**	$\mathbf{F_{1/2}}$/ $\mathbf{F_{1/2}}$**(wt)**	τ_{diss}/ τ_{diss}**(wt)**	τ_{bound}/ τ_{bound}**(wt)**	$\mathbf{k_D}$/ $\mathbf{k_D}$**(wt)**
wt				1	1	1	1
α	B1.1.7	UK	N501Y	1.17	0.21	3.82	0.02
β	B1.1.351	South Africa	N501Y E484K K417N	1.01	0.37	1.79	0.12
γ	P1	Brasil	N501Y E484K K417T	1.06	0.27	4.55	0.15
δ	B1.617.2	India	L452R T478K	1.00	0.18	3.52	0.01

Table 6.1: Overview over SARS-CoV-2 variants of concern. Comparison of mean parameters of SARS-CoV-2 VOC to wt. Statistics reflect 13 molecules (wt), 11 molecules (α), 10 molecules (β), 14 molecules (γ), 20 molecules (δ).

7

Conclusions and Outlook

MT-based SMFS is a valuable tool for studying the force-response of proteins. With my work, I contributed to the growing field of protein SMFS using MT. As described in section 1.4.3.2, most protein MT assays so far rely on the biotin:streptavidin bond to couple proteins to magnetic beads. Together with Dr. Achim Löf and Dr. Steffen Sedlak, I developed a protocol based on controlling the anchoring geometry of streptavidin that drastically increases the lifetime of this interaction (Chapter 3). This will be beneficial for all future (force spectroscopy) experiments relying on biotin:streptavidin coupling.

Based on this stable coupling geometry I could shed light on the (un-)folding kinetics and stability of a range of medically relevant proteins and protein:protein interactions. Together with Dr. Achim Löf, I examined a structural transition in the D'D3 domain of the multimeric glycoprotein von Willebrand Factor (VWF), exposing two previously buried unbound cysteines (Chapter 4). Based on previous hypotheses [164;181] and the pronounced pH dependence of this interaction we could conclude that this transition is crucial for multimerization of VWF in the Golgi apparatus. On the basis of our data, we could furthermore support the hypothesis of a factor VIII binding site in the D submodules; a fact that had been hypothesized multiple times [173;176;177], but was never clearly shown.

The characterized transition is quite relevant for VWF's biosynthesis, but from what we know it is not force-, but pH-induced *in-vivo*. In future, our assay could be used to study force-induced stem dynamics. Opening of the "dimeric stem" formed by the six small C-terminal domains of two VWF dimers is one of the first responses of VWF to force [38;158;170]. As the hydrodynamic force VWF multimers experience scales with the square of VWF's length [5;6], understanding initial length incrementation upon force-activation is particularly interesting. Preliminary data have been published, showing that stem opening and closing is observable as extremely fast transitions in MT SMFS experiments, happening at forces of ~ 1 pN under physiological conditions [38]. However, a more detailed analysis of these transitions could shed more light upon the dynamics of stem opening and closing. Cooperativity in domain opening was hypothesized based on the primary structure of the C domains. Analyzing the transitions recorded in MT with hidden Markov models could help finding previously missed states and provide information on this hypothesis. Furthermore, investigating stem dynamics at physiologically relevant, low pH values could validate the previously described role of compaction during biosynthesis [158;168–170]. Lastly, there are point mutations located in the stem region of VWF, associated with increased VWF activation leading to an increased risk of arterial thrombosis [279–281]. This increased activation could be caused by altered stem dynamics. Studying VWF dimers with these point mutations and comparing their stem dynamics to the stem dynamics in wild-type VWF molecules could shed light on the mechanism causing increased force-sensitivity.

During my dissertation a novel SARS-Coronavirus (SARS-CoV-2) emerged, causing a global pandemic [7–9]. Pioneering a novel tethered-ligand assay, Dr. Magnus Bauer and I were able to study the stability of the bond formed by the receptor binding domain (RBD) of SARS-CoV-2 with the human receptor ACE2, initiating viral cell entry and thus infection (Chap-

ter 5). We teamed up with Dr. Rafael Bernardi (Auburn University) and in a never-seen-before way, combined three techniques - MT SMFS, AFM SMFS and *in-silico* steered molecular dynamics simulations - to investigate the bond under the whole physiologically relevant force range. We could show a significant increase in interface stability comparing the SARS-CoV-1 (the causative agent of the 2002 epidemic) with the SARS-CoV-2 RBD throughout all three techniques. In a proof-of-concept study we could furthermore show that our MT assay is sensitive to agents blocking the RBD:ACE2 interactions, suggesting it as a potential screening tool for therapeutic antibodies. Building upon this initial work, we implemented variant-of-concern (VOC) mutations located in the RBD into our tethered RBD, comparing their force-stability in MT with the force-stability of the wild-type (wt) (Chapter 6). Extrapolating the force-dependent lifetimes to zero force, we could accurately reproduce affinity data reported in literature [11–17], finding an increased affinity for all VOC compared to wt. In contradiction to these results, only the α VOC significantly differed from wt under force. This hints at force as an evolutionary selection criterion, complementary to zero-force affinity. In future, it would be interesting to combine the proof-of-concept blocking experiments (Chapter 5) with the experiments performed on the VOC (Chapter 6). Investigating antibody blocking for the wild-type RBD:ACE2 interaction and comparing this to the capability of the same antibodies to block the interaction between ACE2 and VOCs, our assay could give information on immune escape of C1 or C2 ABs binding to the RBD [282]. For this purpose, however, the currently limited throughput of our experiments needs to be drastically increased. This could probably be achieved by higher protein concentration gained from protein expression in insect cells (as opposed to currently used *in vitro* expression). Furthermore, a switch in attachment chemistry, replacing the sortase-mediated protein:ELP attachment with another attachment not relying on sortase, could be beneficial to increase experimental throughput. As discussed in more detail in section 2.3.3.2, sortase-mediated coupling is reversible, requiring careful optimization. Replacing the sortase tags on proteins and ELPs with OaAEP1 tags for example, covalent ligation of the two proteins would no longer rely on sortase, but on more robust, irreversible OaAEP1-mediated attachment [283]. This would drastically facilitate measurement optimization and would probably also lead to higher yield and measurement throughput. The successful utilization of OaAEP1- mediated attachment was already shown in the context of AFM SMFS experiments [40;127].

In the long run, it would be interesting to combine MT SMFS experiments with the capability of single-molecule fluorescence detection. The value of combining these two single-molecule techniques has been shown previously in the context of vinculin binding studies [97;100] (Chapter 1.4.4.2). In these experiments, however, force-application and fluorescence detection were carried out sequentially. In order to perform both processes simultaneously, MT setups need to be modified to allow simultaneous camera-based bead tracking for MT and fluorescence detection. Such setup designs have been presented previously [123;284–287]. With the ability of simultaneous force-spectroscopy and fluorescence detection, force-activated proteins can be stretched and successful activation can be monitored in real-time by binding of fluorescently-labelled ligands. Implementing excitation lasers with two different wavelengths into these setups would even increase measurement possibilities by allowing single-molecule FRET-based force-activation studies or distance measurements upon force activation. Together with my Master student Nina Beier, I started setting up an MT setup designed to enable exactly these types of measurements. Due to lack of time, however, only one laser wavelength was implemented up to now. A detailed description and characterization of this setup can be found in her Master's thesis alongside initial proof-of-concept total internal reflection fluorescence (TIRF) measurements. In future, a second laser needs to be implemented and further characterization measurements need to be performed, before being able to exploit the whole intended functionality of this setup.

A

List of Publications

Publications included in this work

- Sophia Gruber[†] and Jan Lipfert. Multiplexed protein force spectroscopy with magnetic tweezers. Invited Chapter at *Methods of Molecular Biology*, 2021
- Sophia Gruber[†], Achim Löf[†], Steffen M. Sedlak[†], Martin Benoit, Hermann E. Gaub, and Jan Lipfert. Designed Anchoring Geometries Determine Lifetimes of Biotin-Streptavidin Bonds under Constant Load and Enable Ultra-Stable Coupling. *Nanoscale*, 2020, http://dx.doi.org/10.1039/D0NR03665J
- Sophia Gruber[†], Achim Löf[†], Adina Hausch, Res Jöhr, Tobias Obser, Gesa König, Reinhard Schneppenheim, Maria A. Brehm, Martin Benoit, and Jan Lipfert. Single-Molecule Force Spectroscopy Reveals Conformational Change in the D'D3 Domain Relevant in von Willebrand Factor Biosynthesis. *BioRxiv*, 2021, https://doi.org/10.1101/2021.11.29.470312, under review at *Blood Advances*
- Magnus S. Bauer[†], Sophia Gruber[†], Adina Hausch, Lukas F. Milles, Thomas Nicolaus, Leonard C. Schendel, Pilar López Navajasd, Erik Procko, Daniel Lietha, Rafael C. Bernardi, Hermann E. Gaub, and Jan Lipfert. A Tethered Ligand Assay to Probe SARS-CoV-2:ACE2 Interactions. *BioRxiv*, 2021, https://doi.org/10.1101/2021.08.08.455468, in press at *PNAS*
- Sophia Gruber[†], Magnus S. Bauer[†], Adina Hausch[†], Rafael C. Bernardi, Marcelo C. R. Melo, Priscila S. Figueiredo Celestino Gomes, Hermann E. Gaub, and Jan Lipfert. Stability of SARS-CoV-2 variants of concern under constant force. *In preparation*

Publications not included in this work

- Achim Löf, Philipp U. Walker, Steffen M. Sedlak, Sophia Gruber, Tobias Obser, Maria A. Brehm, Martin Benoit, and Jan Lipfert. Multiplexed protein force spectroscopy reveals equilibrium protein folding dynamics and the low-force response of von Willebrand factor. *PNAS*, 2019, https://doi.org/10.1073/pnas.1901794116

[†] authors contributed equally

B

Technical Drawings

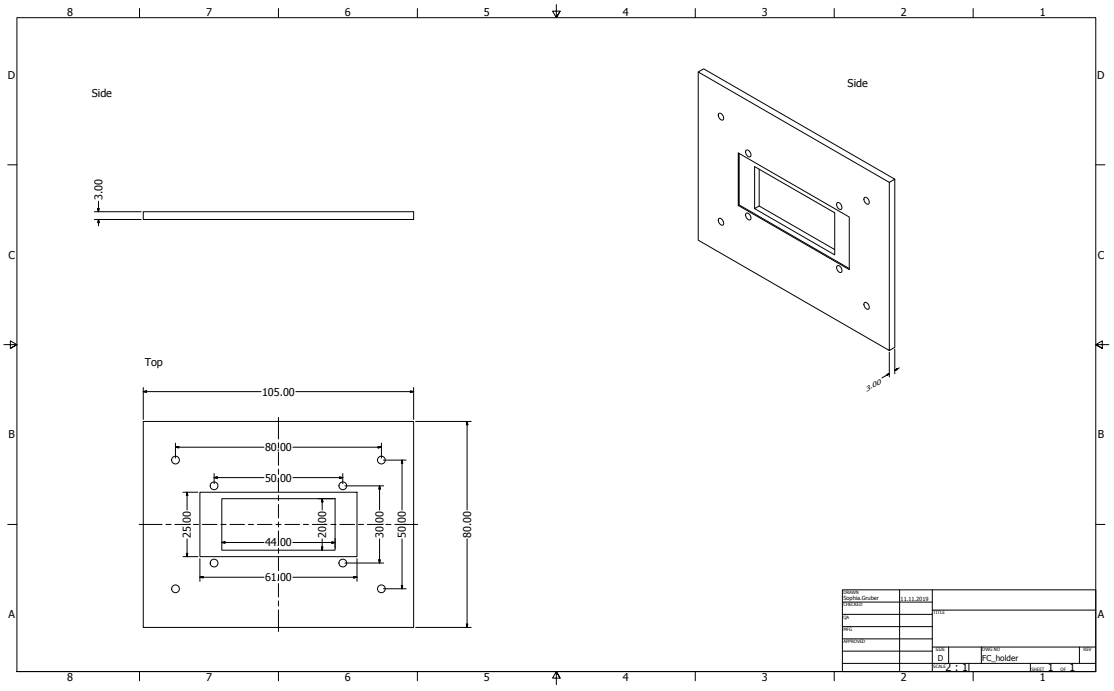

Figure B.1: Technical drawing FC holder bottom. Bottom of regular FC holder; made either of aluminium or iron.

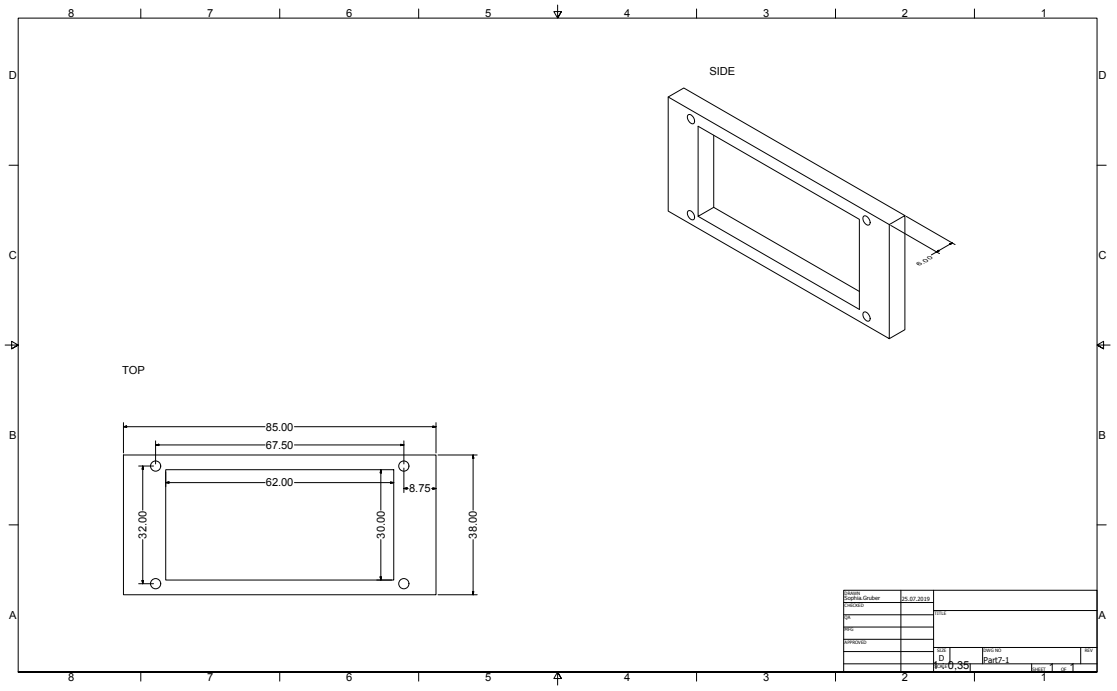

Figure B.2: Technical drawing multichannel FC holder top. Top of multichannel FC holder; made either of aluminium or iron.

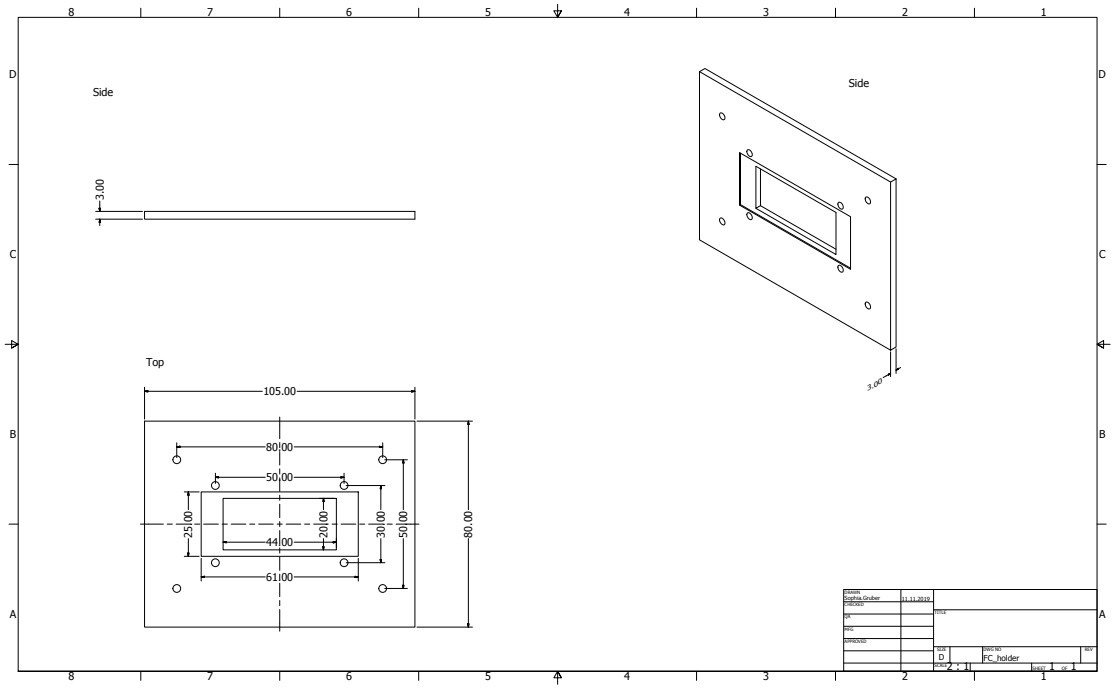

Figure B.3: Technical drawing multichannel FC holder bottom. Bottom of multichannel FC holder; made either of aluminium or iron.

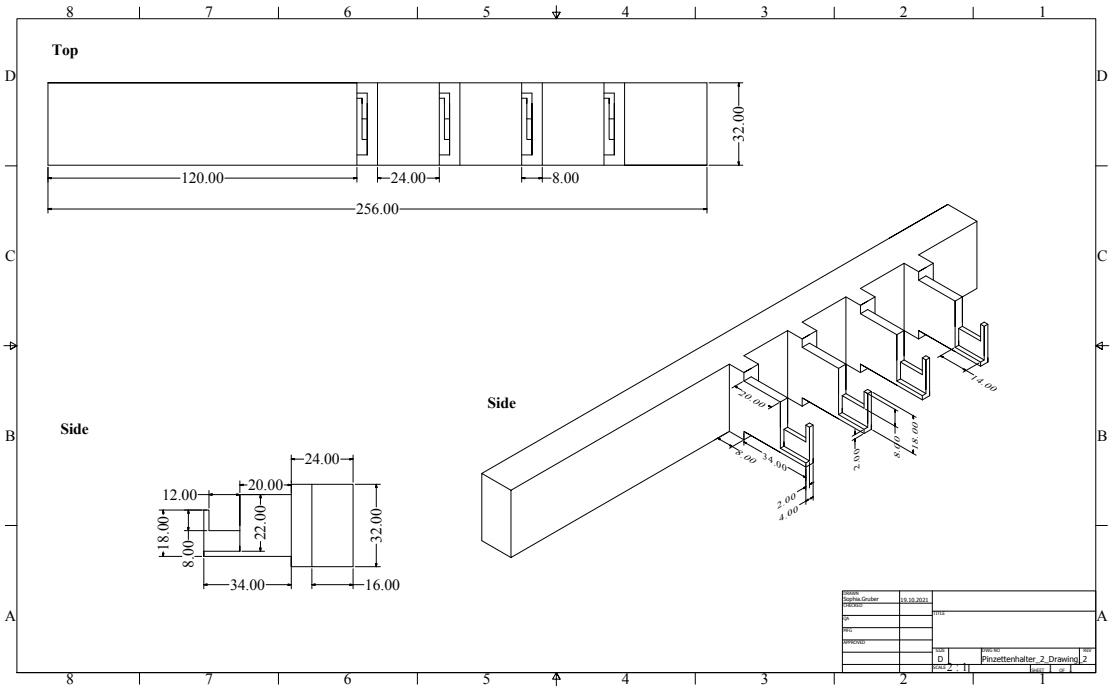

Figure B.4: Technical drawing holder reverse tweezers. Holder for one to four reverse tweezers; made from teflon. Designed by Adina Hausch.

C

Custom MT Setup

Most measurements presented in Chapters 3 and 4 were conducted on a custom setup presented in detail in Dr. Achim Löfs dissertation[76]. The measurements presented in Chapters 5 and 6, as well as some of the measurements in Chapter 4 were conducted on a newly built MT setup, which was assembled and characterized by my Bachelor student Benedikt Böck with my support (Figure C.1A, B). The characterization of the setup can be found in his Bachelor thesis. The camera we implemented has 5120 x 5120 pixels, allowing a FOV of 680 x 680 µm at unprecedented resolution (Figure C.1C, D) and a maximal frame rate of 72 Hz. The setup was calibrated with M270 beads according to a description in the PhD thesis of Dr. Philipp Walker[74] (Figure C.2). Here is a list of components installed in this setup:

part	name	vendor
LED	M625F2	Thorlabs
fiber coupler	PAF2-7B	Thorlabs
multimode fiber	M76L01	Thorlabs
optical rail	X48-0.5	Newport
mounting adapter	EQ80-E	Newport
mounting adapter	EQ80-I	Newport
cage system	CP02T	Thorlabs
translation motor	M-126.PD2	Physical Instruments
rotation motor	C-150.PD	Physical Instruments
motor controllers	C863	Physical Instruments
translation stages	M-UMR8.25	Newport
objective	RMS40X-PFO	Olympus
piezo positioner	P-726.1CD	Physical Instruments
piezo positioner controller	E753	Physical Instruments
mirror	30D20ER	Newport
tube lens	SWTLU-C	Olympus
CMOS camera	CP80-25-M-72	Optronis
framegrabber	CYT-PCE-CXP4	Bitflow
syringe pump	ISM596	Ismatec

Table C.1: Parts implemented into custom MT setup used for most experiments. System was controlled with a custom LabView Code[64].

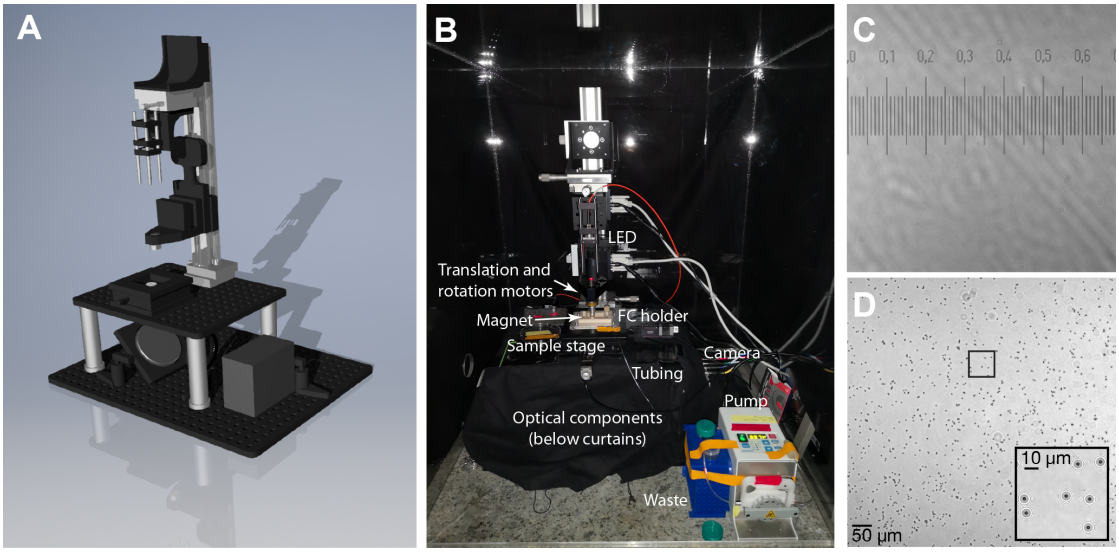

Figure C.1: Custom MT Setup. Custom MT setup. **A** CAD drawing of MT setup. **B** Foto of setup with components indicated. **C** Calibration slide for FOV size determination. FOV size is 680 x 680 µm. **D** Flowcell with M270 dynabeads. More than 150 beads can be tracked simultaneously.

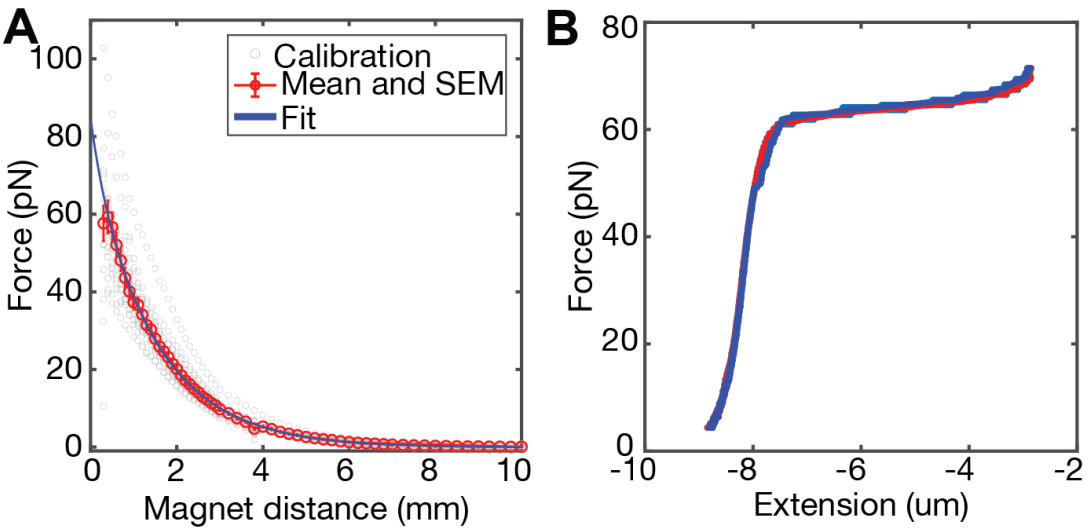

Figure C.2: Calibration of custom MT setup. The setup was calibrated with double-stranded, 21 kbp DNA according to a protocol in Dr. Philip Walkers dissertation[74]. DNA was attached to an amino-silanized glass slide via dig-antidig interaction and to a streptavidin-coated M270 dynabead via a biotin handle. Magnets were moved to a distance of 0.1 mm from the surface of the flowcell and subsequently moved upwards in steps of 0.1 mm. The time spent at each distance was increased according to the expected corner frequency, based on previous calibrations. **A** Forces were calculated based on the Allan variance[68;72;73]. Grey circles correspond to force-distance relations of 18 DNA tethers. Red circles and errorbars show mean and standard error of the mean for these 18 tethers. Blue curve shows a double exponential fit ($a_1 \cdot e^{-x/b_1} + a_2 \cdot e^{-x/b_2} + c$) with fit parameters: a_1 = 10.13, b_1 = 0.31, a_2 = 74.53, b_2 = 1.51, c = -0.08. Force-distance curves of the same molecule in two different field of views (FOVs) with the molecule being in the center in FOV1 and in the right upper corner in FOV2 were compared and showed no qualitative difference. Thus the magnetic force applied throughout the whole FOV seems to be approximately constant. This measurement should however be repeated with more molecules to verify the finding. **B** Overstretching of double-stranded DNA. To check if maximal forces > 65 pN can be obtained, the DNA overstretching transition around 65 pN can be used. In a force-extension plot it is characterized by a sudden lengthening in extension by a factor ≈ 1.7 at forces around 65 pN[58;74]. The blue curve is is the force-extension when increasing the force, while the red curve is the force-extension when decreasing it.

Bibliography

[1] Jeung Hoi Ha and Stewart N. Loh. Protein conformational switches: From nature to design. *Chemistry - A European Journal*, 18(26):7984–7999, jun 2012. ISSN 09476539. doi: 10.1002/chem.201200348.

[2] Edward C. Eckels, Rafael Tapia-Rojo, Jamie Andrés Rivas-Pardo, and Julio M. Fernández. The Work of Titin Protein Folding as a Major Driver in Muscle Contraction. *Annual Review of Physiology*, 80: 327–351, feb 2018. ISSN 15451585. doi: 10.1146/annurev-physiol-021317-121254.

[3] Lukas F. Milles, Klaus Schulten, Hermann E. Gaub, and Rafael C. Bernardi. Molecular mechanism of extreme mechanostability in a pathogen adhesin. *Science*, 359(6383):1527–1533, mar 2018. ISSN 10959203. doi: 10.1126/science.aar2094.

[4] Sophia Gruber, Achim Löf, Steffen M. Sedlak, Martin Benoit, Hermann E. Gaub, and Jan Lipfert. Designed anchoring geometries determine lifetimes of biotin-streptavidin bonds under constant load and enable ultra-stable coupling. *Nanoscale*, 12(41):21131–21137, 2020. ISSN 20403372. doi: 10.1039/d0nr03665j.

[5] Timothy A. Springer. Von Willebrand factor, Jedi knight of the bloodstream. *Blood*, 124(9):1412–1425, aug 2014. ISSN 15280020. doi: 10.1182/blood-2014-05-378638.

[6] Xiaohui Zhang, Kenneth Halvorsen, Cheng Zhong Zhang, Wesley P. Wong, and Timothy A. Springer. Mechanoenzymatic cleavage of the ultralarge vascular protein von willebrand factor. *Science*, 324(5932): 1330–1334, 2009. ISSN 00368075. doi: 10.1126/science.1170905.

[7] Yinon M. Bar-On, Avi Flamholz, Rob Phillips, and Ron Milo. Sars-cov-2 (Covid-19) by the numbers. *eLife*, 9, mar 2020. ISSN 2050084X. doi: 10.7554/eLife.57309.

[8] Ben Hu, Hua Guo, Peng Zhou, and Zheng Li Shi. Characteristics of SARS-CoV-2 and COVID-19. *Nature Reviews Microbiology*, 19(3):141–154, oct 2021. ISSN 17401534. doi: 10.1038/s41579-020-00459-7.

[9] Cody B. Jackson, Michael Farzan, Bing Chen, and Hyeryun Choe. Mechanisms of SARS-CoV-2 entry into cells. *Nature reviews. Molecular cell biology*, pages 1–18, oct 2021. ISSN 1471-0080. doi: 10.1038/s41580-021-00418-x.

[10] Magnus S. Bauer, Sophia Gruber, Adina Hausch, Lukas F. Milles, Thomas Nicolaus, Leonard C. Schendel, Pilar Lopez Navajas, Erik Procko, Daniel Lietha, Rafael C. Bernardi, Hermann E. Gaub, and Jan Lipfert. A Tethered Ligand Assay to Probe SARS-CoV-2:ACE2 Interactions. *bioRxiv*, page 2021.08.08.455468, aug 2021. doi: 10.1101/2021.08.08.455468.

[11] Charlie Laffeber, Kelly de Koning, Roland Kanaar, and Joyce H.G. Lebbink. Experimental Evidence for Enhanced Receptor Binding by Rapidly Spreading SARS-CoV-2 Variants. *Journal of Molecular Biology*, 433(15):167058, jul 2021. ISSN 10898638. doi: 10.1016/j.jmb.2021.167058.

[12] Michael I. Barton, Stuart Macgowan, Mikhail Kutuzov, Omer Dushek, Geoffrey J. Barton, and P. Anton Van Der Merwe. Effects of common mutations in the sars-cov-2 spike rbd and its ligand the human ace2 receptor on binding affinity and kinetics. *eLife*, 10, aug 2021. ISSN 2050084X. doi: 10.7554/eLife.70658.

[13] Shang Yu Gong, Debashree Chatterjee, Jonathan Richard, Jérémie Prévost, Alexandra Tauzin, Romain Gasser, Yuxia Bo, Dani Vézina, Guillaume Goyette, Gabrielle Gendron-Lepage, Halima Medjahed, Michel Roger, Marceline Côté, and Andrés Finzi. Contribution of single mutations to selected SARS-CoV-2 emerging variants spike antigenicity. *bioRxiv*, 563:134–145, aug 2021. doi: 10.1101/2021.08.04.455140.

[14] Maaran Michael Rajah, Mathieu Hubert, Elodie Bishop, Nell Saunders, Remy Robinot, Ludivine Grzelak, Delphine Planas, Jérémy Dufloo, Stacy Gellenoncourt, Alice Bongers, Marija Zivaljic,

Cyril Planchais, Florence Guivel-Benhassine, Françoise Porrot, Hugo Mouquet, Lisa Chakrabarti, Julian Buchrieser, and Olivier Schwartz. SARS-CoV-2 Alpha, Beta and Delta variants display enhanced Spike-mediated Syncytia Formation. *bioRxiv*, page 2021.06.11.448011, aug 2021. doi: 10.1101/2021.06.11.448011.

[15] Sophie M.C. M.-C. Gobeil, Katarzyna Janowska, Shana McDowell, Katayoun Mansouri, Robert Parks, Victoria Stalls, Megan F. Kopp, Kartik Manne, Dapeng Li, Kevin Wiehe, Kevin O. Saunders, Robert J. Edwards, Bette Korber, Barton F. Haynes, Rory Henderson, and Priyamvada Acharya. Effect of natural mutations of SARS-CoV-2 on spike structure, conformation, and antigenicity. *Science*, 373(6555), aug 2021. ISSN 10959203. doi: 10.1126/science.abi6226.

[16] Wenlin Ren, Xiaohui Ju, Mingli Gong, Jun Lan, Yanying Yu, Quanxin Long, Yu Zhang, Jin Zhong, Guocai Zhong, Xinquan Wang, Ailong Huang, Rong Zhang, and Qiang Ding. Characterization of SARS-CoV-2 variants B.1.617.1 (Kappa), B.1.617.2 (Delta) and B.1.618 on cell entry, host range, and sensitivity to convalescent plasma and ACE2 decoy receptor. *bioRxiv*, page 2021.09.03.458829, sep 2021. doi: 10.1101/2021.09.03.458829.

[17] Matthew McCallum, Alexandra C. Walls, Kaitlin R. Sprouse, John E. Bowen, Laura Rosen, Ha V. Dang, Anna DeMarco, Nicholas Franko, Sasha W Tilles, Jennifer Logue, Marcos C. Miranda, Margaret Ahlrichs, Lauren Carter, Gyorgy Snell, Matteo Samuele Pizzuto, Helen Y. Chu, Wesley C Van Voorhis, Davide Corti, and David Veesler. Molecular basis of immune evasion by the delta and kappa SARS-CoV-2 variants. *bioRxiv : the preprint server for biology*, page 2021.08.11.455956, aug 2021. doi: 10.1101/2021.08.11.455956.

[18] Subash Adhikari, Edouard C. Nice, Eric W. Deutsch, Lydie Lane, Gilbert S. Omenn, Stephen R. Pennington, Young Ki Paik, Christopher M. Overall, Fernando J. Corrales, Ileana M. Cristea, Jennifer E. Van Eyk, Mathias Uhlén, Cecilia Lindskog, Daniel W. Chan, Amos Bairoch, James C. Waddington, Joshua L. Justice, Joshua LaBaer, Henry Rodriguez, Fuchu He, Markus Kostrzewa, Peipei Ping, Rebekah L. Gundry, Peter Stewart, Sanjeeva Srivastava, Sudhir Srivastava, Fabio C.S. Nogueira, Gilberto B. Domont, Yves Vandenbrouck, Maggie P.Y. Lam, Sara Wennersten, Juan Antonio Vizcaino, Marc Wilkins, Jochen M. Schwenk, Emma Lundberg, Nuno Bandeira, Gyorgy Marko-Varga, Susan T. Weintraub, Charles Pineau, Ulrike Kusebauch, Robert L. Moritz, Seong Beom Ahn, Magnus Palmblad, Michael P. Snyder, Ruedi Aebersold, and Mark S. Baker. A high-stringency blueprint of the human proteome. *Nature Communications*, 11(1):1–16, oct 2020. ISSN 20411723. doi: 10.1038/s41467-020-19045-9.

[19] Bruce Alberts, Alexander Johnson, Julian Lewis, David Morgan, Martin Raff, Keith Roberts, and Peter Walter. *Molecular Biology of the Cell*. W.W. Norton & Company, aug 2017. ISBN 9781315735368. doi: 10.1201/9781315735368.

[20] John Kuriyan, Boyana Konforti, and David Wemmer. *The Molecules of Life*. W.W. Norton & Company, jul 2012. ISBN 9780429258787. doi: 10.1201/9780429258787.

[21] Shibom Basu, Aaron Finke, Laura Vera, Meitian Wang, and Vincent Olieric. Making routine native SAD a reality: lessons from beamline X06DA at the Swiss Light Source. *Acta Crystallographica Section D: Structural Biology*, 75(3):262–271, mar 2019. ISSN 20597983. doi: 10.1107/S2059798319003103.

[22] William Humphrey, Andrew Dalke, and Klaus Schulten. VMD: Visual molecular dynamics. *Journal of Molecular Graphics*, 14(1):33–38, feb 1996. ISSN 02637855. doi: 10.1016/0263-7855(96)00018-5.

[23] Tapan K. Chaudhuri and Subhankar Paul. Protein-misfolding diseases and chaperone-based therapeutic approaches. *FEBS Journal*, 273(7):1331–1349, apr 2006. ISSN 1742464X. doi: 10.1111/j.1742-4658.2006.05181.x.

[24] Abhisek Mukherjee and Claudio Soto. Prion-like protein aggregates and type 2 diabetes. *Cold Spring Harbor Perspectives in Medicine*, 7(5), may 2017. ISSN 21571422. doi: 10.1101/cshperspect.a024315.

[25] Xiao chen Bai, Greg McMullan, and Sjors H.W Scheres. How cryo-EM is revolutionizing structural biology. *Trends in Biochemical Sciences*, 40(1):49–57, jan 2015. ISSN 13624326. doi: 10.1016/j.tibs.2014.10.005.

[26] Ewen Callaway. The revolution will not be crystallized: A new method sweeps through structural biology. *Nature*, 525(7568):172–174, sep 2015. ISSN 14764687. doi: 10.1038/525172a.

[27] Yigong Shi. A glimpse of structural biology through X-ray crystallography. *Cell*, 159(5):995–1014, nov 2014. ISSN 10974172. doi: 10.1016/j.cell.2014.10.051.

[28] K. Wuthrich. Protein structure determination in solution by NMR spectroscopy. *Journal of Biological Chemistry*, 265(36):22059–22062, 1990. ISSN 00219258. doi: 10.1016/s0021-9258(18)45665-7.

[29] Sheng Wang, Jian Peng, Jianzhu Ma, and Jinbo Xu. Protein Secondary Structure Prediction Using Deep Convolutional Neural Fields. *Scientific Reports*, 6(1):1–11, jan 2016. ISSN 20452322. doi: 10.1038/srep18962.

[30] Ken A. Dill and Justin L. MacCallum. The protein-folding problem, 50 years on. *Science*, 338(6110): 1042–1046, nov 2012. ISSN 10959203. doi: 10.1126/science.1219021.

[31] Brian Kuhlman and Philip Bradley. Advances in protein structure prediction and design. *Nature Reviews Molecular Cell Biology*, 20(11):681–697, aug 2019. ISSN 14710080. doi: 10.1038/s41580-019-0163-x.

[32] Mohammed Alquraishi. AlphaFold at CASP13. *Bioinformatics*, 35(22):4862–4865, nov 2019. ISSN 14602059. doi: 10.1093/bioinformatics/btz422.

[33] Mohammed AlQuraishi. A watershed moment for protein structure prediction. *Nature*, 577(7792): 627–628, jan 2020. ISSN 14764687. doi: 10.1038/d41586-019-03951-0.

[34] Joseph M. Cunningham, Grigoriy Koytiger, Peter K. Sorger, and Mohammed AlQuraishi. Biophysical prediction of protein–peptide interactions and signaling networks using machine learning. *Nature Methods*, 17(2):175–183, jan 2020. ISSN 15487105. doi: 10.1038/s41592-019-0687-1.

[35] Keir C. Neuman and Attila Nagy. Single-molecule force spectroscopy: Optical tweezers, magnetic tweezers and atomic force microscopy. *Nature Methods*, 5(6):491–505, 2008. ISSN 15487091. doi: 10.1038/nmeth.1218.

[36] Paola Fucini, Christian Renner, Christoph Herberhold, Angelika A. Noegel, and Tad A. Holak. The repeating segments of the F-actin cross-linking gelation factor (ABP-120) have an immunoglobulin-like fold. *Nature Structural Biology*, 4(3):223–230, mar 1997. ISSN 10728368. doi: 10.1038/nsb0397-223.

[37] Ingo Schwaiger, Angelika Kardinal, Michael Schleicher, Angelika A. Noegel, and Matthias Rief. A mechanical unfolding intermediate in an actin-crosslinking protein. *Nature Structural and Molecular Biology*, 11(1):81–85, jan 2004. ISSN 15459993. doi: 10.1038/nsmb705.

[38] Achim Löf, Philipp U. Walker, Steffen M. Sedlak, Sophia Gruber, Tobias Obser, Maria A. Brehm, Martin Benoit, and Jan Lipfert. Multiplexed protein force spectroscopy reveals equilibrium protein folding dynamics and the low-force response of von Willebrand factor. *Proceedings of the National Academy of Sciences of the United States of America*, 116(38):18798–18807, sep 2019. ISSN 10916490. doi: 10.1073/pnas.1901794116.

[39] Allison B. Churnside and Thomas T. Perkins. Ultrastable atomic force microscopy: Improved force and positional stability. *FEBS Letters*, 588(19):3621–3630, oct 2014. ISSN 18733468. doi: 10.1016/j.febslet.2014.04.033.

[40] Byeongseon Yang, Zhaowei Liu, Haipei Liu, and Michael A. Nash. Next Generation Methods for Single-Molecule Force Spectroscopy on Polyproteins and Receptor-Ligand Complexes. *Frontiers in Molecular Biosciences*, 7(May):1–19, may 2020. ISSN 2296889X. doi: 10.3389/fmolb.2020.00085.

[41] Ernst Ludwig Florin, Vincent T. Moy, and Hermann E. Gaub. Adhesion forces between individual ligand-receptor pairs. *Science*, 264(5157):415–417, 1994. ISSN 00368075. doi: 10.1126/science.8153628.

[42] Matthias Rief, Mathias Gautel, Filipp Oesterhelt, Julio M. Fernandez, and Hermann E. Gaub. Reversible unfolding of individual titin immunoglobulin domains by AFM. *Science*, 276(5315):1109–1112, may 1997. ISSN 00368075. doi: 10.1126/science.276.5315.1109.

[43] F. Oesterhelt, D. Oesterhelt, M. Pfeiffer, A. Engel, H. E. Gaub, and D. J. Müller. Unfolding pathways of individual bacteriorhodopsins. *Science*, 288(5463):143–146, apr 2000. ISSN 00368075. doi: 10.1126/science.288.5463.143.

[44] Elias M. Puchner and Hermann E. Gaub. Force and function: probing proteins with AFM-based force spectroscopy. *Current Opinion in Structural Biology*, 19(5):605–614, oct 2009. ISSN 0959440X. doi: 10.1016/j.sbi.2009.09.005.

[45] Julio M. Fernandez and Hongbin Li. Force-Clamp Spectroscopy Monitors the Folding Trajectory of a Single Protein. *Science*, 303(5664):1674–1678, mar 2004. ISSN 00368075. doi: 10.1126/science.1092497.

[46] Gil U. Lee, Linda A. Chrisey, and Richard J. Colton. Direct measurement of the forces between complementary strands of DNA. *Science*, 266(5186):771–773, 1994. ISSN 00368075. doi: 10.1126/science.7973628.

[47] Michel Grandbois, Martin Beyer, Matthias Rief, Hauke Clausen-Schaumann, and Hermann E. Gaub. How strong is a covalent bond. *Science*, 283(5408):1727–1730, mar 1999. ISSN 00368075. doi: 10.1126/science.283.5408.1727.

[48] Devin T. Edwards, Jaevyn K. Faulk, Marc André LeBlanc, and Thomas T. Perkins. Force Spectroscopy with 9-μs Resolution and Sub-pN Stability by Tailoring AFM Cantilever Geometry. *Biophysical Journal*, 113(12):2595–2600, dec 2017. ISSN 15420086. doi: 10.1016/j.bpj.2017.10.023.

[49] Devin T. Edwards and Thomas T. Perkins. Optimizing force spectroscopy by modifying commercial cantilevers: Improved stability, precision, and temporal resolution. *Journal of Structural Biology*, 197(1): 13–25, jan 2017. ISSN 10958657. doi: 10.1016/j.jsb.2016.01.009.

[50] Douglas E. Smith, Sander J. Tans, Steven B. Smith, Shelley Grimes, Dwight L. Anderson, and Carlos Bustamante. The bacteriophage ϕ29 portal motor can package DNA against a large internal force. *Nature*, 413(6857):748–752, oct 2001. ISSN 00280836. doi: 10.1038/35099581.

[51] Steven M. Block, Lawrence S.B. Goldstein, and Bruce J. Schnapp. Bead movement by single kinesin molecules studied with optical tweezers. *Nature*, 348(6299):348–352, 1990. ISSN 00280836. doi: 10.1038/348348a0.

[52] Miklós S.Z. Kellermayer, Steven B. Smith, Henk L. Granzier, and Carlos Bustamante. Folding-unfolding transitions in single titin molecules characterized with laser tweezers. *Science*, 276(5315):1112–1116, may 1997. ISSN 00368075. doi: 10.1126/science.276.5315.1112.

[53] Jan Liphardt, Bibiana Onoa, Steven B. Smith, Jr Tinoco I., and Carlos Bustamante. Reversible unfolding of single RNA molecules by mechanical force. *Science*, 292(5517):733–737, apr 2001. ISSN 00368075. doi: 10.1126/science.1058498.

[54] Ken Halvorsen and Wesley P. Wong. Massively parallel single-molecule manipulation using centrifugal force. *Biophysical Journal*, 98(11):L53–L55, jun 2010. ISSN 15420086. doi: 10.1016/j.bpj.2010.03.012.

[55] Darren Yang, Andrew Ward, Ken Halvorsen, and Wesley P. Wong. Multiplexed single-molecule force spectroscopy using a centrifuge. *Nature Communications*, 7(1):1–7, mar 2016. ISSN 20411723. doi: 10.1038/ncomms11026.

[56] Michael W.H. Kirkness and Nancy R. Forde. Single-Molecule Assay for Proteolytic Susceptibility: Force-Induced Collagen Destabilization. *Biophysical Journal*, 114(3):570–576, feb 2018. ISSN 15420086. doi: 10.1016/j.bpj.2017.12.006.

[57] Gerrit Sitters, Douwe Kamsma, Gregor Thalhammer, Monika Ritsch-Marte, Erwin J.G. Peterman, and Gijs J.L. Wuite. Acoustic force spectroscopy. *Nature Methods*, 12(1):47–50, nov 2014. ISSN 15487105. doi: 10.1038/nmeth.3183.

[58] Franziska Kriegel, Niklas Ermann, and Jan Lipfert. Probing the mechanical properties, conformational changes, and interactions of nucleic acids with magnetic tweezers. *Journal of Structural Biology*, 197(1): 26–36, 2017. ISSN 10958657. doi: 10.1016/j.jsb.2016.06.022.

[59] Jan Lipfert, Xiaomin Hao, and Nynke H. Dekker. Quantitative modeling and optimization of magnetic tweezers. *Biophysical Journal*, 96(12):5040–5049, jun 2009. ISSN 15420086. doi: 10.1016/j.bpj.2009.03.055.

[60] Alvaro Alonso-Caballero, Rafael Tapia-Rojo, Carmen L. Badilla, and Julio M. Fernandez. Magnetic tweezers meets AFM: ultra-stable protein dynamics across the force spectrum. *bioRxiv*, pages 1–22, jan 2021. doi: 10.1101/2021.01.04.425265.

[61] Ruchuan Liu, Sergi Garcia-Manyes, Atom Sarkar, Carmen L. Badilla, and Julio M. Fernández. Mechanical characterization of protein L in the low-force regime by electromagnetic tweezers/evanescent nanometry. *Biophysical Journal*, 96(9):3810–3821, may 2009. ISSN 15420086. doi: 10.1016/j.bpj.2009.01.043.

[62] Iwijn de Vlaminck, Thomas Henighan, Marijn T.J. van Loenhout, Daniel R. Burnham, and Cees Dekker. Magnetic forces and dna mechanics in multiplexed magnetic tweezers. *PLoS ONE*, 7(8):e41432, 2012. ISSN 19326203. doi: 10.1371/journal.pone.0041432.

[63] Xiaodan Zhao, Xiangjun Zeng, Chen Lu, and Jie Yan. Studying the mechanical responses of proteins using magnetic tweezers. *Nanotechnology*, 28(41), 2017. ISSN 13616528. doi: 10.1088/1361-6528/aa837e.

[64] J. P. Cnossen, D. Dulin, and N. H. Dekker. An optimized software framework for real-time, high-throughput tracking of spherical beads. *Review of Scientific Instruments*, 85(10):103712, oct 2014. ISSN 10897623. doi: 10.1063/1.4898178.

[65] Zhongbo Yu, David Dulin, Jelmer Cnossen, Mariana Köber, Maarten M. Van Oene, Orkide Ordu, Bojk A. Berghuis, Toivo Hensgens, Jan Lipfert, and Nynke H. Dekker. A force calibration standard for magnetic tweezers. *Review of Scientific Instruments*, 85(12):123114, dec 2014. ISSN 10897623. doi: 10.1063/1.4904148.

[66] Charlie Gosse and Vincent Croquette. Magnetic tweezers: Micromanipulation and force measurement at the molecular level. *Biophysical Journal*, 82(6):3314–3329, jun 2002. ISSN 00063495. doi: 10.1016/S0006-3495(02)75672-5.

[67] Peter Daldrop, Hergen Brutzer, Alexander Huhle, Dominik J. Kauert, and Ralf Seidel. Extending the range for force calibration in magnetic tweezers. *Biophysical Journal*, 108(10):2550–2561, may 2015. ISSN 15420086. doi: 10.1016/j.bpj.2015.04.011.

[68] Aartjan J.W. Te Velthuis, Jacob W.J. Kerssemakers, Jan Lipfert, and Nynke H. Dekker. Quantitative guidelines for force calibration through spectral analysis of magnetic tweezers data. *Biophysical Journal*, 99(4):1292–1302, aug 2010. ISSN 15420086. doi: 10.1016/j.bpj.2010.06.008.

[69] Hu Chen, Hongxia Fu, Xiaoying Zhu, Peiwen Cong, Fumihiko Nakamura, and Jie Yan. Improved high-force magnetic tweezers for stretching and refolding of proteins and short DNA. *Biophysical Journal*, 100 (2):517–523, jan 2011. ISSN 15420086. doi: 10.1016/j.bpj.2010.12.3700.

[70] T. R. Strick, J. F. Allemand, D. Bensimon, A. Bensimon, and V. Croquette. The elasticity of a single supercoiled DNA molecule. *Science*, 271(5257):1835–1837, 1996. ISSN 00368075. doi: 10.1126/science.271.5257.1835.

[71] Wesley P. Wong and Ken Halvorsen. The effect of integration time on fluctuation measurements: calibrating an optical trap in the presence of motion blur. *Optics Express*, 14(25):12517, dec 2006. ISSN 1094-4087. doi: 10.1364/oe.14.012517.

[72] David W. Allan. Statistics of Atomic Frequency Standards. *Proceedings of the IEEE*, 54(2):221–230, 1966. ISSN 15582256. doi: 10.1109/PROC.1966.4634.

[73] Bob M. Lansdorp and Omar A. Saleh. Power spectrum and Allan variance methods for calibrating single-molecule video-tracking instruments. *Review of Scientific Instruments*, 83(2), 2012. ISSN 00346748. doi: 10.1063/1.3687431.

[74] Philipp U. Walker. *Fast Dynamics of Biological Systems Investigated with Magnetic Tweezers and Small-Angle X-Ray Scattering*. Phd thesis, LMU Munich, 2018.

[75] Achim Löf, Jochen P. Müller, and Maria A. Brehm. A biophysical view on von Willebrand factor activation. *Journal of Cellular Physiology*, 233(2):799–810, feb 2018. ISSN 10974652. doi: 10.1002/jcp.25887.

[76] Achim Löf. *Single-molecule mechanics and regulatory conformational transitions of the force-sensing protein von Willebrand factor*. Phd thesis, LMU Munich, 2019.

[77] Eugen Ostrofet, Flávia Stal Papini, and David Dulin. Correction-free force calibration for magnetic tweezers experiments. *Scientific Reports*, 8(1):1–10, oct 2018. ISSN 20452322. doi: 10.1038/s41598-018-34360-4.

[78] Ionel Popa, Jaime Andrés Rivas-Pardo, Edward C. Eckels, Daniel J. Echelman, Carmen L. Badilla, Jessica Valle-Orero, and Julio M. Fernández. A HaloTag Anchored Ruler for Week-Long Studies of Protein Dynamics. *Journal of the American Chemical Society*, 138(33):10546–10553, aug 2016. ISSN 15205126. doi: 10.1021/jacs.6b05429.

[79] I. D. Vilfan, J. Lipfert, D. A. Koster, S. G. Lemay, and N. H. Dekker. Magnetic Tweezers for Single-Molecule Experiments. In Peter Hinterdorfer and Antoine Oijen, editors, *Handbook of Single-Molecule Biophysics*, pages 371–395. Springer US, New York, NY, 2009. ISBN 978-0-387-76497-9. doi: 10.1007/978-0-387-76497-9-13.

[80] Jan Lipfert, Jacob W.J. Kerssemakers, Tessa Jager, and Nynke H. Dekker. Magnetic torque tweezers: Measuring torsional stiffness in DNA and RecA-DNA filaments. *Nature Methods*, 7(12):977–980, dec 2010. ISSN 15487091. doi: 10.1038/nmeth.1520.

[81] Zev Bryant, Michael D. Stone, Jeff Gore, Steven B. Smith, Nicholas R. Cozzarelli, and Carlos Bustamante. Structural transitions and elasticity from torque measurements on DNA. *Nature*, 424(6946):338–341, jul 2003. ISSN 00280836. doi: 10.1038/nature01810.

[82] Maxim Y. Sheinin, Scott Forth, John F. Marko, and Michelle D. Wang. Underwound DNA under tension: Structure, elasticity, and sequence-dependent behaviors. *Physical Review Letters*, 107(10):108102, sep 2011. ISSN 00319007. doi: 10.1103/PhysRevLett.107.108102.

[83] Zev Bryant, Florian C. Oberstrass, and Aakash Basu. Recent developments in single-molecule DNA mechanics. *Current Opinion in Structural Biology*, 22(3):304–312, jun 2012. ISSN 0959440X. doi: 10.1016/j.sbi.2012.04.007.

[84] David Dulin, Bojk A. Berghuis, Martin Depken, and Nynke H. Dekker. Untangling reaction pathways through modern approaches to high-throughput single-molecule force-spectroscopy experiments. *Current Opinion in Structural Biology*, 34:116–122, oct 2015. ISSN 1879033X. doi: 10.1016/j.sbi.2015.08.007.

[85] David Dulin, Jan Lipfert, M. Charl Moolman, and Nynke H. Dekker. Studying genomic processes at the single-molecule level: Introducing the tools and applications. *Nature Reviews Genetics*, 14(1):9–22, oct 2013. ISSN 14710056. doi: 10.1038/nrg3316.

[86] Jan Lipfert, Maarten M. Van Oene, Mina Lee, Francesco Pedaci, and Nynke H. Dekker. Torque spectroscopy for the study of rotary motion in biological systems. *Chemical Reviews*, 115(3):1449–1474, feb 2015. ISSN 15206890. doi: 10.1021/cr500119k.

[87] Sangjin Kim, Paul C Blainey, Charles M Schroeder, and X Sunney Xie. Multiplexed single-molecule assay for enzymatic activity on flow-stretched DNA. *Nature Methods*, 4(5):397–399, apr 2007. ISSN 15487091. doi: 10.1038/nmeth1037.

[88] Rohit Agarwal and Karl E. Duderstadt. Multiplex flow magnetic tweezers reveal rare enzymatic events with single molecule precision. *Nature Communications*, 11(1):1–10, sep 2020. ISSN 20411723. doi: 10.1038/s41467-020-18456-y.

[89] Hu Chen, Guohua Yuan, Ricksen S. Winardhi, Mingxi Yao, Ionel Popa, Julio M. Fernandez, and Jie Yan. Dynamics of Equilibrium Folding and Unfolding Transitions of Titin Immunoglobulin Domain under Constant Forces. *Journal of the American Chemical Society*, 137(10):3540–3546, mar 2015. ISSN 15205126. doi: 10.1021/ja5119368.

[90] Jessica Valle-Orero, Jaime Andrés Rivas-Pardo, and Ionel Popa. Multidomain proteins under force. *Nanotechnology*, 28(17):174003, apr 2017. ISSN 13616528. doi: 10.1088/1361-6528/aa655e.

[91] Rafayel Petrosyan. Improved approximations for some polymer extension models. *Rheologica Acta*, 56 (1):21–26, oct 2017. ISSN 00354511. doi: 10.1007/s00397-016-0977-9.

[92] Angelo Perico, Sergio Bisio, and Carla Cuniberti. Polymer Dynamics in Dilute Solutions. The Freely Rotating Chain. *Macromolecules*, 17(12):2686–2689, 1984. ISSN 15205835. doi: 10.1021/ma00142a041.

[93] George I. Bell. Models for the specific adhesion of cells to cells. *Science*, 200(4342):618–627, may 1978. ISSN 00368075. doi: 10.1126/science.347575.

[94] Elena Pérez-Ruiz, Marijn Kemper, Dragana Spasic, Ann Gils, Leo J. Van Ijzendoorn, Jeroen Lammertyn, and Menno W.J. Prins. Probing the force-induced dissociation of aptamer-protein complexes. *Analytical Chemistry*, 86(6):3084–3091, mar 2014. ISSN 15206882. doi: 10.1021/ac404107s.

[95] Arjun S. Adhikari, Jack Chai, and Alexander R. Dunn. Mechanical load induces a 100-fold increase in the rate of collagen proteolysis by MMP-1. *Journal of the American Chemical Society*, 133(6):1686–1689, feb 2011. ISSN 00027863. doi: 10.1021/ja109972p.

[96] Arjun S. Adhikari, Emerson Glassey, and Alexander R. Dunn. Conformational dynamics accompanying the proteolytic degradation of trimeric collagen I by collagenases. *Journal of the American Chemical Society*, 134(32):13259–13265, aug 2012. ISSN 00027863. doi: 10.1021/ja212170b.

[97] Armando Del Rio, Raul Perez-Jimenez, Ruchuan Liu, Pere Roca-Cusachs, Julio M. Fernandez, and Michael P. Sheetz. Stretching single talin rod molecules activates vinculin binding. *Science*, 323(5914): 638–641, jan 2009. ISSN 00368075. doi: 10.1126/science.1162912.

[98] Hu Chen, Saranya Chandrasekar, Michael P. Sheetz, Thomas P. Stossel, Fumihiko Nakamura, and Jie Yan. Mechanical perturbation of filamin A immunoglobulin repeats 20-21 reveals potential non-equilibrium mechanochemical partner binding function. *Scientific Reports*, 3(1):1–6, apr 2013. ISSN 20452322. doi: 10.1038/srep01642.

[99] Hu Chen, Xiaoying Zhu, Peiwen Cong, Michael P. Sheetz, Fumihiko Nakamura, and Jie Yan. Differential mechanical stability of filamin A rod segments. *Biophysical Journal*, 101(5):1231–1237, sep 2011. ISSN 00063495. doi: 10.1016/j.bpj.2011.07.028.

[100] Mingxi Yao, Wu Qiu, Ruchuan Liu, Artem K. Efremov, Peiwen Cong, Rima Seddiki, Manon Payre, Chwee Teck Lim, Benoit Ladoux, René Marc Mège, and Jie Yan. Force-dependent conformational switch of α -catenin controls vinculin binding. *Nature Communications*, 5(1):1–12, jul 2014. ISSN 20411723. doi: 10.1038/ncomms5525.

[101] Mingxi Yao, Benjamin T. Goult, Hu Chen, Peiwen Cong, Michael P. Sheetz, and Jie Yan. Mechanical activation of vinculin binding to talin locks talin in an unfolded conformation. *Scientific Reports*, 4(1): 1–7, apr 2014. ISSN 20452322. doi: 10.1038/srep04610.

[102] Yukinori Taniguchi and Masaru Kawakami. Application of Halotag protein to covalent immobilization of recombinant proteins for single molecule force spectroscopy. *Langmuir*, 26(13):10433–10436, jul 2010. ISSN 07437463. doi: 10.1021/la101658a.

[103] Ionel Popa, Ronen Berkovich, Jorge Alegre-Cebollada, Carmen L. Badilla, Jaime Andrés Rivas-Pardo, Yukinori Taniguchi, Masaru Kawakami, and Julio M. Fernandez. Nanomechanics of HaloTag tethers. *Journal of the American Chemical Society*, 135(34):12762–12771, aug 2013. ISSN 00027863. doi: 10.1021/ja4056382.

[104] Shubhasis Haldar, Rafael Tapia-Rojo, Edward C. Eckels, Jessica Valle-Orero, and Julio M. Fernandez. Trigger factor chaperone acts as a mechanical foldase. *Nature Communications*, 8(1):1–7, sep 2017. ISSN 20411723. doi: 10.1038/s41467-017-00771-6.

[105] Jaime Andrés Rivas-Pardo, Yong Li, Zsolt Mártonfalvi, Rafael Tapia-Rojo, Andreas Unger, Ángel Fernández-Trasancos, Elías Herrero-Galán, Diana Velázquez-Carreras, Julio M. Fernández, Wolfgang A. Linke, and Jorge Alegre-Cebollada. A HaloTag-TEV genetic cassette for mechanical phenotyping of proteins from tissues. *Nature Communications*, 11(1):1–13, apr 2020. ISSN 20411723. doi: 10.1038/s41467-020-15465-9.

[106] Rafael Tapia-Rojo, Alvaro Alonso-Caballero, and Julio M. Fernandez. Direct observation of a coil-to-helix contraction triggered by vinculin binding to talin. *Science Advances*, 6(21):4707–4729, may 2020. ISSN 23752548. doi: 10.1126/sciadv.aaz4707.

[107] Rafael Tapia-Rojo, Álvaro Alonso-Caballero, and Julio M. Fernández. Talin folding as the tuning fork of cellular mechanotransduction. *Proceedings of the National Academy of Sciences of the United States of America*, 117(35):21346–21353, sep 2020. ISSN 10916490. doi: 10.1073/pnas.2004091117.

[108] Rafael Tapia-Rojo, Edward C. Eckels, and Julio M. Fernández. Ephemeral states in protein folding under force captured with a magnetic tweezers design. *Proceedings of the National Academy of Sciences of the United States of America*, 116(16):7873–7878, apr 2019. ISSN 10916490. doi: 10.1073/pnas.1821284116.

[109] Guohua Yuan, Shimin Le, Mingxi Yao, Hui Qian, Xin Zhou, Jie Yan, and Hu Chen. Elasticity of the Transition State Leading to an Unexpected Mechanical Stabilization of Titin Immunoglobulin Domains. *Angewandte Chemie*, 129(20):5582–5585, may 2017. ISSN 1521-3757. doi: 10.1002/ange.201700411.

[110] Mingxi Yao, Benjamin T. Goult, Benjamin Klapholz, Xian Hu, Christopher P. Toseland, Yingjian Guo, Peiwen Cong, Michael P. Sheetz, and Jie Yan. The mechanical response of talin. *Nature Communications*, 7(1):1–11, jul 2016. ISSN 20411723. doi: 10.1038/ncomms11966.

[111] Jaime Andrés Rivas-Pardo, Edward C. Eckels, Ionel Popa, Pallav Kosuri, Wolfgang A. Linke, and Julio M. Fernández. Work Done by Titin Protein Folding Assists Muscle Contraction. *Cell Reports*, 14(6):1339–1347, feb 2016. ISSN 22111247. doi: 10.1016/j.celrep.2016.01.025.

[112] Bijan Zakeri, Jacob O. Fierer, Emrah Celik, Emily C. Chittock, Ulrich Schwarz-Linek, Vincent T. Moy, and Mark Howarth. Peptide tag forming a rapid covalent bond to a protein, through engineering a bacterial adhesin. *Proceedings of the National Academy of Sciences of the United States of America*, 109(12):E690–E697, mar 2012. ISSN 00278424. doi: 10.1073/pnas.1115485109.

[113] Alvaro Alonso-Caballero, Daniel J. Echelman, Rafael Tapia-Rojo, Shubhasis Haldar, Edward C. Eckels, and Julio M. Fernandez. Protein folding modulates the chemical reactivity of a Gram-positive adhesin. *Nature Chemistry*, 13(2):172–181, nov 2021. ISSN 17554349. doi: 10.1038/s41557-020-00586-x.

[114] Narayan Dahal, Joel Nowitzke, Annie Eis, and Ionel Popa. Binding-Induced Stabilization Measured on the Same Molecular Protein Substrate Using Single-Molecule Magnetic Tweezers and Heterocovalent Attachments. *Journal of Physical Chemistry B*, 124(16):3283–3290, feb 2020. ISSN 15205207. doi: 10.1021/acs.jpcb.0c00167.

[115] Shimin Le, Xian Hu, Mingxi Yao, Hu Chen, Miao Yu, Xiaochun Xu, Naotaka Nakazawa, Felix M. Margadant, Michael P. Sheetz, and Jie Yan. Mechanotransmission and Mechanosensing of Human alpha-Actinin 1. *Cell Reports*, 21(10):2714–2723, dec 2017. ISSN 22111247. doi: 10.1016/j.celrep.2017.11.040.

[116] Shimin Le, Miao Yu, and Jie Yan. Direct single-molecule quantification reveals unexpectedly high mechanical stability of vinculin—talin/α-catenin linkages. *Science Advances*, 5(12):eaav2720, 2019. ISSN 23752548. doi: 10.1126/sciadv.aav2720.

[117] Huanhuan Su, Hao Sun, Haiyan Hong, Zilong Guo, Ping Yu, and Hu Chen. Equilibrium folding and unfolding dynamics to reveal detailed free energy landscape of src SH3 protein by magnetic tweezers. *Chinese Physics B*, 30(7):078201, jul 2021. ISSN 20583834. doi: 10.1088/1674-1056/abfb56.

[118] Domenica Spadaro, Shimin Le, Thierry Laroche, Isabelle Mean, Lionel Jond, Jie Yan, and Sandra Citi. Tension-Dependent Stretching Activates ZO-1 to Control the Junctional Localization of Its Interactors. *Current Biology*, 27(24):3783–3795.e8, dec 2017. ISSN 09609822. doi: 10.1016/j.cub.2017.11.014.

[119] Jun Yin, Paul D. Straight, Shaun M. McLoughlin, Zhe Zhou, Alison J. Lin, David E. Golan, Neil L. Kelleher, Roberto Kolter, and Christopher T. Walsh. Genetically encoded short peptide tag for versatile protein labeling by Sfp phosphopantetheinyl transferase. *Proceedings of the National Academy of Sciences of the United States of America*, 102(44):15815–15820, nov 2005. ISSN 00278424. doi: 10.1073/pnas.0507705102.

[120] Wolfgang Ott, Markus A. Jobst, Magnus S. Bauer, Ellis Durner, Lukas F. Milles, Michael A. Nash, and Hermann E. Gaub. Elastin-like Polypeptide Linkers for Single-Molecule Force Spectroscopy. *ACS Nano*, 11(6):6346–6354, jun 2017. ISSN 1936086X. doi: 10.1021/acsnano.7b02694.

[121] Jingqi Lv, Yingfeng Li, Kai Zhou, Pei Guo, Yang Liu, Ke Ding, Ke Li, Chao Zhong, and Botao Xiao. Force spectra of single bacterial amyloid CsgA nanofibers. *RSC Advances*, 10(37):21986–21992, jun 2020. ISSN 20462069. doi: 10.1039/d0ra02749a.

[122] Ian L Morgan, Ram Avinery, Gil Rahamim, Roy Beck, and Omar A Saleh. Glassy Dynamics and Memory Effects in an Intrinsically Disordered Protein Construct. *Physical Review Letters*, 125(5), 2020. ISSN 10797114. doi: 10.1103/PhysRevLett.125.058001.

[123] Qing Guo, Yufan He, and H. Peter Lu. Manipulating and probing enzymatic conformational fluctuations and enzyme-substrate interactions by single-molecule FRET-magnetic tweezers microscopy. *Physical Chemistry Chemical Physics*, 16(26):13052–13058, jun 2014. ISSN 14639076. doi: 10.1039/c4cp01454e.

[124] Qing Guo, Yufan He, and H. Peter Lu. Interrogating the activities of conformational deformed enzyme by single-molecule fluorescencemagnetic tweezers microscopy. *Proceedings of the National Academy of Sciences of the United States of America*, 112(45):13904–13909, nov 2015. ISSN 10916490. doi: 10.1073/pnas.1506405112.

[125] Irwin Chen, Brent M. Dorr, and David R. Liu. A general strategy for the evolution of bond-forming enzymes using yeast display. *Proceedings of the National Academy of Sciences of the United States of America*, 108(28):11399–11404, jul 2011. ISSN 00278424. doi: 10.1073/pnas.1101046108.

[126] Ellis Durner, Wolfgang Ott, Michael A. Nash, and Hermann E. Gaub. Post-Translational Sortase-Mediated Attachment of High-Strength Force Spectroscopy Handles. *ACS Omega*, 2(6):3064–3069, jun 2017. ISSN 24701343. doi: 10.1021/acsomega.7b00478.

[127] Wolfgang Ott, Ellis Durner, and Hermann E. Gaub. Enzyme-Mediated, Site-Specific Protein Coupling Strategies for Surface-Based Binding Assays. *Angewandte Chemie - International Edition*, 57(39): 12666–12669, 2018. ISSN 15213773. doi: 10.1002/anie.201805034.

[128] O. H. Laitinen, V. P. Hytönen, H. R. Nordlund, and M. S. Kulomaa. Genetically engineered avidins and streptavidins. *Cellular and Molecular Life Sciences*, 63(24):2992–3017, dec 2006. ISSN 1420682X. doi: 10.1007/s00018-006-6288-z.

[129] Christopher M. Dundas, Daniel Demonte, and Sheldon Park. Streptavidin-biotin technology: Improvements and innovations in chemical and biological applications. *Applied Microbiology and Biotechnology*, 97(21):9343–9353, nov 2013. ISSN 01757598. doi: 10.1007/s00253-013-5232-z.

[130] Meir Wilchek and Edward A. Bayer. The avidin-biotin complex in bioanalytical applications. *Analytical Biochemistry*, 171(1):1–32, may 1988. ISSN 10960309. doi: 10.1016/0003-2697(88)90120-0.

[131] Vladimir V. Didenko. Biotinylation of DNA on membrane supports: A procedure for preparation and easy control of labeling of nonradioactive single-stranded nucleic acid probes. *Analytical Biochemistry*, 213(1):75–78, aug 1993. ISSN 10960309. doi: 10.1006/abio.1993.1388.

[132] Franziska Kriegel, Willem Vanderlinden, Thomas Nicolaus, Angelika Kardinal, and Jan Lipfert. Measuring single-molecule twist and torque in multiplexed magnetic tweezers. *Methods in Molecular Biology*, 1814:75–98, 2018. ISSN 10643745. doi: 10.1007/978-1-4939-8591-36.

[133] Edward A. Bayer and Meir Wilchek. Protein biotinylation. *Methods in Enzymology*, 184(C):138–160, 1990. ISSN 15577988. doi: 10.1016/0076-6879(90)84268-L.

[134] Millard G. Cull and Peter J. Schatz. Biotinylation of proteins in vivo and in vitro using small peptide tags. *Methods in Enzymology*, 326:430–440, 2000. ISSN 00766879. doi: 10.1016/s0076-6879(00)26068-0.

[135] Scott M. Cannizzaro, Robert F. Padera, Robert Langer, Rick A. Rogers, Fiona E. Black, Martyn C. Davies, Saul J.B. Tendler, and Kevin M. Shakesheff. A novel biotinylated degradable polymer for cell-interactive applications. *Biotechnology and Bioengineering*, 58(5):529–535, jun 1998. ISSN 00063592. doi: 10.1002/(SICI)1097-0290(19980605)58:5<529::AID-BIT9>3.0.CO;2-F.

[136] Vincent T. Moy, Ernst Ludwig Florin, and Hermann E. Gaub. Intermolecular forces and energies between ligands and receptors. *Science*, 266(5183):257–259, oct 1994. ISSN 00368075. doi: 10.1126/science.7939660.

[137] R. Merkel, P. Nassoy, A. Leung, K. Ritchie, and E. Evans. Energy landscapes of receptor-ligand bonds explored with dynamic force spectroscopy. *Nature*, 397(6714):50–53, jan 1999. ISSN 00280836. doi: 10.1038/16219.

[138] Claudia Danilowicz, Derek Greenfield, and Mara Prentiss. Dissociation of ligand-receptor complexes using magnet tweezers. *Analytical Chemistry*, 77(10):3023–3028, may 2005. ISSN 00032700. doi: 10.1021/ac050057+.

[139] Felix Rico, Andreas Russek, Laura González, Helmut Grubmüller, and Simon Scheuring. Heterogeneous and rate-dependent streptavidin–biotin unbinding revealed by high-speed force spectroscopy and atomistic simulations. *Proceedings of the National Academy of Sciences of the United States of America*, 116(14):6594–6601, apr 2019. ISSN 10916490. doi: 10.1073/pnas.1816909116.

[140] Fabian Baumann, Magnus S. Bauer, Lukas F. Milles, Alexander Alexandrovich, Hermann E. Gaub, and Diana A. Pippig. Monovalent Strep-Tactin for strong and site-specific tethering in nanospectroscopy. *Nature Nanotechnology*, 11(1):89–94, jan 2016. ISSN 17483395. doi: 10.1038/nnano.2015.231.

[141] Wolfgang Ott, Markus A. Jobst, Constantin Schoeler, Hermann E. Gaub, and Michael A. Nash. Single-molecule force spectroscopy on polyproteins and receptor–ligand complexes: The current toolbox. *Journal of Structural Biology*, 197(1):3–12, jan 2017. ISSN 10958657. doi: 10.1016/j.jsb.2016.02.011.

[142] Robert Walder, Marc André Leblanc, William J. Van Patten, Devin T. Edwards, Jacob A. Greenberg, Ayush Adhikari, Stephen R. Okoniewski, Ruby May A. Sullan, David Rabuka, Marcelo C. Sousa, and Thomas T. Perkins. Rapid Characterization of a Mechanically Labile α-Helical Protein Enabled by Efficient Site-Specific Bioconjugation. *Journal of the American Chemical Society*, 139(29):9867–9875, jul 2017. ISSN 15205126. doi: 10.1021/jacs.7b02958.

[143] Ziad Ganim and Matthias Rief. Mechanically switching single-molecule fluorescence of GFP by unfolding and refolding. *Proceedings of the National Academy of Sciences of the United States of America*, 114 (42):11052–11056, oct 2017. ISSN 10916490. doi: 10.1073/pnas.1704937114.

[144] Michael Krieg, Gotthold Fläschner, David Alsteens, Benjamin M. Gaub, Wouter H. Roos, Gijs J.L. Wuite, Hermann E. Gaub, Christoph Gerber, Yves F. Dufrêne, and Daniel J. Müller. Atomic force microscopy-based mechanobiology. *Nature Reviews Physics*, 1(1):41–57, 2019. ISSN 25225820. doi: 10.1038/s42254-018-0001-7.

[145] Steffen M. Sedlak, Magnus S. Bauer, Carleen Kluger, Leonard C. Schendel, Lukas F. Milles, Diana A. Pippig, and Hermann E. Gaub. Monodisperse measurement of the biotin-streptavidin interaction strength in a well-defined pulling geometry. *PLoS ONE*, 12(12):e0188722, 2017. ISSN 19326203. doi: 10.1371/journal.pone.0188722.

[146] G Fonnum, N K Hofslokken, E Aksnes, L Killas, P Stenstad, R Schmid, J O Bjorgum, T N Nilsen, and A T Berge. Process for preparing coated magnetic particles. *EU Patent EP1*, 693, 2006.

[147] Steffen M. Sedlak, Leonard C. Schendel, Marcelo C.R. Melo, Diana A. Pippig, Zaida Luthey-Schulten, Hermann E. Gaub, and Rafael C. Bernardi. Direction Matters: Monovalent Streptavidin/Biotin Complex under Load. *Nano Letters*, 19(6):3415–3421, jun 2019. ISSN 15306992. doi: 10.1021/acs.nanolett.8b04045.

[148] Steffen M. Sedlak, Leonard C. Schendel, Hermann E. Gaub, and Rafael C. Bernardi. Streptavidin/biotin: Tethering geometry defines unbinding mechanics. *Science Advances*, 6(13):eaay5999, mar 2020. ISSN 23752548. doi: 10.1126/sciadv.aay5999.

[149] Mark Howarth, Daniel J.F. Chinnapen, Kimberly Gerrow, Pieter C. Dorrestein, Melanie R. Grandy, Neil L. Kelleher, Alaa El-Husseini, and Alice Y. Ting. A monovalent streptavidin with a single femtomolar biotin binding site. *Nature Methods*, 3(4):267–273, apr 2006. ISSN 15487091. doi: 10.1038/nmeth861.

[150] Ashutosh Chilkoti and Patrick S. Stayton. Molecular Origins of the Slow Streptavidin—Biotin Dissociation Kinetics. *Journal of the American Chemical Society*, 117(43):10622–10628, nov 1995. ISSN 15205126. doi: 10.1021/ja00148a003.

[151] Mona Sarter, Doreen Niether, Bernd W. Koenig, Wiebke Lohstroh, Michaela Zamponi, Niina H. Jalarvo, Simone Wiegand, Jörg Fitter, and Andreas M. Stadler. Strong Adverse Contribution of Conformational Dynamics to Streptavidin-Biotin Binding. *Journal of Physical Chemistry B*, 124(2):324–335, jan 2020. ISSN 15205207. doi: 10.1021/acs.jpcb.9b08467.

[152] Magnus S. Bauer, Lukas F. Milles, Steffen M. Sedlak, and Hermann E. Gaub. Monomeric streptavidin: A versatile regenerative handle for force spectroscopy. *bioRxiv*, page 276444, jan 2018. ISSN 2692-8205. doi: 10.1101/276444.

[153] Evan Evans and Ken Ritchie. Dynamic strength of molecular adhesion bonds. *Biophysical Journal*, 72 (4):1541–1555, apr 1997. ISSN 00063495. doi: 10.1016/S0006-3495(97)78802-7.

[154] Leonard C. Schendel, Steffen M. Sedlak, and Hermann E. Gaub. Switchable reinforced streptavidin. *Nanoscale*, 12(12):6803–6809, mar 2020. ISSN 20403372. doi: 10.1039/d0nr00265h.

[155] S. K. Kufer, E. M. Puchner, H. Gumpp, T. Liedl, and H. E. Gaub. Single-molecule cut-and-paste surface assembly. *Science*, 319(5863):594–596, feb 2008. ISSN 00368075. doi: 10.1126/science.1151424.

[156] Katherine R. Erlich, Steffen M. Sedlak, Markus A. Jobst, Lukas F. Milles, and Hermann E. Gaub. DNA-free directed assembly in single-molecule cut-and-paste. *Nanoscale*, 11(2):407–411, jan 2019. ISSN 20403372. doi: 10.1039/c8nr08636b.

[157] Lukas F. Milles, Edward A. Bayer, Michael A. Nash, and Hermann E. Gaub. Mechanical Stability of a High-Affinity Toxin Anchor from the Pathogen Clostridium perfringens. *Journal of Physical Chemistry B*, 121(15):3620–3625, apr 2017. ISSN 15205207. doi: 10.1021/acs.jpcb.6b09593.

[158] Jochen P. Müller, Achim Löf, Salomé Mielke, Tobias Obser, Linda K. Bruetzel, Willem Vanderlinden, Jan Lipfert, Reinhard Schneppenheim, and Martin Benoit. pH-Dependent Interactions in Dimers Govern the Mechanics and Structure of von Willebrand Factor. *Biophysical Journal*, 111(2):312–322, jul 2016. ISSN 15420086. doi: 10.1016/j.bpj.2016.06.022.

[159] Tine Brouns, Herlinde De Keersmaecker, Sebastian F. Konrad, Noriyuki Kodera, Toshio Ando, Jan Lipfert, Steven De Feyter, and Willem Vanderlinden. Free Energy Landscape and Dynamics of Supercoiled DNA by High-Speed Atomic Force Microscopy. *ACS Nano*, 12(12):11907–11916, dec 2018. ISSN 1936086X. doi: 10.1021/acsnano.8b06994.

[160] Philipp U. Walker, Willem Vanderlinden, and Jan Lipfert. Dynamics and energy landscape of DNA plectoneme nucleation. *Physical Review E*, 98(4):42412, oct 2018. ISSN 24700053. doi: 10.1103/PhysRevE.98.042412.

[161] Hongxia Fu, Yan Jiang, Darren Yang, Friedrich Scheiflinger, Wesley P. Wong, and Timothy A. Springer. Flow-induced elongation of von Willebrand factor precedes tension-dependent activation. *Nature Communications*, 8(1), 2017. ISSN 20411723. doi: 10.1038/s41467-017-00230-2.

[162] Yan Feng Zhou, Edward T. Eng, Jieqing Zhu, Chafen Lu, Thomas Walz, and Timothy A. Springer. Sequence and structure relationships within von Willebrand factor. *Blood*, 120(2):449–458, jul 2012. ISSN 00064971. doi: 10.1182/blood-2012-01-405134.

[163] Ren Huai Huang, Ying Wang, Robyn Roth, Xiong Yu, Angie R. Purvis, John E. Heuser, Edward H. Egelman, and J. Evan Sadler. Assembly of Weibel-Palade body-like tubules from N-terminal domains of von Willebrand factor. *Proceedings of the National Academy of Sciences of the United States of America*, 105(2):482–487, jan 2008. ISSN 00278424. doi: 10.1073/pnas.0710079105.

[164] Xianchi Dong, Nina C. Leksa, Ekta Seth Chhabra, Joseph W. Arndt, Qi Lu, Kevin E. Knockenhauer, Robert T. Peters, and Timothy A. Springer. The von Willebrand factor D'D3 assembly and structural principles for factor VIII binding and concatemer biogenesis. *Blood*, 133(14):1523–1533, 2019. ISSN 15280020. doi: 10.1182/blood-2018-10-876300.

[165] D. D. Wagner and V. J. Marder. Biosynthesis of von Willebrand protein by human endothelial cells. Identification of a large precursor polypeptide chain. *Journal of Biological Chemistry*, 258(4):2065–2067, feb 1983. ISSN 00219258. doi: 10.1016/s0021-9258(18)32879-5.

[166] Denisa D Wagner and Victor J Marder. Biosynthesis of von Willebrand protein by human endothelial cells: Processing steps and their intracellular localization. *Journal of Cell Biology*, 99(6):2123–2130, 1984. ISSN 00219525. doi: 10.1083/jcb.99.6.2123.

[167] Denisa D Wagner, Tanya Mayadas, and Victor J Marder. Initial glycosylation and acidic pH in the Golgi apparatus are required for multimerization of von Willebrand factor. *Journal of Cell Biology*, 102(4): 1320–1324, 1986. ISSN 00219525. doi: 10.1083/jcb.102.4.1320.

[168] Denisa D. Wagner. Cell Biology of von Willebrand Factor. *Annual Review of Cell Biology*, 6(1):217–242, nov 1990. ISSN 0743-4634. doi: 10.1146/annurev.cb.06.110190.001245.

[169] T. A. Springer. Biology and physics of von Willebrand factor concatamers. *Journal of Thrombosis and Haemostasis*, 9(1 S):130–143, jul 2011. ISSN 15387933. doi: 10.1111/j.1538-7836.2011.04320.x.

[170] Yan Feng Zhou, Edward T. Eng, Noritaka Nishida, Chafen Lu, Thomas Walz, and Timothy A. Springer. A pH-regulated dimeric bouquet in the structure of von Willebrand factor. *EMBO Journal*, 30(19): 4098–4111, 2011. ISSN 02614189. doi: 10.1038/emboj.2011.297.

[171] Zhengyu Dong, Richard S. Thoma, Dan L. Crimmins, David W. McCourt, Elodee A. Tuley, and J. Evan Sadler. Disulfide bonds required to assemble functional von Willebrand factor multimers. *Journal of Biological Chemistry*, 269(9):6753–6758, mar 1994. ISSN 00219258. doi: 10.1016/s0021-9258(17)37439-2.

[172] Angie R. Purvis, Julia Gross, Luke T. Dang, Ren Huai Huang, Milan Kapadia, R. Reid Townsend, and J. Evan Sadler. Two Cys residues essential for von Willebrand factor multimer assembly in the Golgi. *Proceedings of the National Academy of Sciences of the United States of America*, 104(40):15647–15652, oct 2007. ISSN 00278424. doi: 10.1073/pnas.0705175104.

[173] James R. Fuller, Kevin E. Knockenhauer, Nina C. Leksa, Robert T. Peters, and Joseph D. Batchelor. Molecular determinants of the factor VIII/von Willebrand factor complex revealed by BIVV001 cryo-electron microscopy. *Blood*, 137(21):2970–2980, may 2021. ISSN 15280020. doi: 10.1182/blood.2020009197.

[174] David Lillicrap. von Willebrand disease: advances in pathogenetic understanding, diagnosis, and therapy. *Hematology / the Education Program of the American Society of Hematology. American Society of Hematology. Education Program*, 2013(23):254–260, 2013. ISSN 15204383. doi: 10.1182/asheducation-2013.1.254.

[175] Nuha Shiltagh, John Kirkpatrick, Lisa D. Cabrita, Tom A.J. McKinnon, Konstantinos Thalassinos, Edward G.D. Tuddenham, and D. Flemming Hansen. Solution structure of the major factor VIII binding region on von Willebrand factor. *Blood*, 123(26):4143–4151, jun 2014. ISSN 15280020. doi: 10.1182/blood-2013-07-517086.

[176] Po Lin Chiu, George M. Bou-Assaf, Ekta Seth Chhabra, Melissa G. Chambers, Robert T. Peters, John D. Kulman, and Thomas Walz. Mapping the interaction between factor VIII and von Willebrand factor by electron microscopy and mass spectrometry. *Blood*, 126(8):935–938, aug 2015. ISSN 15280020. doi: 10.1182/blood-2015-04-641688.

[177] Andrew Yee, Austin N. Oleskie, Anne M. Dosey, Colin A. Kretz, Robert D. Gildersleeve, Somnath Dutta, Min Su, David Ginsburg, and Georgios Skiniotis. Visualization of an N-terminal fragment of von Willebrand factor in complex with factor VIII. *Blood*, 126(8):939–942, aug 2015. ISSN 15280020. doi: 10.1182/blood-2015-04-641696.

[178] Shimin Le, Ruchuan Liu, Chwee Teck Lim, and Jie Yan. Uncovering mechanosensing mechanisms at the single protein level using magnetic tweezers. *Methods*, 94:13–18, 2016. ISSN 10959130. doi: 10.1016/j.ymeth.2015.08.020.

[179] Jochen P. Müller, Salomé Mielke, Achim Löf, Tobias Obser, Christof Beer, Linda K. Bruetzel, Diana A. Pippig, Willem Vanderlinden, Jan Lipfert, Reinhard Schneppenheim, and Martin Benoit. Force sensing by the vascular protein von Willebrand factor is tuned by a strong intermonomer interaction. *Proceedings of the National Academy of Sciences of the United States of America*, 113(5):1208–1213, feb 2016. ISSN 10916490. doi: 10.1073/pnas.1516214113.

[180] Yi Cao, Rachel Kuske, and Hongbin Li. Direct observation of Markovian behavior of the mechanical unfolding of individual proteins. *Biophysical Journal*, 95(2):782–788, 2008. ISSN 15420086. doi: 10.1529/biophysj.107.128298.

[181] Xianchi Dong and Timothy A. Springer. Disulfide Exchange in von Willebrand factor Dimerization in the Golgi. *Blood*, 137(9):1263–1267, 2020. ISSN 15280020. doi: 10.1182/blood.2020005989.

[182] Jason Phan, Alexander Zdanov, Artem G. Evdokimov, Joseph E. Tropea, Howard K. Peters, Rachel B. Kapust, Mi Li, Alexander Wlodawer, and David S. Waugh. Structural basis for the substrate specificity of tobacco etch virus protease. *Journal of Biological Chemistry*, 277(52):50564–50572, 2002. ISSN 00219258. doi: 10.1074/jbc.M207224200.

[183] Christopher S. Theile, Martin D. Witte, Annet E.M. Blom, Lenka Kundrat, Hidde L. Ploegh, and Carla P. Guimaraes. Site-specific N-terminal labeling of proteins using sortase-mediated reactions. *Nature Protocols*, 8(9):1800–1807, 2013. ISSN 17542189. doi: 10.1038/nprot.2013.102.

[184] Maria A. Brehm, Volker Huck, Camilo Aponte-Santamaría, Tobias Obser, Sandra Grässle, Florian Oyen, Ulrich Budde, Sonja Schneppenheim, Carsten Baldauf, Frauke Gräter, Stefan W. Schneider, and Reinhard Schneppenheim. von Willebrand disease type 2A phenotypes IIC, IID and IIE: A day in the life of shear-stressed mutant von Willebrand factor. *Thrombosis and Haemostasis*, 112(1):96–108, 2014. ISSN 03406245. doi: 10.1160/TH13-11-0902.

[185] Svenja Lippok, Katra Kolšek, Achim Löf, Dennis Eggert, Willem Vanderlinden, Jochen P. Müller, Gesa König, Tobias Obser, Karoline Röhrs, Sonja Schneppenheim, Ulrich Budde, Carsten Baldauf, Camilo Aponte-Santamaría, Frauke Gräter, Reinhard Schneppenheim, Joachim O. Rädler, and Maria A. Brehm. Von Willebrand factor is dimerized by protein disulfide isomerase. *Blood*, 127(9):1183–1191, mar 2016. ISSN 15280020. doi: 10.1182/blood-2015-04-641902.

[186] João V. Ribeiro, Rafael C. Bernardi, Till Rudack, John E. Stone, James C. Phillips, Peter L. Freddolino, and Klaus Schulten. QwikMD - Integrative Molecular Dynamics Toolkit for Novices and Experts. *Scientific Reports*, 6(1):1–14, may 2016. ISSN 20452322. doi: 10.1038/srep26536.

[187] Robert B Best, Xiao Zhu, Jihyun Shim, Pedro E.M. Lopes, Jeetain Mittal, Michael Feig, and Alexander D. MacKerell. Optimization of the additive CHARMM all-atom protein force field targeting improved sampling of the backbone ϕ, ψ and side-chain $\chi 1$ and $\chi 2$ Dihedral Angles. *Journal of Chemical Theory and Computation*, 8(9):3257–3273, 2012. ISSN 15499626. doi: 10.1021/ct300400x.

[188] A. D. MacKerell, D Bashford, M. Bellott, R. L. Dunbrack, J D Evanseck, M J Field, S. Fischer, J. Gao, H. Guo, S. Ha, D. Joseph-McCarthy, L. Kuchnir, K. Kuczera, F. T.K. Lau, C. Mattos, S Michnick, T. Ngo, D. T. Nguyen, B. Prodhom, W. E. Reiher, B. Roux, M. Schlenkrich, J C Smith, R. Stote, J. Straub, M. Watanabe, J. Wiórkiewicz-Kuczera, D. Yin, and M Karplus. All-atom empirical potential for molecular modeling and dynamics studies of proteins. *Journal of Physical Chemistry B*, 102(18):3586–3616, 1998. ISSN 15206106. doi: 10.1021/jp973084f.

[189] Fabian Czerwinski, Andrew C. Richardson, and Lene B. Oddershede. Quantifying Noise in Optical Tweezers by Allan Variance. *Optics Express*, 17(15):13255, 2009. ISSN 1094-4087. doi: 10.1364/oe.17.013255.

[190] Maarten M. van Oene, Seungkyu Ha, Tessa Jager, Mina Lee, Francesco Pedaci, Jan Lipfert, and Nynke H. Dekker. Quantifying the Precision of Single-Molecule Torque and Twist Measurements Using Allan Variance. *Biophysical Journal*, 114(8):1970–1979, 2018. ISSN 15420086. doi: 10.1016/j.bpj.2018.02.039.

[191] Wenhui Li, Michael J. Moore, Natalya Vasllieva, Jianhua Sui, Swee Kee Wong, Michael A. Berne, Mohan Somasundaran, John L. Sullivan, Katherine Luzuriaga, Thomas C. Greeneugh, Hyeryun Choe, and Michael Farzan. Angiotensin-converting enzyme 2 is a functional receptor for the SARS coronavirus. *Nature*, 426(6965):450–454, nov 2003. ISSN 00280836. doi: 10.1038/nature02145.

[192] Hong Peng Jia, Dwight C. Look, Lei Shi, Melissa Hickey, Lecia Pewe, Jason Netland, Michael Farzan, Christine Wohlford-Lenane, Stanley Perlman, and Paul B. McCray. ACE2 Receptor Expression and Severe Acute Respiratory Syndrome Coronavirus Infection Depend on Differentiation of Human Airway Epithelia. *Journal of Virology*, 79(23):14614–14621, dec 2005. ISSN 0022-538X. doi: 10.1128/jvi.79.23.14614-14621.2005.

[193] Markus Hoffmann, Hannah Kleine-Weber, Simon Schroeder, Nadine Krüger, Tanja Herrler, Sandra Erichsen, Tobias S. Schiergens, Georg Herrler, Nai Huei Wu, Andreas Nitsche, Marcel A. Müller, Christian Drosten, and Stefan Pöhlmann. SARS-CoV-2 Cell Entry Depends on ACE2 and TMPRSS2 and Is Blocked by a Clinically Proven Protease Inhibitor. *Cell*, 181(2):271–280.e8, apr 2020. ISSN 10974172. doi: 10.1016/j.cell.2020.02.052.

[194] Jian Shang, Gang Ye, Ke Shi, Yushun Wan, Chuming Luo, Hideki Aihara, Qibin Geng, Ashley Auerbach, and Fang Li. Structural basis of receptor recognition by SARS-CoV-2. *Nature*, 581(7807):221–224, mar 2020. ISSN 14764687. doi: 10.1038/s41586-020-2179-y.

[195] Peng Zhou, Xing-Lou Yang, Xian-Guang Wang, Ben Hu, Lei Zhang, Wei Zhang, Hao-Rui Si, Yan Zhu, Bei Li, Chao-Lin Huang, Hui-Dong Chen, Jing Chen, Yun Luo, Hua Guo, Ren-Di Jiang, Mei-Qin Liu, Ying Chen, Xu-Rui Shen, Xi Wang, Xiao-Shuang Zheng, Kai Zhao, Quan-Jiao Chen, Fei Deng, Lin-Lin Liu, Bing Yan, Fa-Xian Zhan, Yan-Yi Wang, Geng-Fu Xiao, and Zheng-Li Shi. A pneumonia outbreak associated with a new coronavirus of probable bat origin. *Nature*, 2019(January), 2020. ISSN 0028-0836. doi: 10.1038/s41586-020-2012-7.

[196] Maolin Lu, Pradeep D. Uchil, Wenwei Li, Desheng Zheng, Daniel S. Terry, Jason Gorman, Wei Shi, Baoshan Zhang, Tongqing Zhou, Shilei Ding, Romain Gasser, Jérémie Prévost, Guillaume Beaudoin-Bussières, Sai Priya Anand, Annemarie Laumaea, Jonathan R. Grover, Lihong Liu, David D. Ho, John R. Mascola, Andrés Finzi, Peter D. Kwong, Scott C. Blanchard, and Walther Mothes. Real-Time Conformational Dynamics of SARS-CoV-2 Spikes on Virus Particles. *Cell Host and Microbe*, 28(6):880–891.e8, 2020. ISSN 19346069. doi: 10.1016/j.chom.2020.11.001.

[197] Mart M. Lamers, Joep Beumer, Jelte Van Der Vaart, Kèvin Knoops, Jens Puschhof, Tim I. Breugem, Raimond B.G. Ravelli, J. Paul Van Schayck, Anna Z. Mykytyn, Hans Q. Duimel, Elly Van Donselaar, Samra Riesebosch, Helma J.H. Kuijpers, Debby Schipper, Willine J.Van De Wetering, Miranda De Graaf, Marion Koopmans, Edwin Cuppen, Peter J. Peters, Bart L. Haagmans, and Hans Clevers. SARS-CoV-2 productively infects human gut enterocytes. *Science*, 369(6499):50–54, jul 2020. ISSN 10959203. doi: 10.1126/science.abc1669.

[198] Roman Wölfel, Victor M. Corman, Wolfgang Guggemos, Michael Seilmaier, Sabine Zange, Marcel A. Müller, Daniela Niemeyer, Terry C. Jones, Patrick Vollmar, Camilla Rothe, Michael Hoelscher, Tobias Bleicker, Sebastian Brünink, Julia Schneider, Rosina Ehmann, Katrin Zwirglmaier, Christian Drosten, and Clemens Wendtner. Virological assessment of hospitalized patients with COVID-2019. *Nature*, 581 (7809):465–469, apr 2020. ISSN 14764687. doi: 10.1038/s41586-020-2196-x.

[199] Michael R. Knowles and Richard C. Boucher. Mucus clearance as a primary innate defense mechanism for mammalian airways. *Journal of Clinical Investigation*, 109(5):571–577, mar 2002. ISSN 00219738. doi: 10.1172/JCI0215217.

[200] Jaime Andrés Rivas-Pardo, Carmen L. Badilla, Rafael Tapia-Rojo, Álvaro Alonso-Caballero, and Julio M. Fernández. Molecular strategy for blocking isopeptide bond formation in nascent pilin proteins. *Proceedings of the National Academy of Sciences of the United States of America*, 115(37):9222–9227, sep 2018. ISSN 10916490. doi: 10.1073/pnas.1807689115.

[201] David Alsteens, Richard Newton, Rajib Schubert, David Martinez-Martin, Martin Delguste, Botond Roska, and Daniel J. Müller. Nanomechanical mapping of first binding steps of a virus to animal cells. *Nature Nanotechnology*, 12(2):177–183, 2017. ISSN 17483395. doi: 10.1038/nnano.2016.228.

[202] Jose Luis Cuellar-Camacho, Sumati Bhatia, Valentin Reiter-Scherer, Daniel Lauster, Susanne Liese, Jürgen P. Rabe, Andreas Herrmann, and Rainer Haag. Quantification of Multivalent Interactions between Sialic Acid and Influenza A Virus Spike Proteins by Single-Molecule Force Spectroscopy. *Journal of the American Chemical Society*, 142(28):12181–12192, jul 2020. ISSN 15205126. doi: 10.1021/jacs.0c02852.

[203] Melanie Koehler, Martin Delguste, Christian Sieben, Laurent Gillet, and David Alsteens. Initial Step of Virus Entry: Virion Binding to Cell-Surface Glycans. *Annual Review of Virology*, 7:143–165, sep 2020. ISSN 23270578. doi: 10.1146/annurev-virology-122019-070025.

[204] Jun Lan, Jiwan Ge, Jinfang Yu, Sisi Shan, Huan Zhou, Shilong Fan, Qi Zhang, Xuanling Shi, Qisheng Wang, Linqi Zhang, and Xinquan Wang. Structure of the SARS-CoV-2 spike receptor-binding domain bound to the ACE2 receptor. *Nature*, 581(7807):215–220, mar 2020. ISSN 14764687. doi: 10.1038/s41586-020-2180-5.

[205] Jongseong Kim, Cheng Zhong Zhang, Xiaohui Zhang, and Timothy A. Springer. A mechanically stabilized receptor-ligand flex-bond important in the vasculature. *Nature*, 466(7309):992–995, 2010. ISSN 00280836. doi: 10.1038/nature09295.

[206] Lorenz Rognoni, Johannes Stigler, Benjamin Pelz, Jari Ylänne, and Matthias Rief. Dynamic force sensing of filamin revealed in single-molecule experiments. *Proceedings of the National Academy of Sciences of the United States of America*, 109(48):19679–19684, 2012. ISSN 00278424. doi: 10.1073/pnas.1211274109.

[207] Fabian Kilchherr, Christian Wachauf, Benjamin Pelz, Matthias Rief, Martin Zacharias, and Hendrik Dietz. Single-molecule dissection of stacking forces in DNA. *Science*, 353(6304), sep 2016. ISSN 10959203. doi: 10.1126/science.aaf5508.

[208] Res Jöhr, Magnus S. Bauer, Leonard C. Schendel, Carleen Kluger, and Hermann E. Gaub. Dronpa: A Light-Switchable Fluorescent Protein for Opto-Biomechanics. *Nano Letters*, 19(5):3176–3181, may 2019. ISSN 15306992. doi: 10.1021/acs.nanolett.9b00639.

[209] Dorota Kostrz, Hannah K. Wayment-Steele, Jing L. Wang, Maryne Follenfant, Vijay S. Pande, Terence R. Strick, and Charlie Gosse. A modular DNA scaffold to study protein–protein interactions at single-molecule resolution. *Nature Nanotechnology*, 14(10):988–993, 2019. ISSN 1748-3387. doi: 10.1038/s41565-019-0542-7.

[210] Prakash Shrestha, Darren Yang, Toma E. Tomov, James I. MacDonald, Andrew Ward, Hans T. Bergal, Elisha Krieg, Serkan Cabi, Yi Luo, Bhavik Nathwani, Alexander Johnson-Buck, William M. Shih, and Wesley P. Wong. Single-molecule mechanical fingerprinting with DNA nanoswitch calipers. *Nature Nanotechnology*, pages 1–9, oct 2021. ISSN 17483395. doi: 10.1038/s41565-021-00979-0.

[211] Fang Li, Wenhui Li, Michael Farzan, and Stephen C. Harrison. Structure of SARS coronavirus spike receptor-binding domain complexed with receptor. *Science*, 309(5742):1864–1868, 2005. ISSN 00368075. doi: 10.1126/science.1116480.

[212] David Dulin, Tao Ju Cui, Jelmer Cnossen, Margreet W. Docter, Jan Lipfert, and Nynke H. Dekker. High Spatiotemporal-Resolution Magnetic Tweezers: Calibration and Applications for DNA Dynamics. *Biophysical Journal*, 109(10):2113–2125, 2015. ISSN 15420086. doi: 10.1016/j.bpj.2015.10.018.

[213] Alexander Huhle, Daniel Klaue, Hergen Brutzer, Peter Daldrop, Sihwa Joo, Oliver Otto, Ulrich F. Keyser, and Ralf Seidel. Camera-based three-dimensional real-time particle tracking at kHz rates and Ångström accuracy. *Nature Communications*, 6(1):1–8, 2015. ISSN 20411723. doi: 10.1038/ncomms6885.

[214] H. Gumpp, S. W. Stahl, M. Strackharn, E. M. Puchner, and H. E. Gaub. Ultrastable combined atomic force and total internal fluorescence microscope. *Review of Scientific Instruments*, 80(6):63704, 2009. ISSN 00346748. doi: 10.1063/1.3148224.

[215] Fabian Baumann, Magnus Sebastian Bauer, Martin Rees, Alexander Alexandrovich, Mathias Gautel, Diana Angela Pippig, and Hermann Eduard Gaub. Increasing evidence of mechanical force as a functional regulator in smooth muscle myosin light chain kinase. *eLife*, 6:e26473, 2017. ISSN 2050084X. doi: 10.7554/eLife.26473.

[216] Magnus Sebastian Bauer, Fabian Baumann, Csaba Daday, Pilar Redondo, Ellis Durner, Markus Andreas Jobst, Lukas Frederik Milles, Davide Mercadante, Diana Angela Pippig, Hermann Eduard Gaub, Frauke Gräter, and Daniel Lietha. Structural and mechanistic insights into mechanoactivation of focal adhesion kinase. *Proceedings of the National Academy of Sciences of the United States of America*, 116(14):6766–6774, 2019. ISSN 10916490. doi: 10.1073/pnas.1820567116.

[217] Elias M. Puchner, Gereon Franzen, Mathias Gautel, and Hermann E. Gaub. Comparing proteins by their unfolding pattern. *Biophysical Journal*, 95(1):426–434, 2008. ISSN 15420086. doi: 10.1529/biophysj.108.129999.

[218] Sanchita Hati and Sudeep Bhattacharyya. Impact of Thiol-Disulfide Balance on the Binding of Covid-19 Spike Protein with Angiotensin-Converting Enzyme 2 Receptor. *ACS Omega*, 5(26):16292–16298, 2020. ISSN 24701343. doi: 10.1021/acsomega.0c02125.

[219] James C. Phillips, David J. Hardy, Julio D.C. Maia, John E. Stone, João V. Ribeiro, Rafael C. Bernardi, Ronak Buch, Giacomo Fiorin, Jérôme Hénin, Wei Jiang, Ryan McGreevy, Marcelo C.R. Melo, Brian K. Radak, Robert D. Skeel, Abhishek Singharoy, Yi Wang, Benoît Roux, Aleksei Aksimentiev, Zaida Luthey-Schulten, Laxmikant V. Kalé, Klaus Schulten, Christophe Chipot, and Emad Tajkhorshid. Scalable molecular dynamics on CPU and GPU architectures with NAMD. *Journal of Chemical Physics*, 153(4): 44130, 2020. ISSN 10897690. doi: 10.1063/5.0014475.

[220] John Marko, Eric Siggia, S Smith, and Carlos Bustamante. Entropic elasticity of lambda-phage DNA. *Science*, 265:1599–1600, 1994. ISSN 0036-8075.

[221] C. Bouchiat, M. D. Wang, J. F. Allemand, T. Strick, S. M. Block, and Vincent Croquette. Estimating the persistence length of a worm-like chain molecule from force-extension measurements. *Biophysical Journal*, 76(1 I):409–413, 1999. ISSN 00063495. doi: 10.1016/S0006-3495(99)77207-3.

[222] Hendrik Dietz and Matthias Rief. Exploring the energy landscape of GFP by single-molecule mechanical experiments. *Proceedings of the National Academy of Sciences of the United States of America*, 101(46): 16192–16197, 2004. ISSN 00278424. doi: 10.1073/pnas.0404549101.

[223] Tobias Verdorfer, Rafael C. Bernardi, Aylin Meinhold, Wolfgang Ott, Zaida Luthey-Schulten, Michael A. Nash, and Hermann E. Gaub. Combining in Vitro and in Silico Single-Molecule Force Spectroscopy to Characterize and Tune Cellulosomal Scaffoldin Mechanics. *Journal of the American Chemical Society*, 139(49):17841–17852, dec 2017. ISSN 15205126. doi: 10.1021/jacs.7b07574.

[224] R. A. Laskowski. PDBsum: Summaries and analyses of PDB structures. *Nucleic Acids Research*, 29(1): 221–222, jan 2001. ISSN 03051048. doi: 10.1093/nar/29.1.221.

[225] Benjamin Webb and Andrej Sali. Comparative protein structure modeling using MODELLER. *Current Protocols in Bioinformatics*, 2016(1):5.6.1–5.6.37, jun 2016. ISSN 1934340X. doi: 10.1002/cpbi.3.

[226] Stefan Ståhl, Torbjörn Gräslund, Amelie Eriksson Karlström, Fredrik Y. Frejd, Per Åke Nygren, and John Löfblom. Affibody Molecules in Biotechnological and Medical Applications. *Trends in Biotechnology*, 35(8):691–712, aug 2017. ISSN 18793096. doi: 10.1016/j.tibtech.2017.04.007.

[227] Rafael C. Bernardi, Ellis Durner, Constantin Schoeler, Klara H. Malinowska, Bruna G. Carvalho, Edward A. Bayer, Zaida Luthey-Schulten, Hermann E. Gaub, and Michael A. Nash. Mechanisms of Nanonewton Mechanostability in a Protein Complex Revealed by Molecular Dynamics Simulations and Single-Molecule Force Spectroscopy. *Journal of the American Chemical Society*, 141(37):14752–14763, sep 2019. ISSN 15205126. doi: 10.1021/jacs.9b06776.

[228] Marcelo C.R. Melo, Rafael C. Bernardi, Cesar De La Fuente-Nunez, and Zaida Luthey-Schulten. Generalized correlation-based dynamical network analysis: A new high-performance approach for identifying allosteric communications in molecular dynamics trajectories. *Journal of Chemical Physics*, 153(13): 134104, oct 2020. ISSN 10897690. doi: 10.1063/5.0018980.

[229] Chunyan Yi, Xiaoyu Sun, Jing Ye, Longfei Ding, Meiqin Liu, Zhuo Yang, Xiao Lu, Yaguang Zhang, Liyang Ma, Wangpeng Gu, Aidong Qu, Jianqing Xu, Zhengli Shi, Zhiyang Ling, and Bing Sun. Key residues of the receptor binding motif in the spike protein of SARS-CoV-2 that interact with ACE2 and neutralizing antibodies. *Cellular and Molecular Immunology*, 17(6):621–630, may 2020. ISSN 20420226. doi: 10.1038/s41423-020-0458-z.

[230] Rodrigo A. Moreira, Mateusz Chwastyk, Joseph L. Baker, Horacio V. Guzman, and Adolfo B. Poma. Quantitative determination of mechanical stability in the novel coronavirus spike protein. *Nanoscale*, 12 (31):16409–16413, 2020. ISSN 20403372. doi: 10.1039/d0nr03969a.

[231] Wenpeng Cao, Chuqiao Dong, Seonghan Kim, Decheng Hou, Wanbo Tai, Lanying Du, Wonpil Im, and X. Frank Zhang. Biomechanical characterization of SARS-CoV-2 spike RBD and human ACE2 protein-protein interaction. *Biophysical Journal*, 120(6):1011–1019, 2021. ISSN 15420086. doi: 10.1016/j.bpj.2021.02.007.

[232] Tyler N. Starr, Allison J. Greaney, Sarah K. Hilton, Daniel Ellis, Katharine H.D. Crawford, Adam S. Dingens, Mary Jane Navarro, John E. Bowen, M. Alejandra Tortorici, Alexandra C. Walls, Neil P. King, David Veesler, and Jesse D. Bloom. Deep Mutational Scanning of SARS-CoV-2 Receptor Binding Domain Reveals Constraints on Folding and ACE2 Binding. *Cell*, 182(5):1295–1310.e20, 2020. ISSN 10974172. doi: 10.1016/j.cell.2020.08.012.

[233] Alexandra C. Walls, Young Jun Park, M. Alejandra Tortorici, Abigail Wall, Andrew T. McGuire, and David Veesler. Structure, Function, and Antigenicity of the SARS-CoV-2 Spike Glycoprotein. *Cell*, 181 (2):281–292.e6, apr 2020. ISSN 10974172. doi: 10.1016/j.cell.2020.02.058.

[234] Qihui Wang, Yanfang Zhang, Lili Wu, Sheng Niu, Chunli Song, Zengyuan Zhang, Guangwen Lu, Chengpeng Qiao, Yu Hu, Kwok Yung Yuen, Qisheng Wang, Huan Zhou, Jinghua Yan, and Jianxun Qi. Structural and Functional Basis of SARS-CoV-2 Entry by Using Human ACE2. *Cell*, 181(4): 894–904.e9, 2020. ISSN 10974172. doi: 10.1016/j.cell.2020.03.045.

[235] Daniel Wrapp, Dorien De Vlieger, Kizzmekia S. Corbett, Gretel M. Torres, Nianshuang Wang, Wander Van Breedam, Kenny Roose, Loes van Schie, Markus Hoffmann, Stefan Pöhlmann, Barney S. Graham, Nico Callewaert, Bert Schepens, Xavier Saelens, and Jason S. McLellan. Structural Basis for Potent Neutralization of Betacoronaviruses by Single-Domain Camelid Antibodies. *Cell*, 181(5):1004–1015.e15, 2020. ISSN 10974172. doi: 10.1016/j.cell.2020.04.031.

[236] Jinsung Yang, Simon J.L. Petitjean, Melanie Koehler, Qingrong Zhang, Andra C. Dumitru, Wenzhang Chen, Sylvie Derclaye, Stéphane P. Vincent, Patrice Soumillion, and David Alsteens. Molecular interaction and inhibition of SARS-CoV-2 binding to the ACE2 receptor. *Nature Communications*, 11(1): 1–10, 2020. ISSN 20411723. doi: 10.1038/s41467-020-18319-6.

[237] Charlotte S. Sørensena and Magnus Kjaergaarda. Effective concentrations enforced by intrinsically disordered linkers are governed by polymer physics. *Proceedings of the National Academy of Sciences of the United States of America*, 116(46):23124–23131, 2019. ISSN 10916490. doi: 10.1073/pnas.1904813116.

[238] Eric M. Mulhall, Andrew Ward, Darren Yang, Mounir A. Koussa, David P. Corey, and Wesley P. Wong. Single-molecule force spectroscopy reveals the dynamic strength of the hair-cell tip-link connection. *Nature Communications*, 12(1):1–15, feb 2021. ISSN 20411723. doi: 10.1038/s41467-021-21033-6.

[239] Vijay M. Krishnamurthy, Vincent Semetey, Paul J. Bracher, Nan Shen, and George M. Whitesides. Dependence of effective molarity on linker length for an intramolecular protein-ligand system. *Journal of the American Chemical Society*, 129(5):1312–1320, feb 2007. ISSN 00027863. doi: 10.1021/ja066780e.

[240] Udo Seifert. Rupture of multiple parallel molecular bonds under dynamic loading. *Physical Review Letters*, 84(12):2750–2753, mar 2000. ISSN 10797114. doi: 10.1103/PhysRevLett.84.2750.

[241] Raymond W. Friddle, Aleksandr Noy, and James J. De Yoreo. Interpreting the widespread nonlinear force spectra of intermolecular bonds. *Proceedings of the National Academy of Sciences of the United States of America*, 109(34):13573–13578, aug 2012. ISSN 10916490. doi: 10.1073/pnas.1202946109.

[242] Vaibhav Tiwari, Jacob C Beer, Nehru Viji Sankaranarayanan, Michelle Swanson-Mungerson, and Umesh R Desai. Discovering small-molecule therapeutics against SARS-CoV-2. *Drug discovery today*, 25(8):1535–1544, 2020. ISSN 1359-6446.

[243] Alina Baum, Benjamin O. Fulton, Elzbieta Wloga, Richard Copin, Kristen E. Pascal, Vincenzo Russo, Stephanie Giordano, Kathryn Lanza, Nicole Negron, Min Ni, Yi Wei, Gurinder S. Atwal, Andrew J. Murphy, Neil Stahl, George D. Yancopoulos, and Christos A. Kyratsous. Antibody cocktail to SARS-CoV-2 spike protein prevents rapid mutational escape seen with individual antibodies. *Science*, 369 (6506):1014–1018, 2020. ISSN 10959203. doi: 10.1126/science.abd0831.

[244] Jiangdong Huo, Audrey Le Bas, Reinis R. Ruza, Helen M.E. Duyvesteyn, Halina Mikolajek, Tomas Malinauskas, Tiong Kit Tan, Pramila Rijal, Maud Dumoux, Philip N. Ward, Jingshan Ren, Daming Zhou, Peter J. Harrison, Miriam Weckener, Daniel K. Clare, Vinod K. Vogirala, Julika Radecke, Lucile Moynié, Yuguang Zhao, Javier Gilbert-Jaramillo, Michael L. Knight, Julia A. Tree, Karen R. Buttigieg, Naomi Coombes, Michael J. Elmore, Miles W. Carroll, Loic Carrique, Pranav N.M. Shah, William James, Alain R. Townsend, David I. Stuart, Raymond J. Owens, and James H. Naismith. Neutralizing nanobodies bind SARS-CoV-2 spike RBD and block interaction with ACE2. *Nature Structural and Molecular Biology*, 27(9):846–854, 2020. ISSN 15459985. doi: 10.1038/s41594-020-0469-6.

[245] Michael Schoof, Bryan Faust, Reuben A Saunders, Smriti Sangwan, Veronica Rezelj, Nick Hoppe, Morgane Boone, Christian Bache Billesbølle, Marcell Zimanyi, Ishan Deshpande, Jiahao Liang, Aditya A Anand, Niv Dobzinski, Beth Shoshana Zha, Benjamin Barsi-Rhyne, Vladislav Belyy, Andrew W Barile-Hill, Sayan Gupta, Camille R Simoneau, Kristoffer Leon, Kris M White, Silke Nock, Yuwei Liu, Nevan J Krogan, Corie Y Ralston, Danielle L Swaney, Adolfo García-Sastre, Melanie Ott, Marco Vignuzzi, Peter Walter, and Aashish Manglik. An ultra-high affinity synthetic nanobody blocks SARS-CoV-2 infection by locking Spike into an inactive conformation. *bioRxiv : the preprint server for biology*, 2020. doi: 10.1101/2020.08.08.238469.

[246] Longxing Cao, Inna Goreshnik, Brian Coventry, James Brett Case, Lauren Miller, Lisa Kozodoy, Rita E. Chen, Lauren Carter, Alexandra C. Walls, Young Jun Park, Eva Maria Strauch, Lance Stewart, Michael S. Diamond, David Veesler, and David Baker. De novo design of picomolar SARS-CoV-2 miniprotein inhibitors. *Science*, 370(6515), oct 2020. ISSN 10959203. doi: 10.1126/science.abd9909.

[247] Kui K. Chan, Danielle Dorosky, Preeti Sharma, Shawn A. Abbasi, John M. Dye, David M. Kranz, Andrew S. Herbert, and Erik Procko. Engineering human ACE2 to optimize binding to the spike protein of SARS coronavirus 2. *Science*, 369(6508):1261–1265, 2020. ISSN 10959203. doi: 10.1126/SCIENCE.ABC0870.

[248] Takami Komatsu, Yutaka Suzuki, Junichi Imai, Sumio Sugano, Munetomo Hida, Akira Tanigami, Sawako Muroi, Yoshitsugu Yamada, and Kazuo Hanaoka. Molecular cloning, mRNA expression and chromosomal localization of mouse angiotensin-converting enzyme-related carboxypeptidase (mACE2). *Mitochondrial DNA*, 13(4):217–220, 2002. ISSN 19401736. doi: 10.1080/1042517021000021608.

[249] Marco A. Marra, Steven J.M. Jones, Caroline R. Astell, Robert A. Holt, Angela Brooks-Wilson, Yaron S.N. Butterfield, Jaswinder Khattra, Jennifer K. Asano, Sarah A. Barber, Susanna Y. Chan, Alison Cloutier, Shaun M. Coughlin, Doug Freeman, Noreen Girn, Obi L. Griffith, Stephen R. Leach, Michael Mayo, Helen McDonald, Stephen B. Montgomery, Pawan K. Pandoh, Anca S. Petrescu, A. Gordon Robertson, Jacqueline E. Schein, Asim Siddiqui, Duane E. Smailus, Jeff M. Stott, George S. Yang, Francis Plummer, Anton Andonov, Harvey Artsob, Nathatie Bastien, Kathy Bernard, Timothy F. Booth, Donnie Bowness, Martin Czub, Michael Drebot, Lisa Fernando, Ramon Flick, Michael Garbutt, Michael Gray, Allen Grolla, Steven Jones, Heinz Feldmann, Adrienne Meyers, Amin Kabani, Yan Li, Susan Normand, Ute Stroher, Graham A. Tipples, Shaun Tyler, Robert Vogrig, Diane Ward, Brynn Watson, Robert C. Brunham, Mel Krajden, Martin Petric, Danuta M. Skowronski, Chris Upton, and Rachel L. Roper. The genome sequence of the SARS-associated coronavirus. *Science*, 300(5624):1399–1404, may 2003. ISSN 00368075. doi: 10.1126/science.1085953.

[250] Lukas F. Milles and Hermann E. Gaub. Is mechanical receptor ligand dissociation driven by unfolding or unbinding? *bioRxiv*, page 593335, apr 2019. ISSN 2692-8205. doi: 10.1101/593335.

[251] Fan Wu, Su Zhao, Bin Yu, Yan Mei Chen, Wen Wang, Zhi Gang Song, Yi Hu, Zhao Wu Tao, Jun Hua Tian, Yuan Yuan Pei, Ming Li Yuan, Yu Ling Zhang, Fa Hui Dai, Yi Liu, Qi Min Wang, Jiao Jiao Zheng, Lin Xu, Edward C. Holmes, and Yong Zhen Zhang. A new coronavirus associated with human respiratory disease in China. *Nature*, 579(7798):265–269, feb 2020. ISSN 14764687. doi: 10.1038/s41586-020-2008-3.

[252] Jeffrey L. Hutter and John Bechhoefer. Calibration of atomic-force microscope tips. *Review of Scientific Instruments*, 64(7):1868–1873, sep 1993. ISSN 00346748. doi: 10.1063/1.1143970.

[253] H. J. Butt and M. Jaschke. Calculation of thermal noise in atomic force microscopy. *Nanotechnology*, 6 (1):1–7, jan 1995. ISSN 09574484. doi: 10.1088/0957-4484/6/1/001.

[254] Charles R. Harris, K. Jarrod Millman, Stéfan J. van der Walt, Ralf Gommers, Pauli Virtanen, David Cournapeau, Eric Wieser, Julian Taylor, Sebastian Berg, Nathaniel J. Smith, Robert Kern, Matti Picus, Stephan Hoyer, Marten H. van Kerkwijk, Matthew Brett, Allan Haldane, Jaime Fernández del Río, Mark Wiebe, Pearu Peterson, Pierre Gérard-Marchant, Kevin Sheppard, Tyler Reddy, Warren Weckesser, Hameer Abbasi, Christoph Gohlke, and Travis E. Oliphant. Array programming with NumPy. *Nature*, 585(7825):357–362, sep 2020. ISSN 14764687. doi: 10.1038/s41586-020-2649-2.

[255] John D. Hunter. Matplotlib: A 2D graphics environment. *Computing in Science and Engineering*, 9(3): 90–95, may 2007. ISSN 15219615. doi: 10.1109/MCSE.2007.55.

[256] F Pedregosa, G Varoquaux, A Gramfort, V Michel, B Thirion, O Grisel, M Blondel, A Müller, J Nothman, and G Louppe. Scikit-learn: machine learning in python. arXiv. *arXiv preprint arXiv:1201.0490*, 2012.

[257] Thomas Kluyver, Benjamin Ragan-Kelley, Fernando Pérez, Brian Granger, Matthias Bussonnier, Jonathan Frederic, Kyle Kelley, Jessica Hamrick, Jason Grout, Sylvain Corlay, Paul Ivanov, Damián Avila, Safia Abdalla, and Carol Willing. *Jupyter Notebooks—a publishing format for reproducible computational workflows*, volume 2016. 2016. ISBN 9781614996484. doi: 10.3233/978-1-61499-649-1-87.

[258] L. Livadaru, R. R. Netz, and H. J. Kreuzer. Stretching response of discrete semiflexible polymers. *Macromolecules*, 36(10):3732–3744, may 2003. ISSN 00249297. doi: 10.1021/ma020751g.

[259] William L. Jorgensen, Jayaraman Chandrasekhar, Jeffry D. Madura, Roger W. Impey, and Michael L. Klein. Comparison of simple potential functions for simulating liquid water. *The Journal of Chemical Physics*, 79(2):926–935, aug 1983. ISSN 00219606. doi: 10.1063/1.445869.

[260] Tom Darden, Darrin York, and Lee Pedersen. Particle mesh Ewald: An N·log(N) method for Ewald sums in large systems. *The Journal of Chemical Physics*, 98(12):10089–10092, aug 1993. ISSN 00219606. doi: 10.1063/1.464397.

[261] James C. Phillips, Rosemary Braun, Wei Wang, James Gumbart, Emad Tajkhorshid, Elizabeth Villa, Christophe Chipot, Robert D. Skeel, Laxmikant Kalé, and Klaus Schulten. Scalable molecular dynamics with NAMD. *Journal of Computational Chemistry*, 26(16):1781–1802, dec 2005. ISSN 1096987X. doi: 10.1002/jcc.20289.

[262] S. Izrailev, S. Stepaniants, M. Balsera, Y. Oono, and K. Schulten. Molecular dynamics study of unbinding of the avidin-biotin complex. *Biophysical Journal*, 72(4):1568–1581, apr 1997. ISSN 00063495. doi: 10.1016/S0006-3495(97)78804-0.

[263] Constantin Schoeler, Rafael C. Bernardi, Klara H. Malinowska, Ellis Durner, Wolfgang Ott, Edward A. Bayer, Klaus Schulten, Michael A. Nash, and Hermann E. Gaub. Mapping Mechanical Force Propagation through Biomolecular Complexes. *Nano Letters*, 15(11):7370–7376, nov 2015. ISSN 15306992. doi: 10.1021/acs.nanolett.5b02727.

[264] Marijn T.J. Van Loenhout, Jacob W.J. Kerssemakers, Iwijn De Vlaminck, and Cees Dekker. Non-bias-limited tracking of spherical particles, enabling nanometer resolution at low magnification. *Biophysical Journal*, 102(10):2362–2371, may 2012. ISSN 00063495. doi: 10.1016/j.bpj.2012.03.073.

[265] Julia L. Zimmermann, Thomas Nicolaus, Gregor Neuert, and Kerstin Blank. Thiol-based, site-specific and covalent immobilization of biomolecules for single-molecule experiments. *Nature Protocols*, 5(6): 975–985, may 2010. ISSN 17502799. doi: 10.1038/nprot.2010.49.

[266] Jun Yin, Alison J. Lin, David E. Golan, and Christopher T. Walsh. Site-specific protein labeling by Sfp phosphopantetheinyl transferase. *Nature Protocols*, 1(1):280–285, jun 2006. ISSN 17542189. doi: 10.1038/nprot.2006.43.

[267] Samuel K. Lai, Ying Ying Wang, Denis Wirtz, and Justin Hanes. Micro- and macrorheology of mucus. *Advanced Drug Delivery Reviews*, 61(2):86–100, feb 2009. ISSN 0169409X. doi: 10.1016/j.addr.2008.09.012.

[268] Na Zhu, Dingyu Zhang, Wenling Wang, Xingwang Li, Bo Yang, Jingdong Song, Xiang Zhao, Baoying Huang, Weifeng Shi, Roujian Lu, Peihua Niu, Faxian Zhan, Xuejun Ma, Dayan Wang, Wenbo Xu, Guizhen Wu, George F. Gao, and Wenjie Tan. A Novel Coronavirus from Patients with Pneumonia in China, 2019. *New England Journal of Medicine*, 382(8):727–733, feb 2020. ISSN 0028-4793. doi: 10.1056/nejmoa2001017.

[269] Guillermina R. Ramirez-San Juan, Arnold J.T.M. Mathijssen, Mu He, Lily Jan, Wallace Marshall, and Manu Prakash. Multi-scale spatial heterogeneity enhances particle clearance in airway ciliary arrays. *Nature Physics*, 16(9):958–964, jun 2020. ISSN 17452481. doi: 10.1038/s41567-020-0923-8.

[270] Xuefeng Wang and Taekjip Ha. Defining single molecular forces required to activate integrin and Notch signaling. *Science*, 340(6135):991–994, may 2013. ISSN 10959203. doi: 10.1126/science.1231041.

[271] A. F. Oberhauser, P. E. Marszalek, H. P. Erickson, and J. M. Fernandez. The molecular elasticity of the extracellular matrix protein tenascin. *Nature*, 393(6681):181–185, may 1998. ISSN 00280836. doi: 10.1038/30270.

[272] P. Carl. Forced unfolding modulated by disulfide bonds in the Ig domains of a cell adhesion molecule. *Proceedings of the National Academy of Sciences*, 98(4):1565–1570, feb 2001. ISSN 00278424. doi: 10.1073/pnas.031409698.

[273] Raul Perez-Jimenez, Alvaro Alonso-Caballero, Ronen Berkovich, David Franco, Ming Wei Chen, Patricia Richard, Carmen L. Badilla, and Julio M. Fernandez. Probing the effect of force on HIV-1 receptor CD4. *ACS Nano*, 8(10):10313–10320, oct 2014. ISSN 1936086X. doi: 10.1021/nn503557w.

[274] Paolo Maiuri, Emmanuel Terriac, Perrine Paul-Gilloteaux, Timothée Vignaud, Krista McNally, James Onuffer, Kurt Thorn, Phuong A. Nguyen, Nefeli Georgoulia, Daniel Soong, Asier Jayo, Nina Beil, Jürgen Beneke, Joleen Chooi Hong Lim, Chloe Pei-Ying Sim, Yeh Shiu Chu, Andrea Jiménez-Dalmaroni, Jean François Joanny, Jean Paul Thiery, Holger Erfle, Maddy Parsons, Timothy J. Mitchison, Wendell A. Lim, Ana Maria Lennon-Duménil, Matthieu Piel, and Manuel Théry. The first World Cell Race. *Current Biology*, 22(17):R673–R675, sep 2012. ISSN 09609822. doi: 10.1016/j.cub.2012.07.052.

[275] Tina Wiegand, Marta Fratini, Felix Frey, Klaus Yserentant, Yang Liu, Eva Weber, Kornelia Galior, Julia Ohmes, Felix Braun, Dirk Peter Herten, Steeve Boulant, Ulrich S. Schwarz, Khalid Salaita, E. Ada Cavalcanti-Adam, and Joachim P. Spatz. Forces during cellular uptake of viruses and nanoparticles at the ventral side. *Nature Communications*, 11(1):1–13, jan 2020. ISSN 20411723. doi: 10.1038/s41467-019-13877-w.

[276] Ponraj Prabakaran, Jianhua Gan, Yang Feng, Zhongyu Zhu, Vidita Choudhry, Xiaodong Xiao, Xinhua Ji, and Dimiter S. Dimitrov. Structure of severe acute respiratory syndrome coronavirus receptor-binding domain complexed with neutralizing antibody. *Journal of Biological Chemistry*, 281(23):15829–15836, jun 2006. ISSN 00219258. doi: 10.1074/jbc.M600697200.

[277] Jiří Zahradník, Shir Marciano, Maya Shemesh, Eyal Zoler, Daniel Harari, Jeanne Chiaravalli, Björn Meyer, Yinon Rudich, Chunlin Li, Ira Marton, Orly Dym, Nadav Elad, Mark G. Lewis, Hanne Andersen, Matthew Gagne, Robert A. Seder, Daniel C. Douek, and Gideon Schreiber. SARS-CoV-2 variant prediction and antiviral drug design are enabled by RBD in vitro evolution. *Nature Microbiology*, 6(9):1188–1198, aug 2021. ISSN 20585276. doi: 10.1038/s41564-021-00954-4.

[278] Haolin Liu, Qianqian Zhang, Pengcheng Wei, Zhongzhou Chen, Katja Aviszus, John Yang, Walter Downing, Chengyu Jiang, Bo Liang, Lyndon Reynoso, Gregory P. Downey, Stephen K. Frankel, John Kappler, Philippa Marrack, and Gongyi Zhang. The basis of a more contagious 501Y.V1 variant of SARS-CoV-2. *Cell Research*, 31(6):720–722, jun 2021. ISSN 17487838. doi: 10.1038/s41422-021-00496-8.

[279] Reinhard Schneppenheim, Natalie Hellermann, Maria A. Brehm, Ulrike Klemm, Tobias Obser, Volker Huck, Stefan W. Schneider, Cécile V. Denis, Alexander Tischer, Matthew Auton, Winfried März, Emma Ruoqi Xu, Matthias Wilmanns, and Rainer B. Zotz. The von Willebrand factor Tyr2561 allele is a gain-of-function variant and a risk factor for early myocardial infarction. *Blood*, 133(4):356–365, jan 2019. ISSN 15280020. doi: 10.1182/blood-2018-04-843425.

[280] Frank W.G. Leebeek. A prothrombotic von Willebrand factor variant. *Blood*, 133(4):288–289, jan 2019. ISSN 15280020. doi: 10.1182/blood-2018-11-883488.

[281] Volker Huck, Po Chia Chen, Emma Ruoqi Xu, Alexander Tischer, Ulrike Klemm, Camilo Aponte-Santamaría, Christian Mess, Tobias Obser, Fabian Kutzki, Gesa König, Cécile V. Denis, Frauke Gräter, Matthias Wilmanns, Matthew Auton, Stefan W. Schneider, Reinhard Schneppenheim, Janosch Hennig, and Maria A. Brehm. Gain-of-Function Variant pPro2555Arg of von Willebrand Factor Increases Aggregate Size through Altering Stem Dynamics. *Thrombosis and Haemostasis*, dec 2021. ISSN 03406245. doi: 10.1055/a-1344-4405.

[282] Ashlesha Deshpande, Bethany D. Harris, Luis Martinez-Sobrido, James J. Kobie, and Mark R. Walter. Epitope Classification and RBD Binding Properties of Neutralizing Antibodies Against SARS-CoV-2 Variants of Concern. *Frontiers in Immunology*, 12:2185, jun 2021. ISSN 16643224. doi: 10.3389/fimmu.2021.691715.

[283] Renliang Yang, Yee Hwa Wong, Giang K.T. Nguyen, James P Tam, Julien Lescar, and Bin Wu. Engineering a Catalytically Efficient Recombinant Protein Ligase. *Journal of the American Chemical Society*, 139 (15):5351–5358, apr 2017. ISSN 15205126. doi: 10.1021/jacs.6b12637.

[284] J. Madariaga-Marcos, S. Hormeño, C. L. Pastrana, G. L.M. Fisher, M. S. Dillingham, and F. Moreno-Herrero. Force determination in lateral magnetic tweezers combined with TIRF microscopy. *Nanoscale*, 10(9):4579–4590, mar 2018. ISSN 20403372. doi: 10.1039/c7nr07344e.

[285] Thorsten Hugel, Jens Michaelis, Craig L Hetherington, Paul J Jardine, Shelley Grimes, Jessica M Walter, Wayne Falk, Dwight L Anderson, and Carlos Bustamante. Experimental test of connector rotation during DNA packaging into bacteriophage ϕ29 capsids. *PLoS Biology*, 5(3):0558–0567, 2007. ISSN 15449173. doi: 10.1371/journal.pbio.0050059.

[286] Felix E. Kemmerich, Marko Swoboda, Dominik J. Kauert, M. Svea Grieb, Steffen Hahn, Friedrich W. Schwarz, Ralf Seidel, and Michael Schlierf. Simultaneous Single-Molecule Force and Fluorescence Sampling of DNA Nanostructure Conformations Using Magnetic Tweezers. *Nano Letters*, 16(1):381–386, jan 2016. ISSN 15306992. doi: 10.1021/acs.nanolett.5b03956.

[287] Evan T Graves, Camille Duboc, Jun Fan, François Stransky, Mathieu Leroux-Coyau, and Terence R Strick. A dynamic DNA-repair complex observed by correlative single-molecule nanomanipulation and fluorescence. *Nature Structural and Molecular Biology*, 22(6):452–457, may 2015. ISSN 15459985. doi: 10.1038/nsmb.3019.

Acknowledgements

During the last three years I experienced fun, challenges, and frustration. I have learned a lot both scientifically and beyond science. My experiences and learnings would not have been possible without the help and support of many people. I am genuinely grateful to everyone involved! Special thanks go to:

Jan Lipfert for being a great and supportive supervisor. Thanks, Jan, for keeping your office doors open to always be accessible for questions and discussions. You have created an atmosphere, in which I learned a lot and had a great time. I enjoyed our uncountable discussions on proteins, moppeldocs, and magnetic tweezers almost as much as the wonderful group activities and heated kicker tournaments. Also, thanks for supporting me in applying to various scholarships and attending multiple conferences.

Hermann Gaub for "adopting" me and becoming my second supervisor. Discussing science with you has always been instructive and very interesting for me. It has been a pleasure to intensively work together with you on the SARS projects! Thanks for all the advice you gave me on science as well as my personal career.

Magnus Bauer for being a great colleague and friend. I admire your diligence and dedication to research. Working together with you, I learned many theoretical and technical aspects of single-molecule experiments, and more generally, what thorough scientific work is. Thanks for being happy to help on the ELP protocol and the productive and pleasant collaboration on our SARS projects. I enjoyed the uncountable hours we spent on zoom or on the phone (thanks for giving me your nümbör), talking about science, work attitude, or (jokingly) complaining about how horrible research can be. I also had a lot of fun on the conferences we attended together!

Adina Hausch for the great time we had together in- and outside the lab. Working together with you on so many different projects has always been uncomplicated and productive. But also aside work, I enjoyed the time we spent together during bouldering, cooking, or drinking coffee and I am really looking forward to my first via ferrata together with you! :-)

Samuel Stubhan for being the most enthusiastic person about almost anything - preparation of experiments for physics for refugees (which has always been a lot of fun), the verticoal (which is obviously the best barbecue in the world), or paragliding (which I am looking forward to joining one day). Thanks for all the times you surprised me with some pastry in the basement when I was hangry and frustrated because of unsuccessful experiments.

Sebastian Konrad for all the interesting and funny conversations we had on science and beyond science, and for significantly expanding my vocabulary. I admire your calmness and determination, even if things don't directly work out the way you want them to. Thanks for making me laugh with bad jokes and patiently accepting me as a horrible kicker team mate!

Tamara Ehm for always having time for a nice conversation about our research and reminding me that there are people whose day seems to have more than 24 hours ;-)

My students **Benedikt Böck, Nina Beier, Adina Hausch** and **Bernhard Kirchmair** for being the best students I could imagine. I don't think many PhD students have the luck of not only supervising one, but four excellent students. Each of you was impressively independent, fast-learning, and most importantly: a great person to be around. I enjoyed working together with you on setting up a new MT setup (Bene), and a second, combined fluorescence-MT setup (Nina), working on VWF stem dynamics (Adina), and on bringing AFM and MT together by doing dynamic MT force spectroscopy (Bernhard)!

The whole **LipfertLab** for creating a wonderful work atmosphere. I enjoyed our scientific discussions and all the activities including group trips, slacklining or barbecuing together! Particularly, I would like to thank **Pauline Kolbeck, Willem Vanderlinden**, and **YiYun Lin** for always helping with DNA-related questions.

Achim Löf for being the father of the MT protein experiments at our chair. I am deeply impressed by what

you achieved during your PhD and am grateful that I could build upon your achievements. Working together with you for half a year, I admired how structured and well-organized you went about things. Also on a personal level, I always enjoyed spending time with you (and also Gesa) in Munich as well as in Hamburg.

Steffen Sedlak for being such a fun and competent friend and colleague. I greatly enjoyed working with you on our streptavidin MT project as well as on the beloved film-balance experiment. But more than our joint scientific work, I enjoyed all the times you made me laugh with some stupid (Swabian) joke. This has really been hilarious! :-)

Ellis Durner for always taking the time to help and support me. No matter if we had problems setting up a new magnetic tweezer instrument, or difficulties interpreting our experimental data - you were always an inexhaustible source of advice and help. I am impressed by the diligence in everything you do!

Wolfgang Ott and **Lukas Milles** for respectively introducing ELP linkers and tethered ligands to the chair and thus laying the foundation for our coupling strategy as well as our tethered ligand assay.

Thomas Nicolaus for his endless supply with silanized slides and joyful conversations during my many hours of slide washing. One day, I will buy a lemon tree ;-)

The whole former **Gaub lab** for creating an inspiring work environment. I appreciate the productive and valuable scientific conversations we had during our group seminars and the huge knowledge and experimental skill on single-molecule force spectroscopy that I could profit from. Furthermore, I would like to thank **Sylvia Kreuzer, Sabine Hohenester** and **Barbara Müller** for the constant and patient support with everything concerning administration. Apart from this, I always enjoyed taking a break from science and stopping by your office for having a nice little chat!

Kasia Tych for all the fun times we had measuring Hsp90. I very much enjoyed our conversations on (women in) science, self-confidence, but also on our common hobbies food and bouldering! :-) Also, a huge thanks for encouraging me when I was stressed!

Our collaboration partners in Hamburg: **Tobias Obser, Maria Brehm, Reinhard Schneppenheim** and **Gesa König** for all the VWF constructs that you sent us and the interesting and valuable discussions we had on VWF.

Our collaboration partners in the US: **Rafael Bernardi, Marcelo Melo**, and **Priscila Gomes** for the SMD simulations on the SARS-CoV:ACE2 interactions and countless hours of zoom discussions where you presented your results and patiently explained them to us. Thanks for finally solving the riddle, why Magnus' and my data are not fitting together!

The **Faculty of physics** for supporting me with the LMU mentoring scholarship. This allowed me to attend interesting conferences in Les Houches and San Diego. Here, I was both able to get insight into the fascinating research of other groups as well as get valuable input for my own research. Furthermore, the program allowed me to choose a mentor. I would really like to thank **Bettina Lotsch** for offering to become my mentor and visit you and your group in Stuttgart. I am deeply impressed by what you achieved during your (short but very steep) career and sincerely enjoyed talking to you about (women in) science.

The **Center for NanoScience** for bringing together young, motivated students at the interface of physics, biology and chemistry and thus fostering vivid interdisciplinary discussion. I enjoyed my role as CeNS student representative at the side of **Annalena Salditt** and **Lennart Grabenhorst**, where we organized some cool events despite the ongoing pandemic. Special thanks also to **Susanne Hennig**, without whom all of this would not be possible. It has always been a pleasure working together with you, Susanne, but also privately chatting while eating ice or going hiking in the Kleinwalsertal!

All the researchers I have met and worked with before starting my PhD. I am especially grateful to **Anita Reiser** and **Joachim Rädler** who were the supervisors of my Bachelors thesis and who arouse my fascination for research. This fascination was increased during my Masters thesis in the lab of **Sarah Bohndiek** in Cambridge. Here, **Calum Williams** had the largest influence on my development towards becoming an *independent researcher*. Thanks, Calum, for challenging and encouraging me, for motivating me and eventually convincing

me that I can and should do a PhD!

My friends and companions during the physics Bachelors and Masters. Particularly the Huhnfriendshipgang with **Freddy** and **Fred**, without whom I would definitely have quit studying physics before the end of the first term.

My family for supporting me throughout my whole physics studies and showing active interest in my work. Thanks for making me laugh about my failures and constantly reminding me not to take things too seriously.

Freddy for giving me the best support I can imagine. Thanks for comforting me when I was discouraged and celebrating with me when I was enthusiastic. You patiently listened to all my problems and tried to help me with finding solutions - sometimes even by coming to the lab and helping me to align optics :-)